Thermoeconomic Modeling and Parametric Study of Hybrid Solid Oxide Fuel Cell – Gas Turbine – Steam Turbine Power Plants Ranging from 1.5 MWe to 10 MWe

Alexandros Arsalis

Thesis submitted to the faculty of the
Virginia Polytechnic Institute and State University
in partial fulfillment of the requirements for the degree of

Master of Science
in
Mechanical Engineering

Chair: Dr. Michael R. von Spakovsky
Dr. Michael W. Ellis
Dr. Douglas J. Nelson

January 10, 2007
Blacksburg, Virginia

Keywords: Solid oxide fuel cells (SOFC), hybrid fuel cell systems, thermoeconomic analysis, thermodynamic analysis, synthesis, design

Thermoeconomic Modeling and Parametric Study of Hybrid Solid Oxide Fuel Cell – Gas Turbine – Steam Turbine Power Plants Ranging from 1.5 MWe to 10 MWe

Alexandros Arsalis

Abstract

Detailed thermodynamic, kinetic, geometric, and cost models are developed, implemented, and validated for the synthesis/design and operational analysis of hybrid solid oxide fuel cell (SOFC) – gas turbine (GT) – steam turbine (ST) systems ranging in size from 1.5 MWe to 10 MWe. The fuel cell model used in this thesis is based on a tubular Siemens-Westinghouse-type SOFC, which is integrated with a gas turbine and a heat recovery steam generator (HRSG) integrated in turn with a steam turbine cycle. The SOFC/GT subsystem is based on previous work done by Francesco Calise during his doctoral research (Calise, 2005). In that work, a HRSG is not used. Instead, the gas turbine exhaust is used by a number of heat exchangers to preheat the air and fuel entering the fuel cell and to provide energy for district heating. The current work considers instead the possible benefits of using the exhaust gases in a HRSG in order to produce steam which drives a steam turbine for additional power output.

Four different steam turbine cycles are considered in this M.S. thesis work: a single-pressure, a dual-pressure, a triple-pressure, and a triple-pressure with reheat. The models have been developed to function both at design (full load) and off-design (partial load) conditions. In addition, different solid oxide fuel cell sizes are examined to assure a proper selection of SOFC size based on efficiency or cost. The thermoeconomic analysis includes cost functions developed specifically for the different system and component sizes (capacities) analyzed. A parametric study is used to determine the most viable system/component syntheses/designs based on maximizing total system efficiency or minimizing total system life cycle cost.

Acknowledgements

I would like to thank my advisor Dr. Michael R. von Spakovsky for giving me the opportunity to write a thesis in the area of fuel cell systems. Without his tireless interest and continuous guidance the completion of this thesis work would have been impossible.

I would also like to thank Dr. Michael W. Ellis, and Dr. Douglas J. Nelson for serving in my committee.

Special thanks to Dr. Francesco Calise for his assistance with the application of the computerized simulation to the present research work. His suggestions and insights are greatly appreciated.

Thanks to Manousos Valyrakis for helping me with many graphs and tables included in the present research work.

Finally, I would like to emphasize my love and encomium to my family for their continuous encouragement in idiomorphic times. My efforts would have been fruitless without their zeal to support me throughout this difficult scope.

Alexandros Arsalis

Table of Contents

List of Figures

List of Tables

Nomenclature

a	Activity
A	Heat transfer area, m^2
A_{cell}	Cell active area, m^2
A_{cr}	Cross-sectional area, m^2
A_s	Bundle cross-flow area, m^2
B	Baffle spacing, m
Bo	Boiling number
c_p	Specific heat, kJ/kg-K
C_j	Cost of the j-component, $
$C_{\min}$	Minimum heat capacity, kJ/K
$C_{\max}$	Maximum heat capacity, kJ/K
C_p	Concentration, kg/m^3
C_r	Heat capacity ratio
CL	Tube layout constant
Co	Convection number
CTP	Tube count calculation constant
d_i	Internal diameter, m
d_o	External diameter, m
D_{eq}	Shell-side equivalent diameter, m
D_m	Mean diameter, m
D_s	Shell diameter, m
$\tilde{ex}_{ch}$	Molar-specific chemical energy, kJ/kmol
ex_{ph}	Mass-specific physical energy, kJ/kg
E	Theoretical maximum voltage, v
E_0	Electromotive force (EMF) at standard pressure, v
$\dot{E}_{inlet}$	Inlet energy rate, kW
$\dot{E}_{outlet}$	Outlet energy rate, kW
$\dot{E}_{react}$	Reaction energy rate, kW
f	Fanning friction factor
f_{p_i}	Heat exchanger pressure factor
f_{p_j}	Piping pressure factor
f_T	Temperature factor

F Faraday's constant, 96,439 C/moles of electrons

Fr Froude number

$\overline{g}$ Gibbs-specific molar energy, kJ/kmol

G_s Shell-side mass velocity, m/s

G_{tube} Tube-side mass velocity, m/s

h Specific enthalpy, kJ/kg

$\overline{h}$ Specific molar enthalpy, kJ/kmol

h_m Mean diffusion coefficient

h_m^j Heat transfer coefficient of the j-component, W/m^2-^{o}C

i Current density, mA/m^2

i_l Limiting current density, mA/m^2

i_n Internal and fuel crossover equivalent current density, mA/m^2

i_0 Exchange current density, mA/m^2

I Current, A

k Thermal conductivity, kW/m-K

k_0 Frequency factor, kmol/mm^2-Pa.s

K_i LMTD correction factor, kW/K

K_{react} Reaction rate constant

K_{ref} Steam methane reforming reaction equilibrium constant

K_{shift} Water-gas shift reaction equilibrium constant

L Length, m

L_R Reactor length, m

$\dot{m}_c$ Corrected mass flow rate, kg/s

$\dot{m}$ Mass flow rate, kg/s

n_e Number of electrons reacted

$\dot{n}$ Molar flow rate, kmol/s

n_{passes} Number of passes

n_t Number of tubes

N Rotor speed, rpm

N_c Corrected rotor speed, rpm

NTU Number of transfer units

Nu Nusselt number

p Pressure, bar

P_T Pitch, m

Pr Prandtl number

q'' Heat flux, kW/m^2

$\dot{Q}$ Heat transfer rate, kW

r Area-specific resistance, Ω

R	Molar gas constant, 8.31 kJ/kmol	$\overline{y}_j$	Mean molar fraction of the j_{th}-component
R_f	Fouling resistance, m^2-^oC/W	y_j	Molar fraction of the j_{th}-component
R_t	Total thermal resistance, m^2-^oC/W	z	Anode electrochemical reaction rate coordinate
Re	Reynolds number		
s	Specific entropy, kJ/kg-K		
SC	Steam-to-carbon ratio		
t	Temperature, ^oC		
t_w	Tube wall thickness, cm		
T	Temperature, K		
$T_{reactor}$	Reactor temperature, K		
T_s	Temperature of the solid structure, K		
U	Overall heat transfer coefficient, W/m^2-^oC		
V	Actual fuel cell potential, v		
V_{act}	Activation overvoltage, v		
V_{cell}	SOFC voltage, v		
V_{conc}	Concentration overvoltage, v		
V_{ohm}	Ohmic overvoltage, v		
w	Fluid velocity, m/s		
$\dot{W}$	Power output, kW		
x	Methane reaction rate coordinate		
y	CO reaction rate coordinate		

Greek

α	Charge transfer coefficient	ξ	Resistivity pre-exponential constant, Ω.cm
γ	Exchange current density constant, mA/cm^2	ρ	Cell electrical resistivity, Ω/cm
γ_{compr}	Compressor polytropic process exponent	ρ_m	Mean density, kg/m^3
γ_{GT}	GT polytropic process exponent	ς_{CH_4}	Degree of demethanization
δ	Cell material thickness, cm	χ	Mass quality
$\Delta\bar{g}_f^0$	Gibbs free energy of formation, kJ/kmol		
$\Delta\bar{h}_f^0$	Enthalpy of formation, kJ/kmol		
ΔT_{lm}	Logarithmic mean temperature difference, K		
ΔT_w	Saturation and fouling surface temperature difference, K		
ε	Effectiveness		
η_{ex}	Exergetic efficiency		
η_{IRSOFC}	IRSOFC energetic efficiency		
η_s	Isentropic efficiency		
$\eta_{\max}$	Theoretical maximum cell efficiency		
λ	Resistivity exponential constant, K		
μ	Dynamic viscosity, kg/m-s		
ν	Stoichiometric coefficient		

Subscripts/Superscripts

0	Reference point	*Gen*	Electric Generator
a	Ambient	*GT*	Gas turbine
actual	Actual	*h*	Hot stream
anode	SOFC anode	*HE*	Heat exchanger
aux	Auxiliary	*HEC*	Counter-flow heat exchanger
A	Anode	*HP*	High pressure
c	Cold stream	*HRSG*	Heat recovery steam generator
cap	Capital	*i*	Inlet stream
cathode	SOFC cathode	*ins*	Insurance
cell	SOFC stack	*int*	Interest on outside capital
compr	Compressor	*inv*	Inverter
cw	Cooling water	*IP*	Intermediate pressure
C	Cathode	*IRSOFC*	Internal Reforming SOFC
COND	Condenser	*l*	Liquid
dep	Depreciation	*liq*	Saturated water
dual	Dual-pressure cycle	*LP*	Low pressure
DEA	Deaerator	*m*	Mean
ext	Extraction	*mai*	Maintenance
EC	Economizer	max	Maximum
EV	Evaporator	min	Minimum
f	Formation	*o*	Outlet stream
gas	Gas-side	*ope*	Operating

piping	HRSG piping
PR	Pre-reformer
PUMP	Pump
ref	Reference point
RH	Reheat
s	Solid structure
single	Single-pressure cycle
steam	Steam-side
ST	Steam turbine
SU	Superheater
tax	Taxation
tot	Total
triple	Triple-pressure cycle
vap	Saturated vapor
w	Tube wall surface

1 Introduction

The fuel cell is an electrochemical device, which converts the chemical energy of a fuel into electric power directly, i.e., without any intermediate conversion processes. Its benefits are that the electric power can be generated at high energy efficiency and with very low environmental emissions both at full and partial loads. For the last thirty years, federal and industrial support to develop fuel cell technologies has been considerable. The use of fuel cell systems has been strongly promoted in the United States and Japan for medium scale cogeneration plants. Nowadays, this interest has been extended to a smaller scale, namely, that at the residential level. At the same time, increased interest has arisen for the application of fuel cell systems to automotive propulsion and auxiliary power, although there is not yet a clear choice on the direct use of hydrogen stored on board or the installation of a hydrogen generating plant on board. The current research work of this thesis is focused on the use of this newly emerging technology for stationary cogeneration applications, in particular residential/commercial applications.

1.1 History of Fuel Cells

William Robert Grove, a British jurist with a hobby in science, in 1839 in Swansea, Wales, first discovered the principle of the fuel cell. Grove utilized four large cells, each containing hydrogen and oxygen, to produce electric power which was then used to split the water in the smaller upper cell into hydrogen and oxygen (see Figure 1.1). Fifty years later, Ludwig Mond and Charles Langer, who first used the term "fuel cell" in 1889, tried to build a power generating device using air and industrial coal gas. However it was not until 1932 that Francis Bacon developed the first successful fuel cell. It would take another 27 years to apply their invention to a practical application, a 5 kWe system capable of powering a welding machine. More recently, NASA used fuel cells during the 1960s to power onboard electronics for the Gemini and Apollo spacecrafts. In fact, NASA still uses fuel cells to provide electricity and water for its space shuttle missions.

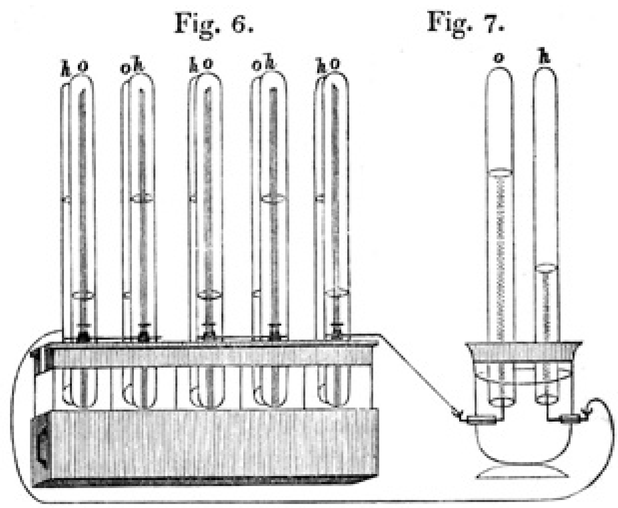

Figure 1.1. William Grove's drawing of an experimental "gas battery" (Grove, 1843).

It is expected that fuel cells will break through economic and technical barriers in a wide range of applications including among others: stationary power generation, portable devices, and hybrid vehicular applications. For energy providers, fuel cells offer a safe, efficient, and reliable power solution that addresses critical issues such as deregulation, rising energy costs, increasing load factors, severe power outages, and increasing power consumption. For vehicle manufacturers, fuel cells represent the single greatest technology advancement in the last 100 years to replace the internal combustion engine and address growing environmental concerns over issues such as global warming and air pollution.

1.2 Fuel Cell Types

The classification of fuel cells is primarily based on the kind of electrolyte they utilize. This determines the kind of electrochemical reactions that take place in the cell, the kind of catalysts required, the fuel cell operating temperature and pressure range, the fuel required, and other factors. In turn, these characteristics affect the applications for which these cells are most suitable. There are several types of fuel cells currently under development, each with its own advantages, limitations, and potential applications.
The main fuel cell types are:

- Polymer Electrolyte Membrane Fuel Cells

- Direct Methanol Fuel Cells
- Alkaline Fuel Cells
- Phosphoric Acid Fuel Cells
- Molten Carbonate Fuel Cells
- Solid Oxide Fuel Cells
- Regenerative Fuel Cells

1.3 Solid Oxide Fuel Cells

The first breakthrough for the solid oxide fuel cell (SOFC) came in the late 1890s when Walther Hermann Nernst discovered various types of conductivity in doped zirconium oxide (Singhal and Kendall, 2003). He also discovered that the material emitted a white light when hot, and this led to a patented light bulb. The patent was later sold to George Westinghouse who produced light bulbs until tungsten filament based lamps took over (Singhal and Kendall, 2003). However, it was not until the 1930s that a SOFC was demonstrated; and in the late 1950s, Westinghouse started experimenting with stabilized zirconia in fuel cells (Singhal and Kendall, 2003). The research has continued until today, and Siemens Westinghouse Power Corporation is today considered to be the world leader in SOFC technology. Siemens Westinghouse is also the first company to demonstrate a SOFC-GT power cycle, but growing interest is steadily increasing the competition.

The SOFC has to compete with existing heat engines that are currently used to produce electricity from hydrocarbon combustion. Such engines operate by burning fuel to heat a volume of gas, followed, for example, by the expansion of the hot gas in a piston or gas turbine device driving a dynamo. Although for many applications conventional heat engines are in theory less efficient and more polluting than fuel cells, they possess a significantly lower initial cost as a result of rigorous development, optimization, and mass manufacturing for almost a century. Ostwald got it famously wrong in 1892 when he said that 'the next century will be one of electrochemical combustion' (Singhal and Kendall, 2003). Fuel cells are still significantly more costly than conventional engines which can be manufactured for less than \$50 per kWe (Singhal and Kendall, 2003).

In the 1980s, it was envisaged that SOFCs could compete commercially with other power generation systems, including large centralized power stations and smaller cogeneration units. This has not yet happened because costs have remained high despite large injections of government funding for SOFC development in the USA, Japan and Europe (Fuel Cell Handbook, 2004).

One of the most promising applications of SOFCs for the future is in combination with a gas turbine as described in Chapters 2 and 3. The SOFC stack forms the combustor unit in a gas turbine system. Compressed air is fed into the SOFC stack where fuel is injected and electrical power drawn off. Operating at 50 plus percent conversion of fuel to electrical power, this SOFC then provides pressurized hot gases to a turbine operating at 35 percent electrical efficiency. The overall electrical conversion efficiency of this system can approach 65 plus percent, which can be further improved by adding a steam turbine cycle to drive the overall electrical efficiency into the mid seventies.

1.4 Thesis Objectives

The overall goal of this research work is to make a thorough investigation of the design and performance characteristics of hybrid power system configurations consisting of a solid oxide fuel cell, gas turbine, and steam turbine for stationary power applications which provide power to a large number of residence or commercial buildings. For example, a 10 MWe hybrid system can fulfill the needs of 2000 family residences based on an average four person family residence in the US which requires on average 5 kWe. To model and then analyze the hybrid system configurations as realistically as possible, detailed system and component thermodynamic, kinetic, geometric, and cost models will be developed, implemented, and validated and then used to conduct a parametric analysis of the key system and component parameters. This thesis work will, thus, investigate both thermodynamically (i.e. by maximizing efficiency) and economically (i.e., by minimizing total life cycle cost) the advantages that such SOFC-GT-ST hybrid systems might have over more conventional GT-ST combined cycle systems, standalone SOFC systems, and hybrid SOFC-GT systems. Thus, the major objectives of this thesis are the following:

- Become familiar with the system and component thermodynamic, kinetic, geometric and cost models and software for a 1.5 MWe hybrid SOFC – gas turbine cycle developed by Calise et al. (2006);
- Develop a number of realistic hybrid SOFC – gas turbine – steam turbine system configurations in the range of 1.5 MWe to 10 MWe;
- Create the thermodynamic models for the components of the steam turbine cycle configurations considered in this research, i.e., single, dual, and triple pressure with and without reheat;
- Implement and validate these models in the software developed by Calise et al. (2006) mentioned above;
- Develop, implement, and validate geometric models for the off-design behavior of the steam cycle components and system configurations; which will make possible the simulation and parametric analysis of the hybrid system over an entire operational cycle; these geometric models will be based on classic methods such as effectiveness-NTU and LMTD for the heat exchangers, as well as on performance maps for the turbomachinery;
- Expand the hybrid SOFC-GT-ST system's net power output to larger plant sizes; these will include 5 MWe and 10 MWe net power output in addition to 1.5 MWe.
- Develop, implement, and validate appropriate component cost models, which relate cost to appropriate decision (synthesis/design and operational) variables.
- Perform separate thermoeconomic and thermodynamic parametric studies to minimize the total life cycle cost and maximize the total system efficiency.
- Analyze the results and draw conclusions.

2 Hybrid Fuel Cell Systems

Fuel Cells appear to be very attractive power generation systems, promising highly efficient electricity generation with very low negative effects to the environment. These efficiencies can be further increased by integration of high temperature fuel cells (SOFCs, MCFCs) into hybrid cycles. While a wide variety of potential bottoming technologies for the exploitation of the high temperature exhaust gases waste heat is available, a lot of research effort is needed to determine the optimal integration of well established technologies with these very novel conversion devices.

Hybrid fuel cell systems are combinations of conventional heat engines (e.g., gas turbines, steam turbines, etc.) and different types of fuel cells (e.g., SOFC, MCFC) or even combinations of two different types of fuel cells (e.g., a SOFC and a PEMFC).

These aforementioned systems are extremely efficient. They have the potential of achieving efficiencies near or even higher than 70 percent. This also means that they can be environmentally friendly due to their reduced emissions. With such capabilities these engines are better than any other known engines today. They are a perfect match for stationary applications (centralized or distributed) while there are still significant difficulties in utilizing them in mobile and vehicular applications due to issues primarily of cost. Fortunately, however, during the last few years, this cost has dropped significantly with the use of cheaper materials and is expected to drop even lower with the expected mass manufacture and commercialization of these systems. Also, due to the high full and part load efficiency potential, the operating cost is already lower compared to conventional power generating systems.

2.1 Hybrid Solid Oxide Fuel Cell – Gas Turbine Cycles

This hybrid system combines a SOFC with a low-pressure-ratio gas turbine, air compressor, fuel compressor, pre-reformer, combustor, ejector, and possible heat exchangers for air and fuel preheating. Such a system is shown in Figure 2.1 (Calise et al., 2006). The combination of the SOFC and gas turbine operates by using the rejected thermal energy and residual fuel from the fuel cell to drive the gas turbine. The unfired gas turbine replaces its conventional combustor with an external one in which the fuel cell exhaust gases are mixed with the residual fuel and burned, raising the gas turbine inlet temperature.

With such a combination, there is flexibility for different cycle configurations. A direct system is one which has the SOFC subsystem containing the combustor for the gas turbine while the gas turbine with some generation serves as the balance-of-plant for the fuel cell. In turn, the gas turbine exhaust can be used as an oxygen supply. A different configuration is an indirect system where high temperature heat exchangers are used. In the indirect mode, the recuperator transfers fuel cell exhaust energy to the compressed air supply, which in turn drives the turbine. The expanded air is supplied to the fuel cell. The indirect mode uncouples the turbine compressor pressure and the fuel cell operating pressure, which increases flexibility in turbine selection.

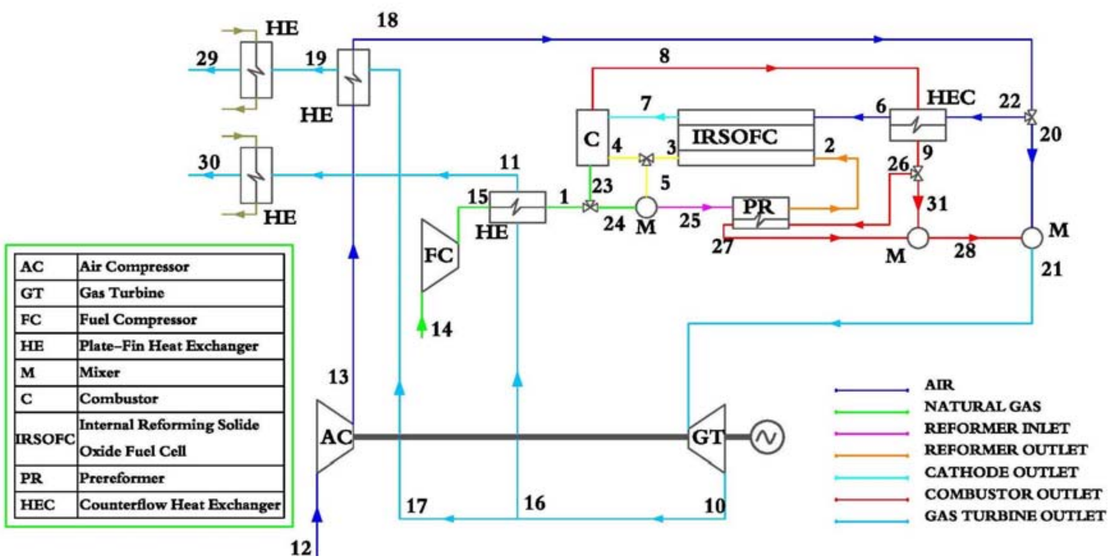

Figure 2.1. A 1.5 MWe hybrid SOFC-GT system (Calise et al., 2006).

In the hybrid cycle shown in Figure 2.1, air is compressed by the air compressor up to the cell operating pressure, is then preheated in the plate-fin heat exchanger, and is brought subsequently to the cathode compartment of the SOFC stack. In the same way, fuel (natural gas) is compressed by the fuel compressor, preheated in the fuel-exhaust gas plate-fin heat exchanger, and then brought to the anode compartment of the stack. Both fuel and air can by-pass the fuel cell: a certain amount of fuel flow can be brought directly to the combustor by-passing the electrochemical reaction occurring within the stack; excess air can be brought to the gas turbine. In the stack, fuel is mixed with the anode re-circulation stream in order to support the steam reforming reaction in the pre-reformer and in the anode compartment of the fuel cell. The energy required to support the pre-reforming reaction of the natural gas-water mixture is derived from the hot stream of exhaust gases. Any non-reformed fuel is then internally reformed within the anode compartment of the SOFC stack to produce hydrogen which then along with that produced in the pre-reformer participates in the electrochemical reaction which occurs at the anode.

On the cathode side of the cycle, air is first preheated by a counter-flow heat exchanger and then brought into the annulus of the SOFC air pipe where at the three phase boundaries of the electrode, the cathode electrochemical reactions occur. The ionic and electronic currents which are generated then complete a circuit from which DC power is generated. This DC power is converted in a more suitable AC current by an inverter, while energy released in the fuel cell in a heat interaction is used by the internal reforming reaction and to heat-up the fuel cell stack. Anode and cathode outlet streams meet at the top of the fuel cell where the combustor is placed. Non-reacted fuel and depleted air participate in the combustion reaction within the catalytic burner. The exhaust gases from this combustor are used first to preheat air in a counter-flow heat exchanger, then to supply heat to the pre-reforming reaction and finally to generate mechanical power in the gas turbine and in turn electricity in the electrical generator. The exhaust exiting the GT is then used to preheat both the fuel and air streams and finally to provide heat available for cogeneration via the two subcooled water-gas plate-fin heat exchangers. The overall effect of the working principle of the plant is the conversion of fuel and air into electrical power (part by the stack and part by the GT) and low-temperature heat (Calise et al., 2006, Calise, 2005).

In terms of performance such a system can reach efficiencies of 68% for a 1.5 MWe system operating close to 1000 ^{o}C and 8 bar SOFC operating temperature and pressure, respectively. The SOFC contributes 74.8% of the total power output while the remaining 25.2% is contributed by the GT (Calise et al., 2006).

The most significant variables characterizing the cycle are the fuel cell operating temperature range and the temperature and pressure at the gas turbine expander inlet. These variables are directly related to certain operating variables: the air/fuel ratio entering the fuel cell, the fraction of the fuel leaving the cell unburned, and the temperature difference between the combustion products and air at the high temperature end of the recuperative heat exchanger. The operating variables must be selected and controlled to allow effective operation of the fuel cell, combustor, and gas turbine (Fuel Cell Handbook, 2004).

The main advantages of such a system include a simple cycle arrangement with a minimum number of components, low compressor and turbine pressure ratio, low fuel cell operating pressure, low turbine inlet temperature without turbine rotor blade cooling, simple heat removal arrangements for the SOFC, maximum fuel cell conversion, and compatibility to small scale power generation systems.

The main disadvantages are rigorous compressor and turbine design compatible with SOFC requirements, the need for a large gas to gas heat exchanger for high temperature heat recuperation, and finally the total efficiency and net work output of the system is sensitive to SOFC, gas turbine, and compressors efficiencies, pressure losses, and temperature differences.

The first complete SOFC-GT hybrid system was delivered by Siemens-Westinghouse to Southern Californian Edison in May of 2000 (Larminie and Dicks, 2003). Additional systems have followed in North America and Europe.

2.2 Hybrid Solid Oxide Fuel Cell – Steam Turbine Cycles

The arrangement shown in Figure 2.2 (Fuel Cell Handbook, 2004), employs a heat recovery steam generator operating on the exhaust combustion product stream from the solid oxide fuel cell and combustor at atmospheric pressure. This exhaust stream first provides the heat required to preheat and reform the fuel (methane), providing carbon monoxide and hydrogen at the required temperature to operate the fuel cell. Partially combusted fuel from the cell is recycled to provide water to reform the fuel. Depleted air from the cell exhaust is recycled to the air feed stream to raise its temperature to the desired value at the cell inlet. The operating conditions for this cycle are identical to those for the combined SOFC-GT cycle described in section 2.1.

The performance results for this configuration indicate that the efficiency of the overall system defined as the net work output divided by the lower heating value of the fuel is increased from 57 percent for the fuel cell alone to 72 percent for the hybrid system defined as the net work output divided by the lower heating value of the fuel. The fuel cell contributes 79.1% and the steam turbine 20.9% of the total work output. The steam turbine cycle heat-fuel recovery arrangement is less complex but less efficient than the combined gas turbine-steam turbine cycle system discussed in Section 2.3 and more complex and less efficient than the gas turbine cycle of the hybrid arrangement in Section 2. However, it possesses the advantage of eliminating the requirement for a large, high temperature gas-to-gas heat exchanger. Also, in applications where cogeneration and the heat supply are needed, it provides a source of steam.

Since in the hybrid system of Figure 2.2, energy is recovered from the exhaust gases to heat and reform the fuel feed, the temperature of the hot gas entering the heat recovery steam generator is significantly lower than in the hybrid SOFC-gas turbine-steam turbine cycle configuration. Therefore, an increased surface area is required in the heat recovery steam generator for this SOFC-steam turbine cycle power system.

2.3 Hybrid Solid Oxide Fuel Cell – Gas Turbine – Steam Turbine Cycles

In this hybrid cycle, shown in Figure 2.3 (Fuel Cell Handbook, 2004), a SOFC, a gas turbine, and a steam turbine are combined. The fuel cell has the role of being the topping cycle as in the previous configurations (Sections 2.1 and 2.2). However, in this system, the gas turbine has a dual role: it is the bottoming cycle with respect to the fuel cell, but it is also a topping cycle with respect to the steam turbine.

Similar to the previous configurations, air and fuel streams enter the cathode and anode compartments of the SOFC. The separate streams leaving the cell enter the combustor and then the gas turbine. The gas turbine exhaust flows into the heat recovery steam generator and then to the stack. The steam produced drives the steam turbine. It is then condensed and pumped back to the steam generator.

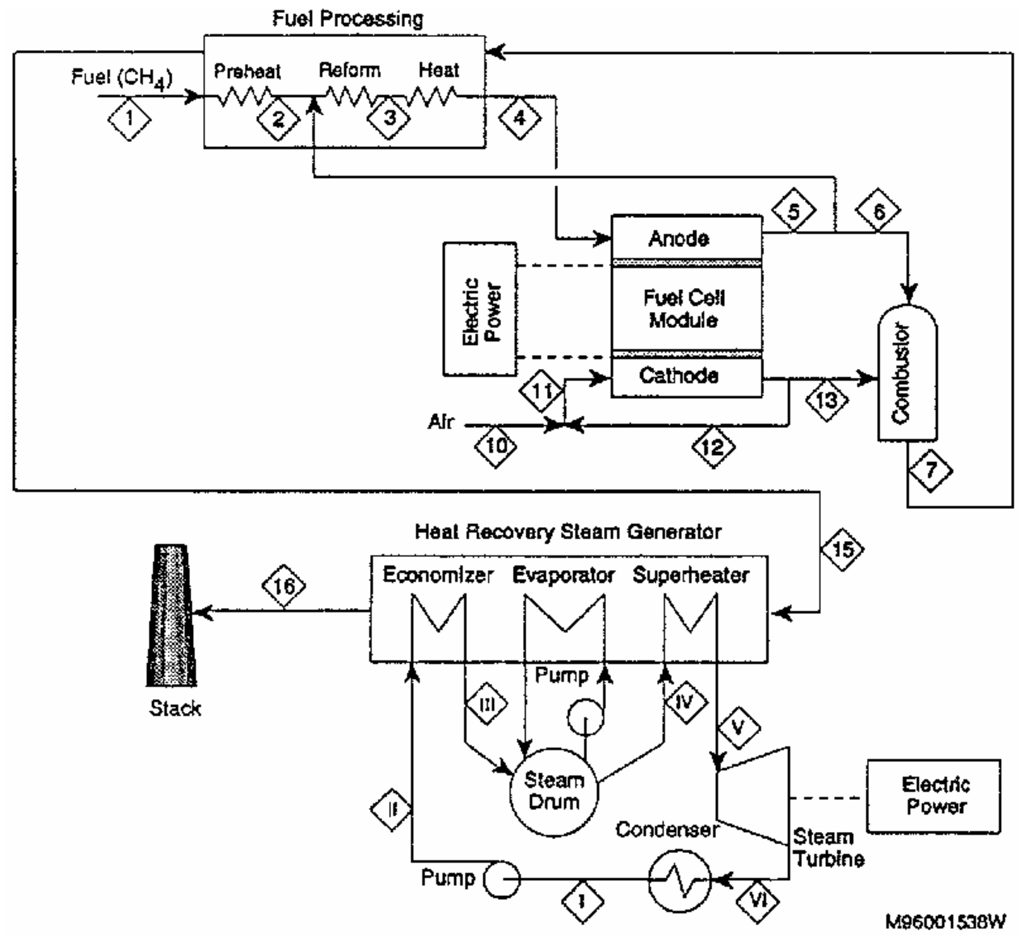

Figure 2.2. A hybrid SOFC-steam turbine system (Fuel Cell Handbook, 2004).

The air/fuel ratio entering the fuel cell and the fraction of the fuel consumed in the cell are selected to achieve the desired fuel cell operating temperature range and gas turbine operating temperature and pressure ratio. The latter are selected to correspond with those of a conventional, large-scale, utility gas turbine.

Performance results for this hybrid cycle are given below and are based on the idealized gas and steam turbine cycles illustrated in the T-s diagrams shown in Figure 2.4. For this hybrid cycle, the pressure and the temperature increases during fuel and air compression are significantly greater than in the gas turbine cycle described in Section 2.1. Furthermore, the heating of the air and fuel, the operation of the fuel cell, and the burning of the residual fuel are assumed to occur at constant pressure. The expansion of the combustion product gases in the gas turbine is represented as an adiabatic, reversible (constant entropy) process. Energy is recovered from these gases at nearly constant pressure in the heat recovery steam generator after which they pass out of the system via the stack.

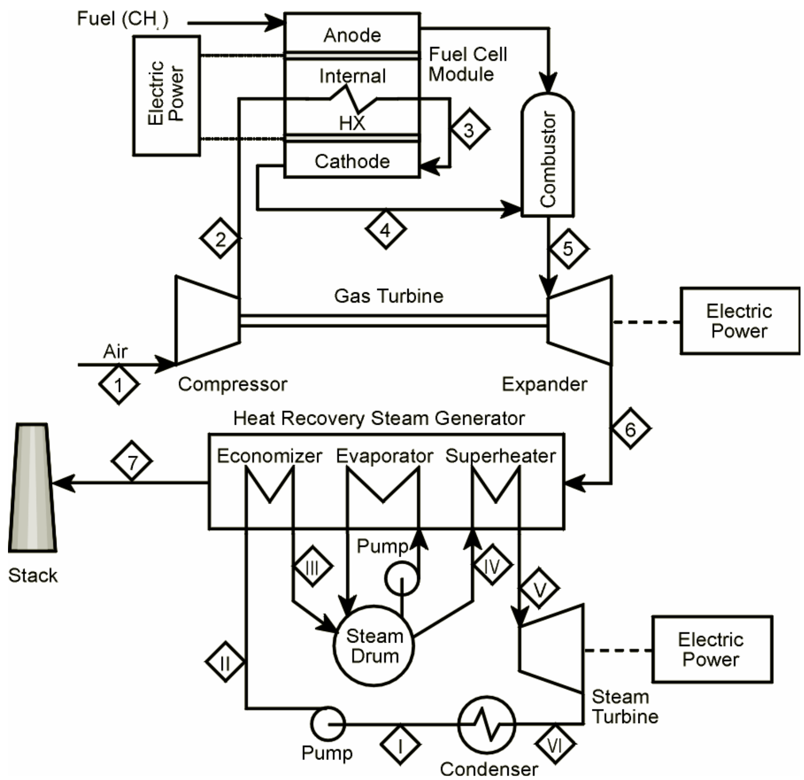

Figure 2.3. A hybrid SOFC-gas turbine-steam turbine system (Fuel Cell Handbook, 2004).

For the steam turbine cycle, a T-s diagram (see Figure 2.4) a single-pressure with superheat but no reheat cycle. The main thermodynamic advantage of the steam turbine bottoming cycle, is the lowered temperature of heat rejection to the environment.

Performance results for this hybrid cycle assume gas turbine compressor and expander efficiencies of 83 percent and 89 percent and a steam turbine efficiency of 90 percent. The principal result is that the efficiency (as defined previously in Section 2.2) of the overall system is increased from 57 percent for the fuel cell alone to 75 percent for the overall system. This combined gas turbine-steam turbine cycle heat-fuel recovery arrangement is significantly more complex than the simple gas turbine cycle approach. It does, however, eliminate the requirement for a large, high temperature gas-to-gas heat exchanger.

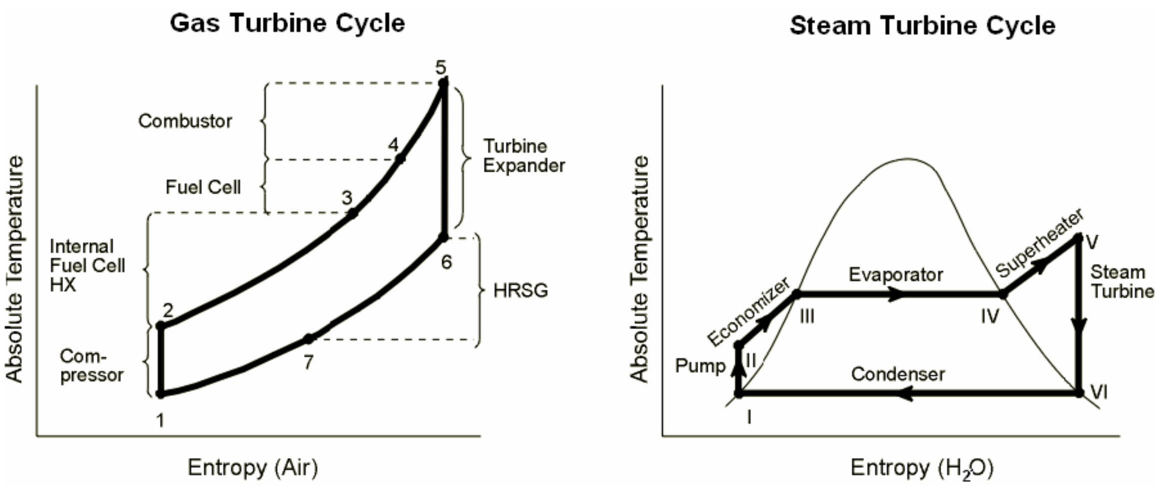

Figure 2.4. A T-s diagram representation of the gas and steam turbine cycles of a hybrid SOFC-gas turbine-steam turbine system (Fuel Cell Handbook, 2004).

The key component between the gas turbine cycle and the steam turbine cycle is the heat recovery steam generator. Its operation is illustrated by the temperature-heat transfer presented plot in Figure 2.5 which shows the evolution in temperature of the hot gases and water as a function of the heat transferred from the combustion product gases to the water in the steam generator. The area between the temperature curves proportional to the irreversibilities resulting from the transfer of energy in a heat interaction across a finite temperature difference. Reducing this area by moving the gas and steam curves closer requires increased heat transfer surface area. Steam reheat and multi-pressure level heat recovery boilers are frequently proposed in order to minimize the losses due to heat transfer irreversibilities.

In general, the heat transfer in an HRSG entails losses associated with three main factors:

1. The physical properties of the water, steam and exhaust gases do not match causing exergetic and energetic losses.
2. The heat transfer surface cannot be infinitely large.
3. The temperature of the feedwater must be high enough to prevent corrosive acids forming in the exhaust gas where it comes into contact with the cold tubes. This

limits the energy utilization by limiting the temperature to which the exhaust gas can be cooled.

The extent to which these losses can be minimized (and the heat utilization maximized) depends on the concept and on the main parameters of the cycle. In a more complex cycle, the heat will generally be used more efficiently, improving the performance but also increasing the cost. In practice, a compromise between performance and cost must always be made (Kehlhofer, 1999). It is these tradeoffs which will be examined in some detail in the multiple hybrid system configurations presented in succeeding chapters.

2.4 Hybrid Molten Carbonate Fuel Cell – Gas Turbine Cycles

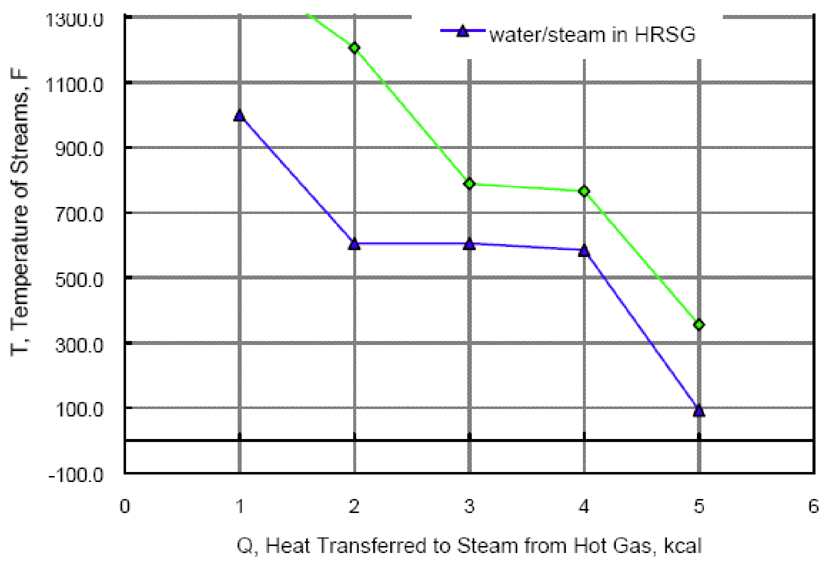

Figure 2.5. Temperature versus heat transferred in the heat recovery steam generator (Fuel Cell Handbook, 2004).

An example of this type of hybrid system is shown in Figure 2.6 (Lunghi, Ubertini, and Desideri, 2001). In this configuration, rejected thermal energy and the combustion of residual fuel from an MCFC is used to drive a gas turbine. A preliminary 5 MWe power plant has been proposed by Lunghi, Ubertini, and Desideri (2001). The reactant gases consist of methane and ambient air. A hydrodesulfurizer removes the sulfur since the fuel cell and its reformer catalysts are not sulfur tolerant. The methane entering the anode is internally steam reformed, producing hydrogen and carbon monoxide. The exothermic oxidation reaction produces heat at the required temperature for fuel reforming while a supported catalyst provides sufficient catalytic activity to sustain the steam reforming reaction at 923 K. Moreover, no external fuel processor is present in the cycle. Steam and methane enter the fuel cell at 673 K.

The fuel cell stack is composed of a certain number of fuel cell units, each consisting of an anode, a cathode, and an electrolyte matrix between them. All reactions in the cell take place at an average temperature of 923 K, which represents the best compromise for reaction kinetics, voltage cell loss, and high temperature corrosion problems. The flow exits the anode at a temperature of 973 K and is sent to a catalytic combustor where the non-oxidized part is burned with the oxygen present in the air blown inside by an electric fan. Twenty percent excess air is required to run the combustor and provide enough oxygen for the electrochemical reduction reactions at the cathode.

In the basic configuration no air preheating is considered. The methane and the steam entering the stack are preheated by the cathode exhaust gases. The combusted gas exits the burner at a temperature of 943 K, and it is used as the oxidant for the cathode side of the cell. The depleted oxidant exits the cathode at about 943 K. The gas turbine bottoming cycle follows a similar path as that described for the hybrid SOFC-GT plant given in Section 2.1. For the hybrid cycle shown in Figure 2.6, a 67 percent overall efficiency is reported in Lunghi, Ubertini, and Desideri (2001).

In summary, MCFC hybrid plants offer further opportunities for significant performance improvements. However, as with other fuel cell systems, a number of technical problems, such as corrosion and electrode stability, have to be solved to increase component durability and reduce cost. More aggressive MCFC full scale power plant tests are needed to achieve a more complete and successful commercial scale demonstration.

2.5 Hybrid Solid Oxide Fuel Cell – Polymer Electrolyte Membrane Fuel Cell Cycles

As mentioned in the introduction of this chapter, there also exists the possibility of combining two different types of fuel cells. In such a hybrid cycle, a high-temperature SOFC is used to produce electricity and carry out the fuel reforming. The anode exhaust stream from the SOFC is then processed by water-gas shift and if needed PROX (preferential oxidation) reactors and supplied to a low-temperature PEMFC. The overall efficiency predicted for the hybrid system is shown to be significantly better (61%) than a reformer-PEMFC system (37-42%) or a SOFC system (52-57%) alone (Dicks et al., 2000). Approximate capital and operating cost estimates for the hybrid system also show significant benefits compared to the other two standalone systems ($645,000 for the hybrid system compared to $911,000 and $795,000 for the PEMFC and SOFC systems, respectively).

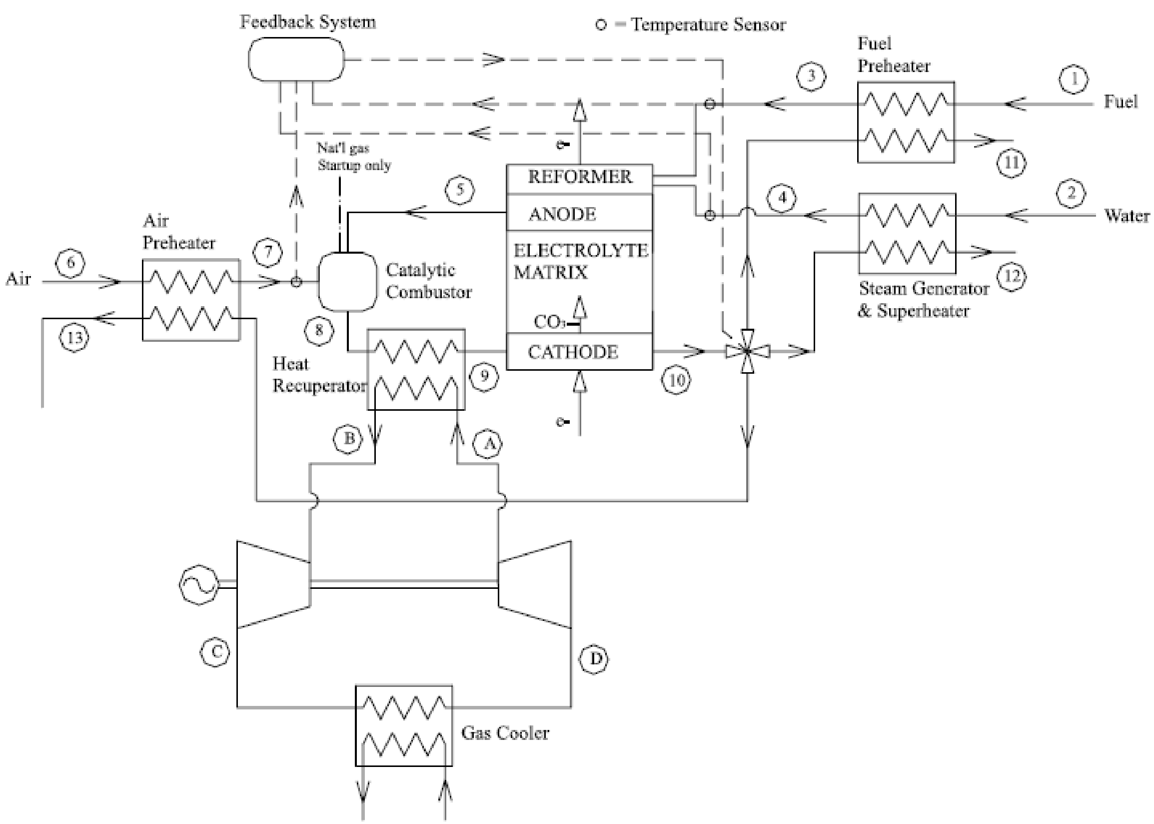

Figure 2.6. A hybrid MCFC-gas turbine system (Lunghi et al., 2000).

An example of a hybrid SOFC-PEMFC system configuration is shown in Figure 2.7 (Dicks et al., 2000). Natural gas enters the SOFC section where catalytic reforming and electrochemical reactions occur. The SOFC stack produces electrical power together with an anode exhaust stream containing unused carbon monoxide and hydrogen. This exhaust stream is cooled and passed to the shift reactors where the carbon monoxide reacts with water to produce carbon dioxide and hydrogen. There is sufficient water in the stream to convert all the carbon monoxide, provided the SOFC fuel utilization exceeds 0.5% (Dicks et al., 2000). When operating at utilizations below this level, water needs to be injected and recovered downstream. After the shift reactors, the remaining traces of carbon monoxide are removed by selective catalytic oxidation (PROX). This is necessary to prevent poisoning of the catalysts used in the PEM stack. The resulting hydrogen-rich stream is cooled to about 70 degrees C before entry to the PEM section. As the anode stream from the PEMFC section contains unused hydrogen, it is reheated and combusted using the air stream to the SOFC cathode and then utilized as an energy source for the fuel reforming in the SOFC section. Dicks et al. (2000) reports, an overall system efficiency of 61 percent for a net power output of 489.7 kW.

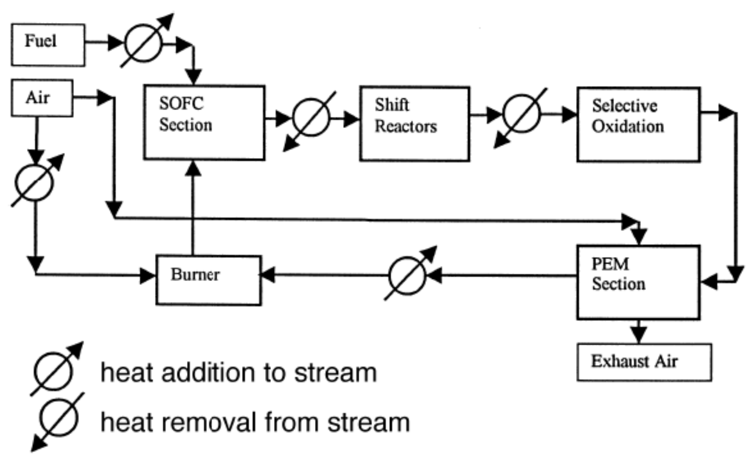

Figure 2.7. A hybrid SOFC-PEMFC system (Dicks et al., 2000).

3 Hybrid SOFC-GT-ST Plant: Configurations and Models

In the preceding chapter a variety of hybrid fuel cell power plants were reviewed. This chapter will focus on a particular type of hybrid plant, namely, a hybrid SOFC-GT-ST cycle. A number of different system configurations are presented and appropriate system and component thermodynamic, kinetic, geometric, and cost models developed.

It is expected that a more complex system will yield increased overall efficiencies, however, at the expense of equipment costs (both capital and maintenance). Thus, in modeling and analyzing the different configurations, a number of system characteristics will be considered. These include

- Total plant efficiency at full and part load;
- Total lifecycle cost;
- Flexibility in operation with varying demands (i.e. electric loads);
- Simple operation;
- Ease of maintenance;
- Investment profitability.

The latter characteristic is of tremendous significance since the hybrid fuel cell power plant will not be successful unless it manages to be competitive with conventional and other novel power generating plants. Therefore, complex systems and expensive components should be minimized as much as possible. The objective of this thesis work is to model, synthesize, and design a hybrid power plant utilizing all the advantages offered by highly promising fuel cell technology minimizing via a parametric study the current high capital costs of these systems and suggesting economically feasible and attractive systems.

As mentioned earlier, during this research work, the modeling and computer code as well as parametric study and optimization results of a previously developed 1.5 MWe hybrid SOFC-GT plant (Calise, 2005; Calise et al., 2004, 2006). This hybrid system is shown in Figure 3.1. The gas turbine exhaust mixture is re-circulated and used to preheat the input air and fuel streams by means of heat exchangers, while the remaining energy recovered to heat water for residential usage, i.e. district heating. In the current research work, this system has been modified and expanded to include a second bottoming cycle, utilizing various heat recovery steam generators and a steam turbine. In fact, four configurations are modeled and analyzed in detail here with the variations occurring with regard to the ST bottoming cycle, i.e. a single pressure level, a dual pressure level, a triple pressure level without reheat and a triple pressure level with reheat. The next section begins with a presentation of these configurations.

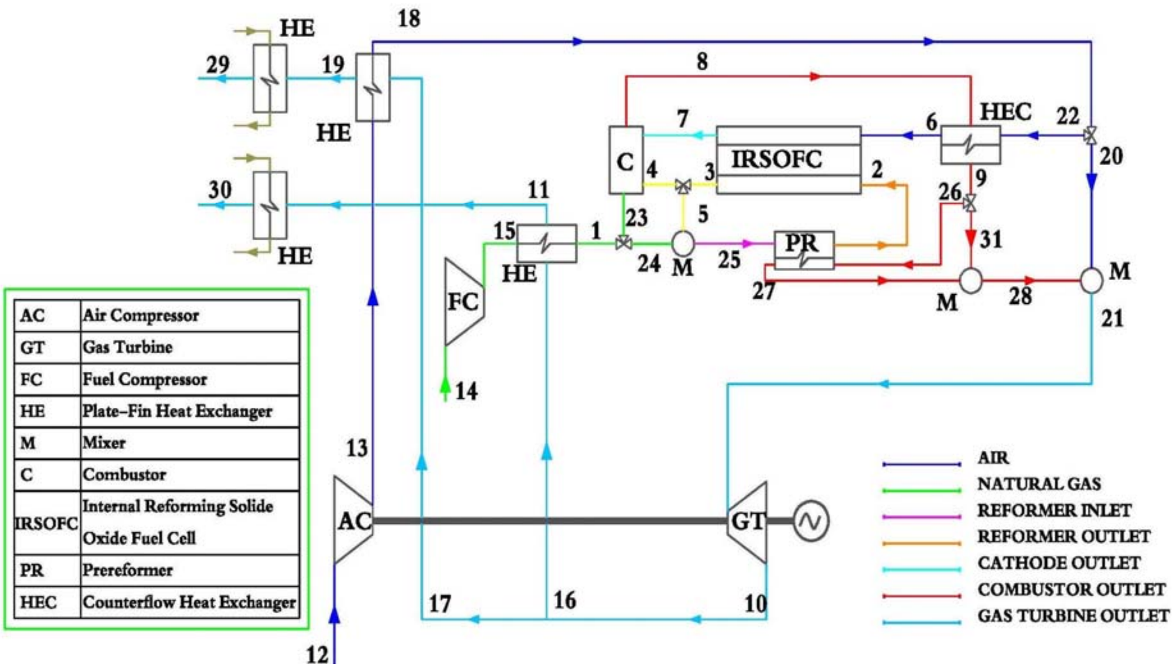

Figure 3.1. SOFC-GT cycle suggested by Calise (Calise, 2006).

3.1 Hybrid System Configurations and Description

There are four configurations under investigation: the only difference between the first three is the pressure level of the heat recovery steam generator, while the fourth includes reheat. The purpose of using multiple pressure levels is to achieve a higher power output from the steam turbine, of course, at the expense of extra equipment. The configuration for the SOFC-GT topping cycle is that shown in Figure 3.1 with a couple of modifications downstream of the GT exhaust. The SOFC-GT topping cycle can be summarized as follows:

1. Air is compressed by the air compressor (AC) up to the fuel cell operating pressure. The air is then brought to the cathode inlet of the SOFC stack (state point 18).
2. Similarly, the fuel (natural gas) is compressed by the fuel compressor (FC) and then brought to the anode compartment of the stack (state point 1).
3. Both fuel and air can by-pass the fuel cell, i.e. a certain amount of fuel can flow directly to the combustor (C) by-passing the electrochemical reaction occurring within the stack (state point 23), while excess air can flow to the GT (state point 20).
4. At the stack, fuel (state point 24) is mixed with the anode recirculation stream (state point 5) in order to support the steam reforming reaction in the pre-reformer and in the anode compartment of the fuel cell. The mixture at state point 25 consists of methane and steam. Thus, in the pre-reformer (PR), the first step in the fuel reforming process occurs. The energy required to support the pre-reforming reaction is derived from the hot stream at state point 26. The non-reacted fuel at state point 2 is involved in the internal reforming reaction within the anode compartment of the SOFC stack. Here, it is converted into the hydrogen that participates in the electrochemical reaction.
5. On the cathode side, air is first preheated by a counter-flow heat exchanger air injection pipe (HEC) and then brought into the annulus (air pipe) of the SOFC where, at the three-phase boundary, the cathode electrochemical reaction occurs (Singhal and Kendall, 2003; Larminie and Dicks, 2003; Benjamin, Camera, and Marianowski, 1995; Fuel Cell Handbook, 2004).
6. The electrochemical reactions, occurring in the fuel cell, produce DC electrical current and release thermal energy. The first of these is converted into AC current by the inverter; the latter is used by the internal reforming reaction and to heat up the fuel cell stack.
7. The high energy flow rate at state point 8 is first used to preheat air in the counter-flow heat exchanger and then to supply energy to the pre-reforming reaction. This stream at state point 21 enters the gas turbine.

8. The expansion in the GT supplies mechanical power which in turn is converted into electric power.

As mentioned above there are four different configurations for the steam turbine cycle (Kehlhofer, 1999). Starting with the single pressure ST cycle shown in Figure 3.2, the principle of operation is summarized as follows:

1. The GT exhaust stream (state point 33) flows to the shell-and-tube heat recovery steam generator (HRSG). The gas mixture side of the HRSG passes through the three heat exchanger sections (superheater (SU), evaporator (EV), and economizer (EC)) and is finally exhausted at state point 34.
2. The superheated steam produced by the SU (state point 35) is supplied to the steam turbine (ST) which during expansion produces mechanical power which in turn is converted into electric power in a generator. A small fraction of the superheated steam at low pressure is extracted (state point 37) to the deaerator (DE) to be used later for feedwater preheating.
3. The wet steam (state point 38) is then condensed in the condenser (CON). The condensate (state point 39) enters the condensate pump (CP) and is then pumped to the DE at state point 40.
4. In the DE, any air oddments and impurities contained by the water are removed while the water is preheated at 60 ^{o}C. The preheated water (state point 41) enters the feedwater pump (FP) and is then pumped to the EC at state point 42.
5. In the EC, the water is heated up to the point of a saturated liquid.
6. The heated feedwater is evaporated at constant temperature and pressure in the EV.
7. The water and the saturated steam are separated in the drum (DR), and the steam is supplied to the SU where it is superheated to the desired live-steam temperature and fed to the ST to repeat the cycle.

For the dual pressure ST cycle shown in Figure 3.3, the principle of operation is summarized as follows:

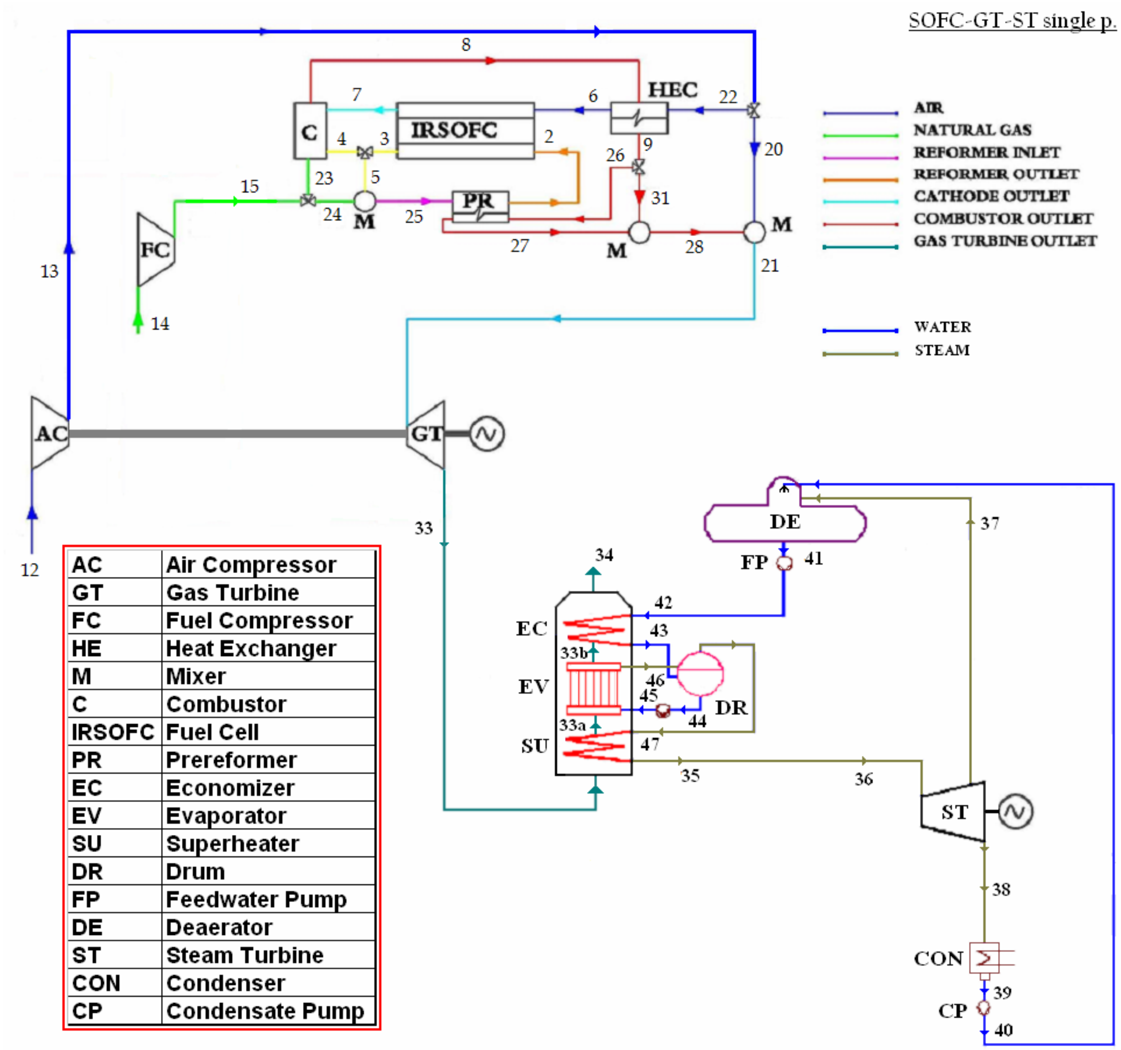

Figure 3.2. SOFC-GT integrated with a single pressure ST cycle.

1. The GT exhaust stream (state point 33) flows to the shell-and-tube heat recovery steam generator (HRSG). The gas mixture side of the HRSG passes through the six heat exchanger sections (high pressure superheater (HP SU), high pressure evaporator (HP EV),
2. The superheated steam produced by the HP SU (state point 35) and the LP SU is supplied to the dual-admission steam turbine (ST) which during expansion produces mechanical power which in turn is then converted into electric power in a generator. A small fraction of the superheated steam at low pressure is extracted (state point 37) to the deaerator (DE) to be used later on for feedwater preheating.

3. The wet steam (state point 38) is then condensed in the condenser (CON). The condensate (state point 39) enters the condensate pump (CP) and is then pumped to the DE at state point 40.

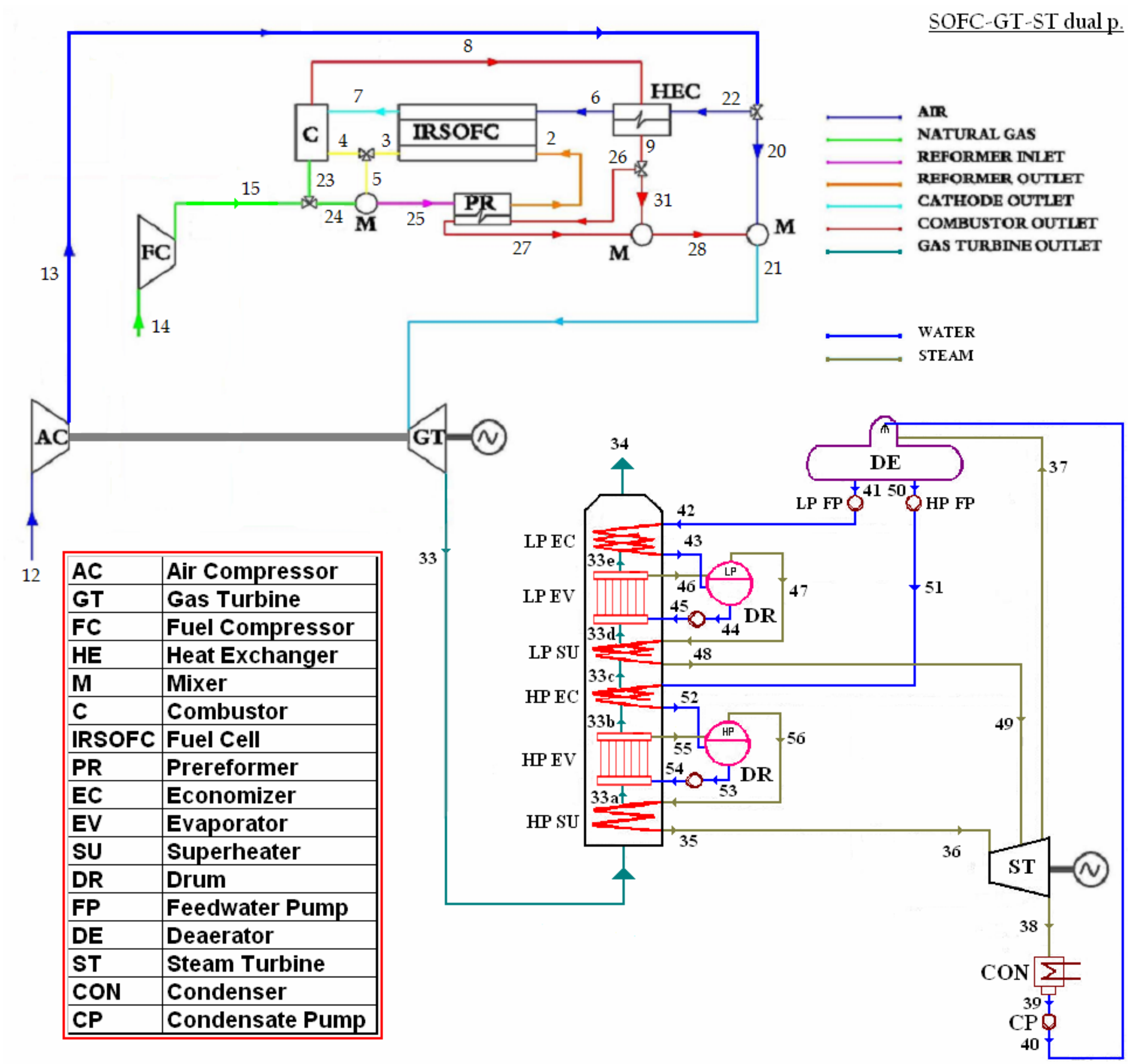

Figure 3.3. SOFC-GT integrated with a dual pressure ST cycle.

4. In the DE, any air oddments and impurities contained by the water are removed while the water is preheated at 60 ^{o}C. The preheated water (state points 50 and 41) enters the high pressure feedwater pump (HP FP) and low pressure feedwater pump (LP FP) and is then pumped to the HP EC and LP EC at state points 51 and 42, respectively.
5. In the economizers, the water is heated up to the point of a saturated liquid.

6. The heated feedwater is evaporated at constant temperature and pressure in the evaporators.
7. The water and the saturated steam are separated in the drums, and the steam is supplied to the superheaters where it is superheated to the desired live-steam temperatures and fed to the ST to repeat the cycle.

For the triple pressure ST cycle shown in Figure 3.4, the principle of operation is summarized as follows:

1. The GT exhaust stream (state point 33) flows to the shell-and-tube heat recovery steam generator (HRSG). The gas mixture side of the HRSG passes through the nine heat exchanger sections (HP SU, HP EV, HP EC, intermediate pressure superheater (IP SU), intermediate pressure evaporator (IP EV), intermediate pressure economizer (IP EC), LP SU, LP EV, and LP EC) and is finally exhausted at state point 34.
2. The superheated steam produced by the HP SU (state point 35), IP SU (state point 56) and the LP SU (state point 48) is supplied to the triple-admission steam turbine (ST) which during expansion produces mechanical power which in turn is converted into electric power in a generator. A small fraction of the superheated steam at low pressure is extracted (state point 37) to the deaerator (DE) to be used later on for feedwater preheating.
3. The wet steam (state point 38) is then condensed to the condenser (CON). The condensate (state point 39) enters the condensate pump (CP) and is then pumped to the DE at state point 40.
4. In the DE any air oddments and impurities contained by the water are removed while the water is preheated at 60 ^{o}C. The preheated water (state points 57, 49, 41) enters the HP FP, intermediate pressure feedwater pump (IP FP) and LP FP and is then pumped to the HP EC, IP EC and LP EC at state points 58, 50, and 42, respectively.
5. In the economizers, the water is heated up to the point of a saturated liquid.

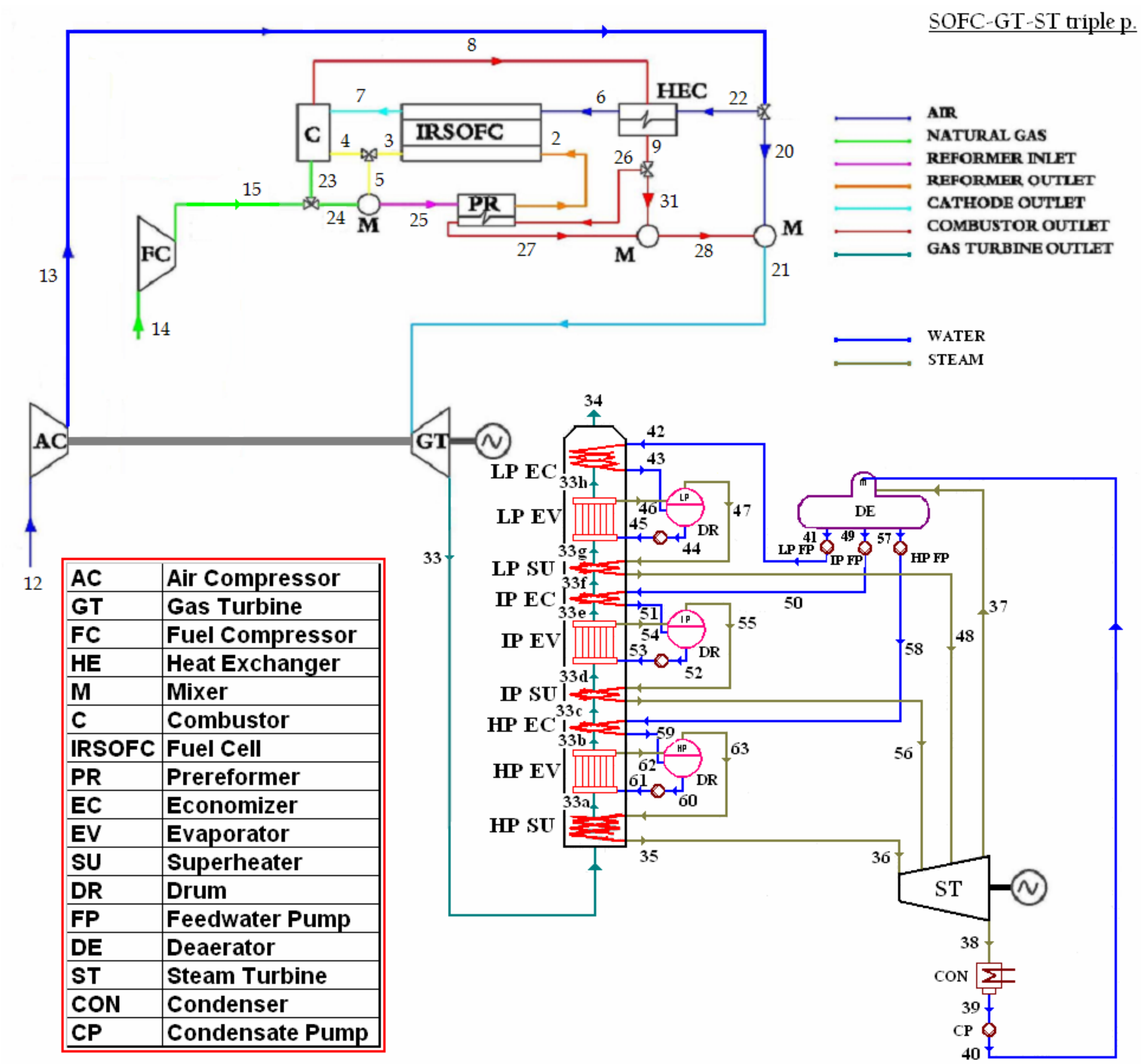

Figure 3.4. SOFC-GT integrated with a triple pressure ST cycle.

6. The heated feedwater is evaporated at constant temperature and pressure in the evaporators.
7. The water and the saturated steam are separated in the drums, and the steam is supplied to the superheaters where it is superheated to the desired live-steam temperatures and fed to the ST to repeat the cycle.

Finally, for the triple pressure with reheat ST cycle shown in Figure 3.5, the principle of operation is summarized as follows:

1. The GT exhaust stream (state point 33) flows to the shell-and-tube heat recovery steam generator (HRSG). The gas mixture side of the HRSG passes through the

ten heat exchanger sections (HP SU, reheater (RH), HP EV, HP EC, IP SU, IP EV, IP EC, LP SU, LP EV, and LP EC) and is finally exhausted at state point 34.

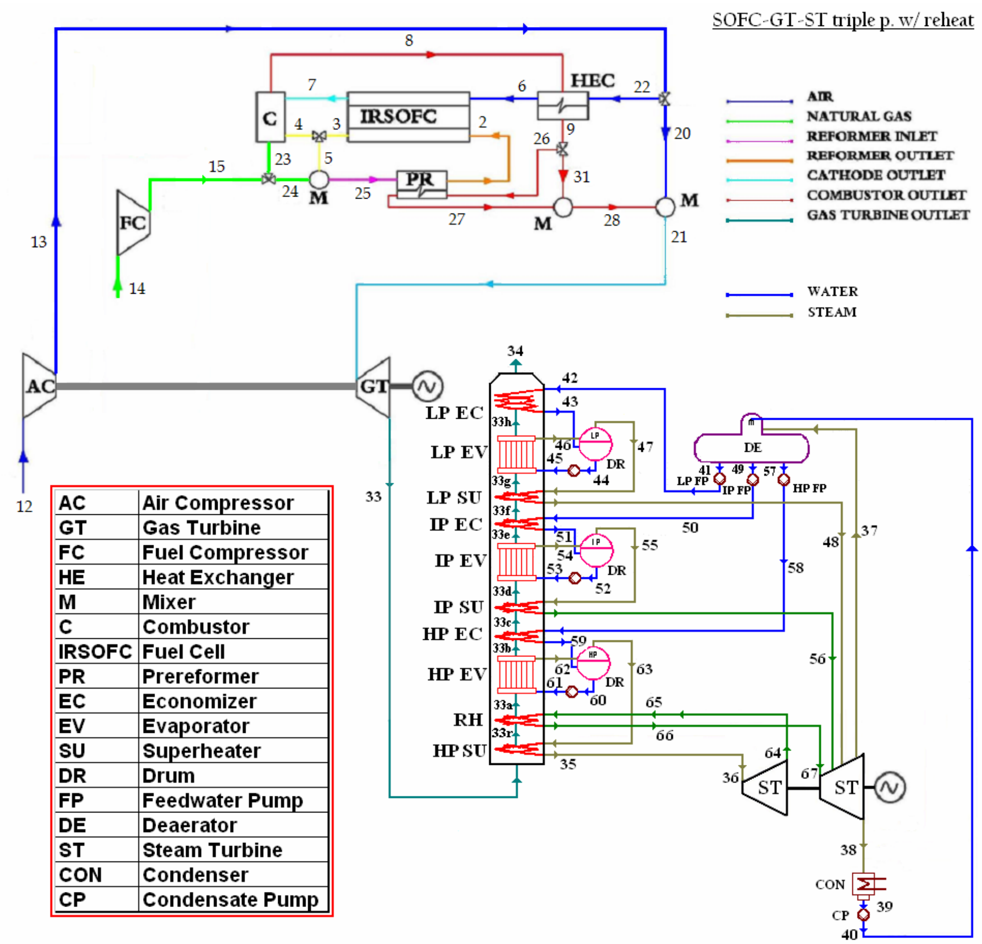

Figure 3.5. SOFC-GT integrated with a triple pressure with reheat ST cycle.

2. The superheated steam produced by the HP SU (state point 35) is supplied to the HP stage of the steam turbine. After expansion the cold reheat (state point 64) at an intermediate pressure returns to the HRSG and there by means of a reheater is superheated (state point 66) and returned to the IP/LP steam turbine stage. Also the IP SU (state point 56) and the LP SU (state point 48) supply superheated steam to the double-admission IP/LP ST which during expansion produces mechanical power which in turn is converted into electric power in a generator. A small fraction of superheated steam at low pressure is extracted (state point 37) to the deaerator (DE) to be used later on for feedwater preheating.

3. The wet steam (state point 38) is then condensed in the condenser (CON). The condensate (state point 39) enters the condensate pump (CP) and is then pumped to the DE at state point 40.
4. In the DE, any air oddments and impurities contained by the water are removed while the water is preheated at 60 ^{o}C. The preheated water (state points 57, 49, 41) enters the HP FP, IP FP, and LP FP, and is then pumped to the HP EC, IP EC and LP EC at state points 58, 50, and 42, respectively.
5. In the economizers, the water is heated up to the point of a saturated liquid.
6. The heated feedwater is evaporated at constant temperature and pressure in the evaporators.
7. The water and the saturated steam are separated in the drums, and the steam is supplied to the superheaters where it is superheated to the desired live-steam temperatures and fed to the ST to repeat the cycle.

The component models of these various configurations will be described in detail in the following sections. Table 3.1 gives a list with a detailed description for every component in the system.

Table 3.1. Power plant component descriptions.

Symbol	***Component***	***Description***
IRSOFC	Internal Reforming Solid Oxide Fuel Cell Stack	A fuel cell of the solid oxide type that performs the shift and steam reforming reactions by converting the fuel into hydrogen; the electrochemical reactions convert the chemical energy of the fuel to electric power.
PR	Pre-reformer	A typical catalytic reactor where hydrogen and carbon dioxide are produced from natural gas and steam.
HEC	Counter-flow heat exchanger air injection pipe	A heat exchanger of the counter-flow type that reheats the air before entering the cathode.
CB	Catalytic Combustor	A combustor that burns the non-oxidized part of the anode exhaust with air blown inside by an air compressor.
INV	Inverter	The inverter converts the DC current produced by the fuel cells into the more suitable AC current.
M	Mixer	The mixer mixes different flows.
VB	Bypass Valve	A valve used to split one flow into two or more flows.
GT	Radial-type Gas Turbine	A gas turbine of the radial-type that uses the exhaust gases from the SOFC to produce mechanical energy, part of which is used to operate the air compressor (which is connected with the same shaft) as well as produce electric power in the electric generator.
FC	Centrifugal-type Fuel Compressor	A compressor of the centrifugal-type used to compress the fuel before it is brought into the anode compartment of the stack.
AC	Centrifugal-type Air Compressor	A compressor of the centrifugal-type used to suck air at ambient pressure and compress it up to the fuel cell operating pressure before it is brought into the cathode compartment of the stack.
EG	Electric Generator	A generator used to convert the mechanical energy produced from the gas turbine or the steam turbine into electric power.
EC	Economizer	A shell and tube heat exchanger in the HRSG that converts the subcooled compressed water into a saturated liquid.
EV	Evaporator	A shell and tube heat exchanger in the HRSG that converts the saturated liquid into a saturated vapor.
SU	Superheater	A shell and tube heat exchanger in the HRSG that converts the saturated vapor into a superheater steam.
RH	Reheater	A shell and tube heat exchanger in the HRSG that converts the saturated vapor (wet steam) expanded by the HP section of the steam turbine into a superheater steam and supplies it to the IP/LP section of the steam turbine.
DR	Drum	The drum separates the liquid water from the saturated steam.
DE	Deaerator	The deaerator removes any air oddments and impurities contained by the water; simultaneously, the water is preheated before entering the HRSG.
FP	Feedwater Pump	A pump that receives the preheated water from the deaerator and pumps it to the HRSG (in particular the economizer).
ST	Steam Turbine	The superheated steam produced by the superheater is supplied to the steam turbine where during expansion mechanical power is produced. A small fraction of the superheated steam at low pressure is extracted to the deaerator to be used later on for deaerating and feedwater preheating.
CON	Condenser	A shell and tube heat exchanger that condenses the wet steam coming from the steam turbine exhaust.
CP	Condensate Pump	A pump that receives the condensate from the condenser and pumps it to the deaerator.

3.2 Thermodynamic, Geometric, Electrochemical and Kinetic IRSOFC Models

The performance of the hybrid plant is influenced substantially by the choice and configuration of the SOFC stack. It is the component which requires the most complex planning since it is difficult for the SOFC to integrate with conventional power generating machines. Therefore, an accurate plant analysis and a thermoeconomic optimization of all chemical, electrochemical, electrical, and thermodynamic models required. The internal reforming solid oxide fuel cell (IRSOFC) cycle, shown in Figure 3.6 (Laosiripojana and Assabumrungrat, 2007), is itself a very complex system with a great number of components and subcomponents such as the fuel cell stack, the pre-reformer, the by-pass valves, the mixers, the counter-flow heat exchanger, and the catalytic combustor. Modeling and simulation of the IRSOFC cycle is complex requiring the following:

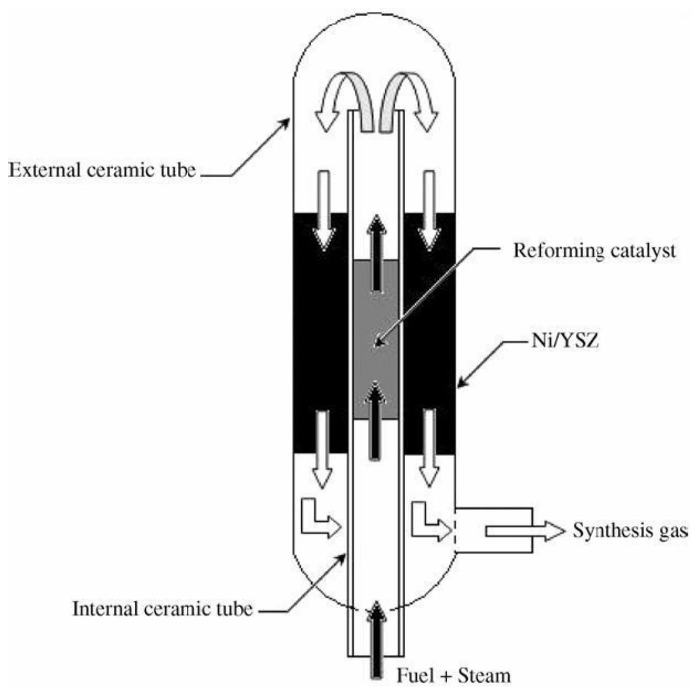

Figure 3.6. IRSOFC (Laosiripojana and Assabumrungrat, 2007).

- Calculation of the electrochemical fuel cell performance and the resulting of the voltages as the geometric and operational parameters of the plant are varied;

obviously such calculations require the evaluation of all polarizations (ohmic, activation, and concentration).

- Calculation of the reaction rate for the reforming and shift reactions in the pre-reformer.
- Calculation of the reaction rate for the electrochemical, reforming and shift reactions in the fuel cell.
- Calculation of the heat transfer in the IRSOFC.
- Calculation of the heat transfer in the pre-reformer.
- Calculation of the heat transfer in the counter-flow heat exchanger air injection pipe.
- Calculation of the reaction rate in the combustor.

3.2.1 Electrochemical IRSOFC Model

The electrochemical model of the IRSOFC under study is based on the model described in Calise et al. (2006) and is validated with data provided by Siemens Westinghouse in Singhal (1997). The hybrid plant performance depends on the electrochemical reactions in the SOFC. A detailed model of this component must take into account a number of chemical, electrochemical and physical phenomena. The fuel cell performance is usually described by its polarization curve that plots the voltage against the current density (Larminie and Dicks, 2003). The shape of this curve is affected by all typical losses of the fuel cell under investigation.

The SOFC anode inlet mixture is composed of hydrogen, carbon monoxide, carbon dioxide, nitrogen, water, and methane. Both hydrogen and carbon monoxide can be electrochemically oxidized within the fuel cell. The SOFC hydrogen and CO electrochemical reactions (Larminie and Dicks, 2003) can be summarized respectively as

Anode, $$\mathrm{H_2{+}O^{-2} \rightarrow H_2O{+}2}e^-, \qquad \mathrm{CO{+}O^{-2} \rightarrow CO_2{+}2}e^- \tag{3.1a}$$

Cathode, $$\frac{1}{2}\mathrm{O_2} + 2e^- \rightarrow \mathrm{O^{-2}}, \qquad \frac{1}{2}\mathrm{O_2} + 2e^- \rightarrow \mathrm{O^{-2}} \tag{3.1b}$$

Overall, $\overline{H_2 + \frac{1}{2}O_2 \rightarrow H_2O,}$ $\overline{CO + \frac{1}{2}O_2 \rightarrow CO_2}$ (3.1c)

However, even if SOFCs are claimed to be able to electrochemically oxidize not only hydrogen but also carbon monoxide, the likelihood is that the latter is primarily converted to hydrogen and carbon dioxide via a water-gas shift catalytic reaction and, thus, in this research study it is assumed that only the hydrogen reacts electrochemically (Chan, Low, and Ding, 2002). Moreover, the whole IRSOFC system is considered to be made up of a number of cells all behaving in the same way (Chan, Low, and Ding, 2002). Therefore, the cell voltage is the same for each cell and the total current is the sum of the single currents.

The SOFC voltage potential depends on a considerable number of parameters:

- Operating temperature and pressure
- Anode, cathode, electrolyte, and interconnection thicknesses
- Fuel cell material
- Fuel cell geometry
- Fuel cell length
- Fuel utilization factor
- Fuel and air composition
- Current density
- Geometric configuration (i.e. flat plate, tubular, monolithic, etc.)

To determine a functional dependence between the fuel cell voltage potential and the aforementioned parameters it is necessary to implement an accurate model to determine the fuel cell polarizations. The overall voltage of the single cell can be calculated as a function of current density, temperatures, pressures, chemical composition, and geometric/material characteristics by calculating the difference between the reversible potential and all the overvoltages (Calise et al. 2006), i.e.

$$V = E - V_{act,A} - V_{act,C} - V_{ohm} - V_{conc,A} - V_{conc,C} \quad (3.2)$$

where V is the actual fuel cell potential (V), E is the theoretical maximum voltage (V), $V_{act,A}$ is the anode activation overvoltage (V), $V_{act,C}$ is the cathode activation overvoltage

(V), V_{ohm} is the ohmic overvoltage (V), $V_{conc,A}$ is the anode concentration overvoltage (V), and $V_{conc,C}$ is the cathode concentration overvoltage (V). Equation (3.1) suggests that in the case of SOFC cells it is possible to neglect crossover, fuel, and internal current losses.

3.2.1.1 Open Circuit Potential

For each mole of reacting hydrogen, two moles of electrons are produced. Consequently the theoretical maximum voltage that could be reached by the SOFC is

$$E = -\frac{\Delta \overline{g}_f^0}{2F} \tag{3.3}$$

where $\Delta \overline{g}_f^0$ is the change in molar Gibbs free energy of formation at standard pressure (kJ/kmol), and F is Faraday's constant (96,439 C/moles of electrons). Obviously, this value is not reachable, even if the cell behavior is completely reversible because of the Nernst equation (Larminie and Dicks, 2003). It is also important to underline that this theoretical voltage decreases with stack temperature because the Gibbs-specific molar energy is a function that increases with temperature. The theoretical maximum cell efficiency can be defined as follows

$$\eta_{\max} = -\frac{\Delta \overline{g}_f^0}{\Delta \overline{h}_f^0} \tag{3.4}$$

where $\Delta \overline{h}_f^0$ is the enthalpy of formation (kJ/kmol).

The model is implemented with a number of routines for calculating the open circuit reversible voltage and activation, ohmic, and concentration losses. Specifically, the open circuit reversible voltage is calculated on the basis of the Nernst equation

$$E = -\frac{\Delta \overline{g}_f^0}{2F} + \frac{RT}{2F} \ln \frac{a_{H_2} a_{O_2}{}^{1/2}}{a_{H_2O}} = E_0 + \frac{RT}{2F} \ln \frac{a_{H_2} a_{O_2}{}^{1/2}}{a_{H_2O}} \tag{3.5}$$

where E_0 is the electromotive force (EMF) at standard pressure, a_{H_2} is the activity of hydrogen, a_{O_2} is the activity of oxygen, and a_{H_2O} is the activity of water.

For the case of high temperatures, and relatively low pressures and since the SOFC operates at temperatures of about 1000 °C, it can be assumed that the reactants behave as ideal gases. Therefore, the Nernst equation simplifies to

$$E = E_0 + \frac{RT}{2F} \ln \frac{p_{H_2} p_{O_2}^{1/2}}{p_{H_2O}} \tag{3.6}$$

where p_{H_2} is the hydrogen partial pressure, p_{O_2} is the oxygen partial pressure, and p_{H_2O} is the water partial pressure.

To keep the reversible voltage at a high range, the hydrogen and the oxygen partial pressures should be sufficiently high, while the steam pressure should be kept low. This is why the fuel and air utilization factors can never reach their unitary limit value (Fuel Cell Handbook, 2004). The calculated fuel cell voltage in equation (3.6) is obtained for an open circuit system. However, when the current produced by the cells is used for the external load, additional losses must be taken into account.

3.2.1.2 Activation Overvoltage

In general, electrochemical reactions are characterized by energetic barriers that must be overcome by the reactants so that the reaction can take place. This barrier is known as the “activation energy” or polarization and can be interpreted as the necessary extra potential needed to overcome the energetic barrier. It is directly proportional to the rate or speed of the reaction. At high temperatures, the speed of the electrochemical reaction is quite high, and, therefore, the polarization for activation is quite low.

In the simulation model (Calise, 2005) the activation polarization for the anode and the cathode is calculated using the Butler-Volmer equation, i.e.

$$i = i_0 \left[\exp\left(\alpha \frac{n_e F}{RT_s} V_{act} \right) - \exp\left(-(1-\alpha) \frac{n_e F}{RT_s} V_{act} \right) \right] \tag{3.7}$$

where i is the current density (mA/cm^2), i_0 is the exchange current density (mA/cm^2), α is the charge transfer coefficient, n_e is the number of moles of electrons per mole of hydrogen reacted, T_s is the temperature of the solid structure (anode, electrolyte, cathode) (K), and V_{act} is the activation overvoltage (V).

A determination of the exchange current density for the anode and for the cathode is one of the greatest problems occurring in the simulation of the electrochemical behavior of a fuel cell. An error in its evaluation can in fact significantly hinder a correct evaluation of the potential of the fuel cell and, therefore, of the power produced. The exchange current densities of the two electrodes can be expressed using the following formulae (Campanari, 1998)

$$i_{0,anode} = \gamma_{anode}\left(\frac{p_{H_2}}{p_{ref}}\right)\left(\frac{p_{H_2O}}{p_{ref}}\right)\exp\left(-\frac{E_{act,anode}}{RT_s}\right) \tag{3.8}$$

$$i_{0,cathode} = \gamma_{cathode}\left(\frac{p_{O_2}}{p_{ref}}\right)^{0.25}\exp\left(-\frac{E_{act,cathode}}{RT_s}\right) \tag{3.9}$$

where γ_{anode}, $\gamma_{cathode}$ are the exchange current density constants at the anode and cathode respectively (mA/cm^2), and p_{ref} is the reference pressure (1 bar). The values for the exchange current densities for the anode and the cathode vary with respect to the values of γ and E_{act}. In Figures 3.7 and 3.8 the effect of temperature variation on anode and cathode exchange current densities, respectively, is shown. These figures show that the anode exchange current density is always higher than that for the cathode. Upon inspection of Equation (3.6), this also leads to the conclusion that the polarization for anodic activation is smaller than that for the cathode which is in complete agreement with what is reported in the literature.

Obviously, the activation overvoltage depends primarily on the exchange current density. This parameter can be considered as the forward and reverse electrode reaction rate at the equilibrium potential. High exchange current density means high electrochemical reaction rate. In this case, good fuel cell performance can be expected. The value of the exchange current density can be improved by increasing the fuel cell operating temperature or using catalytic materials with lower activation energies (Larminie and Dicks, 2003). Under high activation overpotential, the second term of the

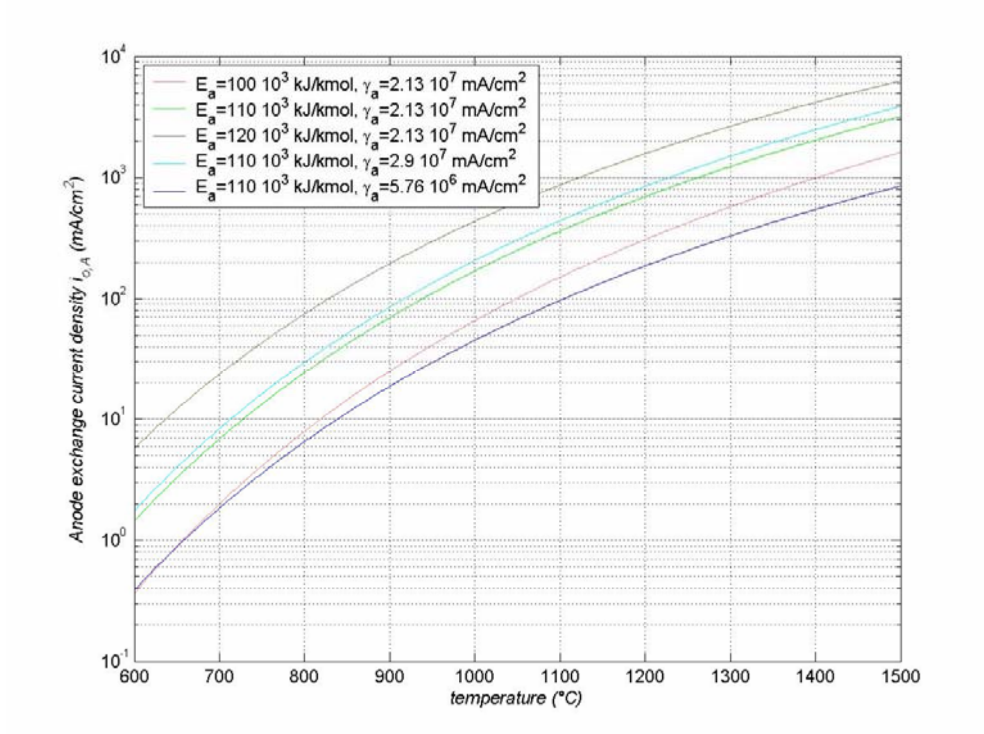

Figure 3.7. Variation of anode exchange current density with temperature, activation energy, and γ.

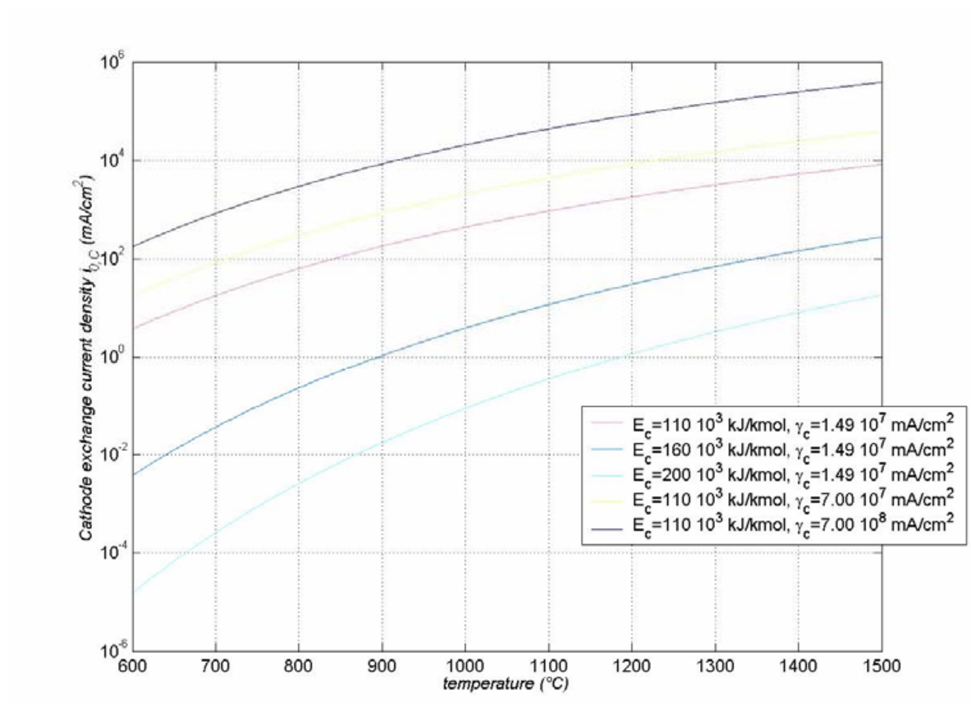

Figure 3.8. Variation of cathode exchange current density with temperature, activation energy, and γ.

Butler-Volmer equation can be neglected and Equation (3.7) can be written as in Chan, Low, and Ding (2002) as

$$\Delta V_{act} = A \ln\left(\frac{i}{i_0}\right) \tag{3.10}$$

where $A = \dfrac{RT_s}{n_e \alpha F}$ and A is the cell active area (cm^2).

Equation (3.10) is called the Tafel equation and is valid only when the current density is higher than the exchange current density. The value of charge coefficient, α, depends on the reactions involved and on the electrode materials. Its typical value is 0.5 and cathode values often vary between 0.1 and 0.5 (Larminie and Dicks, 2003) for a limiting range of 0-1.0. Generally, the anode activation overpotential is much smaller than that of the cathode. The sum of these two activation overpotential losses can be expressed as follows:

$$\Delta V_{TOT} = \left(A_{anode} + A_{cathode}\right) \ln\left(\frac{i}{\left(i_{0,anode}\right)^{\frac{A_{anode}}{A_{anode}+A_{cathode}}} \left(i_{0,cathode}\right)^{\frac{A_{cathode}}{A_{anode}+A_{cathode}}}}\right) \tag{3.11}$$

Finally, when the activation overvoltage is low, it is possible to expand the Tafel equation as a 1st order Taylor series. If, thus, reduce to

$$\Delta V_{act} = \frac{RT_s}{n_e \alpha F}\left(\frac{i}{i_0}\right) \tag{3.12}$$

If as much as a 5 percent error is acceptable, in Chan, Low, and Ding (2002) indicate that it is possible to use i) the Tafel equation, as given by equation (3.10) for $V_{act} > 0.28$ V and ii) the linear Tafel equation given by equation (3.12) for $V_{act} < 0.1$ V.

3.2.1.3 Concentration Overvoltage

The electrochemical reaction that takes place in the anode compartment involves the consumption of hydrogen in the anode-electrolyte interface layer. Similarly, in the cathode compartment, the oxygen contained in the air flow is consumed by the cathode electrochemical reaction in the cathode-electrolyte interface layer. Both reactions only take place at so-called “three phases boundaries” (TPBs), where

- the gas for reduction or oxidation feeds the electrochemical reaction;
- the electrolyte material present allows for ion transfer; and
- the electrode material present allows for electron transfer.

To reach the TPBs, the fuel and the oxidizer must be able to penetrate across the porous electrode material. In effect, the porosity constitutes a resistance to the passage of the reactants so that the more porous the material, the smaller will be the speed with which the gas penetrates the electrode. Obviously, such resistance to flow results in a concentration gradient across the porous electrode from the bulk fluid entering the electrode to the TPBs inside the electrode. For a given porosity, an increase in current density which results in a corresponding increase in reaction rate will result in a proportional increase of the concentration gradient across the electrode. At some when the current density becomes high enough the mass flow into the electrode becomes mass limited with a corresponding share increase in concentration gradient. This is what corresponds to the region on the polarization curve dominated by the concentration polarization.

The diminution of the hydrogen partial pressure reduces the fuel cell potential and therefore the change from $p_{H_{2,1}}$ to $p_{H_{2,2}}$ leads to an open circuit potential difference corresponding to

$$\Delta V = \frac{RT}{2F}\ln\left(\frac{p_{H_{2,2}}}{p_{H_{2,1}}}\right) \tag{3.13a}$$

An analogous phenomenon happens to the cathode compartment with regard to the flow of air. Also here the oxygen is consumed by the electrochemical semi-reaction, resulting in a diminution of the partial pressure of the oxygen and a consequent reduction of the fuel cell potential corresponding to

$$\Delta V = \frac{RT}{4F}\ln\left(\frac{p_{O_{2,2}}}{p_{O_{2,1}}}\right) \tag{3.13b}$$

The fuel gas usage causes a pressure change. If a limiting current density i_l is postulated at which the fuel is used up at a rate equal to its maximum supply speed the current density would reach a maximum at this value because fuel cannot be supplied at a greater rate. Therefore, the pressure reaches zero at such current density. If $p_{H_{2,1}}$ is the pressure when the current density is zero, and with the assumption of linear pressure drop down to zero at i_l, then the pressure $p_{H_{2,2}}$ at any current density i is given by the formula (Larminie and Dicks, 2003)

$$\frac{p_{H_{2,2}}}{p_{H_{2,1}}} = 1 - \frac{i}{i_l} \tag{3.14}$$

Therefore, a rough estimate for concentration losses on the anode side is given by the following equation

$$V_{conc} = \frac{RT}{2F} \ln\left(1 - \frac{i}{i_l}\right) \tag{3.15}$$

where i_l is the limiting current density (mA/cm^2). A similar expression exists for the cathode side but with a 4 instead of a 2 in the denominator.

Unfortunately, these two expressions have a number of weaknesses which follow directly from the assumption that the i_l is constant, i.e.

- temperature and partial pressure dependencies are neglected;
- material characteristics in terms of porosity are not considered (these have a great influence on the calculation of concentration losses);
- there is no explicit dependency on the porous media’s thickness nor on the associated diffusion coefficients.

A more accurate model, which combines the concentration losses on the anode and cathode sides into a single expression is given by Marechal et al. (2004), namely,

$$V_{conc} = \frac{RT_s}{2F} \log\left[\left(i - \frac{i}{i_{l,H_2}}\right)\left(1 - \frac{i}{i_{l,O_2}}\right)^{0.5}\right] \tag{3.16}$$

where $i_{l,H2}$ and $i_{l,O2}$ are the limiting current densities for the hydrogen on the anode side and the oxygen on the cathode side, respectively. These limiting currents are found from

$$i_{l,i} = \frac{n_{e^-}F}{\nu_i}\frac{C_{i,0}}{i/h_m A_{cell}} \tag{3.17}$$

where n_{e^-} is the number of electrons participating in the electrochemical reaction, $C_{i,0}$ is the concentration of the i_{th}-component of the bulk flow (kg/m^3), ν_i is the stoichiometric coefficient of the i_{th}-component in the electrochemical reaction, $i_{l,i}$ is the limiting current density of the i_{th}-component, h_m is the mean diffusion coefficient, and A_{cell} is the cell active area. The latter is defined as

$$A_{cell} = \pi L_{cell} d_o^{cell} \tag{3.18}$$

where L_{cell} is the length of the fuel cell and d_o^{cell} is the external cell diameter. Describing equation (3.13), in detail, in terms of hydrogen and oxygen it becomes

$$i_{l,H_2} = 2F\frac{C_{H_2,0}}{1/h_{m,H_2} A_{cell}} \tag{3.19a}$$

$$i_{l,O_2} = 4F\frac{C_{O2,0}}{1/h_{m,O2} A_{cell}} \tag{3.19b}$$

where $C_{H2,0} = \dfrac{\overline{y}_{H2}^{anode} p_{cell}}{RT_{cell}}$ (3.20a)

$$C_{O2,0} = \frac{\overline{y}_{O2}^{cathode} p_{cell}}{RT_{cell}} \tag{3.20b}$$

$$\overline{y}_{H2}^{anode} = \frac{y_{H2,i}^{anode} + y_{H2,o}^{anode}}{2} \tag{3.21a}$$

$$\overline{y}_{O2}^{cathode} = \frac{y_{O2,i}^{cathode} + y_{O2,o}^{cathode}}{2} \tag{3.21b}$$

where $\overline{y}_{H2}^{anode}$ is the mean hydrogen mole fraction, $\overline{y}_{O2}^{cathode}$ is the mean oxygen mole fraction, $y_{H2,i}^{anode}$ is the hydrogen mole fraction at the inlet, $y_{H2,o}^{anode}$ is the hydrogen mole fraction at the outlet, $y_{O2,i}^{cathode}$ is the oxygen mole fraction at the inlet, and $y_{O2,o}^{cathode}$ is the oxygen mole fraction at the outlet.

3.2.1.4 Ohmic Overvoltage

The ohmic losses are caused due to the electron flow through the anode, cathode, and interconnections and ion flow through the electrolyte. However, the ohmic losses due to the electrodes, given their high electric conductivity, are much lower than those due to the electrolyte and the interconnections.

For the evaluation of these types of losses, the approach used is based on Ohm's law. This method is the one most frequently used because of its simplicity. It assumes a linear relationship between the potential drop and the current density, based on a simple electric circuit in series of the anode, cathode, electrolyte, and interconnections. In Chan, Low, and Ding (2002) it is formulated as

$$V_{ohm} = i\sum_{j=1}^{4} r_j \tag{3.22}$$

where i is the current density of the cell, and r_j is the area-specific resistance (Ω) defined as

$$r_j = \rho_j \delta_j \tag{3.23}$$

where ρ_j is the cell electrical resistivity (Ω/cm), and δ_j is the cell material thickness (cm) (anode, cathode, electrolyte, interconnections). Each resistivity is a function of temperature and two empirically determined constants ρ and λ which are related to ρ as follow (Chan, Low, and Ding, 2002):

$$\rho_{anode} = \xi_{anode} \exp\left(\frac{\lambda_{anode}}{T}\right) \tag{3.24a}$$

$$\rho_{cathode} = \xi_{cathode} \exp\left(\frac{\lambda_{cathode}}{T}\right) \tag{3.24b}$$

$$\rho_{electr} = \xi_{electr} \exp\left(\frac{\lambda_{electr}}{T}\right) \tag{3.24c}$$

$$\rho_{interconn} = \xi_{interconn} \exp\left(\frac{\lambda_{interconn}}{T}\right) \tag{3.24d}$$

The empirical constants ρ_i are the resistivity pre-exponential coefficients with units of Ωcm, while the λ_i are the resistivity exponential constants with units of K. Values for these constants can be found in Costamagna, Magistri, and Massardo (2001).

3.2.1.5 Total Overvoltage

All the aforementioned overvoltages can be substituted into equation (3.2) in order to determine the cell voltage, V_{cell}, i.e.

$$\begin{aligned} V_{cell} &= \frac{\Delta \bar{g}_f^0}{2F} + \frac{RT}{2F}\log\left(\frac{p_{H_2} p_{O_2}^{\;0.5}}{p_{H_2O}}\right) - ir \\ &\quad -\left(A_{anode} + A_{cathode}\right)\ln\left(\frac{i}{\left(i_{0,anode}\right)^{\frac{A_{anode}}{A_{anode}+A_{cathode}}}\left(i_{0,cathode}\right)^{\frac{A_{cathode}}{A_{anode}+A_{cathode}}}}\right) \\ &\quad + \frac{RT_s}{n_e \alpha F}\left(\frac{i}{i_0}\right) \end{aligned} \tag{3.25}$$

3.2.2 Chemical Kinetics

The internal reforming tubular SOFC is a component that can be fed by methane, natural gas, hydrogen, and hydrocarbons in general, and also by biogas or syngas (Larminie and Dicks, 2003, Benjamin, Camera, and Marianowski 1995, Fuel Cell Handbook, 2004). In the present research, the fuel is natural gas. The usually high operating temperature of a SOFC stack allows one to sustain the reforming and the shift reactions within its anode compartment (see Figure 3.11). An internal reforming arrangement also provides additional cooling of the stack because part of the heat released by the electrochemical reaction is used internally by the methane reforming reaction. The internal reforming reaction mechanisms and that for the electrochemical reaction on the anode side can be summarized as follows

- Methane-steam reforming reaction mechanism

$$CH_4 + H_2O \Leftrightarrow CO + 3H_2 \tag{3.26}$$

- Water-gas shift reaction mechanism

$$CO + H_2O \Leftrightarrow CO_2 + H_2 \tag{3.27}$$

- Anode electrochemical reaction mechanism

$$H_2 + O^{2-} \Leftrightarrow H_2O + 2e^- \Rightarrow \text{ overall: } H_2 + \frac{1}{2}O_2 \rightarrow H_2O \tag{3.28}$$

The three aforementioned reactions are assumed to be equilibrium controlled (Chan, Low, and Ding 2002; Calise, 2005a). Consequently, the equilibrium composition which results from these three reaction mechanisms can be found by solving the following system of three equations for x, y, and z:

$$K_{ref}\left(T_{outlet}\right) = \frac{\dot{n}_{H_2}^3 \dot{n}_{CO}}{\dot{n}_{H_2O}\dot{n}_{CH_4}}\left(\frac{p_{cell}}{p_0}\right)^2 \tag{3.29}$$

$$K_{shift}\left(T_{outlet}\right) = \frac{\dot{n}_{H_2}\dot{n}_{CO_2}}{\dot{n}_{H_2O}\dot{n}_{CO}} \tag{3.30}$$

$$z = U_f\left(\dot{n}_{H_2,inlet} + 3x + y\right) \tag{3.31}$$

where K_{ref} is the equilibrium constant for the steam-methane reforming reaction, K_{shift} the equilibrium constant for the water-gas shift reaction, x the methane reforming reaction rate coordinate, y the shift reaction rate coordinate, z the electrochemical reaction rate coordinate, and U_f the fuel utilization factor. The relationship between x, y, and z and the final and initial molar flow rates of the constituents are found from proportionality relations (Gyftopoulos and Beretta, 2005) and the mechanism for the reforming, shift, and electrochemical (overall) reactions, i.e.

$$\dot{n}_{CH_4} = \dot{n}_{CH_4,inlet} - x \tag{3.32a}$$

$$\dot{n}_{H_2O} = \dot{n}_{H_2O,inlet} - x - y + z \tag{3.32b}$$

$$\dot{n}_{CO} = \dot{n}_{CO,inlet} + x - y \tag{3.32c}$$

$$\dot{n}_{H_2} = \dot{n}_{H_2,inlet} + 3x + y - z \tag{3.32d}$$

$$\dot{n}_{O_2} = \dot{n}_{O_2,inlet} - \frac{z}{2} \tag{3.32e}$$

$$\dot{n}_{CO_2} = \dot{n}_{CO_2,inlet} + y \tag{3.32f}$$

The solution of the system of equations, equations (3.28) to (3.30) is frequently very complex because their reaction rate coordinates depend on the inlet molar flow rates, the fuel cell utilization factor, the operating temperature, and the operating pressure. However, the analysis of these chemical processes can be greatly simplified, from a computational point of view, by assuming that the steam-methane reforming reaction is driven to completion (Fuel Cell Handbook, 2004). It is possible to use such a simplification because the hydrogen produced by the reforming reactions is consumed by the electrochemical reaction and because the value of its equilibrium constant is high. In fact, several studies have shown that at typical SOFC operating conditions, the anode methane molar fraction is less than 1 percent (Larminie and Dicks, 2003; Chan, Low, and Ding, 2002).

If equation (3.31) is substituted in equations (3.28) to (3.30) then there will exist three equations but four unknowns $\left(x, y, z, \text{and}, T_{outlet}\right)$. Therefore, a fourth equation is needed which can be added with the application of an energy balance on the fuel cell control volume given by

$$\dot{H}_{react} + \dot{H}_{inlet} = \dot{H}_{outlet} + V_{cell} I \tag{3.33}$$

where the molar inlet energy rate is

$$\begin{aligned} \dot{H}_{inlet} = {} & \left(\sum_i \dot{m}_i c_{pi}\right)_{inlet,a} \left(T_{inlet,a} - T_0\right) + \dot{n}_{H_2O,inlet,a} \overline{h}_{H_2O}\left(T_{inlet,a}, y_{H_2O} p_{inlet,a}\right) \\ & + \left(\sum_i \dot{m}_i c_{pi}\right)_{inlet,c} \left(T_{inlet,c} - T_0\right) \end{aligned} \tag{3.34}$$

the net energy rate generated by the reforming, shift, and electrochemical reactions is

$$\Delta\dot{H}_{react} = -\left(z\Delta h_{H_2} + y\Delta h_{shift} + x\Delta h_{ref}\right) \tag{3.35}$$

Here Δh_{H_2} is the specific enthalpy difference of generated by the electrochemical reaction, Δh_{shift} is the specific enthalpy difference generated by the shift reaction, and Δh_{ref} is the specific enthalpy difference generated by the methane steam-reforming reaction. The molar outlet energy rate is

$$\dot{H}_{outlet} = \left(\sum_i \dot{n}_i c_{pi}\right)_{outlet,c} \left(T_{outlet} - T_0\right) + \dot{n}_{H_2O,outlet,a} \overline{h}_{H_2O}\left(T_{outlet}, y_{outlet}\right) \tag{3.36}$$

and the fuel cell DC current is found from the Farradic efficiency (assuming 100%) such that

$$I = 2\dot{n}_{H_2} F \tag{3.37}$$

These four equations, i.e. Eqs. (3.29), (3.30), (3.31), and (3.33), is a complicated system of equations to solve. An alternative simplified scheme to solve these set of equations is presented in Calise (2005).

Finally, the energy efficiency for the IRSOFC is defined as

$$\eta_{IRSOFC} = \frac{V_{cell} I}{z\left|\Delta h_{H_2}\right|} \tag{3.38}$$

3.2.3 Geometry

The geometric model of the IRSOFC is of significant importance when simulation of the off-design operation needs to be determined. It is configured as follows:

$$A = n_{cell} A_{cell} = n_{cell} \pi D_{cell} L_{cell} \tag{3.39}$$

where A is the SOFC stack area, A_{cell} is the cell area, D_{cell} is the cell diameter, and L_{cell} is the cell length. Also the total current and the cell current (assuming 100% efficiency) are defined as

$$I = 2\dot{n}_{H_2} F \tag{3.40}$$

and $$I_{cell} = 2\dot{n}_{H_{2cell}} F \tag{3.41}$$

where $\dot{n}_{H_2}$ is the total molar flow rate of hydrogen, $\dot{n}_{H_{2cell}}$ is the molar flow rate of hydrogen per cell, and F is Faraday's constant.

Now, $$i = \frac{I}{A} \tag{3.42}$$

and $$P = IV_{cell} \tag{3.43}$$

where i is the current density, P is the SOFC power output, and V_{cell} is the cell voltage.

Furthermore, $$i = \frac{I_{cell}}{A_{cell}} \tag{3.44}$$

Multiplying and dividing Eq. (3.44) by n_{cell}, we get that

$$i = \frac{I_{cell}}{A_{cell}} \frac{n_{cell}}{n_{cell}} \Rightarrow \frac{i}{n_{cell}} = \frac{I_{cell}}{A}$$

However, $$I = 2\dot{n}_{H_{2cell}} n_{cell} F \tag{3.45}$$

Thus, combining with Eq. (3.41) gives

$$I = I_{cell} n_{cell} \tag{3.46}$$

which yields again (3.42)

3.3 Thermodynamic and Geometric IRSOFC Auxiliary Component Models

3.3.1 Pre-reformer

As previously mentioned, one of the main advantages of using high temperature fuel cells is the possibility of feeding the SOFC with natural gas directly, since the reforming process can be supported inside the stack (Singhal and Kendall, 2003; Larminie and Dicks, 2003; Benjamin, Camera, and Marianowski, 1995; Campanari, 1998; Chan, Low, and Ding, 2002). In practice, however, a pre-reforming process is usually necessary. In particular, a couple of considerations must be taken into account, namely,

- the natural gas includes a small fraction of complex hydrocarbons that must be cracked before entering the cell;
- if the cell is directly fed with methane, the bottom of the IRSOFC tube would be unable to produce any voltage, since there would be no hydrogen available for the electrochemical reaction.

The pre-reformer unit, shown in Figure 3.9, consists of a number of tubes located inside a shell and filled with a particular catalyst (Georgopoulos, 2002; Oyarzabal, 2001). The reformate gas flows inside these tubes. Hot gases, coming from the combustor, flow inside the shell external to the tubes, supplying the thermal energy needed to support the process, since the energy provided by the exothermic water-gas shift reaction is not sufficient for the endothermic demethanization of the reforming process (Georgopoulos, 2001; Oyarzabal 2001).

The simulation of the pre-reformer subsystem is rather complex because it needs to simultaneously determine the following:

- Calculate the process reaction rate;
- Calculate the cold and hot fluid heat transfer rates.

To do so, a 0-dimensional or lumped parameter model is used instead of a 1-dimensional model due its simplicity and faster calculation times. A description of the model is given in the next sections.

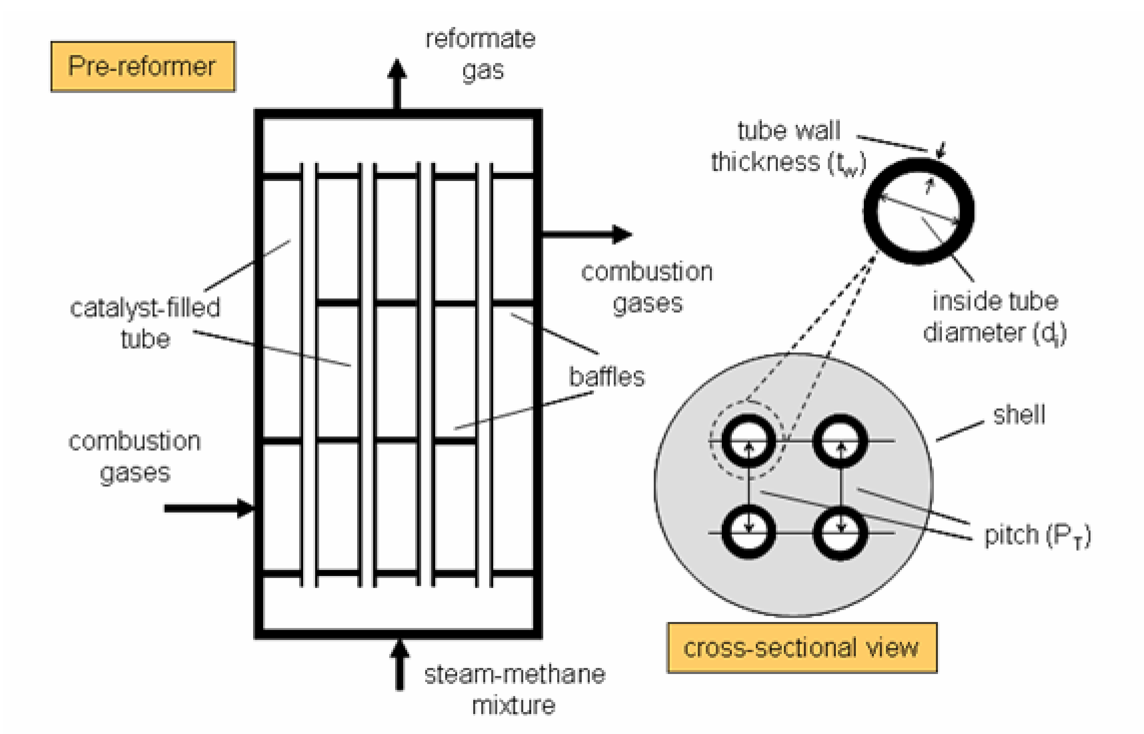

Figure 3.9 Pre-reformer schematic.

3.3.1.1 Chemical Kinetics

The process of steam reforming with catalysts made of nickel-alumina is the principal method used for hydrogen production. In each of the pipe shown in Figure 3.9, the temperature increases from 800 to 1000 ^{o}C, while the pressure varies between 8 and 10 bars. Assuming a negligible content of complex hydrocarbons, the steam reforming process exclusively involves methane. The principal reaction mechanisms are given by

- Steam-Methane Reforming (SMR):

$$CH_4 + H_2O \Leftrightarrow CO + 3H_2 \qquad \Delta H = +206.1 \text{ kJ/mol} \tag{3.47}$$

- Water-Gas Shift Reaction:

$$CO + H_2O \Leftrightarrow CO_2 + H_2 \qquad \Delta H = -41 \text{ kJ/mol} \tag{3.48}$$

Where ΔH is the enthalpy of reaction. In addition to these two reaction mechanisms other non-desirable reactions may also occur. Among these is the most dangerous one, the so-called “carbon deposition” mechanism, which may occur at the sides of the pre-reformer or the cell where little water vapor exists. The reaction mechanism for carbon deposition is given by

$$CH_4 \rightarrow C + 2H_2 \tag{3.49}$$

This and similar phenomena must, of course, be avoided or at least minimized. The risk of carbon deposition can be avoided with the use of excess vapor which is a function of the steam to carbon ratio

$$SC = \frac{n_{H_2O}}{n_{CH_4}} \tag{3.50}$$

where n_{H_2O} is the moles of water vapor and n_{CH_4} is the moles of methane.

The steam reforming of methane is slow and highly endothermic while the water-gas shift reaction is fast and somewhat exothermic. The endothermic reaction requires energy that must be supplied by external sources. It is assumed that it is kinetically controlled while the shift reaction is equilibrium controlled. The latter assumption is reasonable since it is so much faster than the former and is made here in order to simplify the calculations. Now, writing proportionality relations (Gyftopoulos and Beretta, 2005) different species based on the reaction mechanisms involved yields

$$
\begin{aligned}
&n_{CH_{4,0}} = n_{CH_{4,i}} - x \\
&n_{CO_o} = n_{CO_i} + x - y \\
&n_{H_{2,o}} = n_{H_{2,i}} + 3x + y \\
&n_{O_{2,o}} = n_{O_{2,i}} \\
&n_{N_{2,o}} = n_{N_{2,i}} \\
&n_{CO_{2,o}} = n_{CO_{2,i}} + y \\
&n_{H_2Oo} = n_{H_2O_i} - x - y
\end{aligned}
\tag{3.51}
$$

Where x is the methane reaction rate coordinate which is a function of the degree of demethanization given by

$$\varsigma_{CH_4} = \frac{n_{CH_{4,i}} - n_{CH_{4,o}}}{n_{CH_{4,i}}} \tag{3.52}$$

and y (carbon monoxide reaction rate coordinate) is determined from the stable equilibrium condition associated with the water-gas shift reaction mechanism, i.e.

$$K_{shift}\left(T\right) = \frac{\left(n_{CO_{2,i}} + y\right)\left(n_{H_{2,i}} + 3x + y\right)}{\left(n_{H_2O_i} - x - y\right)\left(n_{CO_i} + x - y\right)} \tag{3.53}$$

The geometry of the pre-reformer then comes into play via a number of expressions which relate *x, y,* and ς to the number, length, and diameter of tubes. For example, once y is known one can determine the number of pre-reformer tubes (with their length and diameter fixed) required in order achieve a fixed demethanization rate, using Calise et al. (2006)

$$n_{tubes}^{PR} = \frac{1}{L_R^{PR} A_{cr}^{PR} \rho_B} \int_{\zeta=0}^{\zeta=x} \frac{d\zeta}{-r_{CH_4}} \tag{3.54}$$

where L_R^{PR} is the length of a tube and A_{cr}^{PR} is its cross-sectional area given for a circular pipe by

$$A_{cr}^{PR} = \frac{\pi \left(d_i^{PR}\right)^2}{4} \tag{3.55}$$

Here d_i^{PR} is the inner diameter of the pipe. Furthermore, ρ_B in equation (3.54) is the bulk density while r_{CH_4} is the reaction rate given by Georgopoulos (2002):

$$r_{CH_4} = k \exp\left(\frac{EA}{RT}\right) p_{CH_4} \tag{3.56}$$

The reaction rate constant is given by the relation (Calise, 2005)

$$k(T) = k_0 \exp\left(-\frac{E}{RT_{Reactor}}\right) \tag{3.57}$$

and k_0 is the frequency factor (kmol/mm^2 Pa.s), $T_{Reactor}$ is the reactor temperature (K).

Once the number of tubes is known, the outside diameter of the shell containing all the pipes of the pre-reformer can be determined from (Calise, 2005)

$$D_{shell}^{PR} = 0.661\sqrt{\pi n_{tubes}^{PR}\left(P_T^{PR}\right)^2} \tag{3.58}$$

where the shell has been assumed to be cylindrical and the pitch P_T^{PR} is given by

$$P_T^{PR} = 1.2 d_o^{PR} \tag{3.59}$$

Here the external diameter of the pipes is expressed as

$$d_o^{PR} = d_i^{PR} + 2t_w^{PR} \tag{3.60}$$

where t_w^{PR} is the thickness of the shell wall.

Finally, the calculation procedure for the preceding set of relationships can be summarized as follows:

1. The length and the inlet diameter of the pipes are fixed;
2. The value for the degree of demethanization is fixed to a desired value from which *x* can be determined, i.e.

$$x = \varsigma_{CH_4} n_{CH_{4,i}} \tag{3.61}$$

3. The value of *y* is then calculated using equation (3.53);
4. The required number of pipes is calculated;
5. The equilibrium composition for the demethanization process is determined using

$$K_{ref}(T) = \frac{\left(n_{H_{2,i}} + 3x + y\right)^3 \left(n_{CO_i} + x - y\right)}{\left(n_{H_2O_i} - x - y\right)\left(n_{CH_{4,i}} - x\right)} \tag{3.62}$$

If the value of *x* determined from this relation is less than that found using equation (3.52) then the number of tubes is recalculated using the lower value of x.

3.3.1.2 Heat Transfer

In terms of the heat transfer, the pre-reformer can be analyzed as a counter-flow heat exchanger. For this type of heat exchanger, both the effectiveness-NTU and the LMTD methods can be used. However, both methods are applied with the hypothesis of chemically non-reacting fluids: This means that they are inapplicable for the pre-reformer case. Therefore, a modified 0-dimensional (lumped parameter) heat transfer model was developed by Calise et al. (2004) for the pre-reformer using energy balances applied to the control volumes shown in Figure 3.10, i.e.

$$\delta \dot{Q} = -\dot{m}_h c_{p,h} dT_h + \delta \dot{H}_h \tag{3.63}$$

$$\delta \dot{Q} = -\dot{m}_c c_{p,c} dT_c + \delta \dot{H}_c \tag{3.64}$$

where $\dot{m}_h$, $c_{p,h}$, $\dot{m}_c$, and $c_{p,c}$ are the mass flow rates and specific heats of the hot gases and the fuel-steam mixture, respectively, $\delta \dot{Q}$ is the differential rate of heat transfer into and out of the tube wall, $\delta \dot{H}_h$ the differential rate of heat transfer into the shell wall, and $\delta \dot{H}_c$ the differential rate of heat transfer into the catalyst contained in the tube. Having for the differential temperature differences across the shell and the tube in the direction of the mass flows yield

$$dT_h = -\frac{\delta \dot{Q}}{\dot{C}_h} + \frac{\delta \dot{H}_h}{\dot{C}_h} \tag{3.65}$$

$$dT_c = -\frac{\delta \dot{Q}}{\dot{C}_c} + \frac{\delta \dot{H}_c}{\dot{C}_c} \tag{3.66}$$

Now, $\delta \dot{Q}$ can be written in terms of an overall heat transfer coefficient, U, the differential surface area of the wall, dA, and the temperature difference across the wall such that

$$\delta \dot{Q} = U dA \left(T_h - T_c\right) \tag{3.67}$$

Combining the preceding equations gives

$$d\left(T_h - T_c\right) = dT_h - dT_c = -\frac{\delta \dot{Q}}{\dot{C}_h} + \frac{\delta \dot{H}_h}{\dot{C}_h} + \frac{\delta \dot{Q}}{\dot{C}_c} - \frac{\delta \dot{H}_c}{\dot{C}_c} = UM\left(T_h - T_c\right)dA + \Psi \quad (3.68)$$

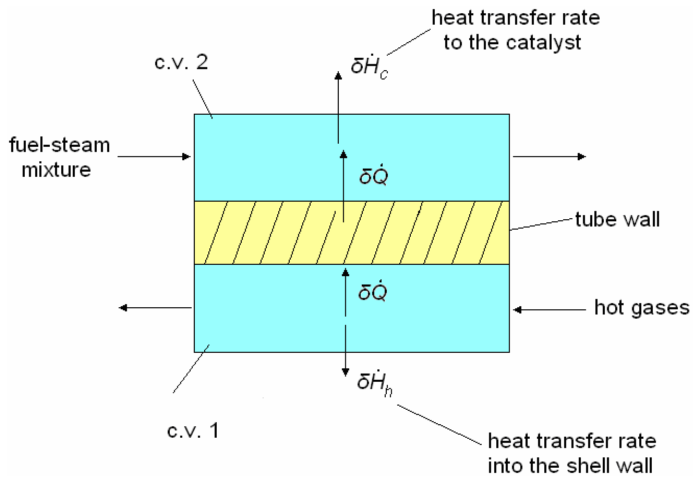

Figure 3.10. Control volume used for the mass and energy balance applied to the pre-reformer.

where $M = \frac{1}{\dot{C}_c} - \frac{1}{\dot{C}_h}$ (3.69)

and $\Psi = +\frac{\delta \dot{H}_h}{\dot{C}_h} - \frac{\delta \dot{H}_c}{\dot{C}_c}$ (3.70)

Now, letting

$$\omega = T_h - T_c \quad (3.71)$$

and $\Theta = +\frac{\delta \dot{H}_h}{dA\,\dot{C}_h} - \frac{\delta \dot{H}_c}{dA\,\dot{C}_c}$ (3.72)

equation (3.68) can be written as

$$\frac{d\omega}{dA} = \omega UM + \Theta \quad (3.73)$$

At this stage, for simplicity, it is assumed that $\omega = \omega\left(A\right)$ in order to integrate equation (3.73) directly. Underlying this assumption are the following:

- U is assumed to be constant since temperature and pressure dependence is neglected;

- Constant specific heats are assumed since temperature and chemical composition dependence are neglected;
- A uniform heat transfer area distribution is assumed.

Thus, with *U, M*, and Θ constant, the solution to equation (3.73) yields

$$\omega = C_1 \exp(UMA) - \frac{\Theta}{UM} \tag{3.74}$$

Applying the appropriate boundary condition results in

$$\omega(A=0) = C_1 - \frac{\Theta}{UM} = \Delta T_a \tag{3.75}$$

$$C_1 = \Delta T_a + \frac{\Theta}{UM} \tag{3.76}$$

Furthermore substitution of equation (3.74) into (3.67) gives

$$\frac{\delta \dot{Q}}{dA} = U\left[C_1 \exp(UMA) - \frac{\Theta}{UM}\right] = \lambda \exp(\Pi A) - \Lambda \tag{3.77}$$

where $\lambda \equiv UC_1$ (3.78a)

$$\Lambda \equiv \frac{\Theta}{\mathrm{M}} \tag{3.78b}$$

and $\Pi \equiv UM$ (3.78c)

Integration of the preceding equation using the boundary condition $\dot{Q}(A=0)=0$ yields

$$\dot{Q} = \frac{\lambda}{\Pi}\exp(\Pi A) - \Lambda A - \frac{\lambda}{\Pi} \tag{3.79}$$

The total energy balance for the reactor now results from integration of the sum of equations (3.63) and (3.64) across the length of the reactor, i.e.

$$\dot{C}_h\left(T_{i,h} - T_{o,h}\right) + \dot{\overline{H}}_h = \dot{C}_h\left(T_{o,c} - T_{i,c}\right) - \dot{\overline{H}}_c \tag{3.80}$$

where the "i" and "o" subscripts refer to the inlets and outlets of the reactor, respectively.

Finally, the accuracy of the preceding calculations is enhanced if average properties based on the inlet and outlet conditions of the reactor are used.

3.3.2 Counter-Flow Heat Exchanger Air Injection Pipe

A counter-flow tube-in-tube heat exchanger is required in order to simulate the heat transfer in the air injection pipe between the air flowing through the fuel cell air tube and the stream coming from inside the stack (Singhal and Kendall 2003; Larminie and Dicks 2003; Benjamin, Camera, and Marianowski 1995; Fuel Cell Handbook 2004; Calise et al., 2004, 2006; Costamagna, Magistri, and Massardo, 2001; Campanari 1998, 2000, 2002). The heat exchange is simulated on the basis of existing models in Calise et al. (2004) and improved to include the effects of pressure drops and to take into account the dependence of the thermophysical and transport properties on temperature.

Heat transfer coefficients and pressure drops are calculated on the basis of appropriate correlations containing Reynolds, Nusselt, and Prandtl numbers found in Kakac and Liu (2002). These parameters depend both on temperature and pressure, varying along the heat exchanger tubes. Consequently, average values are employed, calculated as the mathematical average between inlet and outlet values. Obviously, the overall calculation must be performed iteratively, since heat transfer coefficients and pressure drops depend on the unknown outlet temperatures and pressures. The details of the counter-flow heat exchanger heat transfer model are given in Table 3.2 and are based on the LMTD method.

3.3.3 Catalytic Combustor

The role of the combustor in the hybrid plant under study is very important. It combusts any non-reacted fuel coming out of the fuel cell and, therefore, produces thermal energy for use elsewhere in the system. Its operation is simple, and it is positioned near the fuel cell stack exit. The non-reacted oxygen exiting the cathode side reacts in the combustor with the corresponding species (carbon monoxide, hydrogen, methane) coming out on the anode side.

The catalytic combustor is simulated with mass and energy balances and the associated chemical reaction mechanisms are the following:

$$CH_4 + 2O_2 \rightarrow CO_2 + 2H_2O \tag{3.81}$$

$$CO + \frac{1}{2}O_2 \rightarrow CO_2 \tag{3.82}$$

$$H_2 + \frac{1}{2}O_2 \rightarrow H_2O \tag{3.83}$$

Table 3.2 Heat transfer model of the counter-flow heat exchanger air injection pipe.

Variable	Description	Variable	Description
$T_{h,i}^{HEC}$	Hot fluid inlet temperature	$\dot{n}_{c,i}^{HEC}$	Cold fluid inlet molar flow rate
$T_{c,i}^{HEC}$	Cold fluid inlet temperature	d_o^{HEC}	Tube outer diameter
$p_{h,i}^{HEC}$	Hot fluid inlet pressure	d_i^{HEC}	Tube inside diameter
$p_{c,i}^{HEC}$	Cold fluid inlet pressure	n_t^{HEC}	Number of tubes
$\dot{n}_{h,i}^{HEC}$	Hot fluid inlet molar flow rate	L_t^{HEC}	Length
$c_{p,m}^{HEC}$	Mean specific heat	μ_m^{HEC}	Mean dynamic Viscosity
ρ_m^{HEC}	Mean density	k_m^{HEC}	Mean thermal conductivity
Nu_m^{HEC}	Mean Nusselt number	f_m^{HEC}	Mean Fanning friction factor
A_{cr}^{HEC}	Bundle cross-flow area	$\dot{m}^{HEC}$	Mass flow rate
D_m^{HEC}	Tube mean diameter	p_i^{HEC}	Inlet pressure

Variable	Description	Model Equation
w_m^{HEC}	Mean fluid velocity	$w_m^{HEC} = \dfrac{\dot{m}^{HEC}}{\rho_m^{HEC} A_{cr}^{HEC}}$, $Re_m^{HEC} = \dfrac{\rho_m^{HEC} w_m^{HEC} D_m^{HEC}}{\mu_m^{HEC}}$
Re_m^{HEC}	Mean Reynolds number	
Pr_m^{HEC}	Mean Prandtl number	$Pr_m^{HEC} = \dfrac{\mu_m^{HEC} c_{p,m}^{HEC}}{k_m^{HEC}}$, $h_m^{HEC} = \dfrac{Nu_m^{HEC} k_m^{HEC}}{D_m^{HEC}}$
h_m^{HEC}	Mean heat transfer coefficient	
p_o^{HEC}	Outlet pressure	$p_o^{HEC} = p_i^{HEC} - \dfrac{\rho_m^{HEC} f_m^{HEC} L_t^{HEC} \left(w_m^{HEC}\right)^2}{2D_m^{HEC}} 10^{-5}$
U^{HEC}	Overall heat transfer coefficient	$U^{HEC} = \dfrac{1}{\dfrac{1}{h_{m,h}^{HEC}} + \dfrac{1}{h_{m,c}^{HEC}}}$, $A^{HEC} = \pi d_o^{HEC} L_t^{HEC} n_t^{HEC}$
A^{HEC}	Heat transfer area	
C_{min}^{HEC}	Minimum heat capacity	$C_{min}^{HEC} = \min\left(\dot{m}_h^{HEC} C_{pm,h}, \dot{m}_c^{HEC} C_{pm,c}\right)$
C_{max}^{HEC}	Maximum heat capacity	$C_{max}^{HEC} = \max\left(\dot{m}_h^{HEC} C_{pm,h}, \dot{m}_c^{HEC} C_{pm,c}\right)$
C_r^{HEC}	Heat capacity ratio	$C_r^{HEC} = \dfrac{C_{min}^{HEC}}{C_{max}^{HEC}}$, $NTU^{HEC} = \dfrac{U^{HEC} A^{HEC}}{C_{min}^{HEC}}$
NTU^{HEC}	Number of transfer units	
ε_{HEC}	Effectiveness	$\varepsilon_{HEC} = \dfrac{1 - \exp\left(-NTU^{HEC} + NTU^{HEC} C_r^{HEC}\right)}{1 - C_r^{HEC} \exp\left(-NTU^{HEC} + NTU^{HEC} C_r^{HEC}\right)}$
$\dot{Q}_{HEC}$	Heat transfer rate	$\dot{Q}_{HEC} = \varepsilon_{HEC} C_{min}^{HEC} \left(T_{h,i}^{HEC} - T_{c,i}^{HEC}\right)$
$T_{h,o}^{HEC}$	Hot fluid outlet temperature	$T_{h,o}^{HEC} = T_{h,i}^{HEC} - \dfrac{\dot{Q}_{HEC}}{\dot{m}_h^{HEC} C_{pm,h}}$, $T_{c,o}^{HEC} = T_{c,i}^{HEC} - \dfrac{\dot{Q}_{HEC}}{\dot{m}_c^{HEC} C_{pm,c}}$
$T_{c,o}^{HEC}$	Cold fluid outlet temperature	

For purpose of simplification, the reactions are assumed to be complete and in equilibrium. The mole flow rates for the constituents of the exiting composition are found from the proportionality relations (Gyftopoulos and Beretta, 2005) and the three aforementioned reactions, i.e.

$$\begin{aligned}
&\dot{n}_{CH_{4,i+1}} = \dot{n}_{CH_{4,i}} - x = 0\\
&\dot{n}_{CO_{i+1}} = \dot{n}_{CO_i} - y = 0\\
&\dot{n}_{H_{2,i+1}} = n_{H_{2,i}} - y = 0\\
&\dot{n}_{O_{2,i+1}} = n_{O_{2,i}} - 2x - \frac{1}{2}\left(y+z\right)\\
&\dot{n}_{N_{2,i+1}} = \dot{n}_{N_{2,i}}\\
&\dot{n}_{CO_{2,i+1}} = \dot{n}_{CO_{2,i}} + y\\
&\dot{n}_{H_2Oo} = \dot{n}_{H_2O_i} + x + z
\end{aligned} \tag{3.84}$$

Since the molar compositions at the inlet and outlet, along with the inlet pressures and temperatures are known, using a mass and energy balance on the combustor it is possible to calculate the enthalpy and the temperature at the exit. Furthermore, because the air flow rate is by far greater than that for the fuel, it is the former which is the most responsible for the fuel cell operating temperature being what it is.

3.3.4 Mixer Model

The hybrid plant makes use of three mixers. These are necessary for the operation and the regulation of the plant and have the following principal uses:

- Mixing the exit flow at the anode which contains a significant amount of water with the fuel entering the pre-reformer; so this permits the necessary steam-to-carbon ratio to perform the fuel reforming reaction;
- Controling and regulating the flows when the mixes are positioned downstream of the bypass valves.

The modeling of each mixer is done with simple mass and energy balances, and it is assumed that the pressure at the exit is smaller than at the inlet.

3.4 Thermodynamic and Geometric Gas Turbine Cycle Models

The hybrid plant (SOFC-GT part) utilizes three different turbomachines:

- Air Compressor
- Fuel Compressor
- Gas Turbine

The air compressor and the gas turbine are connected together with a single shaft. The shaft is also connected to an electric generator converting the mechanical power to electrical power. Therefore, these two turbomachines have the same speed of rotation. The fuel compressor, which is far and away smaller than the other two turbomachines is operated by an electric motor that uses a small fraction of the total plant power output.

The selection and modeling of the aforementioned components is extremely complex since the available technology does not include turbomachines with the required size to be integrated with the SOFC under study. Therefore, current technology must be modified based on the hybrid plant's needs to match its characteristics. This means that careful scaling of existing machines must be done in order to correctly modify their geometric characteristics so that they exhibit the following:

- High isentropic power outputs;
- A size compatible with the mass flow rates exiting the IRSOFC;
- Compatible pressure ratios with the IRSOFC;
- Compatible inlet and outlet temperatures with the IRSOFC;
- A wide operating range.

Mass flow rates and rotor speeds are corrected on the basis of their inlet conditions according to the following equations found in Dunbar, Lior and Gaggioli (1991) and Campanari (2000)

$$\dot{m}_c = \frac{\dot{m}\sqrt{\dfrac{T_i}{T_{ref}}}}{\dfrac{p_i}{p_{ref}}} \tag{3.85}$$

$$N_c = \frac{N}{\sqrt{\frac{T_i}{T_{ref}}}} \quad (3.86)$$

where $\dot{m}_c$ is the corrected mass flow rate (kg/s), $\dot{m}$ is the mass flow rate (kg/s), T_i is the temperature (^oC), T_{ref} is the reference temperature (^oC), p_i is the pressure (^oC), p_{ref} is the reference pressure (^oC), N_c is the corrected rotational speed (rpm), and N is the rotational speed (rpm).

The use of turbomachinery maps (e.g. those in Figures 3.11, 3.12, and 3.13 for a 0.508 MWe, 0.024 MWe, and 0.640 MWe air compressor, fuel compressor, and gas turbine, respectively) allows one to account for the geometry of each turbomachine and its effect on the turbomachines part load behavior. These maps also act as constraints to prevent

- Operation beyond the turbomachines operating range;
- A gas turbine outlet pressure lower than atmospheric pressure;
- A gas turbine power output production lower than the air compressor's power consumption.

Furthermore, a unique map for each size compressor and turbine is generated so that the maps shown in Figures 3.11 to 3.13 are simply illustrations since the size or capacity of the compressors and turbine in the SOFC-GT part of the hybrid cycle are varied during the parametric study presented later in this thesis.

3.4.1 Air and Fuel Compressors

Centrifugal compressors meet the technical characteristics of the hybrid plant under study because of their operational flexibility in terms of their mass flow rate capacity and pressure ratio. They also achieve high efficiencies. The calculation of their exit conditions, with respect to entropy and energy, is calculated with the following procedure:

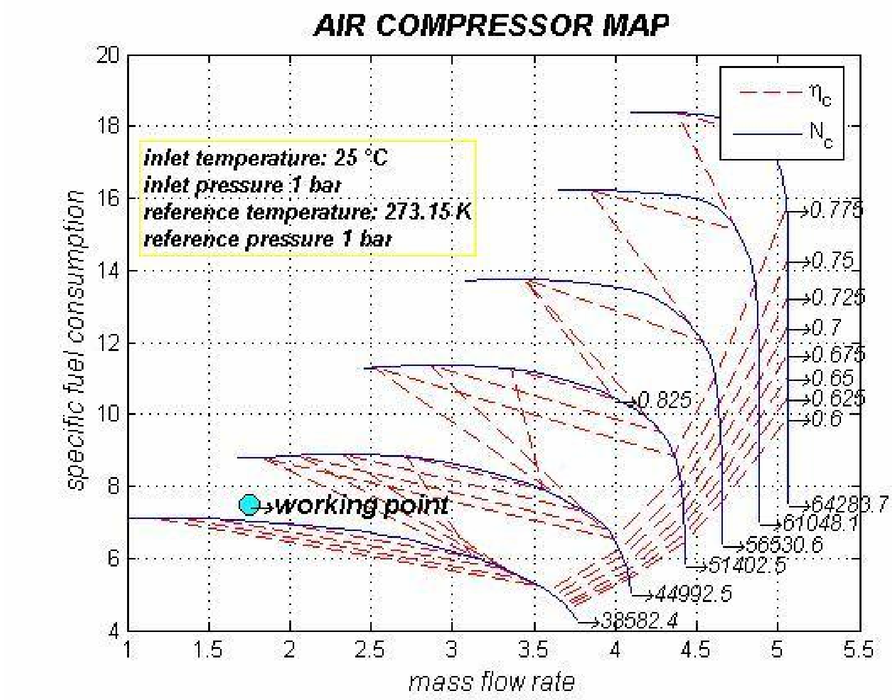

Figure 3.11. Air compressor map for a 508 kW air compressor.

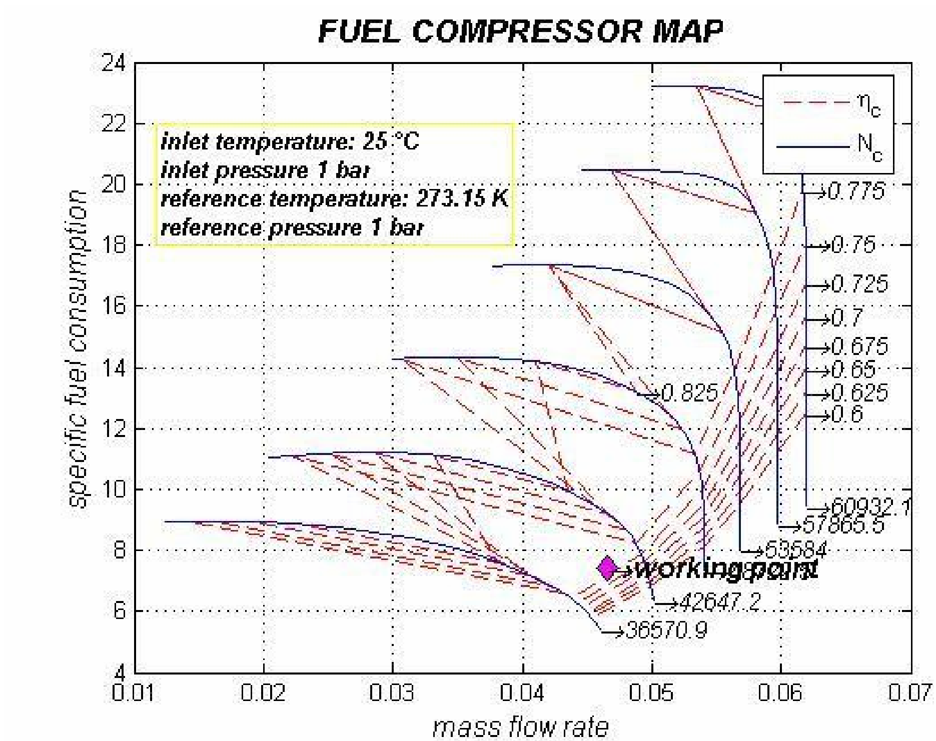

Figure 3.12. Fuel compressor map for a 24 kW fuel compressor.

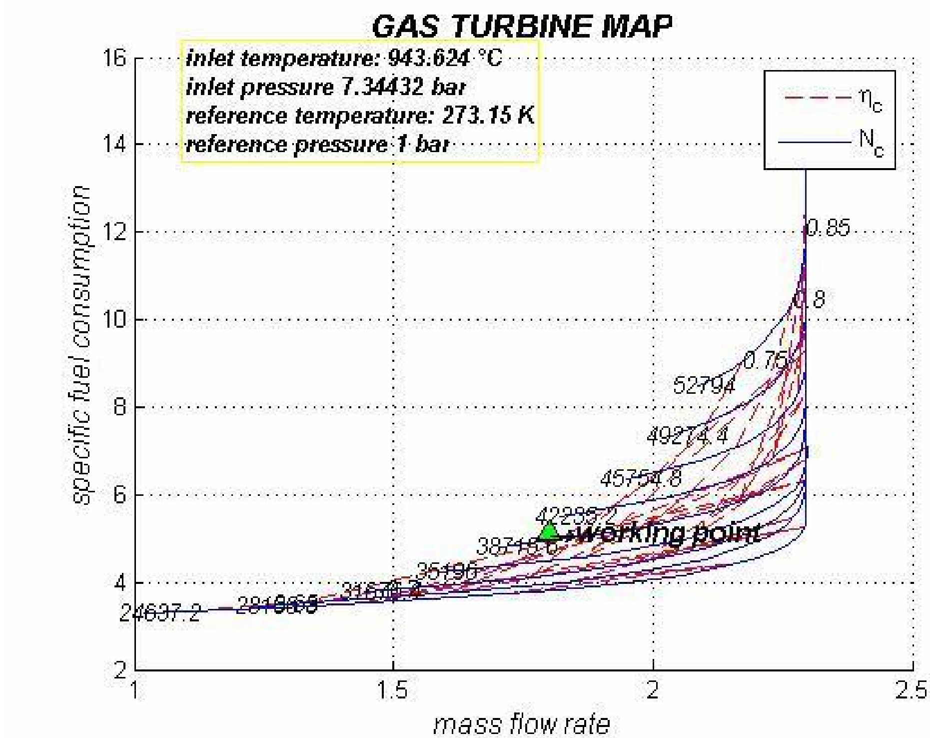

Figure 3.13. Gas turbine map for a 640 kW gas turbine.

- The inlet conditions (temperature, pressure, chemical composition, mass flow rate) are fixed. Therefore, the rotational speed and exit mass flow rate can be calculated using equations (3.85) and (3.86);
- The pressure ratio can be evaluated by "spline" interpolation of the known reference values of mass flow rate, rotational speed, and pressure ratio with the calculated values of rotational speed and mass flow rate;
- The exit pressure can be calculated since the inlet pressure and the pressure ratio are known;
- The isentropic exit temperature can be calculated, assuming an internally reversible adiabatic transformation, using the following entropy balance:

$$s(p_1,T_1)_{compr} = s(p_2,T_{2s})_{compr} \tag{3.87}$$

  where the 1 and 2 subscripts refer to the inlet and exit of the compressor, respectively.
- The exit enthalpy can then be calculated from the isentropic efficiency, η_s, i.e.

$$h\left(T_2, p_2\right)_{compr} = h\left(T_1, p_1\right)_{compr} + \left[\frac{h\left(T_{2s}, p_2\right) - h\left(T_1, p_1\right)}{\eta_s}\right]_{compr} \tag{3.88}$$

- From h_2 and p_2, the actual exit temperature can be found;
- The power input and the efficiency are given by the following expressions

$$\dot{W}_{compr} = \left[\dot{m}c_p\left(T_2 - T_1\right)\right]_{compr} \tag{3.89}$$

$$\left(\eta_s\right)_{compr} = \left[\frac{T_1}{T_2 - T_1}\left[\left(\frac{P_2}{P_1}\right)^{\frac{\gamma-1}{\gamma}} - 1\right]\right]_{compr} \tag{3.90}$$

3.4.2 Gas Turbine

For the gas turbine similar considerations as with the air and fuel compressors can be drawn. The target is a component with increased power outputs, a wide operating range, and pressure ratios and mass flow rates compatible with the fuel cell. These criteria are met by a radial-type turbine. The calculation procedure is similar to the one mentioned for the compressors:

- The inlet conditions (temperature, pressure, chemical composition, mass flow rate) are fixed. Therefore, the rotational speed and exit mass flow rate can be calculated using equations (3.85) and (3.86);
- The pressure ratio can be evaluated by “spline” interpolation of the known reference values of mass flow rate, rotational speed, and pressure ratio with the calculated values of rotational speed and mass flow rate;
- The exit pressure can be calculated since the inlet pressure and the pressure ratio are known;
- The isentropic exit temperature can be calculated, assuming an internally reversible adiabatic transformation, using the following entropy balance:

$$s(p_1, T_1)_{GT} = s(p_2, T_2)_{GT} \tag{3.91}$$

  where the 1 and 2 subscripts refer to the inlet and exit of the turbine, respectively.

- The exit enthalpy can then be calculated from the isentropic efficiency, η_s, i.e.

$$h(T_2, p_2)_{GT} = h(T_1, p_1)_{GT} - \eta_s \left[h(p_1, T_1) - h(p_2, T_2) \right]_{GT} \tag{3.92}$$

- From h_2 and p_2, the actual exit temperature can be determined;
- The power input and the efficiency are given by the following expressions

$$\dot{W}_{GT} = \left[\dot{m} c_p \left(T_1 - T_2 \right) \right]_{GT} \tag{3.93}$$

$$\left(\eta_s\right)_{GT} = \frac{T_1 - T_2}{\left[T_1 \left[1 - \left(\frac{P_2}{P_1} \right)^{\frac{\gamma - 1}{\gamma}} \right] \right]_{GT}} \tag{3.94}$$

3.5 Inverter and Electric Generator Model

The electric power produced by the IRSOFC is dc current. Furthermore, the electric signal exerted by the IRSOFC is extremely unstable, since the current endures notable oscillations and in addition varies with operating conditions. Therefore, the electric signal needs to be conditioned before usage converted to ac current, and filtered from possible oscillations. This is done by a dc-ac inverter. The main parameter of interest is the inverter's efficiency. In other words, the relationship between the unconverted power output to the converted one.

Similarly, the mechanical energy produced by the gas turbine must be converted to electric power. This conversion is accomplished by an electric generator. Again, the main parameter of interest is the efficiency, or in other words, the relationship between the mechanical power output to the ac electric power output. The efficiency for both components is defined as:

$$\eta_{inv} = \frac{\dot{W}_{AC}}{\dot{W}_{DC}} \tag{3.95}$$

where η_{inv} is the inverter efficiency, $\dot{W}_{AC}$ is the ac power, and $\dot{W}_{DC}$ is the dc power.

$$\eta_{gen} = \frac{\dot{W}_{mec}}{\dot{W}_{el}} \tag{3.96}$$

where η_{gen} is the generator efficiency, $\dot{W}_{mec}$ is the mechanical power, and $\dot{W}_{el}$ is the electrical power.

3.6 Thermodynamic and Geometric Steam Turbine Cycle Models

As indicated previously, the steam turbine cycle subsystem model provides four options: a single-pressure, a dual-pressure, a triple-pressure, and a triple-pressure with reheat as shown in Figures 3.14, 3.15, 3.16, and 3.17. These models are based on corresponding configurations suggested by Kehlhofer (1999). All cycle models include steam extraction for cogeneration and deaerator heating. They are composed of models for the heat recovery steam generator, the steam turbine (along with the electric generator), the pumps, the condenser, and the deaerator.

As described in the introduction of the current chapter, the steam turbine is supplied with superheated steam, which is then expanded, producing mechanical power, which is converted to electric power by the electric generator (as with the gas turbine). After expansion, the steam is condensed and the water compressed, preheated, and deaerated in a vacuum deaerator before being fed to the HRSG by a feedwater pump.

The main components of the steam turbine cycle model are:

- A steam turbine (which can be single, dual, or triple admission, depending on the HRSG) and an electric generator;
- A heat recovery steam generator (HRSG) which includes the following heat exchangers: economizer, evaporator, and superheater. It also may include a reheater for the triple-pressure with reheat cycle;
- A condenser which is dimensioned according to the turbine exit pressure and mass flow rate as well as ambient conditions;
- A deaerator heated by steam extracted from the steam turbine;
- A condensate pump;
- From one up to three feedwater pumps.

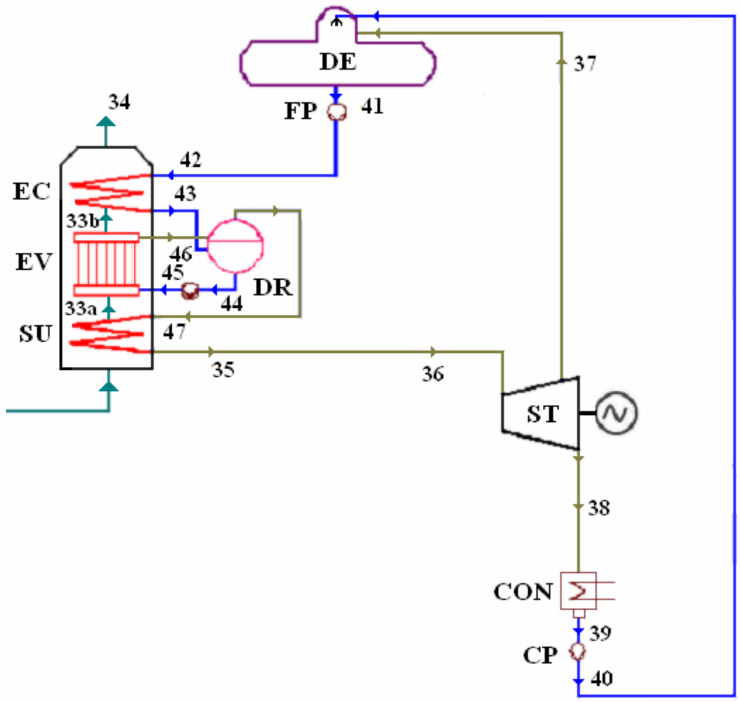

Figure 3.14. Steam turbine subsystem model (single-pressure).

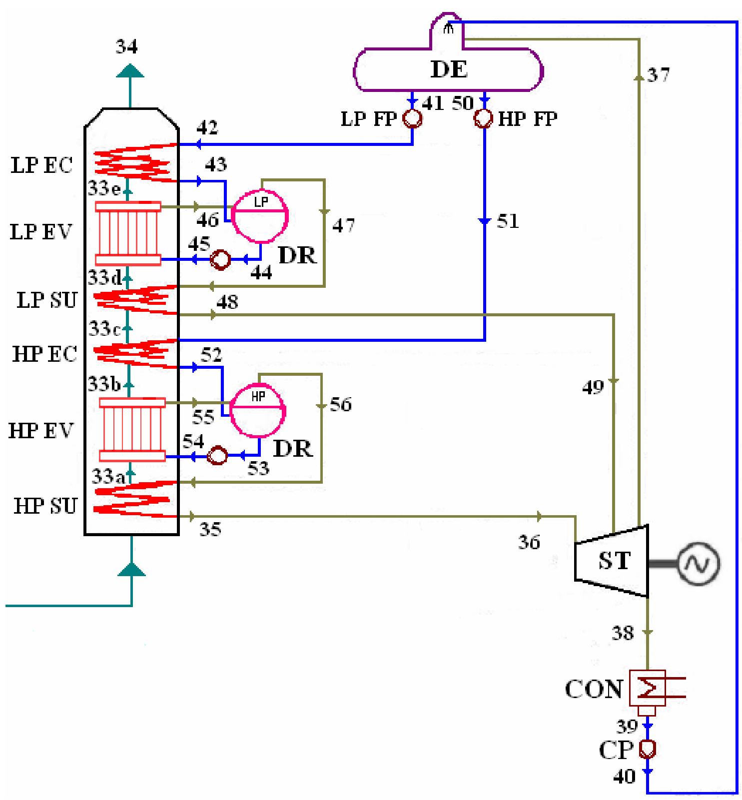

Figure 3.15. Steam turbine subsystem model (dual-pressure).

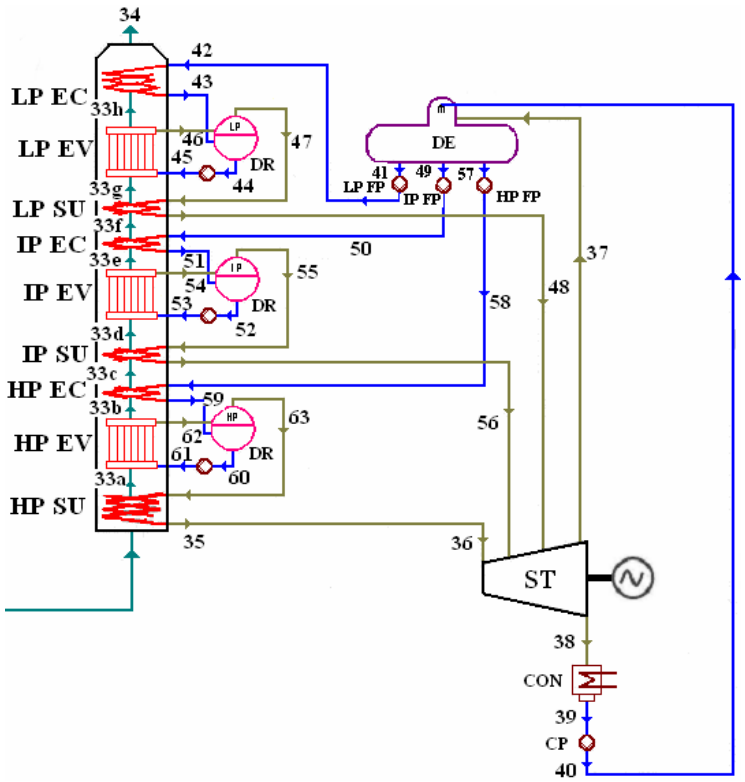

Figure 3.16. Steam turbine subsystem model (triple-pressure).

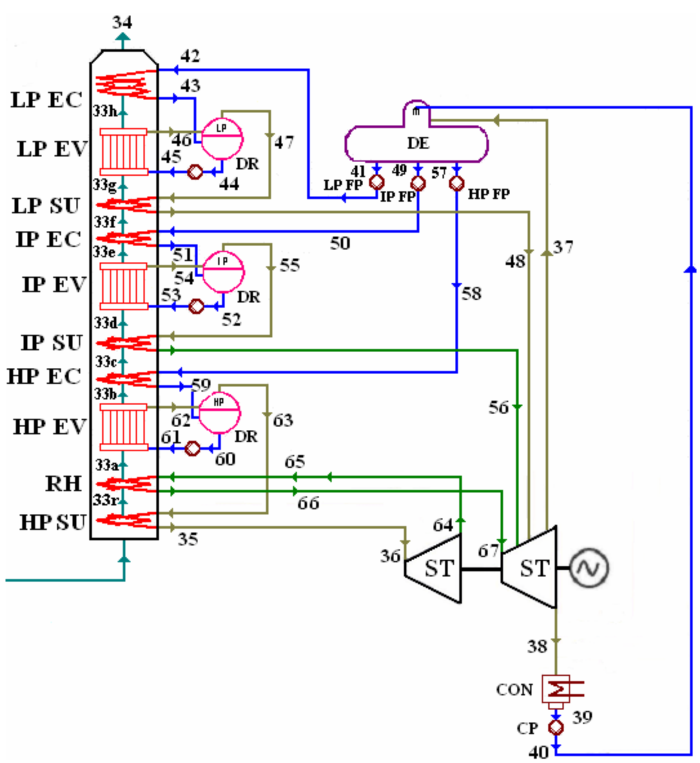

Figure 3.17. Steam turbine subsystem model (triple-pressure with reheat).

3.6.1 Heat Recovery Steam Generator

The HRSG model calculates the live steam mass flow rates and also the exhaust gas conditions at the HRSG exit. In addition, it sizes the different types of heat exchangers included in the HRSG. Depending on the HRSG's number of pressure levels the corresponding live steam mass flow rates are calculated. The water/steam conditions at the inlet and exit of every heat exchanger are defined either directly by the desired live steam conditions or indirectly through conditions on the saturation curve (Pelster, 1998).

An important parameter defining the heating surface and performance of the HRSG is the pinch point. The pinch-point temperature is the difference between the evaporator's outlet temperature on the water/steam side and the inlet temperature on the exhaust gas side. The lower the pinch-point the more heating surface is required and the more steam is generated (Kehlhofer, 1999).

The calculating procedure for the determination of the live-steam mass flow rate is the following (Fuel Cell Handbook, 2004):

- The desired live steam temperatures and pressures are fixed. The evaporator drum pressure can be determined based on a 7-10% loss from the live steam pressure. The pinch points are also selected and fixed.
- The energy balances on the gas and steam sides are the following:

$$\dot{Q}_{SU+EV}^{gas} = \dot{m}_{GTexh} c_p \left(T_{SUin} - T_{EVout} \right) \tag{3.97}$$

$$\dot{Q}_{SU+EV}^{steam} = \dot{m}_{STin} \left(h_{SUout} - h_{EVin} \right) \tag{3.98}$$

- The heat transfer rate is determined from equation (3.97), on the left hand side of each equation and since the two heat transfer rates on the left hand side of each equation are equal to each other, equation (3.98) is solved for the live steam mass flow rate.
- Using simple energy balances, identical to the preceding ones, all temperatures and heat transfer rates can be calculated for all the heat exchangers.

For the geometric models of the heat exchangers both the LMTD and effectiveness-NTU methods are used depending on the exchanger. The geometric models are needed for the determination of off-design conditions behavior. All the heat exchangers are shell-and-tube since they are the appropriate type for compact heat recovery steam generators. A heat exchanger's effectiveness is the ratio of the actual heat transfer rate to the maximum possible heat transfer rate if an infinite heat transfer surface area were available. The actual heat transfer rate is obtained either by the energy given off by the hot fluid or the energy received by the cold fluid. Therefore,

$$\varepsilon = \frac{\dot{Q}_{actual}}{\dot{Q}_{max}} = \frac{\dot{n}_{mix}^{hot} h_{mix}^{hot} \left(T_{hot,i} - T_{hot,o} \right)}{\dot{Q}_{max}} = \frac{\dot{n}_{mix}^{cold} h_{mix}^{cold} \left(T_{cold,o} - T_{cold,i} \right)}{\dot{Q}_{max}} \tag{3.99}$$

Where the "i" and "o" subscripts refer to inlet and outlet, respectively.

The maximum temperature difference occurs on the fluid having the minimum heat capacity. Therefore, the maximum possible heat transfer can be expressed as

$$\dot{Q}_{max} = \dot{n}_{mix}^{hot} h_{mix}^{hot} \left(T_{hot,i} - T_{cold,i} \right) \quad \text{if} \quad \left(\dot{n} C_p \right)_{mix}^{hot} < \left(\dot{n} C_p \right)_{mix}^{cold} \tag{3.100}$$

$$\dot{Q}_{max} = \dot{n}_{mix}^{cold} h_{mix}^{cold} \left(T_{hot,i} - T_{cold,i} \right) \quad \text{if} \quad \left(\dot{n} C_p \right)_{mix}^{cold} < \left(\dot{n} C_p \right)_{mix}^{hot} \tag{3.101}$$

The necessary equations for shell-and-tube heat exchangers are obtained from Kakaç and Liu (2002) and are the appropriate ones for this particular shell-and-tube configuration. The geometric model of the HRSG is shown in Table 3.3.

Table 3.3. Geometric model of the HRSG.

Fixed Parameter Description		Value
t_w	Tube wall thickness (mm)	1.5
n_{passes}^{HRSG}	Number of passes	2
CTP	Tube count calculation constant	0.93
CL	Tube layout constant	1
Variable Description		**Model Equation**
d_i^{HRSG}	Tube inner diameter	Assigned value
n_{tubes}^{HRSG}	Number of tubes	Assigned value
L_{HRSG}	Length	Assigned value
d_o^{HRSG}	Tube outer diameter	$d_o^{HRSG} = d_i^{HRSG} + 2t_w$
P_T^{HRSG}	Pitch	$P_T^{HRSG} = 1.25 d_o^{HRSG}$
D_s^{HRSG}	Shell diameter	$D_s^{HRSG} = 0.637 \sqrt{\frac{CL}{CTP}} \sqrt{\pi n_{tubes}^{HRSG} \left(P_T^{HRSG} \right)^2}$
B	Baffle Spacing	$B = 0.6 D_s^{HRSG}$

The LMTD method is applied to the thermal analysis of the economizer. For the economizer two different expressions for the tube-side heat transfer coefficient are given depending on whether the water flow inside the tubes is fully developed laminar or turbulent. The details of the economizer's heat transfer model are given in Table 3.4.

Table 3.4. Heat transfer model of the economizer.

Variable Description		Model Equation
Re_{eco}	Tube-side Reynolds number	$Re_{eco} = \left(\frac{4\dot{n}_{H_2O}}{\pi d_i \mu_{H_2O} n_{tubes}}\right)_{eco}$ $Pr_{eco} = \left(\frac{\mu_{H_2O} C_{pH_2O}}{k_{H_2O}}\right)_{eco}$
Pr_{eco}	Tube-side Prandtl number	
$h_{H_2O}^{eco}$	Tube-side heat transfer coefficient	If $Re_{eco} \le 2300$ $h_{H_2O}^{eco} = 4.36\left(\frac{k_{H_2O}}{d_i}\right)_{eco}$ otherwise $h_{H_2O}^{eco} = 0.023\left(\frac{k_{H_2O}}{d_i}\right)_{eco} \left(Re_{eco}\right)^{0.8} \left(Pr_{eco}\right)^{0.4}$
D_{eq}^{eco}	Shell-side equivalent diameter	$D_{eq}^{eco} = \frac{4\left(P_T^{eco}\right)^2 - \pi\left(d_o^{eco}\right)^2}{\pi d_o^{eco}}$
A_s^{eco}	Bundle cross-flow area	$A_s^{eco} = \frac{D_s^{eco}\left(P_T^{eco} - d_o^{eco}\right)B_{eco}}{P_T^{eco}}$
G_s^{eco}	Shell-side mass velocity	$G_s^{eco} = \frac{\dot{n}_{gas}}{A_s^{eco}}$
h_{gas}^{eco}	Shell-side heat transfer coefficient	$h_{gas}^{eco} = 0.36\left(\frac{k_{gas}}{D_{eq}}\right)_{eco}\left(\frac{D_{eq} G_s}{\mu_{gas}}\right)_{eco}^{0.55}\left(\frac{C_{pgas}\mu_{gas}}{k_{gas}}\right)_{eco}^{1/3}\left(\frac{\mu_{gas}}{\mu_{wall}}\right)_{eco}^{0.14}$
U_{eco}	Overall heat transfer coefficient	$U_{eco} = \frac{1}{\frac{1}{h_{H_2O}^{eco}} + \frac{1}{h_{gas}^{eco}}}$
A_{eco}	Heat transfer area	$A_{eco} = \left(\pi d_o L n_{tubes} n_{passes}\right)_{eco}$
ΔT_{lm}^{eco}	Log mean temperature difference	$\Delta T_{lm}^{eco} = \frac{\left(T_{gas,i} - T_{H_2O,o}\right)_{eco} - \left(T_{gas,o} - T_{H_2O,i}\right)_{eco}}{\ln\left[\frac{\left(T_{gas,i} - T_{H_2O,o}\right)_{eco}}{\left(T_{gas,o} - T_{H_2O,i}\right)_{eco}}\right]}$
$\dot{Q}_{eco}$	Heat transfer rate	$\dot{Q}_{eco} = \dot{n}_{gas} C_{Pgas}^{eco}\left(T_{gas,i}^{eco} - T_{gas,o}^{eco}\right) = U_{eco} A_{eco} \Delta T_{lm}^{eco}$

As to the evaporator, saturated convective boiling prior to dry out, relations to predict the heat transfer coefficient have been formulated to impose a gradual suppression of nucleate boiling and a gradual increase in liquid film evaporation heat transfer as the quality increases. Kandlikar's correlation has been fit to a broad spectrum of data for both horizontal and vertical tubes, is used to calculate the tube-side heat transfer coefficient for the evaporator. The values for the constants are shown in Table 3.5.

The equations of the evaporator's heat transfer model are presented in detail in Table 3.7 and the values considered for the liquid and vapor water densities as well as for the mass quality are given in Table 3.6. As to the heat transfer model of the superheater (the same model applies for the reheater), this is presented in Table 3.8. The correlations used to calculate the tube-side and shell-side heat transfer coefficients are the same as those appearing in the model for the economizer. The main difference, however, between the two heat transfer models is that the thermal analysis of the superheater is based on the effectiveness-NTU method and not on the LMTD one. The reason why the latter is used to relate the geometric variables of the economizer to its thermodynamic ones is explained below. Let us assume that the effectiveness-NTU method is applied to the modeling of the economizer and that the cold fluid (i.e. the water) is found to have the minimum heat capacity. According to the expression for the maximum possible heat transfer given by equation (3.101), the water stream would then exit the economizer at the inlet temperature of the combustion gases. It is highly likely though that the resulting inlet pressure and temperature of the combustion gases would correspond to a water state at the exit of the economizer different from that for a saturated liquid (e.g., superheated vapor). Such an inconsistency is not desired in the design of the economizer. For that reason, the LMTD method, which does not introduce a discrepancy of this kind, is used (Georgopoulos, 2002).

Table 3.5. Constants for Kandlikar's correlation appearing in Table 3.7.

Constant	**Co < 0.65 (Convective Region)**	**Co ≥ 0.65 (Nucleate Boiling Region)**
C_1	1.136	0.6683
C_2	-0.9	-0.2
C_3	667.2	1058
C_4	0.7	0.7
C_5	0.3	0.3

Table 3.6. Values of the evaporator's heat transfer model parameters.

Parameter Description		**Value**
$\rho_{H_2O}^{liq}$	Liquid water density (kg/m^3)	928.22
$\rho_{H_2O}^{vap}$	Vapor water density (kg/m^3)	1.755
χ	Mass quality	0.5

Table 3.7. Heat transfer model of the evaporator.

Variable	Description	Model Equation
A_{cr}^{eva}	Cross-sectional area	$A_{cr}^{eva}=\dfrac{\pi\left(d_i^{eva}\right)^2}{4}, \quad G_{tube}^{eva}=\dfrac{\dot{n}_{H_2O}}{n_{tubes}^{eva}A_{cr}^{eva}}$
G_{tube}^{eva}	Tube-side mass velocity	
Co	Convection number	$Co=\left(\dfrac{1-\chi}{\chi}\right)^{0.8}\left(\dfrac{\rho_{H_2O}^{vap}}{\rho_{H_2O}^{liq}}\right)^{0.5}$
Fr_{le}	Froude number	$Fr_{le}=\dfrac{\left(G_{tube}^{eva}\right)^2}{\left(\rho_{H_2O}^{liq}\right)^2 g d_i^{eva}}$
Bo	Boiling number	$Bo=\dfrac{q''_{eva}}{G_{tube}^{eva}h_{fg}}$
h_{liq}	Heat transfer coefficient for the liquid phase	$h_{liq}=0.023\dfrac{k_{H_2O}^{liq}}{d_i^{eva}}\left(\dfrac{G_{tube}^{eva}\left(1-\chi\right)d_i^{eva}}{\mu_{H_2O}^{liq}}\right)^{0.8}\left(\dfrac{\mu_{H_2O}^{liq}C_{pH_2O}^{liq}}{k_{H_2O}^{liq}}\right)^{0.4}$
$h_{H_2O}^{eva}$	Tube-side heat transfer coefficient	$h_{H_2O}^{eva}=h_{liq}\left[C_1Co^{C_2}\left(25Fr_{le}\right)^{C_5}+C_3Bo^{C_4}\right]$
D_{eq}^{eva}	Shell-side equivalent diameter	$D_{eq}^{eva}=\dfrac{4\left(P_T^{eva}\right)^2-\pi\left(d_o^{eva}\right)^2}{\pi d_o^{eva}}$
A_s^{eva}	Bundle cross-flow area	$A_s^{eva}=\dfrac{D_s^{eva}\left(P_T^{eva}-d_o^{eva}\right)B_{eva}}{P_T^{eva}}, \quad G_s^{eva}=\dfrac{\dot{n}_{gas}}{A_s^{eva}}$
G_s^{eva}	Shell-side mass velocity	
h_{gas}^{eva}	Shell-side heat transfer coefficient	$h_{gas}^{eva}=0.36\left(\dfrac{k_{gas}}{D_{eq}}\right)_{eva}\left(\dfrac{D_{eq}G_s}{\mu_{gas}}\right)_{eva}^{0.55}\left(\dfrac{C_{pgas}\mu_{gas}}{k_{gas}}\right)_{eva}^{1/3}\left(\dfrac{\mu_{gas}}{\mu_{wall}}\right)_{eva}^{0.14}$
U_{eva}	Overall heat transfer coefficient	$U_{eva}=\dfrac{1}{\dfrac{1}{h_{H_2O}^{eva}}+\dfrac{1}{h_{gas}^{eva}}}$
A_{eva}	Heat transfer area	$A_{eva}=\left(\pi d_o L n_{tubes} n_{passes}\right)_{eva}$
ΔT_{lm}^{eva}	Log mean temperature difference	$\Delta T_{lm}^{eva}=\dfrac{\left(T_{gas,i}-T_{gas,o}\right)_{eva}}{\ln\left[\dfrac{\left(T_{gas,i}-T_{H_2O}\right)_{eva}}{\left(T_{gas,o}-T_{H_2O}\right)_{eva}}\right]}$
q''_{eva}	Surface heat flux (single tube)	$q''_{eva}=\dfrac{\dot{n}_{gas}C_{Pgas}^{eva}\left(T_{gas,i}^{eva}-T_{gas,o}^{eva}\right)}{n_{tubes}^{eva}A_{eva}}=\dfrac{U_{eva}\Delta T_{lm}^{eva}}{n_{tubes}^{eva}}$

3.6.2 Steam Turbine

As mentioned in the introduction of this chapter, the steam turbine (condensing, axial-flow type) can be single, dual, or triple admission depending on the HRSG's pressure level. Furthermore, in the triple-pressure reheat cycle configuration, it is divided into two sections: a high pressure (HP) section and an intermediate/low pressure (IP/LP) section. In this particular configuration, the HP section is supplied with live steam from the superheater. After expansion the wet steam returns to the reheater in the HRSG. After reheating, the superheated steam is supplied to the IP/LP section for further expansion. After expansion in this section the exhaust is fed to the condenser. All the configurations shown in Figure 3.18, include extraction outlets for deaerating/preheating.

Table 3.8. Heat transfer model of the superheater and reheater.

	Variable Description	Model Equation
Re_{sup}	Tube-side Reynolds number	$Re_{sup} = \left(\frac{4\dot{n}_{H_2O}}{\pi d_i \mu_{H_2O} n_{tubes}}\right)_{sup} \quad Pr_{sup} = \left(\frac{\mu_{H_2O} C_{pH_2O}}{k_{H_2O}}\right)_{sup}$
Pr_{sup}	Tube-side Prandtl number	
$h_{H_2O}^{sup}$	Tube-side heat transfer coefficient	$h_{H_2O}^{sup} = 0.023\left(\frac{k_{H_2O}}{d_i}\right)_{sup} \left(Re_{sup}\right)^{0.8} \left(Pr_{sup}\right)^{0.4}$
D_{eq}^{sup}	Shell-side equivalent diameter	$D_{eq}^{sup} = \frac{4\left(P_T^{sup}\right)^2 - \pi\left(d_o^{sup}\right)^2}{\pi d_o^{sup}}$
A_s^{sup}	Bundle cross-flow area	$A_s^{sup} = \frac{D_s^{sup}\left(P_T^{sup} - d_o^{sup}\right) B_{sup}}{P_T^{sup}}, \quad G_s^{sup} = \frac{\dot{n}_{gas}}{A_s^{sup}}$
G_s^{sup}	Shell-side mass velocity	
h_{gas}^{sup}	Shell-side heat transfer coefficient	$h_{gas}^{sup} = 0.36\left(\frac{k_{gas}}{D_{eq}}\right)_{sup} \left(\frac{D_{eq} G_s}{\mu_{gas}}\right)_{sup}^{0.55} \left(\frac{C_{pgas}\mu_{gas}}{k_{gas}}\right)_{sup}^{1/3} \left(\frac{\mu_{gas}}{\mu_{wall}}\right)_{sup}^{0.14}$
U_{sup}	Overall heat transfer coefficient	$U_{sup} = \frac{1}{\frac{1}{h_{H_2O}^{sup}} + \frac{1}{h_{gas}^{sup}}}, \quad A_{sup} = \left(\pi d_o L n_{tubes} n_{passes}\right)_{sup}$
A_{sup}	Heat transfer area	
C_{min}	Minimum heat capacity	$C_{min} = \min\left(\dot{n}_{H_2O} C_{pH_2O}, \dot{n}_{gas} C_{pgas}\right)$
C_{max}	Maximum heat capacity	$C_{max} = \max\left(\dot{n}_{H_2O} C_{pH_2O}, \dot{n}_{gas} C_{pgas}\right)$
C_r	Heat capacity ratio	$C_r = \frac{C_{min}}{C_{max}}, \quad NTU = \frac{U_{sup} A_{sup}}{C_{min}}$
NTU	Number of transfer units	
ε_{sup}	Superheater effectiveness	$\varepsilon_{sup} = \frac{2}{1 + C_r + \sqrt{1 + C_r^2}\,\frac{1 + \exp\left(-NTU\sqrt{1 + C_r^2}\right)}{1 - \exp\left(-NTU\sqrt{1 + C_r^2}\right)}}$

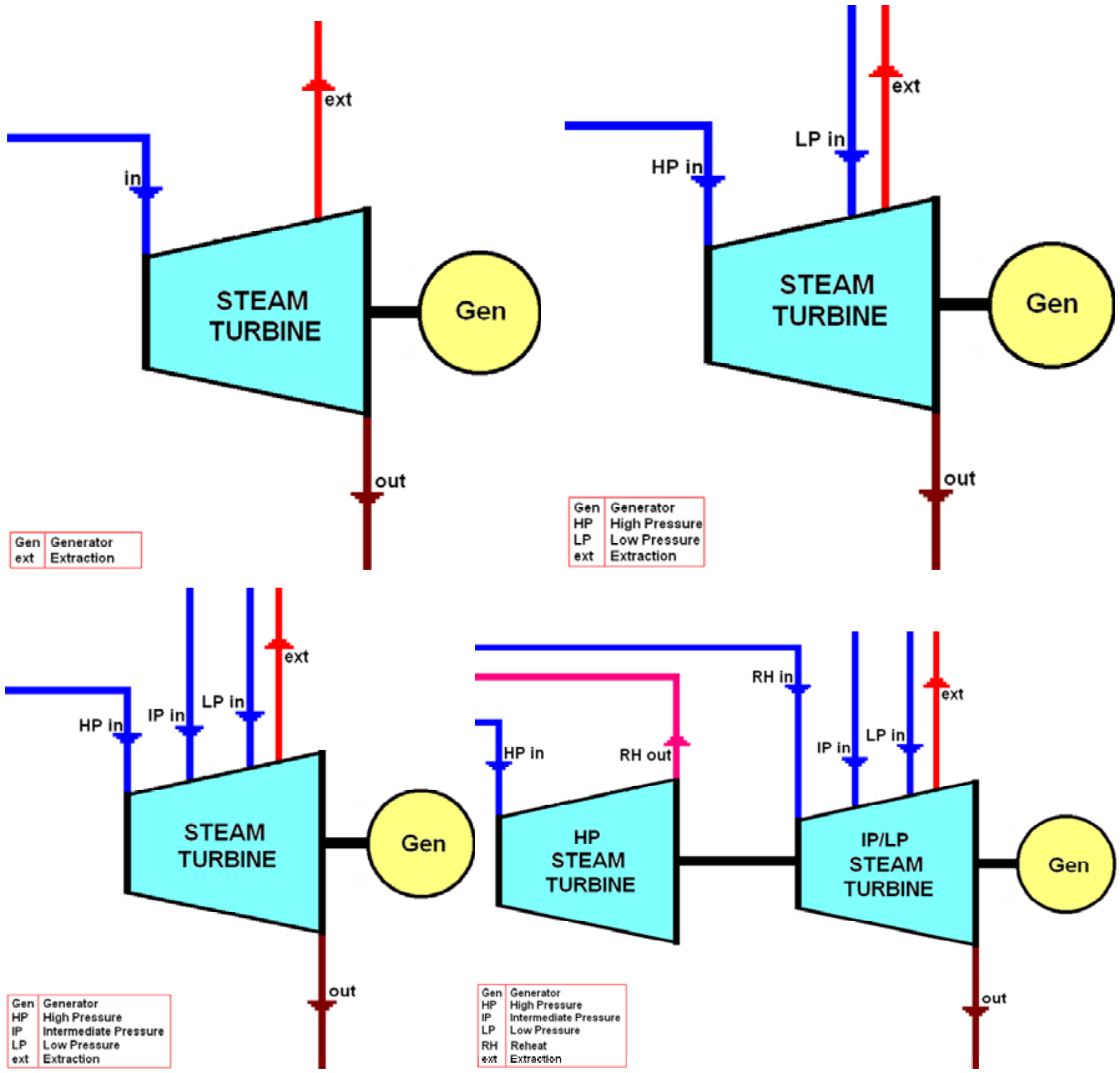

Figure 3.18. Steam turbine configurations (single, dual, triple, triple reheat cycle).

The mass and energy balances for each type of turbine are as follow:

- Single-pressure cycle steam turbine

$$\dot{m}_{in}^{ST} = \dot{m}_{ext}^{ST} + \dot{m}_{out}^{ST} \tag{3.102}$$

$$\dot{W}_{ST}^{single} = \dot{m}_{in}^{ST} h_{in}^{ST} - \dot{m}_{ext}^{ST} h_{ext}^{ST} - \dot{m}_{out}^{ST} h_{out}^{ST} \tag{3.103}$$

where $\dot{m}_{in}^{ST}$ is the mass flow rate of the superheated steam entering the steam turbine, $\dot{m}_{ext}^{ST}$ the mass flow rate of the extracted steam for deaerating, $\dot{m}_{out}^{ST}$ the mass flow rate of the wet exhaust steam after expansion, $\dot{W}_{ST}^{single}$ the work rate produced by the steam turbine, and h_{in}^{ST}, h_{ext}^{ST}, and h_{out}^{ST} are the corresponding enthalpies for the mass flow rates.

- Dual-pressure cycle

$$\dot{m}_{HPin}^{ST} + \dot{m}_{LPin}^{ST} = \dot{m}_{ext}^{ST} + \dot{m}_{out}^{ST} \tag{3.104}$$

$$\dot{W}_{ST}^{dual} = \dot{m}_{HPin}^{ST} h_{HPin}^{ST} + \dot{m}_{LPin}^{ST} h_{LPin}^{ST} - \dot{m}_{ext}^{ST} h_{ext}^{ST} - \dot{m}_{out}^{ST} h_{out}^{ST} \tag{3.105}$$

where $\dot{m}_{HPin}^{ST}$, and $\dot{m}_{LPin}^{ST}$ are the mass flow rate of the HP and LP superheated steam entering the steam turbine, respectively.

- Triple-pressure cycle

$$\dot{m}_{HPin}^{ST} + \dot{m}_{IPin}^{ST} + \dot{m}_{LPin}^{ST} = \dot{m}_{ext}^{ST} + \dot{m}_{out}^{ST} \tag{3.106}$$

$$\dot{W}_{ST}^{triple} = \dot{m}_{HPin}^{ST} h_{HPin}^{ST} + \dot{m}_{IPin}^{ST} h_{IPin}^{ST} + \dot{m}_{LPin}^{ST} h_{LPin}^{ST} - \dot{m}_{ext}^{ST} h_{ext}^{ST} - \dot{m}_{out}^{ST} h_{out}^{ST} \tag{3.107}$$

where $\dot{m}_{HPin}^{ST}$, $\dot{m}_{IPin}^{ST}$, and $\dot{m}_{LPin}^{ST}$ are the mass flow rates of the HP, IP, and LP superheated steam entering the steam turbine, respectively.

- Triple-pressure reheat cycle

$$\dot{m}_{HPin}^{ST} + \dot{m}_{RHin}^{ST} + \dot{m}_{IPin}^{ST} + \dot{m}_{LPin}^{ST} = \dot{m}_{RHout}^{ST} + \dot{m}_{ext}^{ST} + \dot{m}_{out}^{ST} \tag{3.108}$$

$$\begin{aligned} \dot{W}_{ST}^{tripleRH} &= \dot{m}_{HPin}^{ST} h_{HPin}^{ST} + \dot{m}_{RHin}^{ST} h_{RHin}^{ST} + \dot{m}_{IPin}^{ST} h_{IPin}^{ST} \\ &+ \dot{m}_{LPin}^{ST} h_{LPin}^{ST} - \dot{m}_{RHout}^{ST} h_{RHout}^{ST} - \dot{m}_{ext}^{ST} h_{ext}^{ST} - \dot{m}_{out}^{ST} h_{out}^{ST} \end{aligned} \tag{3.109}$$

where $\dot{m}_{HPin}^{ST}$, $\dot{m}_{RHin}^{ST}$, $\dot{m}_{IPin}^{ST}$, and $\dot{m}_{LPin}^{ST}$ are the mass flow rates of the HP, RH, IP, and LP superheated steam entering the steam turbine, respectively, and $\dot{m}_{RHout}^{ST}$ the mass flow rate of the wet steam after expansion in the HP section of the steam turbine.

For off-design purposes (i.e. partial load) steam turbines maps are used in order to capture the effects of geometry on turbine performance. To generate these maps for different size turbines, data is taken from Salisbury (1974). A sample steam turbine map is shown in Figure 3.19.

3.6.3 Pumps

As previously mentioned, the steam turbine cycle includes a condensate pump and one to three feedwater pumps depending on the number of HRSG pressure levels. Since the thermodynamic states in the inlet are known and the outlet thermodynamic states can be fixed as desired, what is left is a calculation of the pump power consumed (see Figure 3.20).

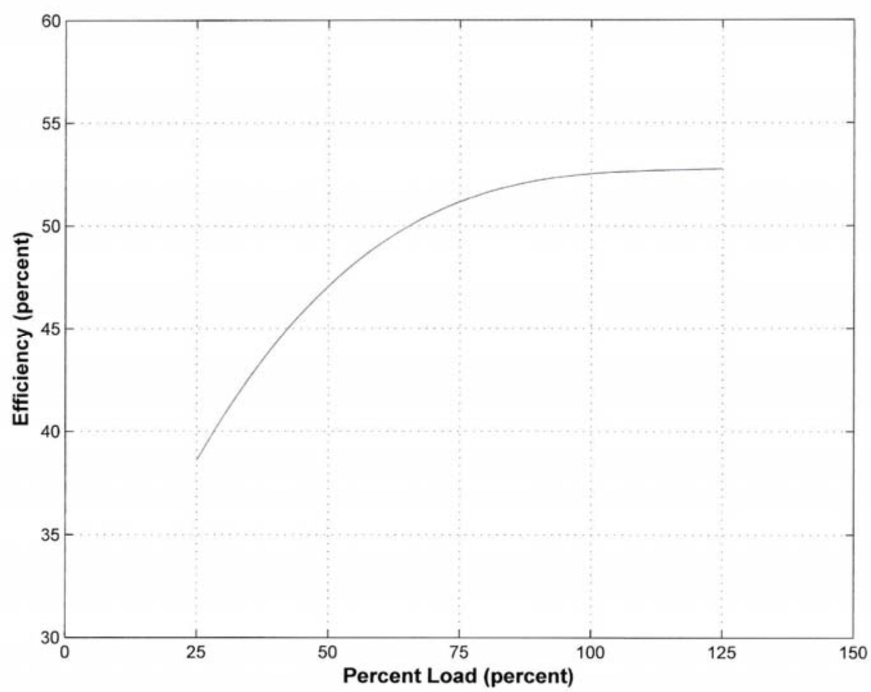

Figure 3.19 Steam turbine map for a 194.4 kW condensing steam turbine.

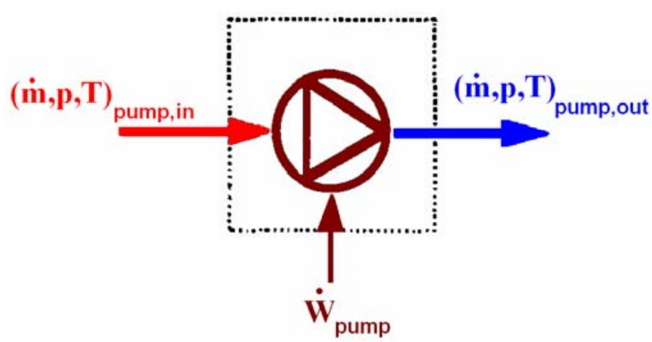

Figure 3.20 Pump schematic.

The corresponding mass and energy balances are given by

$$\dot{m}_{in}^{pump} = \dot{m}_{out}^{pump} \tag{3.110}$$

$$\dot{W}_{pump} = \left[\dot{m}_{in} \left(h_{out} - h_{in} \right) \right]_{pump} \tag{3.111}$$

where $\dot{m}_{in}$ is the non-pressurized mass flow rate entering the pump, $\dot{m}_{out}$ the pressurized mass flow rate exiting the pump, $\dot{W}_{pump}$ the pump work rate consumption, and h_{in}^{pump}, and h_{out}^{pump} are the corresponding enthalpies for the mass flow.

Again, for off-design (part load) purposes pump maps are used. To develop these maps for the various size in order to capture the effects of geometry on performance pumps considered here, actual pump maps found in the literature are rescaled to accommodate the needs of the current research work. For the condensate pump, a map from Skrotzki and Vopat (1960) for a centrifugal type pump is used while for the feedwater pumps, a map for a displacement type pump from Potter (1959) is employed. Sample condensate and feedwater pump maps are shown in Figures 3.21 and 3.22, respectively.

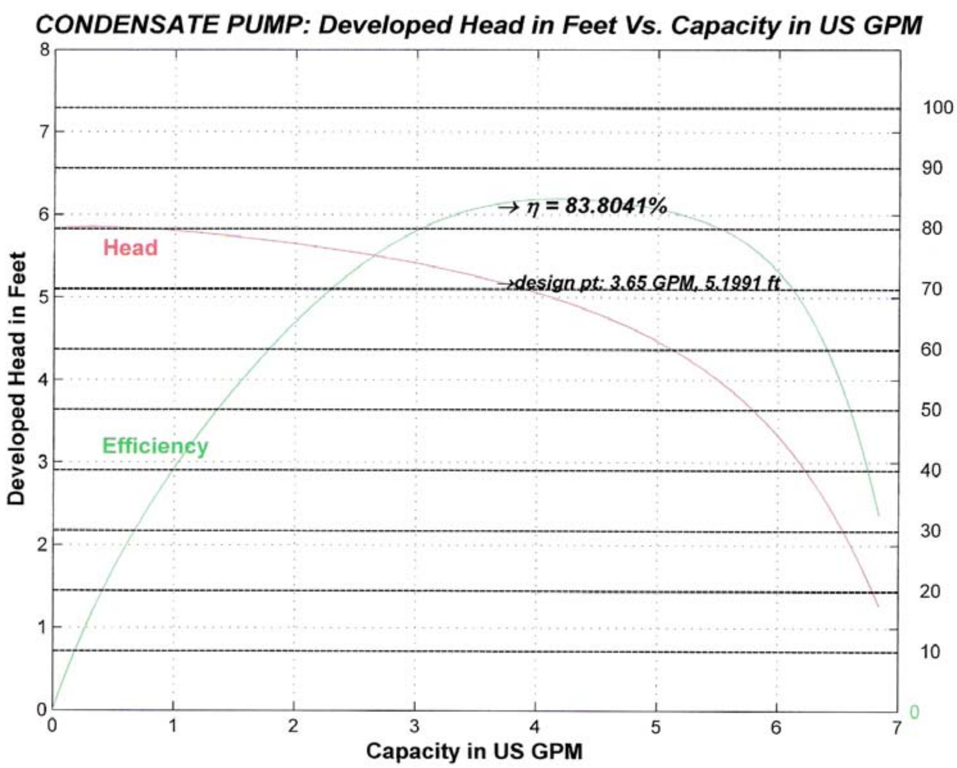

Figure 3.21 Condensate pump map for a centrifugal type 0.02 kW pump.

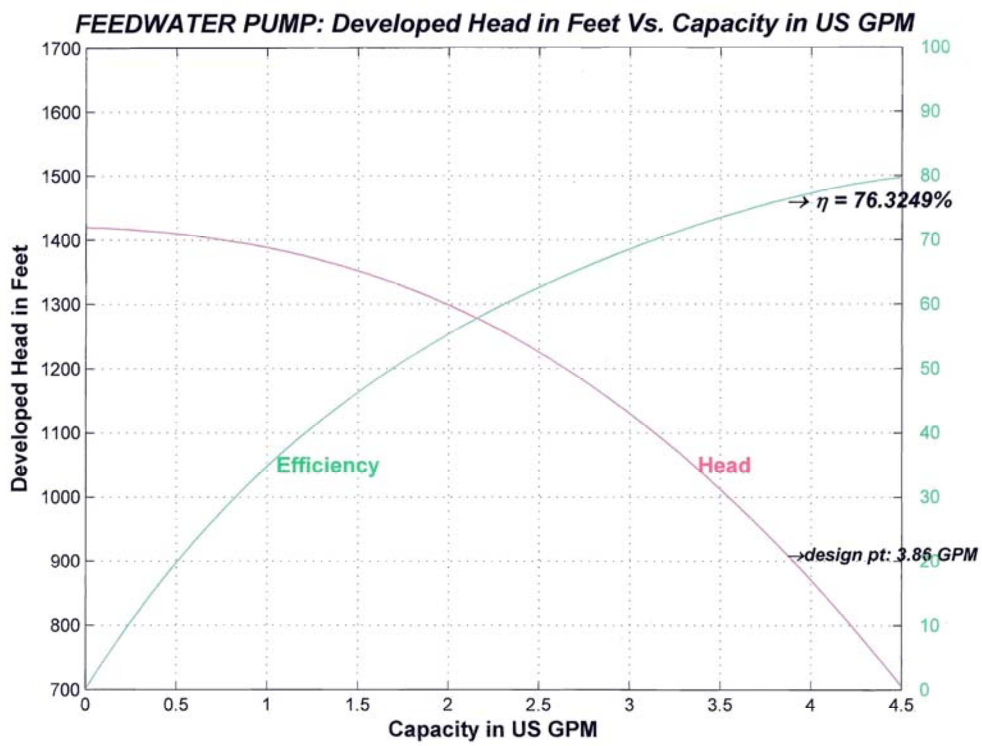

Figure 3.22 Feedwater pump map for a displacement type 12.1 kW pump.

3.6.4 Condenser

The condenser which is a shell-and-tube heat exchanger receives wet steam from the steam turbine's exhaust and condenses it to a saturated liquid. In the condensing process, the temperature and pressure are kept constant. For the purposes of this research study, they have been fixed at 31 ^{o}C and 0.045 bar (Kehlhofer 1999). From a mass balance on the working side of the condenser,

$$\dot{m}_{in}^{cond} = \dot{m}_{out}^{cond} \tag{3.112}$$

where $\dot{m}_{in}^{cond}$ is the mass flow rate of the wet steam entering the condenser and $\dot{m}_{out}^{cond}$ the mass flow rate of the saturated liquid exiting. The heat rejected to the cooling water (cw) is found from an energy balance on the condensing steam, i.e.

$$\dot{Q}_{cond} = \left[\dot{m}_{in}{}^{cond} \left(h_{in}{}^{cond} - h_{out}{}^{cond} \right) \right] \tag{3.113}$$

where $\dot{Q}_{cond}$ is the rejected heat transfer rate and h_{in}^{cond}, and h_{out}^{cond} are the enthalpies for the corresponding mass flow rates.

Table 3.9. Heat transfer model of the condenser.

Fixed Parameter Description		Value	Fixed Parameter Description		Value
$R_{f,i}$	Inside fouling resistance	0.00018	$R_{f,o}$	Outside fouling resistance	0.00009

Variable Description		Model Equation
d_i^{con}	Tube inner diameter	Assigned value
t_w^{con}	Tube wall thickness	
L^{con}	Length	
N_T^{con}	Number of tubes	
d_o^{con}	Tube outer diameter	$d_o^{con} = d_i^{con} + 2t_w^{con}$, $D_m^{con} = \dfrac{d_i^{con} + d_o^{con}}{2}$, $f_{con} = \left(1.58\ln\left(Re_{con}\right) - 3.28\right)^{-2}$
D_m^{con}	Tube mean diameter	
f_{con}	Fanning friction factor	
Re_{con}	Reynolds number	$Re_{con} = \left(\dfrac{U_{cw}\rho_{cw}d_i}{\mu_{cw}}\right)_{con}$ $Nu_{con} = \left(\dfrac{\frac{f}{2}RePr}{1.07 + 12.7\sqrt{\frac{f}{2}}\left(Pr^{2/3} - 1\right)}\right)_{con}$
Nu_{con}	Nusselt number	
h_i^{con}	Inner side heat transfer coefficient	$h_i^{con} = \left(\dfrac{Nuk_{cw}}{d_i}\right)_{con}$, $h_o^{con} = 0.728\left[\dfrac{\left(\rho_l^{con}\right)^2 gh_{fg}^{con}\left(k_l^{con}\right)^3}{\mu_l^{con}\Delta T_w d_o^{con}}\right]^{\frac{1}{4}}$
h_o^{con}	Outer side heat transfer coefficient	
ΔT_{lm}^{con}	Log mean temperature difference	$\Delta T_{lm}^{con} = \dfrac{\left(T - T_{cw,i}\right)_{con} - \left(T - T_{cw,o}\right)_{con}}{\ln\left[\dfrac{\left(T - T_{cw,i}\right)_{con}}{\left(T - T_{cw,o}\right)_{con}}\right]}$
R_t	Total thermal resistance	$R_t = R_{f,o} + \left(\dfrac{1}{h_i^{con}} + R_{f,i}\right)\dfrac{d_o^{con}}{d_i^{con}} + \dfrac{t_w^{con}}{k_w^{con}}\dfrac{d_o^{con}}{D_m^{con}}$
U_{con}	Overall heat transfer coefficient	$U_{con} = \dfrac{1}{R_t + \dfrac{1}{h_{con,o}}}$, $\Delta T_w = \Delta T^{con}\left(1 - R_t U_{con}\right)$
ΔT_w	Saturation and fouling surface temperature difference	
$U_{m,con}$	Mean overall heat transfer coefficient	$U_{m,con} = \dfrac{U_{i,con} + U_{o,con}}{2}$, $A_{con} = \left(N_T \pi d_o L\right)_{con}$
A_{con}	Heat transfer area	
$\dot{Q}_{eco}$	Heat transfer rate	$\dot{Q}_{con} = U_{m,con}A_{con}\Delta T_{lm}^{con}$

The cooling water mass flow rate can be calculated by an energy balance on the cooling water entering and exiting the condenser. Therefore,

$$\dot{m}_{cw} = \frac{\dot{Q}_{cond}}{\left(T_{cw,out} - T_{cw,in}\right)C_{pcw}} \tag{3.114}$$

where $\dot{m}_{cw}$ is the mass flow rate of the cooling water, $T_{cw,in}$ and $T_{cw,out}$ are the inlet and outlet cooling water temperatures, respectively, and $C_{p,cw}$ is the average cooling water specific heat.

The LMTD method is applied to the thermal and geometric analysis of the condenser. The details of the condenser's heat transfer model are given in Table 3.9.

3.6.5 Deaerator

The deaerator, shown in Figure 3.23, removes dissolved gases and impurities from the condensate by keeping it in a reservoir at the state of a saturated liquid. As previously mentioned, it is heated by steam extracted from the steam turbine at a pressure slightly higher than the deaerator pressure.

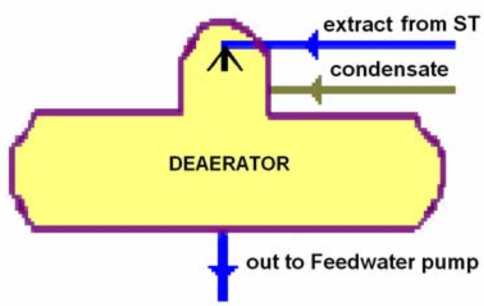

Figure 3.23 Deaerator schematic.

The corresponding mass and energy balances for the deaerator of Figure 3.23 are

$$\dot{m}_{in}^{dea} + \dot{m}_{ext}^{dea} = \dot{m}_{out}^{dea} \tag{3.115}$$

where $\dot{m}_{in}^{dea}$ is the mass flow rate of the saturated liquid coming from the condensate pump, $\dot{m}_{ext}^{dea}$ the mass flow rate of the steam turbine extraction, $\dot{m}_{out}^{dea}$ the mass flow rate of the deaerated/preheated water exiting the deaerator,

$$\dot{m}_{out}^{dea} h_{out}^{dea} - \dot{m}_{ext}^{dea} h_{ext}^{dea} - \dot{m}_{in}^{dea} h_{in}^{dea} = 0 \tag{3.116}$$

where h_{out}^{dea}, h_{ext}^{dea}, and h_{in}^{dea} are the enthalpies for the corresponding mass flow rates.

3.7 Cost Models

For the thermoeconomic analysis of the plant, appropriate cost functions must be formulated to include the following:

- Purchase cost for every component.
- Capital cost per annum.
- Operating cost per annum.
- Total cost per annum.

The expressions for all the component purchase costs are summarized in detail in Table 3.10, while the capital, operating, and total costs per annum are summarized in Table 3.11.

Starting with the gas turbine, the cost function proposed by Traverso et al. (2004) is used. For the centrifugal compressors (air and fuel compressors), the corresponding costs are calculated by interpolating data from the manufacturers as a function of the maximum power required and using information provided by Chiesa and Consonni (2003). For the counter flow heat exchanger, the capital cost is determined on the basis of a cost function from Boehm (1987).

The cost of the SOFC stack is not calculated at present market values, since the technology is still sometime away from full commercialization. Thus, the cost is estimated with reference to market studies in which the expected cost for the case of a significant increase in production volume is assumed. A detailed work performed by Chan, Low, and Ding (2002) relates the SOFC purchase cost to the active area and the operating temperature. Furthermore, the electric energy produced by the SOFC must be filtered by an inverter, whose cost is not negligible and should, therefore, be taken into account. The cost depends primarily on the net power production of the stack.

The SOFC system also consists of a pre-reformer, whose cost is calculated on the basis of its catalysts volume and the finned exchange area (Georgopoulos (2002), Oyarzabal (2001), Boehm (1987)) which in turn is related to the number, diameter,

Table 3.10. Component cost models.

Variable Description		Model Equation
C_{GT}	Gas turbine component cost ($)	$C_{GT} = \left(-98.328\ln\left(\dot{W}_{GT}\right)+1318.5\right)\dot{W}_{GT}$
C_{comp}	Compressor component cost ($)	$C_{comp} = 91562\left(\frac{\dot{W}_{comp}}{445}\right)^{0.67}$
C_{HEC}	Counter-flow heat exchanger component cost ($)	$C_{HEC} = 130\left(\frac{A_{HEC}}{0.093}\right)^{0.78}$
C_{SOFC}	SOFC stack component cost ($)	$C_{SOFC} = \left(n_{cells}\pi D_{cell}L_{cell}\right)\left(2.96T_{cell}-1907\right)$
C_{inv}	Inverter component cost ($)	$C_{inv} = 10^5\left(\frac{\dot{W}_{cell}}{500}\right)^{0.70}$
C_{PR}	Pre-reformer component cost ($)	$C_{PR} = 130\left(\frac{A_{PR,fin}}{0.093}\right)^{0.78} + 3240\left(V_{PR}\right)^{0.4} + 21280.5V_{PR}$
$C_{aux,SOFC}$	SOFC auxiliary components cost ($)	$C_{aux,SOFC} = 0.10C_{SOFC}$
C_{ST}	Steam turbine component cost ($)	$C_{ST} = 3644.3\left(\dot{W}_{ST}\right)^{0.7} - 61.3\left(\dot{W}_{ST}\right)^{0.95}$
f_{p_i}	Heat exchanger pressure factor	$f_{p_i} = 0.0971\left(\frac{p_i}{30}\right)+0.9029$
$f_{T,steam}$	Steam-side temperature factor	$f_{T,steam} = 1+\exp\left(\frac{T_{out,steam}-830}{500}\right)$
$f_{T,gas}$	Gas-side temperature factor	$f_{T,gas} = 1+\exp\left(\frac{T_{out,gas}-990}{500}\right)$
K_i	LMTD correction factor (kW/K)	$K_i = \frac{\dot{Q}_i}{\Delta T_{lm,i}}$
$C_{HE(HRSG)}$	HRSG's heat exchangers component cost ($)	$C_{HE(HRSG)} = 3650\sum_i\left(f_{p_i}f_{T_{i,steam}}f_{T_{i,gas}}K^{0.8}\right)_i$
f_{p_j}	Piping pressure factor	$f_{p_j} = 0.0971\left(\frac{p_j}{30}\right)+0.9029$
C_{piping}	HRSG's piping component cost ($)	$C_{piping} = 11820\sum_j\left(f_{p_j}\dot{m}_{j,steam}\right)$
C_{gas}	HRSG's gas conduit cost ($)	$C_{gas} = 658\dot{m}_{gas}^{1.2}$
C_{HRSG}	HRSG component cost ($)	$C_{HRSG} = C_{HE(HRSG)} + C_{piping} + C_{gas}$
C_{cond}	Condenser component cost ($)	$C_{cond} = 248A_{cond} + 659\dot{m}_{cool}$
f_η	Efficiency correction factor	$f_\eta = 1+\left(\frac{1-0.8}{1-\eta_{pump}}\right)$
C_{pump}	Pump component cost ($)	$C_{pump} = 442\left(\dot{W}_{pump}\right)^{0.71}1.41f_\eta$

Table 3.11. Capital, operating, and total cost models.

Variable Description		Model Equation
$\dot{C}_{dep}$	Depreciation cost ($/yr)	$\dot{C}_{dep} = \dfrac{C_{pur}}{n_{dep}}$, $\dot{C}_{int} = \dfrac{C_{pur}}{n_{dep}} i$, $\dot{C}_{mai} = \dfrac{C_{pur}}{n_{dep}} f_{mai}$
$\dot{C}_{int}$	Interest on outside capital cost ($/yr)	
$\dot{C}_{mai}$	Maintenance cost ($/yr)	
$\dot{C}_{ins}$	Insurance cost ($/yr)	$\dot{C}_{ins} = \dfrac{C_{pur}}{n_{dep}} f_{ins}$, $\dot{C}_{tax} = \dfrac{C_{pur}}{n_{dep}} f_{tax}$
$\dot{C}_{tax}$	Taxation cost ($/yr)	
$\dot{C}_{cap}$	Capital cost ($/yr)	$\dot{C}_{cap} = \dot{C}_{dep} + \dot{C}_{int} + \dot{C}_{mai} + \dot{C}_{ins} + \dot{C}_{tax}$, $\dot{C}_{ope} = c_f \dot{V}_f N_h$
$\dot{C}_{ope}$	Operating cost ($/yr)	
$\dot{C}_{total}$	Total cost ($/yr)	$\dot{C}_{total} = \dot{C}_{cap} + \dot{C}_{ope}$

and length of tubes. Thus, based on these references and updating the functions with literature data, the pre-reformer component cost function has been formulated by Calise (2005). The total cost for SOFC auxiliary devices such as the combustor, mixers, and by-pass valves are calculated as a fixed percentage (10%) of the stack cost.

For the steam turbine cycle, all cost equations, except that for the steam turbine, are based on the research work of Pelster (1998) and have been appropriately adjusted for inflation by using the Plant Cost Index, Chemical Engineering magazine (2005). For the steam turbine, the cost function, which based on the steam turbine power output, is developed based on a personal communication with Traverso (2006).

For the HRSG (which includes the drum and piping costs), the total cost is composed of the cost for the various heat exchangers, the piping, the gas conduit and the pump. It is based on a function used by Frangopoulos (1991). The total cost of the heat exchangers is formed by the sum of the cost for the various heat exchange units (e.g., HP superheater, HP evaporator, HP economizer, reheater, etc.) indicated by the index i. Also the LMTD correction factor, K_i is based on the logarithmic mean temperature difference, $\Delta T_{lm,i}$, while f_{p_i}, $f_{T_{i,steam}}$, and $f_{T_{i,gas}}$ are cost correction factors. The cost functions for the piping and the gas conduit include the factors f_{p_i}, $f_{T_{i,steam}}$, and $f_{T_{i,gas}}$. The factors introduce a sensitivity of cost to pressure as well as to steam and exhaust gas temperature. The pressure factor is calculated as a function of live steam pressure p_i and comes from curve fit data for heat exchangers found in Boehm (1987). The temperature factors are developed using Frangopoulos' (1991) form of the temperature correction factors and the fact that the investment of superheaters is about twice as high as the investment cost for evaporators (Pelster, 1998). The temperature values indicating technical limits are taken from Pelster (1998).

For the condenser, the cost function is based on Frangopoulos (1991). It is calculated as a function of the condenser surface area, A_{cond}, and the cooling water mass flow rate, $\dot{m}_{cool}$. For the deaerator, the cost function is formulated using a cost function found in Boehm (1987).

The cost function for the pumps is taken from Frangopoulos (1991) and calculates the cost as a function of the electric power consumed, $\dot{W}_{pump}$, and an efficiency correction factor f_{η}.

The purchase or capital cost must be placed on an annual basis in order to account for the cost of the investment required. This annual cost is composed of the depreciation cost, $\dot{C}_{dep}$, interest on the investment, $\dot{C}_{int}$, maintenance cost, $\dot{C}_{mai}$, insurance cost, $\dot{C}_{ins}$, and tax cost, $\dot{C}_{tax}$.

The depreciation cost is based on the fact that the equipment deteriorates with time (Peters, Timmerhaus and West, 2003) and, thus, looses value. This loss of value needs to be distributed over the lifetime of the component. This results in a realistic estimation of the cost of the equipment and indicates how much money has to be spent every year in order to save money for future replacement or to pay back loans if the equipment was purchased with outside capital. In the context of thermoeconomic modeling, the common linear depreciation method is used for this cost estimation. Therefore, the annual depreciation (plant lifetime) cost is determined by dividing the total purchase cost, C_{pur}, by the depreciation time, n_{dep}, measured in years. For this research work, n_{dep} has been assumed to be 10 years (Calise, 2005).

The purchase or capital cost must also be financed from outside sources such as bank loans. The associated interest is considered a cost (Peters, Timmerhaus and West, 2003). Even if the financing comes from internal sources, a cost is involved since the money used to purchase the equipment could have been put in a bank or invested elsewhere. The foregone interest, thus, represents an opportunity cost. For the current research work, some simplifying assumptions can be drawn: i) a single interest rate is assumed for the cost of borrowed capital as well as for the opportunity cost of having invested ones own capital and ii) the capital cost is distributed over the lifetime or depreciation time of the plant. The interest rate, *i*, is assumed to be 0.0926 (Peters, Timmerhaus and West, 2003).

The maintenance cost may vary over the lifetime of an installation as the equipment degrades and depends largely on the number of operating hours, the frequency of shutdowns and startups, and the operating environment. A total maintenance cost for the above suggests annual maintenance expenses on the order of 6 percent of the annual depreciation cost (Georgopoulos, 2002), Thus, f_{mai} which is the maintenance cost factor is 0.06.

Similarly, the insurance and taxation cost factors are chosen as 0.2 and 0.54 percent, respectively (Pelster, 1998).

Finally, the operating cost per annum is given in Table 3.12 (Calise, 2005). In this cost function, c_f is the cost of fuel in $/Nm^3, $\dot{V}_f$ is the volumetric flow rate of the fuel in Nm^3/hr, and N_h are the annual hours of operation. The latter is assumed to be 8760 hr/yr (Calise, 2005). Once both the annual operating cost and the capital cost per annum are known, the total cost per annum becomes the sum of the annual capital and operating costs.

4 Results and Discussion

This chapter includes the validation of the SOFC hybrid plant model with existing systems found in the literature. Afterwards, the parametric study's strategy is outlined. Its parametric study purpose is to determine the optimum input parameters for every individual system. Finally, the results for the optimum systems are shown and discussed in detail.

4.1 Model Validation

The SOFC-GT-ST hybrid system needs to be validated in order to have confidence in the model predictions. The validation procedure helps determine the degree of accuracy of the model and any possible mismatches and discrepancies. Each subsystem of the hybrid system is validated separately using manufacturer's data for the SOFC model and measured data from the literature for the four steam turbine cycle and single gas turbine cycle models. Results for the SOC and the steam turbine subsystems are presented below, while those for the gas turbine cycle can be found in Calise (2005).

4.1.1 Validation of the SOFC Model

In the previous chapter, all losses or overvoltages were individually and analytically defined. These aforementioned overvoltages are evaluated at the exiting SOFC temperature as mentioned in the literature by Chan, Low and Ding (2002). The overall voltage of the single cell can be calculated as a function of current density, temperatures, pressures, chemical composition, and geometric/material characteristics by calculating the difference between the reversible potential and all the overvoltages,

$$V = E - V_{ohm} - V_{concentration} - V_{activation} \tag{4.1}$$

In order to validate the model, the polarization curves generated by the code are compared with experimental ones for different values of operating pressure, temperature, and chemical composition of the inlet streams. The results show that the lumped-parameter model achieves errors lower than 5%, no matter the operating pressure, temperature, or inlet chemical composition is considered. Figure 4.1 shows the experimental and simulation results at an operating temperature of 1000 °C, with inlet composition, pressure, and fuel utilization factor as described in Singhal (1997). Unfortunately, the data available from Siemens only deals with hydrogen-fuelled SOFCs, and, therefore, the validation of the internal reforming process is not yet possible.

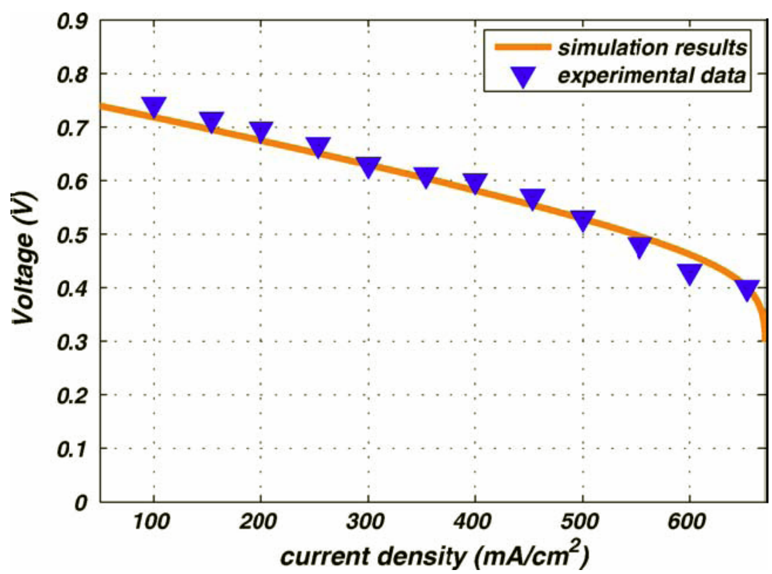

Figure 4.1. SOFC model validation.

4.1.2 Validation of the Steam Turbine Cycle Model

As mentioned in Chapter 3, the steam turbine cycle subsystem models were modeled based on Kehlhofer (1999). Fortunately, the same source includes measured data for the performance of all four steam turbine cycle configurations. This data includes temperatures, pressures, mass flow rates, and steam turbine power output.

In Table 4.1, the input data, which is the same for all four steam turbine cycles, is given. In Tables 4.2, 4.3, 4.4, and 4.5 the input data that is unique for every steam turbine cycle configuration is given along with comparisons to measured data found in Kehlhofer (1999) for these cycles.

Table 4.1. GT input data used in the validation of all four ST cycles for a 275 MWe hybrid cycle.

Input Parameter Description		Value
T_{33}	HRSG gas-side inlet temperature $(^{\circ}\mathrm{C})$	647
p_{33}	HRSG gas-side inlet pressure (bar)	1.013
$\dot{m}_{33}$	HRSG gas-side mass flow rate $(\mathrm{kg/s})$	386.7

Table 4.2. Model validation of the single-pressure ST cycle for a 275 MWe hybrid cycle.

Input Parameter Description		Value		Input Parameter Description		Value
T_{35}	Live-steam temperature $(^{\circ}\mathrm{C})$	568		p_{35}	Live-steam pressure (bar)	105

Output Parameter Description		Measured Value	Model Value
T_{34}	HRSG gas-side outlet temperature $(^{\circ}\mathrm{C})$	133.0	133.3
$\dot{m}_{35}$	Live-steam mass flow rate $(\mathrm{kg/s})$	73.3	70.1
$\dot{m}_{37}$	ST extraction mass flow rate $(\mathrm{kg/s})$	4.00	3.86
$\dot{W}_{ST}$	ST power output (MW)	94.8	90.7

Table 4.3. Model validation of the dual-pressure ST cycle.

Input Parameter Description		Value		Input Parameter Description		Value
T_{35}	Live-steam (HP) temp. $(^{\circ}\mathrm{C})$	568		p_{35}	Live-steam (HP) pressure (bar)	105

Output Parameter Description		Measured Value	Model Value
T_{34}	HRSG gas-side outlet temperature $(^{\circ}\mathrm{C})$	96.0	113.9
$\dot{m}_{35}$	Live-steam (HP) mass flow rate $(\mathrm{kg/s})$	73.3	70.1
$\dot{m}_{37}$	ST extraction mass flow rate $(\mathrm{kg/s})$	4.00	4.11
$\dot{W}_{ST}$	ST power output (MW)	99.0	93.3

Table 4.4. Model validation of the triple-pressure ST cycle for a 275 MWe hybrid cycle.

Input Parameter Description		Value		Input Parameter Description		Value
T_{35}	Live-steam (HP) temp. $(^{\circ}\mathrm{C})$	568		p_{35}	Live-steam (HP) pressure (bar)	105

Parameter Description		Measured Value	Model Value
T_{34}	HRSG gas-side outlet temperature $(^{\circ}\mathrm{C})$	96.0	113.6
$\dot{m}_{35}$	Live-steam (HP) mass flow rate $(\mathrm{kg/s})$	72.5	69.6
$\dot{m}_{37}$	ST extraction mass flow rate $(\mathrm{kg/s})$	4.20	4.09
$\dot{W}_{ST}$	ST power output (MW)	99.7	93.6

From this comparison it is obvious that there is good agreement between the measured values from the literature and those calculated from the models. The few configurational differences which do exist are justified by the differences which exist between the cycles found in the literature and the model configurations used here. These differences include the following: simplification of the HRSG's heat exchangers from dual flow to single flow, a different chemical composition for the GT exhaust gases, a pressure loss (2%) for every heat exchanger in the HRSG for all model calculations different from that in Kehlhofer (1999), and a model pump power expenditure calculation somewhat different than that found in Kehlhofer (1999). The slightly lower live steam production, and in effect the slightly lower ST power output, for all model configurations as compared with Kehlhofer (1999) is mainly caused by the absence of a GT cooler.

Table 4.5. Model validation of the triple-pressure reheat ST cycle for a 275 MWe hybrid cycle.

Input Parameter Description		**Value**	**Input Parameter Description**		**Value**
T_{35}	Live-steam (HP) temp. $\left({}^{\circ}\mathrm{C}\right)$	568	p_{35}	Live-steam (HP) pressure $\left(\mathrm{bar}\right)$	120
Parameter Description			**Measured Value**		**Model Value**
T_{34}	HRSG gas-side outlet temperature $\left({}^{\circ}\mathrm{C}\right)$		103.0		109.5
$\dot{m}_{35}$	Live-steam (HP) mass flow rate $\left(\mathrm{kg/s}\right)$		59.2		56.9
$\dot{m}_{37}$	ST extraction mass flow rate $\left(\mathrm{kg/s}\right)$		3.50		3.36
$\dot{W}_{ST}$	ST power output $\left(\mathrm{MW}\right)$		102.5		98.1

Table 4.6. Model validation of the ST cycle.

Input Parameter Description		**Value**	
T_{33}	HRSG gas-side inlet temperature $\left({}^{\circ}\mathrm{C}\right)$	371	
p_{33}	HRSG gas-side inlet pressure $\left(\mathrm{bar}\right)$	1.01	
$\dot{m}_{33}$	HRSG gas-side mass flow rate $\left(\mathrm{kg/s}\right)$	1.26	
T_{35}	Live-steam temperature $\left({}^{\circ}\mathrm{C}\right)$	204	
p_{35}	Live-steam pressure $\left(\mathrm{bar}\right)$	10.3	
Output Parameter Description		**Literature Value**	**Model Value**
$\dot{m}_{35}$	Live-steam mass flow rate $\left(\mathrm{kg/s}\right)$	0.11	0.12
$\dot{Q}_{TOTAL}$	HRSG total heat transfer rate $\left(\mathrm{kW}\right)$	296	299

A second validation was also made to check in more detail the steam production using results more suitable to fuel cell hybrid systems. These results are from a simple single pressure HRSG. These were found in the Fuel Cell Handbook (2004). The model and literature results comparison is summarized in Table 4.6. The minor differences between the literature and the model results are caused by (1) the assumption of a constant specific heat throughout the HRSG in the literature results and (2) the assumption of no heat exchanger pressure losses in the literature results.

4.2 Parametric Study

As previously mentioned, the purpose of the parametric study is to either maximize the average efficiency or minimize the total cost of the hybrid SOFC-GT-ST power plant. To achieve this, a systematic variation in the values of a number of key decision variables as well as the relative sizes of the SOFC, GT, and ST for a given hybrid plant size, which is also varies, has been made.

4.2.1 Strategy of the Parametric Study

A description of the key decision variables is given in Table 4.7. along with their ranges and initial (setting) values. These values are chosen on the basis of typical hybrid fuel cell systems of the kind found in Calise, (2005).

Table 4.7. Description, initial value, and range of the key decision variables.

Decision Variable Description		Initial Value	Range
U_f	Fuel Utilization Factor	0.85	$0.75 \le U_f \le 0.90$
T_{SOFC}	SOFC Operating Temperature $\left({}^{\circ}\mathrm{C}\right)$	1000	$950 \le U_f \le 1100$
S/C	Steam-to-Carbon ratio	2	$2.0 \le U_f \le 3.5$
p_{SOFC}	SOFC Operating Pressure $\left(\mathrm{bar}\right)$	8	$7 \le U_f \le 10$
c_{fuel}	Unit cost of fuel $\left(\$/\mathrm{Nm}^3\right)$	0.3	$0.1 \le U_f \le 1.2$

The fuel utilization factor is varied from 0.75 to 0.90 in 0.05 increments. Values below 0.75 are not applicable because such values cause an increase in temperature beyond the maximum possible turbine inlet temperature (TIT) and, therefore, a coupling point of the air compressor and the gas turbine cannot be reached. The steam-to-carbon ratio is varied from 2 to 3.5 in 0.5 increments. Values below 2 are not included in order to avoid problems of carbon deposition on the anode of the SOFC stack as reported in Larminie and Dicks (2003), Benjamin, Camera, and Marianowski (1995), and Fuel Cell Handbook (2004). The SOFC operating temperature is varied from 950 to 1100 ${}^{\circ}\mathrm{C}$ in 50 ${}^{\circ}\mathrm{C}$ increments. A value beyond 1100 is not used because it would exceed the operating limit of the SOFC. Also, a value lower than 950 ${}^{\circ}\mathrm{C}$ at full load (i.e. at the design point) is infeasible since the minimum part load (i.e. off-design) SOFC operating temperature is violated at 25% load. The SOFC operating pressure is varied from 7 to 10 bar in 1 bar increments. A value beyond 10 bar is not used because it would exceed the operating limits of the SOFC. Finally, the unit cost of fuel (methane) is varied as follows: 0.1, 0.3, 0.6, 0.9, and 1.2. The initial value of 0.3 is the one published on the U.S. Energy Information Administration website for the year 2005 (U.S. Energy Information Administration, 2006).

As mentioned in Chapter 3, for the purposes of this research study three different hybrid plant sizes are considered: 1.5 MWe, 5 MWe, and 10 MWe. For every size four different steam turbine configurations are considered: single-pressure, dual-pressure, triple-pressure, and triple-pressure with reheat.

Also, two different SOFC sizes are considered based on current density. The operating current density for the selected fuel cell operates from 100 mA/cm^2 to 650 mA/cm^2 (Singhal, 1997). Since the current density decreases at off-design, the small SOFC is selected based on a maximum possible current density of 550 mA/cm^2 (full load or design condition) while the large SOFC is selected based on a minimum possible current density of 100 mA/cm^2 (25% full load condition). The larger SOFC yields higher efficiencies as compared with the smaller SOFC but the latter has a lower capital cost which is significant since the SOFC purchase cost is the most dominant of all the equipment purchase costs. In the parametric study conducted here, the smaller SOFC minimizes the total cost while the larger one maximizes the efficiency.

The performance of each individual system is analyzed at full and part load conditions to determine the average and total efficiencies and total operating cost. The load profile shown in Figure 4.2 is based on a 2-day, (one average winter day and one average summer day) electrical power demand profile for an average four person family household (Rancruel, 2005) scaled appropriately to coincide with the three different sized hybrid plants analyzed here and extended over an entire year. The average efficiency for the plant becomes a time-averaged value based on the time intervals shown in Figure 4.2. It is defined as follows:

$$\eta_{ave} = \frac{\Delta t_1 \eta_1 + \Delta t_2 \eta_2 + \Delta t_3 \eta_3 + \Delta t_4 \eta_4}{\sum \Delta t_i} \tag{4.2}$$

where the $\Delta t_1, \Delta t_2, \Delta t_3$, and Δt_4 are the time intervals corresponding to 25%, 50%, 75%, and 100% load, and the η_1, η_2, η_3, and η_4 are the hybrid plant energetic efficiencies corresponding to the above time intervals. In addition, the total efficiency is defined as

$$\eta_{tot} = \frac{\sum \dot{W}_i \Delta t_i}{\sum \dot{Q}_H \Delta t_i} \tag{4.3}$$

where $\dot{W}$ is the power output corresponding to 25%, 50%, 75%, and 100% load, and $\dot{Q}_H$ is the heat input to the system based on the LHV and fuel flow rates for the aforementioned time intervals.

4.2.2 Results of the Parametric Study

Results for all the hybrid systems modeled and simulated here are shown in Tables A.1 to A.12 in Appendix A, where the top half of every table shows the results for the small SOFC, while the bottom half shows those for the large SOFC. In addition, the decision variable values are plotted against the corresponding objective function values for each size plant and SOFC size to show the trends. These appear in Figures 4.3 to 4.26.

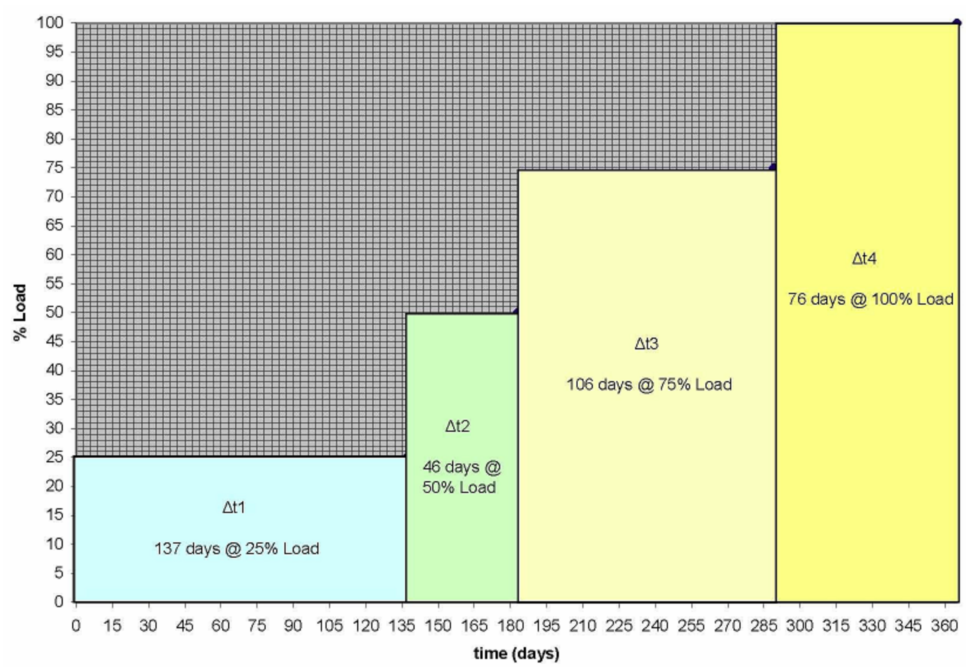

Figure 4.2. Load profile.

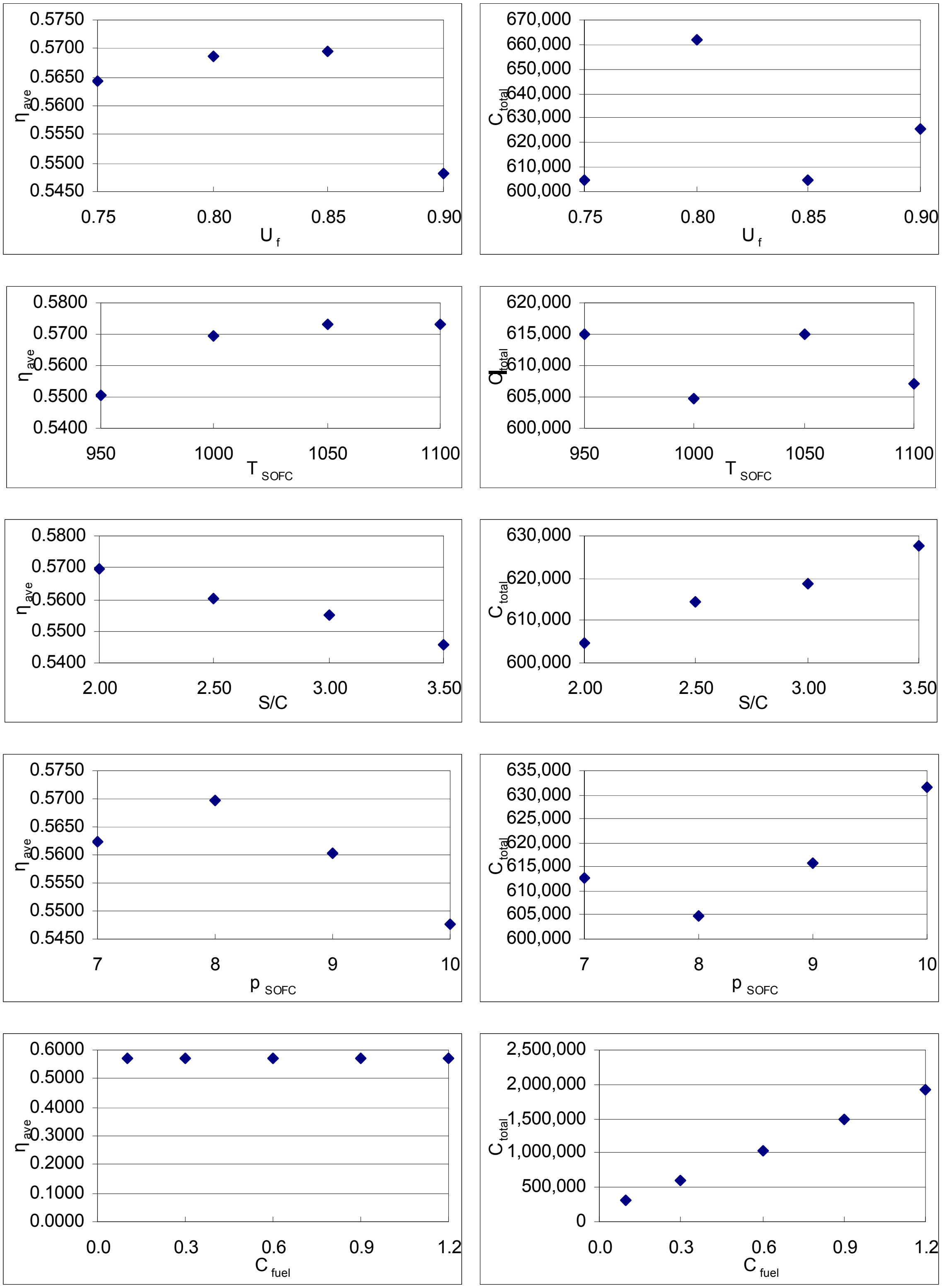

Figure 4.3. Optimizing variables vs. objective functions for the 1.5 MWe single-pressure ST small SOFC.

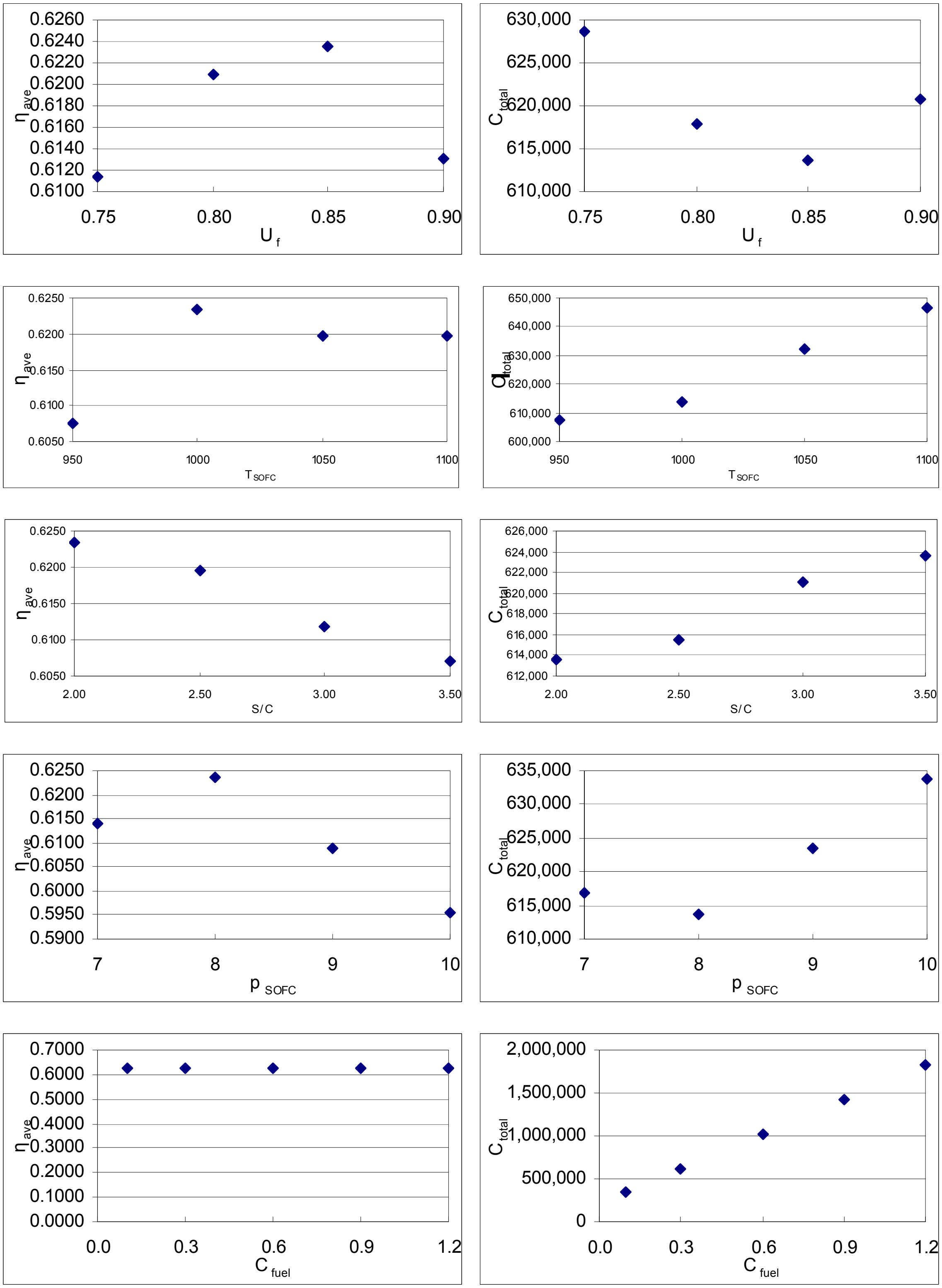

Figure 4.4. Optimizing variables vs. objective functions for the 1.5 MWe single-pressure ST large SOFC.

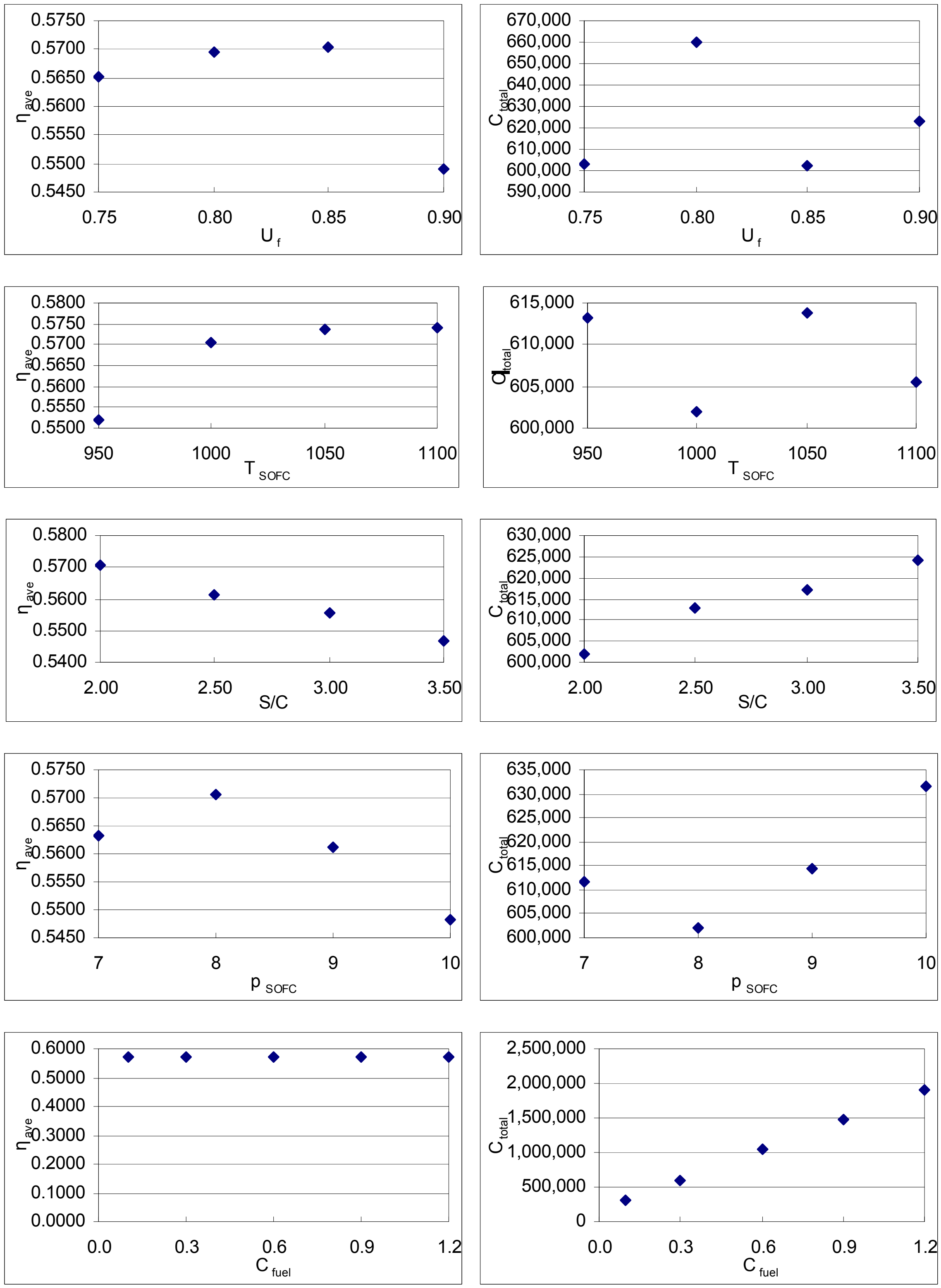

Figure 4.5. Optimizing variables vs. objective functions for the 1.5 MWe dual-pressure ST small SOFC.

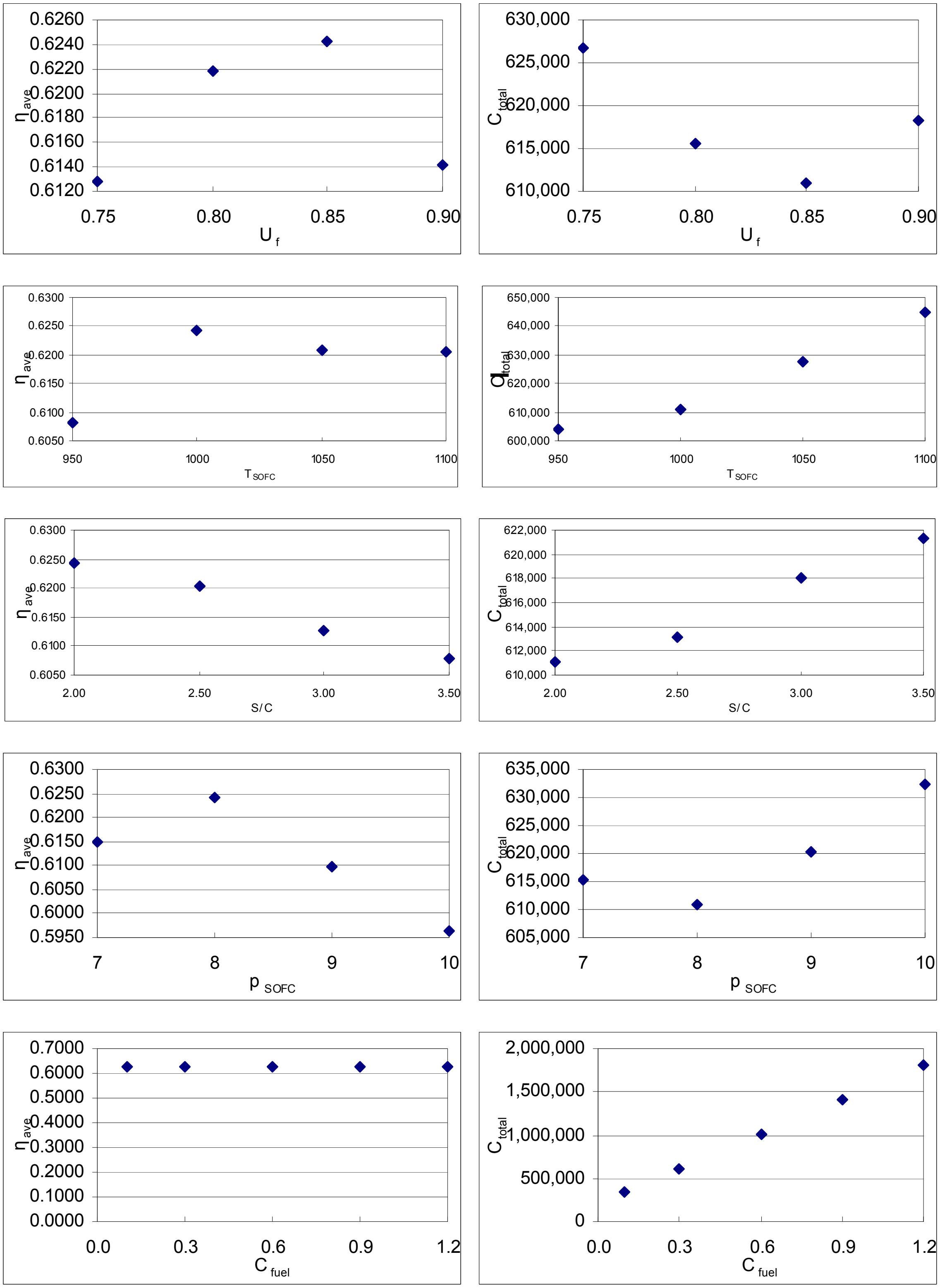

Figure 4.6. Optimizing variables vs. objective functions for the 1.5 MWe dual-pressure ST large SOFC.

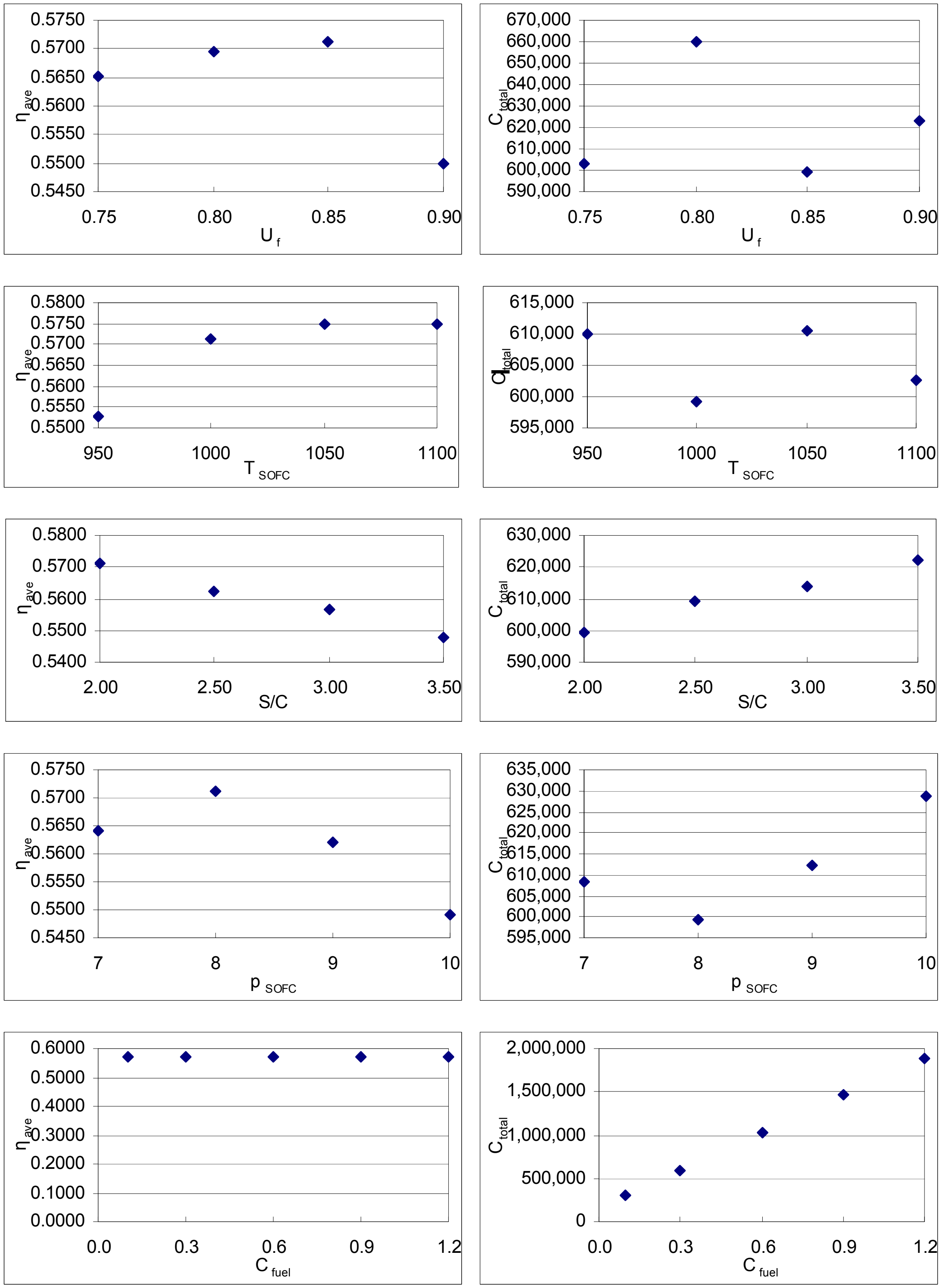

Figure 4.7. Optimizing variables vs. objective functions for the 1.5 MWe triple-pressure ST small SOFC.

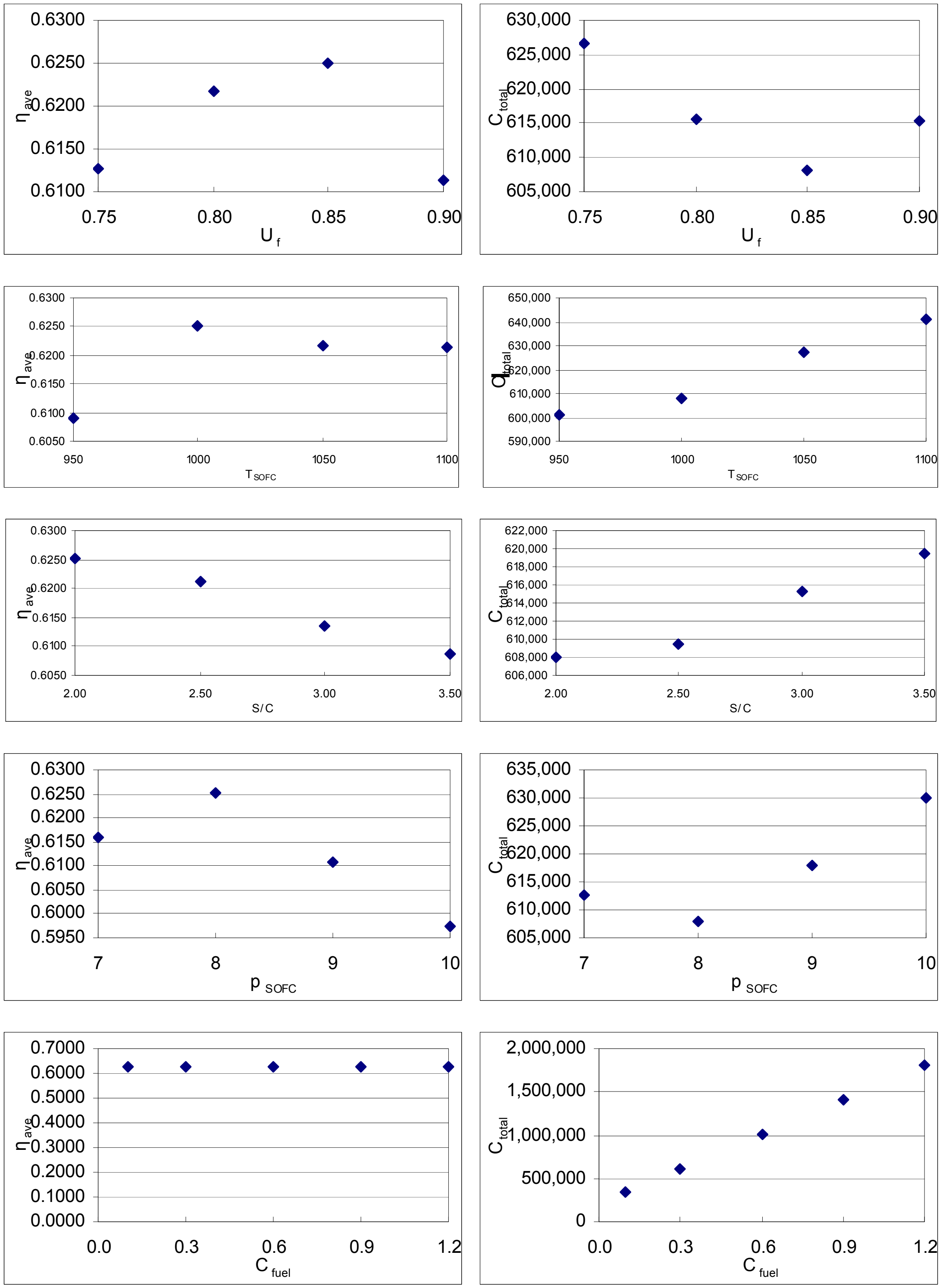

Figure 4.8. Optimizing variables vs. objective functions for the 1.5 MWe triple-pressure ST large SOFC.

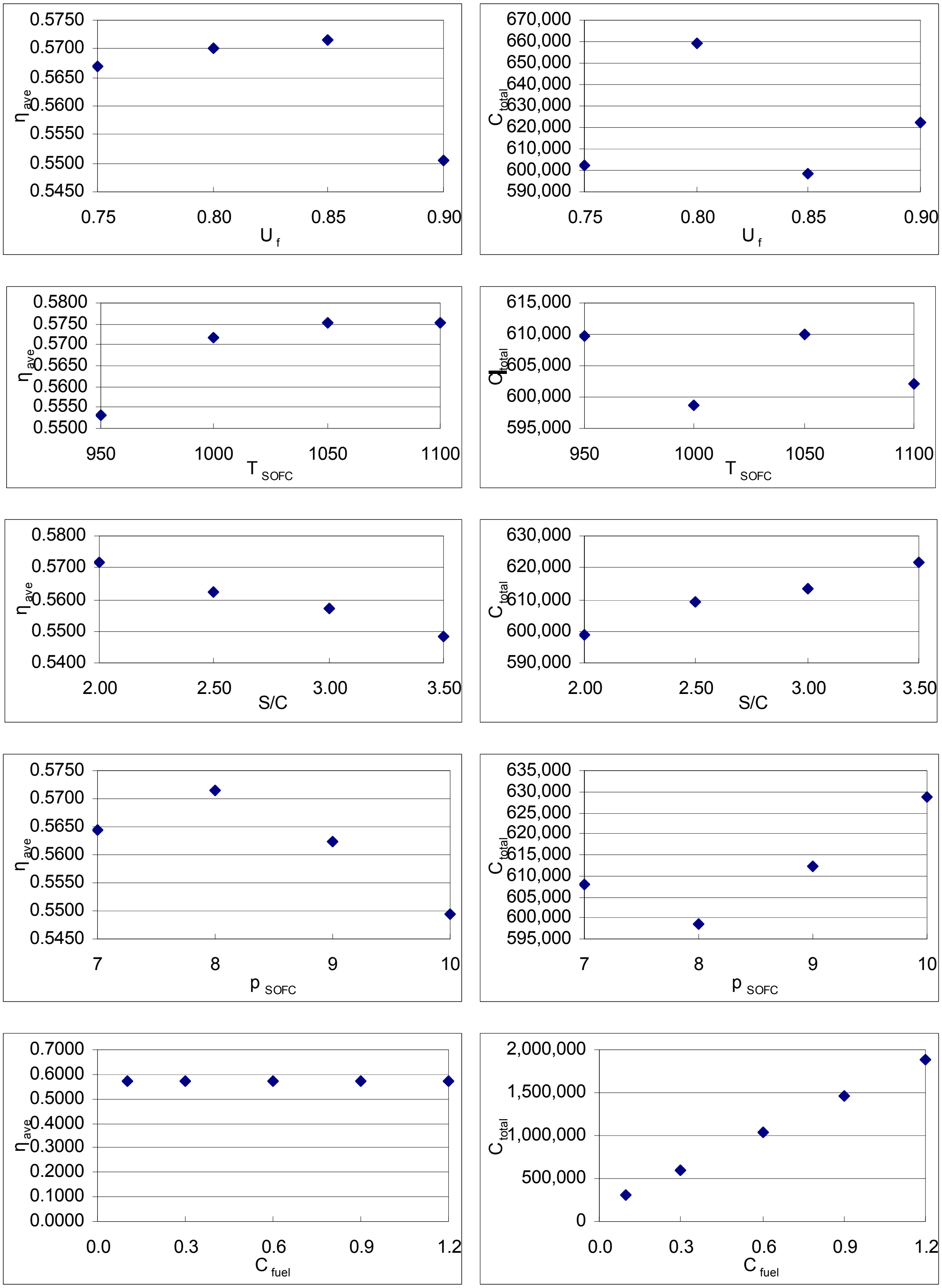

Figure 4.9. Optimizing variables vs. objective functions for the 1.5 MWe triple-pressure w/ RH ST small SOFC.

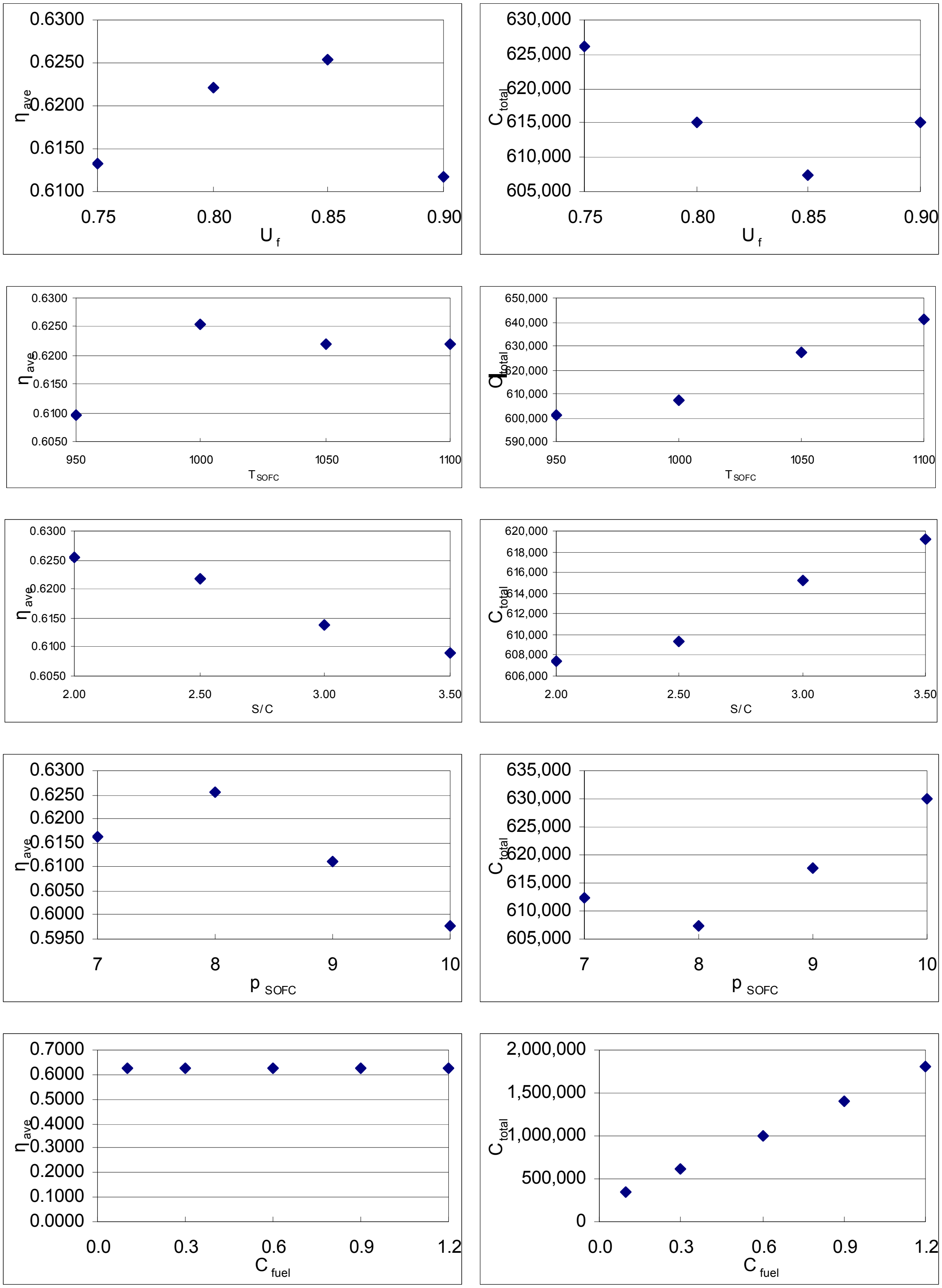

Figure 4.10. Optimizing variables vs. objective functions for the 1.5 MWe triple-pressure w/ RH ST large SOFC.

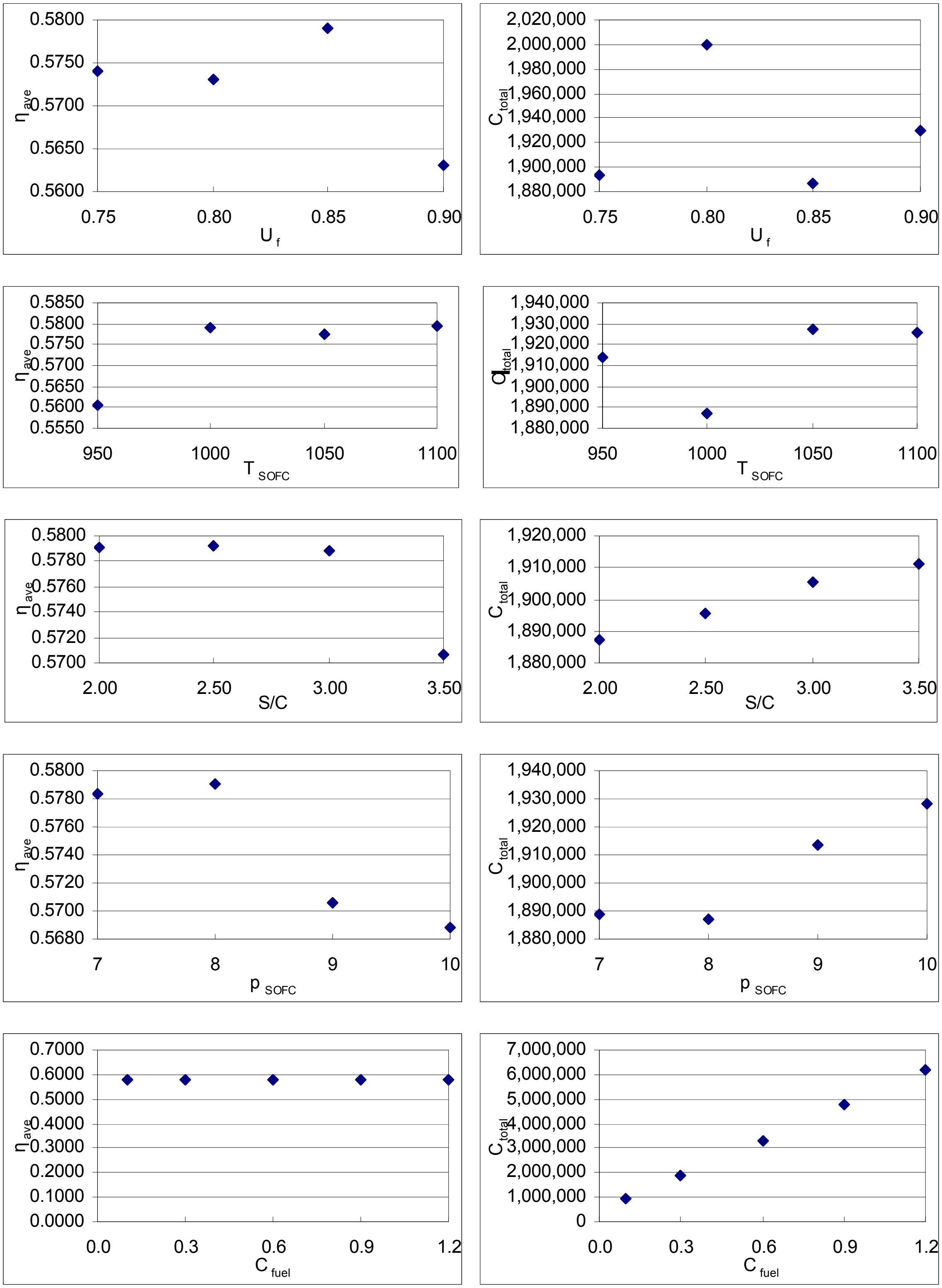

Figure 4.11. Optimizing variables vs. objective functions for the 5 MWe single-pressure ST small SOFC.

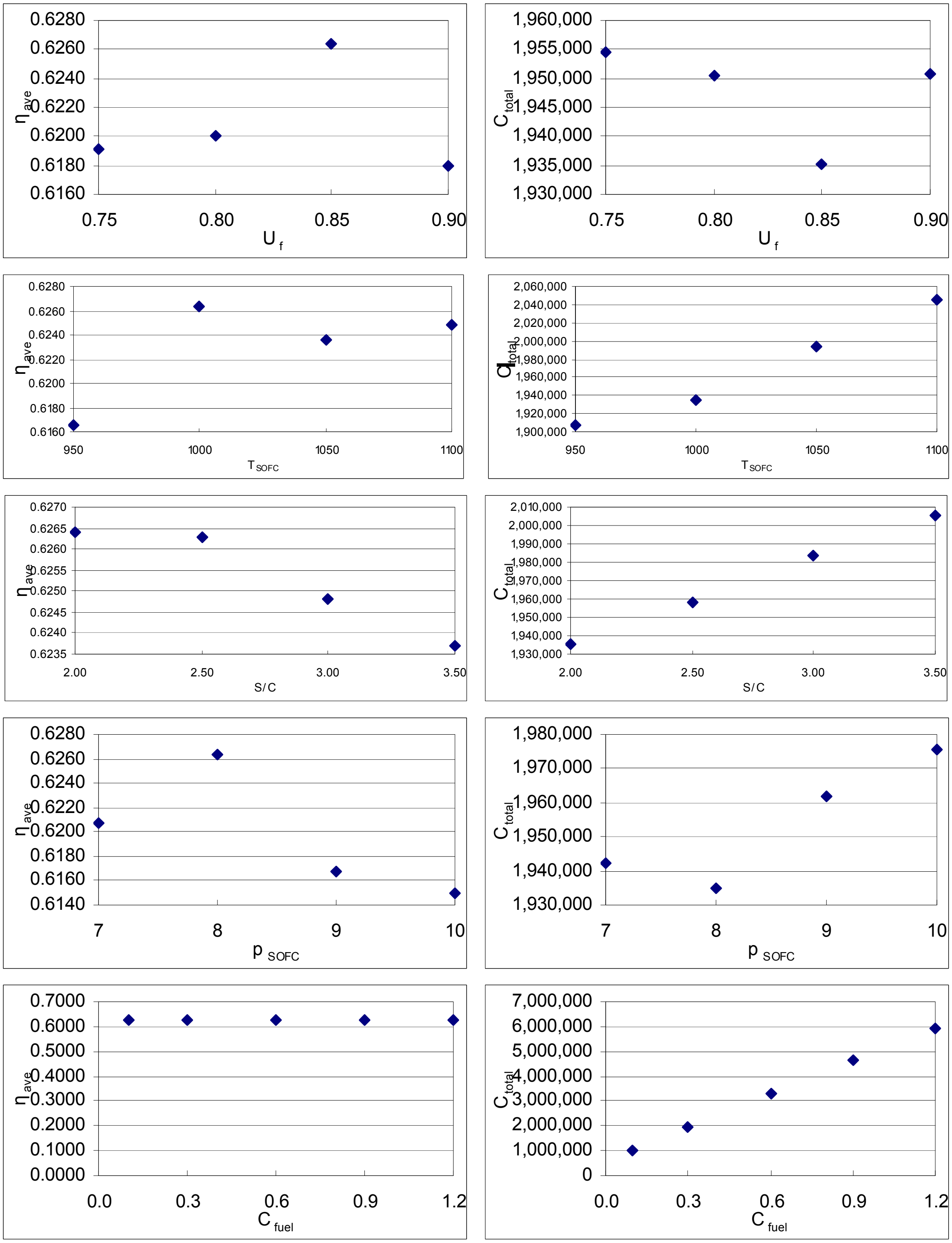

Figure 4.12. Optimizing variables vs. objective functions for the 5 MWe single-pressure ST large SOFC.

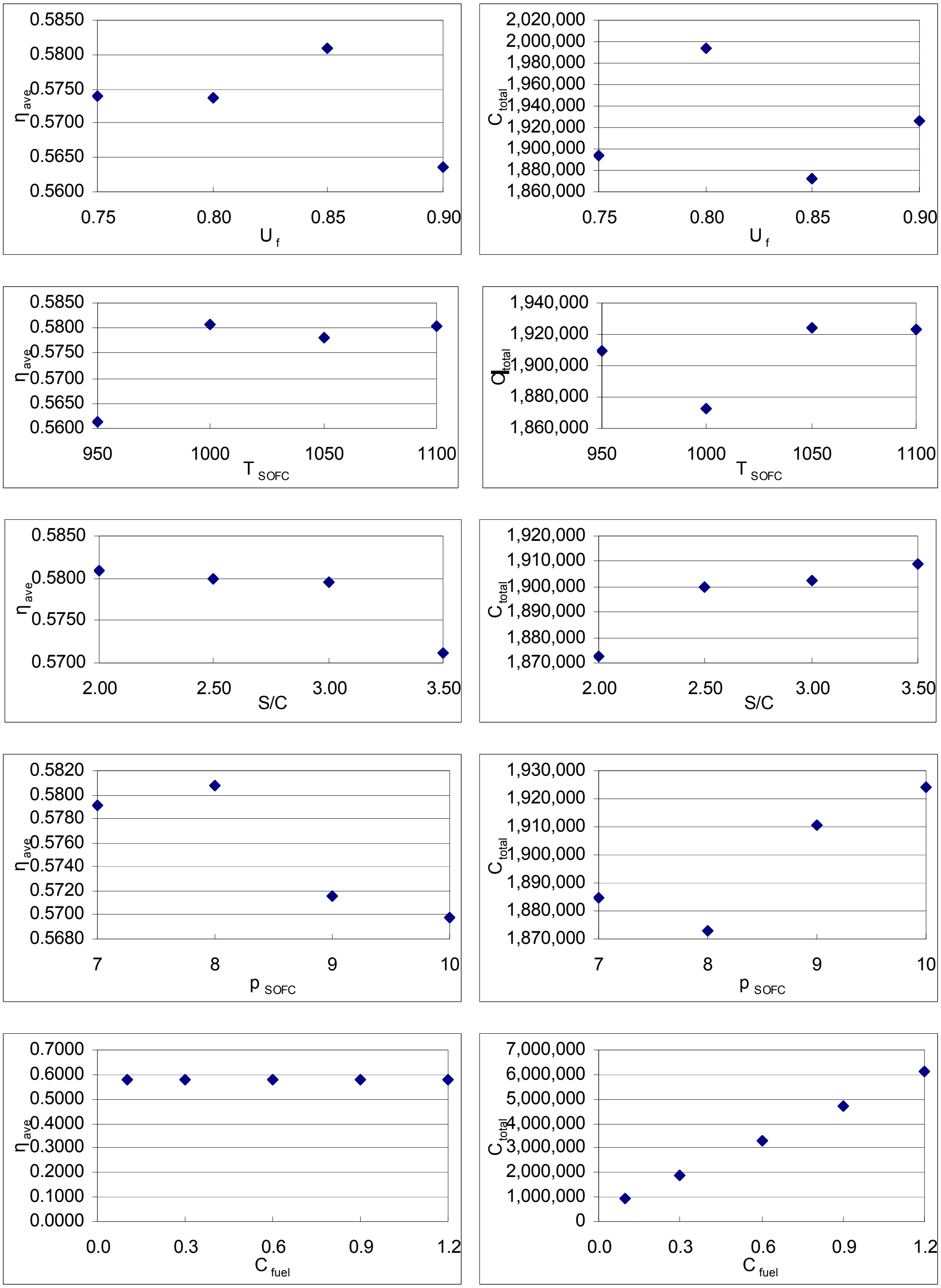

Figure 4.13. Optimizing variables vs. objective functions for the 5 MWe dual-pressure ST small SOFC.

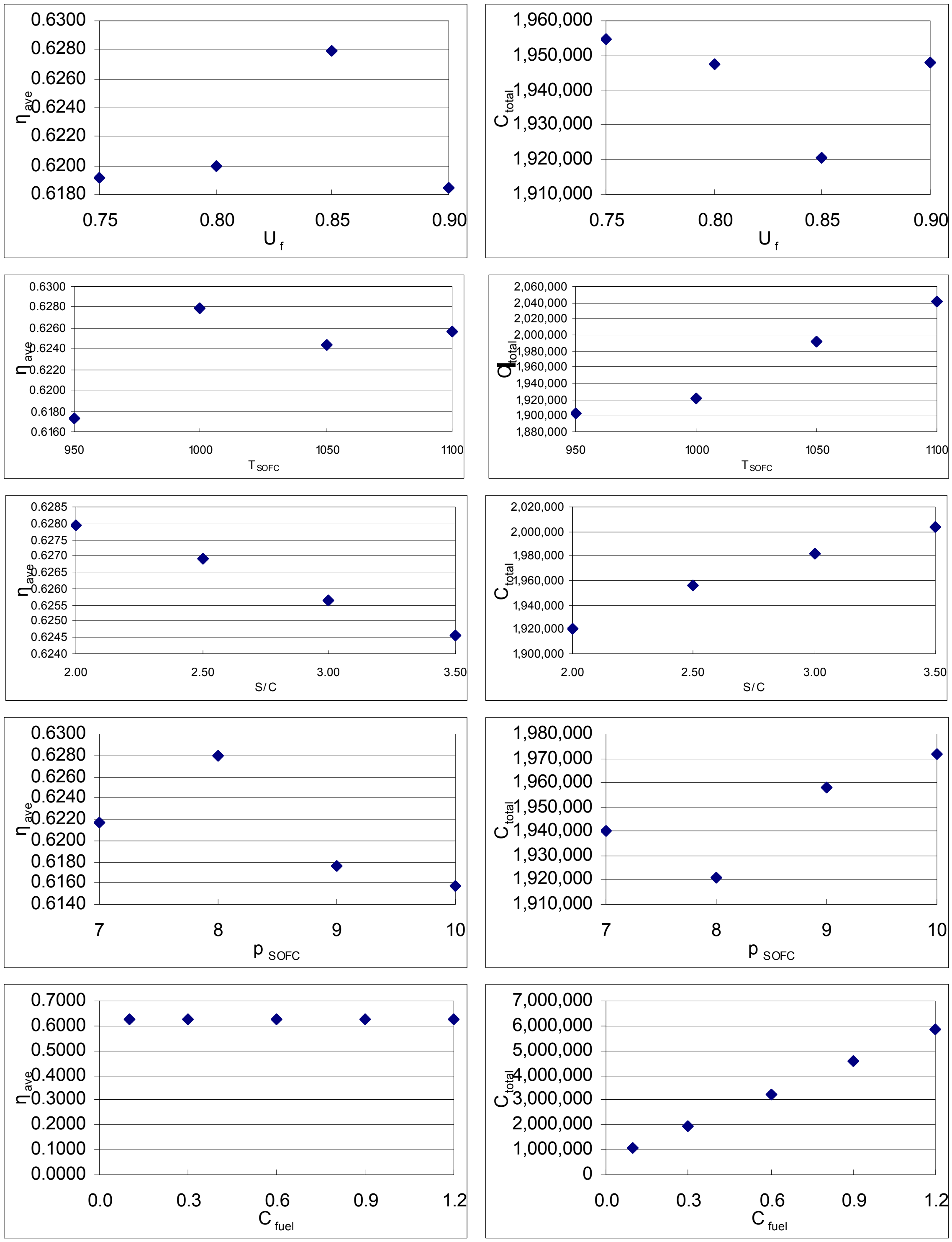

Figure 4.14. Optimizing variables vs. objective functions for the 5 MWe dual-pressure ST large SOFC.

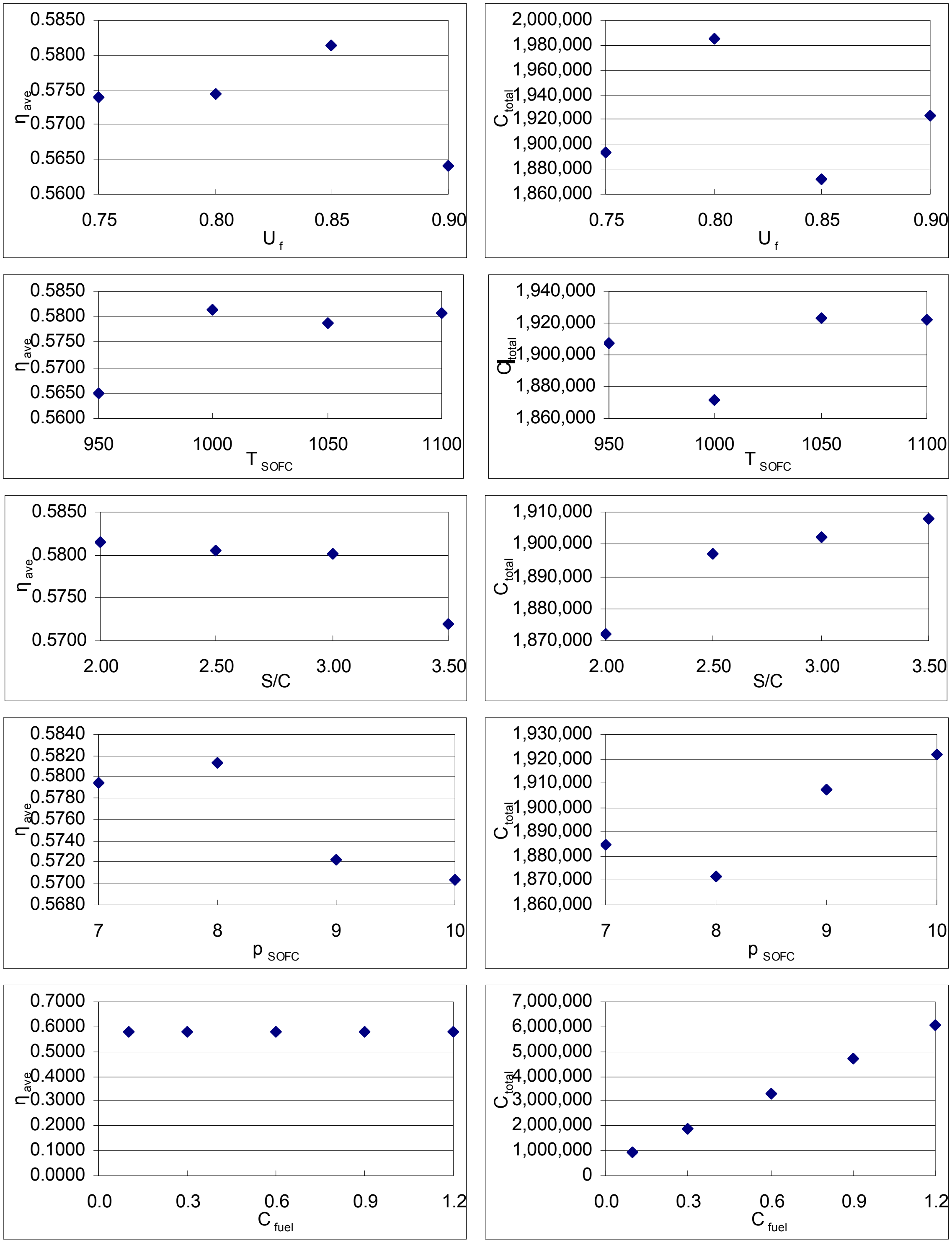

Figure 4.15. Optimizing variables vs. objective functions for the 5 MWe triple-pressure ST small SOFC.

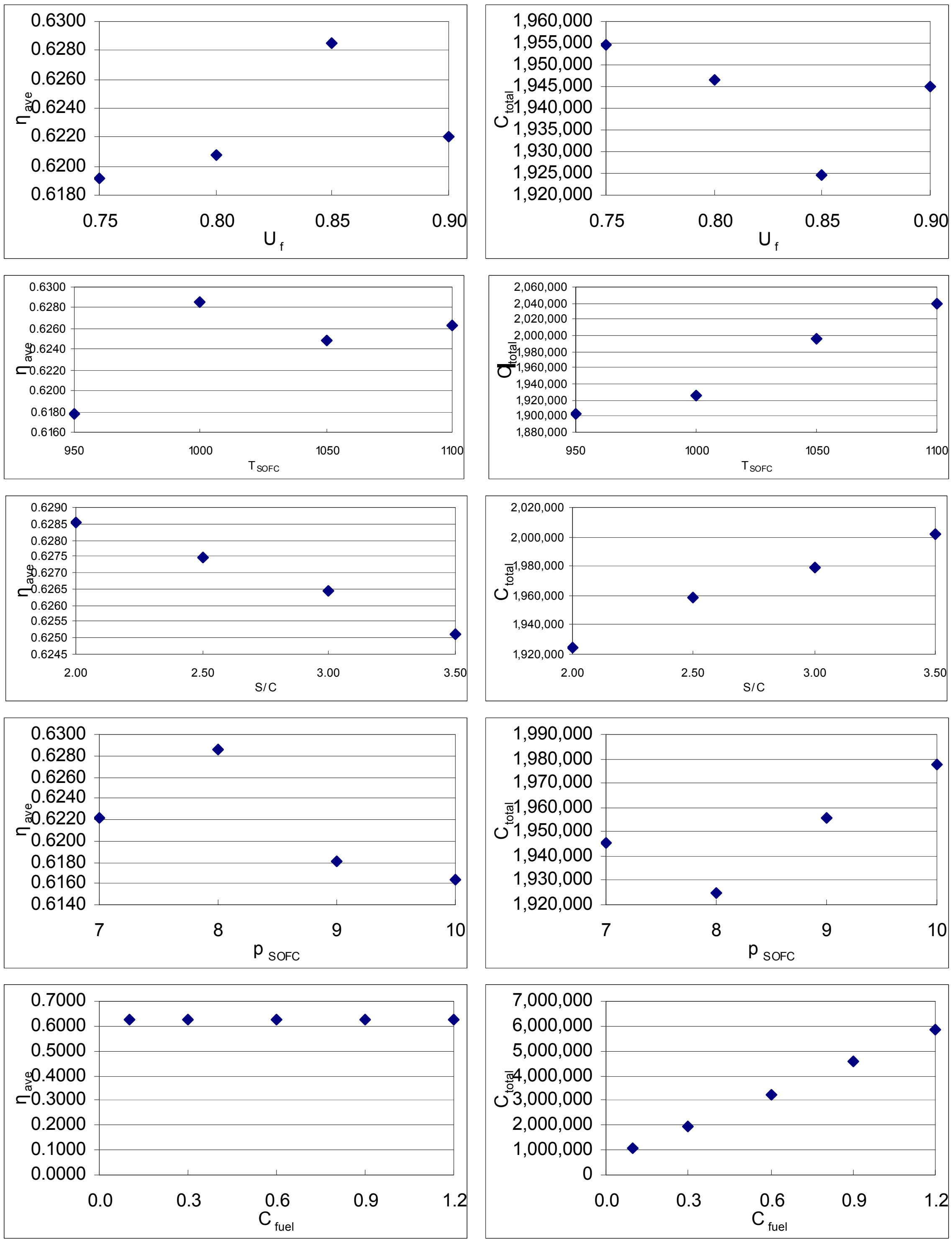

Figure 4.16. Optimizing variables vs. objective functions for the 5 MWe triple-pressure ST large SOFC.

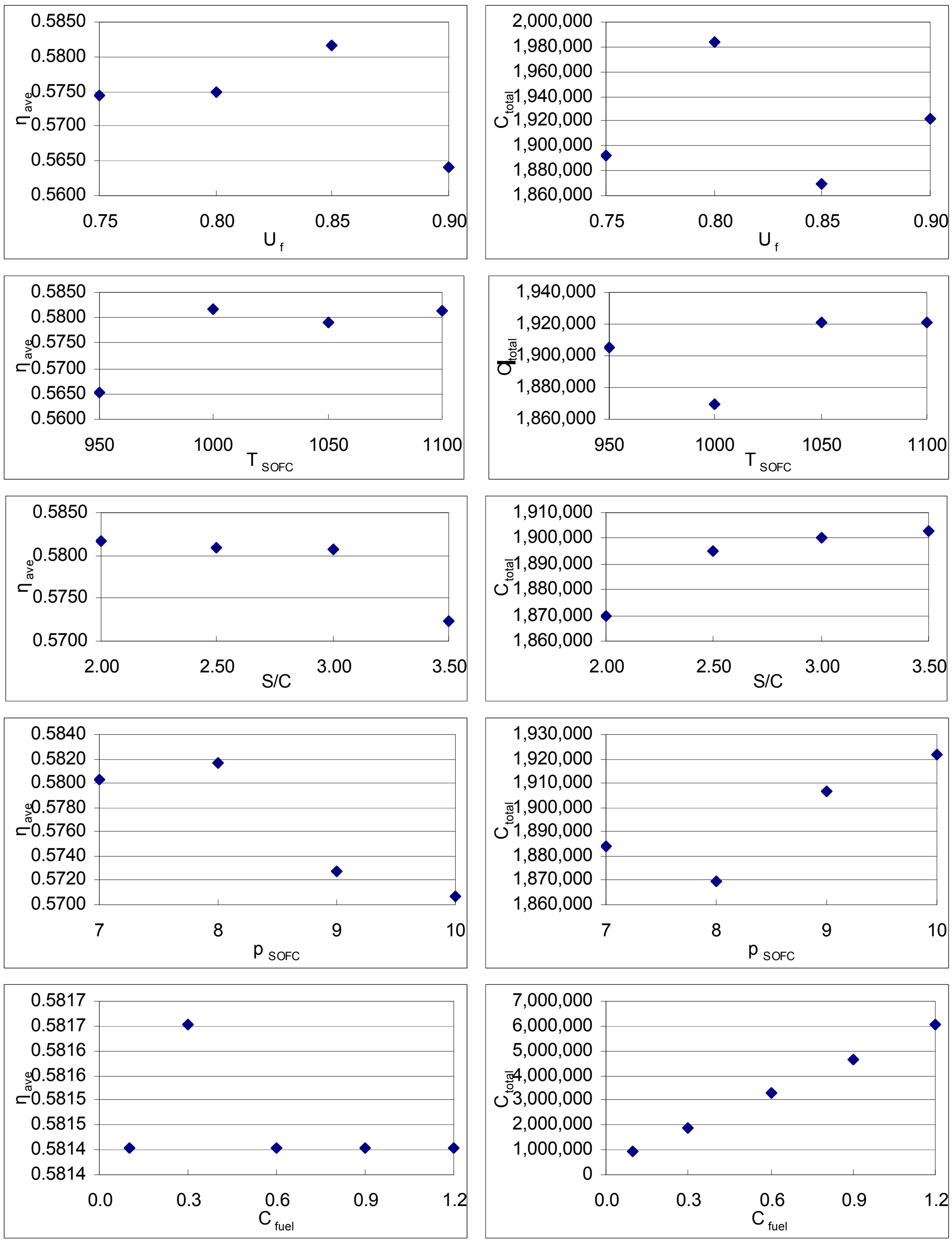

Figure 4.17. Optimizing variables vs. objective functions for the 5 MWe triple-pressure w/RH ST small SOFC.

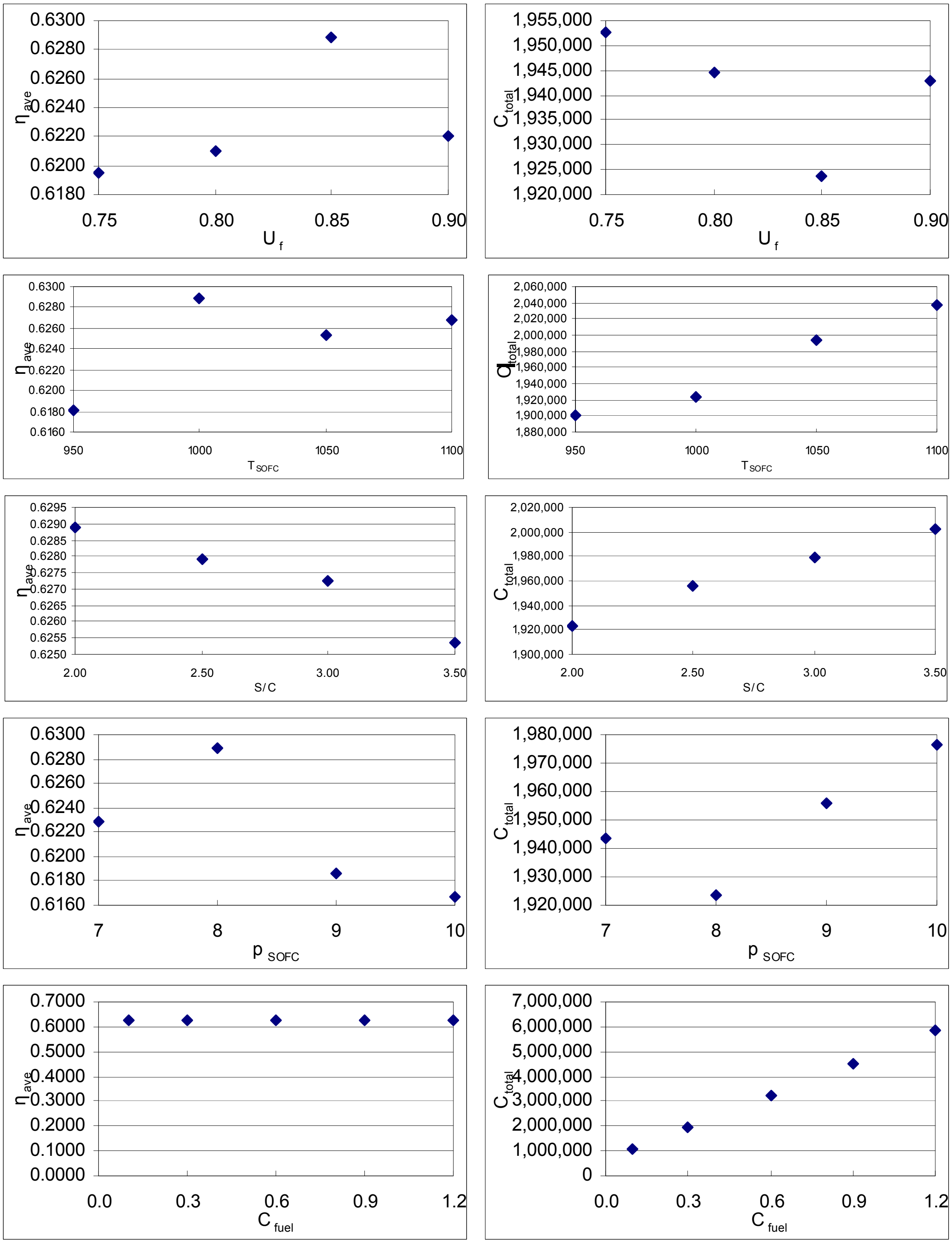

Figure 4.18. Optimizing variables vs. objective functions for the 5 MWe triple-pressure w/RH ST large SOFC.

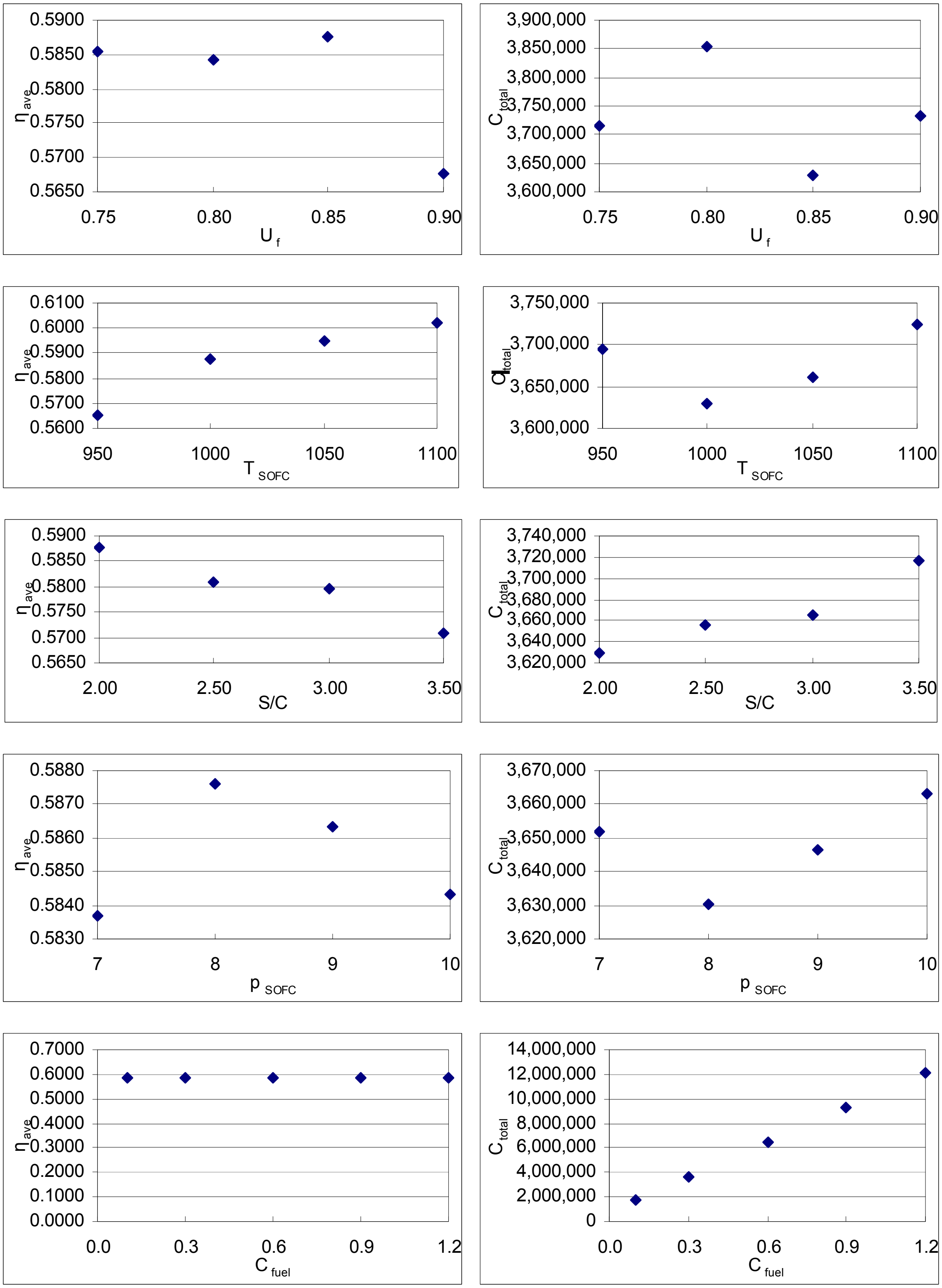

Figure 4.19. Optimizing variables vs. objective functions for the 10 MWe single-pressure ST small SOFC.

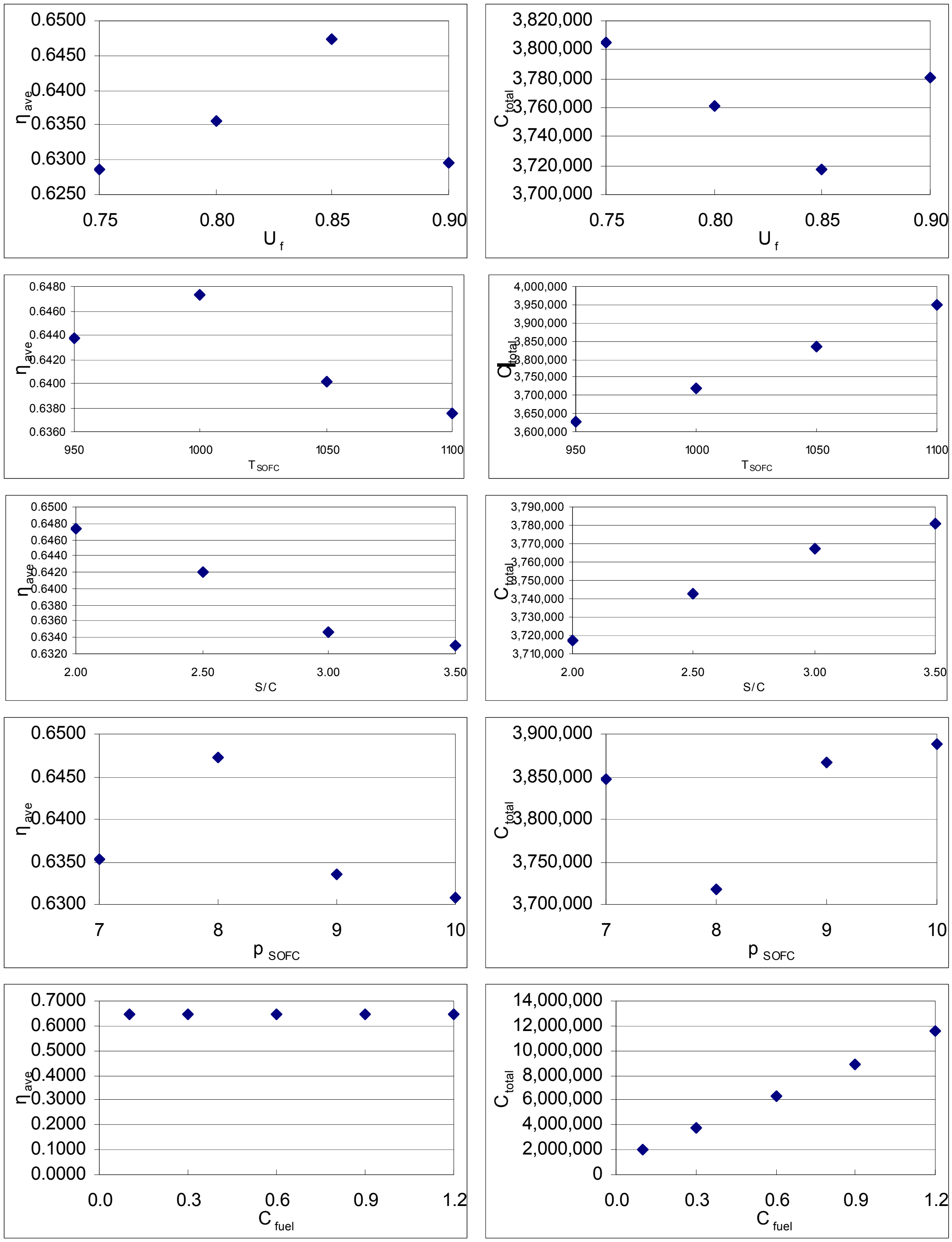

Figure 4.20. Optimizing variables vs. objective functions for the 10 MWe single-pressure ST large SOFC.

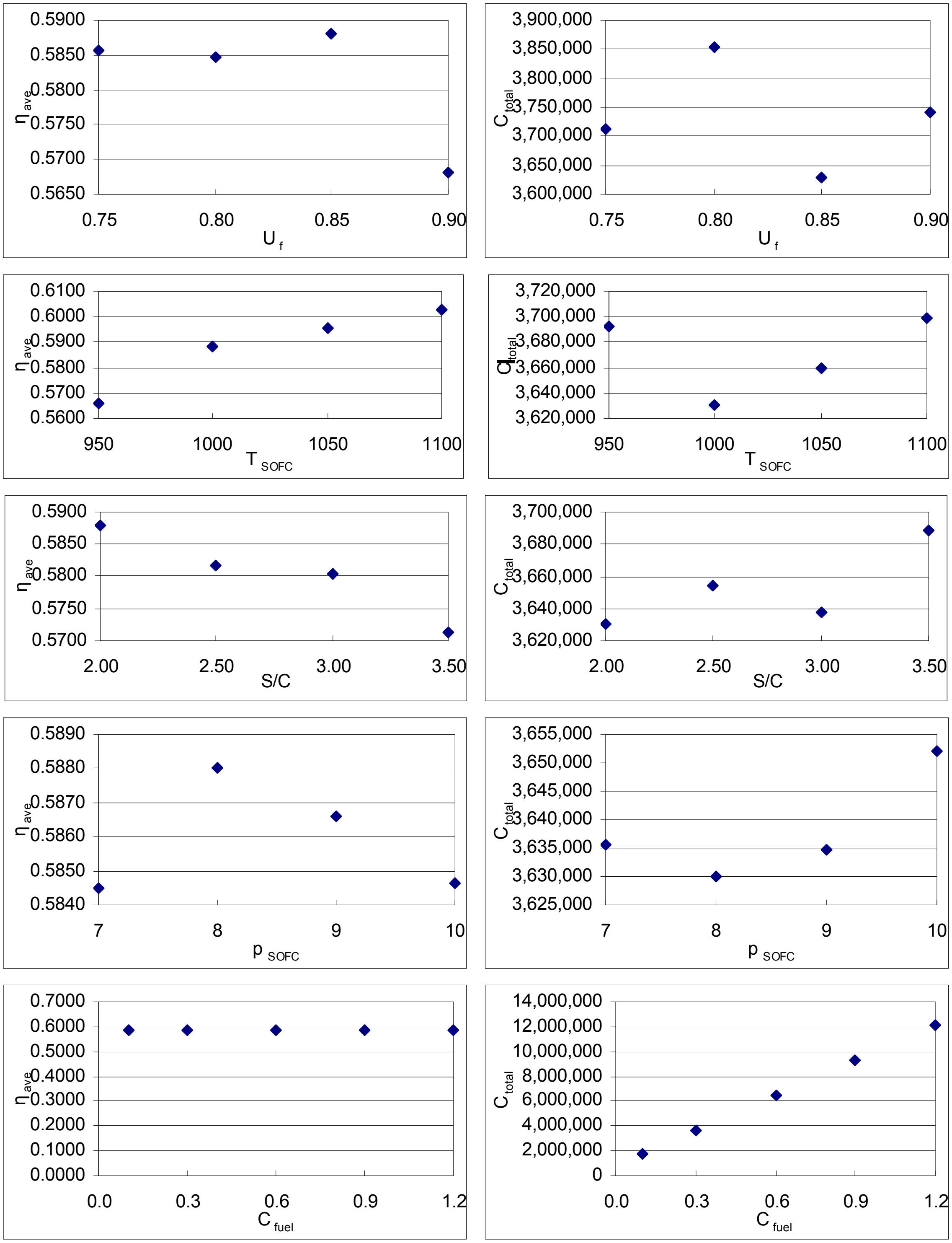

Figure 4.21. Optimizing variables vs. objective functions for the 10 MWe dual-pressure ST small SOFC.

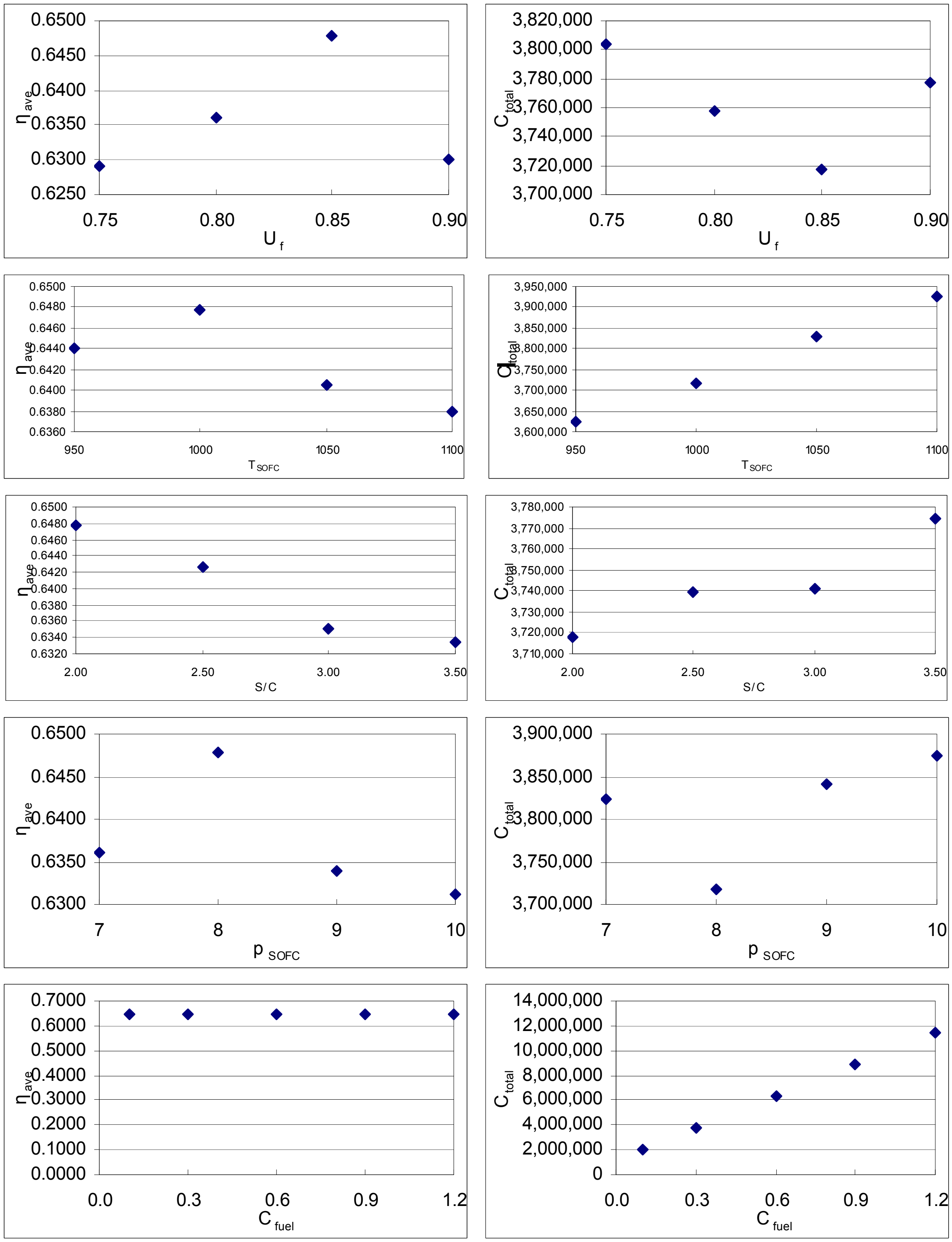

Figure 4.22. Optimizing variables vs. objective functions for the 10 MWe dual-pressure ST large SOFC.

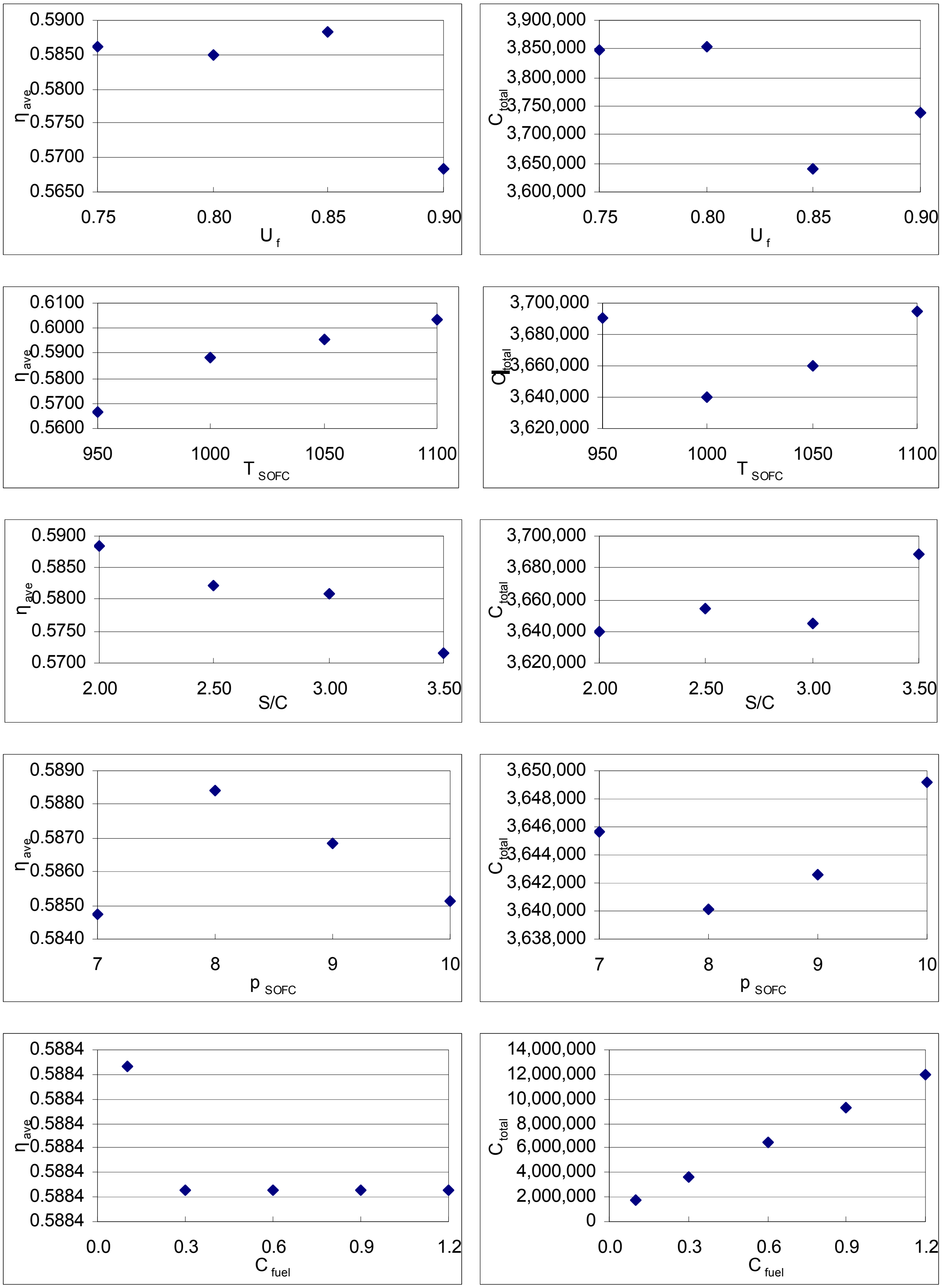

Figure 4.23. Optimizing variables vs. objective functions for the 10 MWe triple-pressure ST small SOFC.

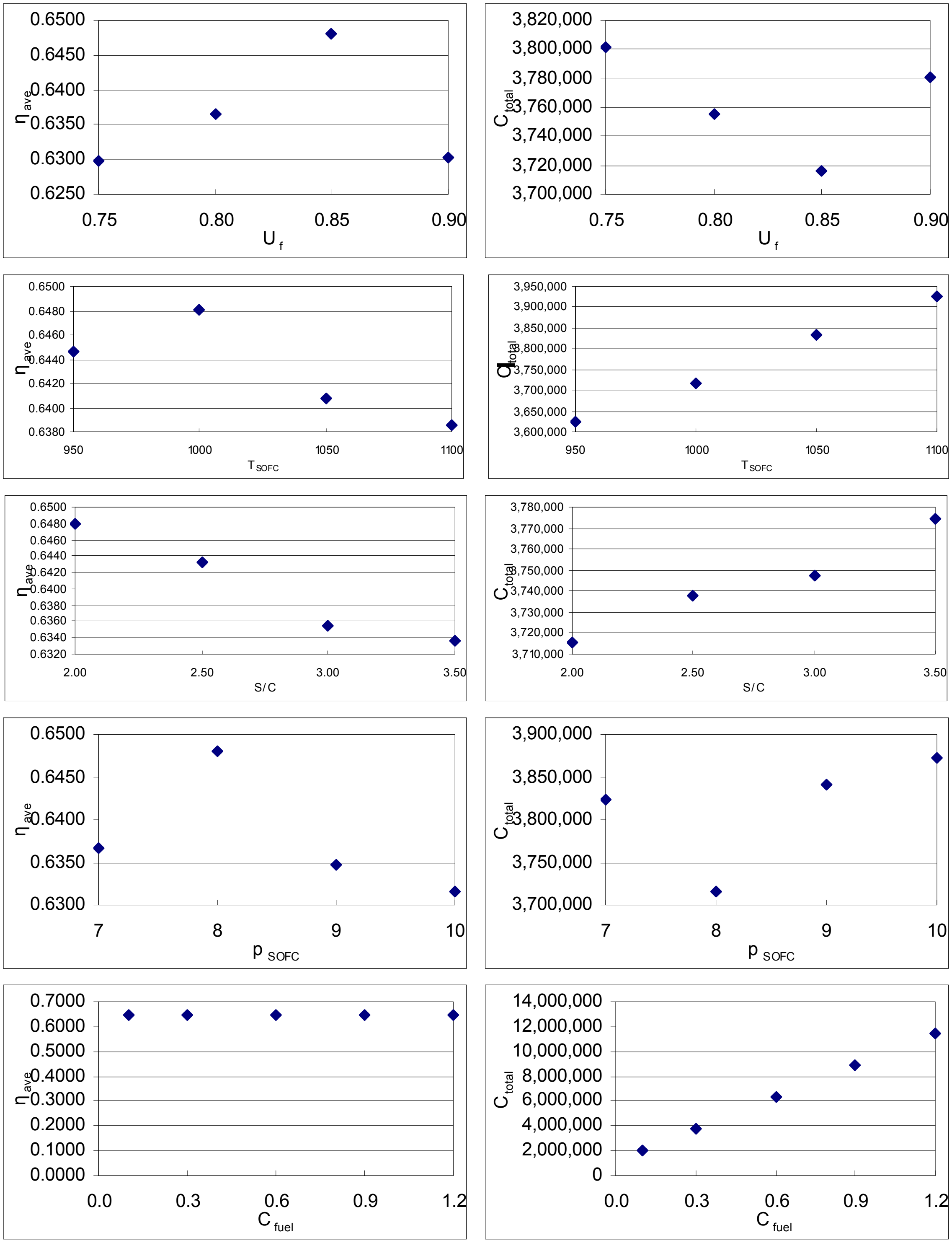

Figure 4.24. Optimizing variables vs. objective functions for the 10 MWe triple-pressure ST large SOFC.

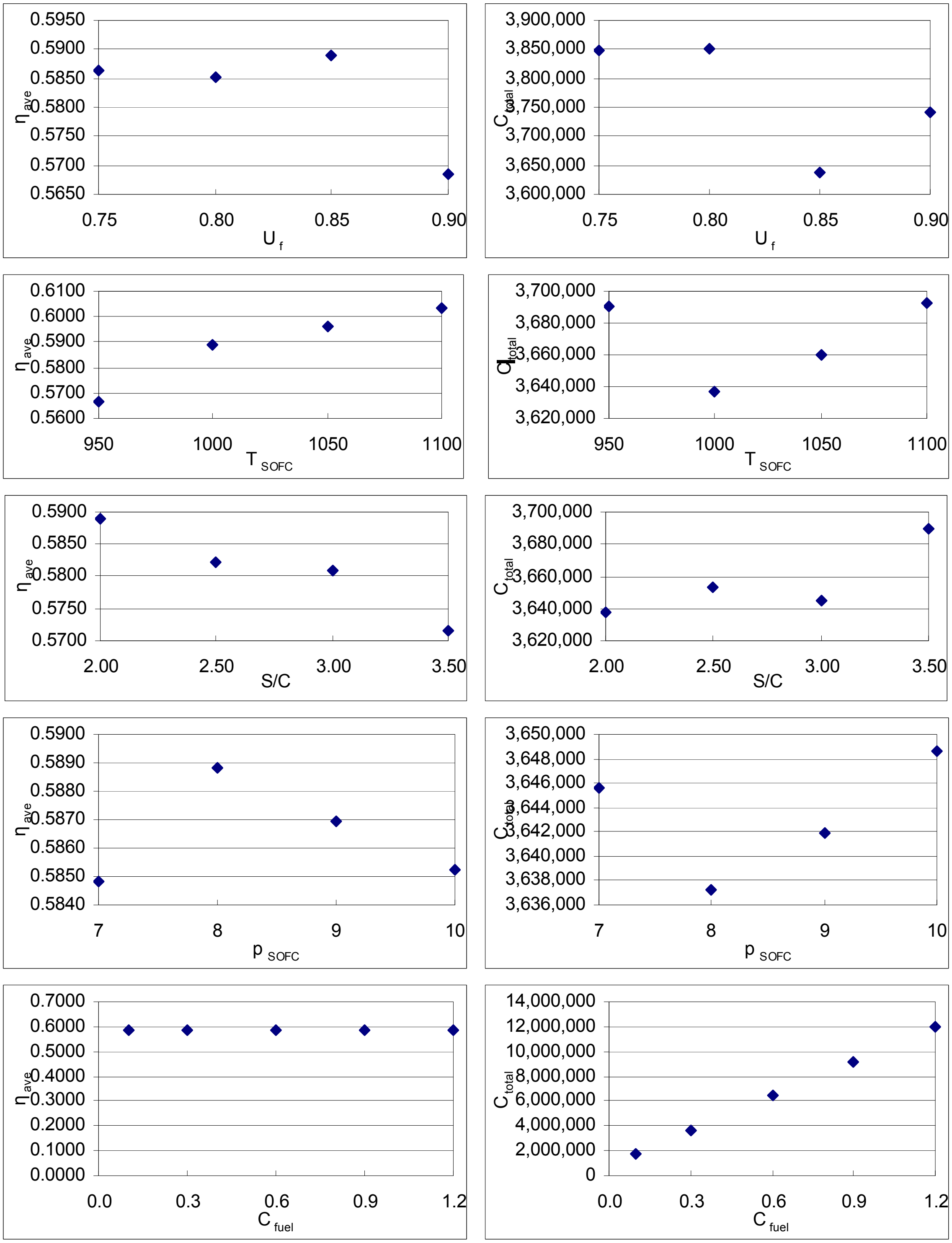

Figure 4.25. Optimizing variables vs. objective functions for the 10 MWe triple-pressure ST small SOFC.

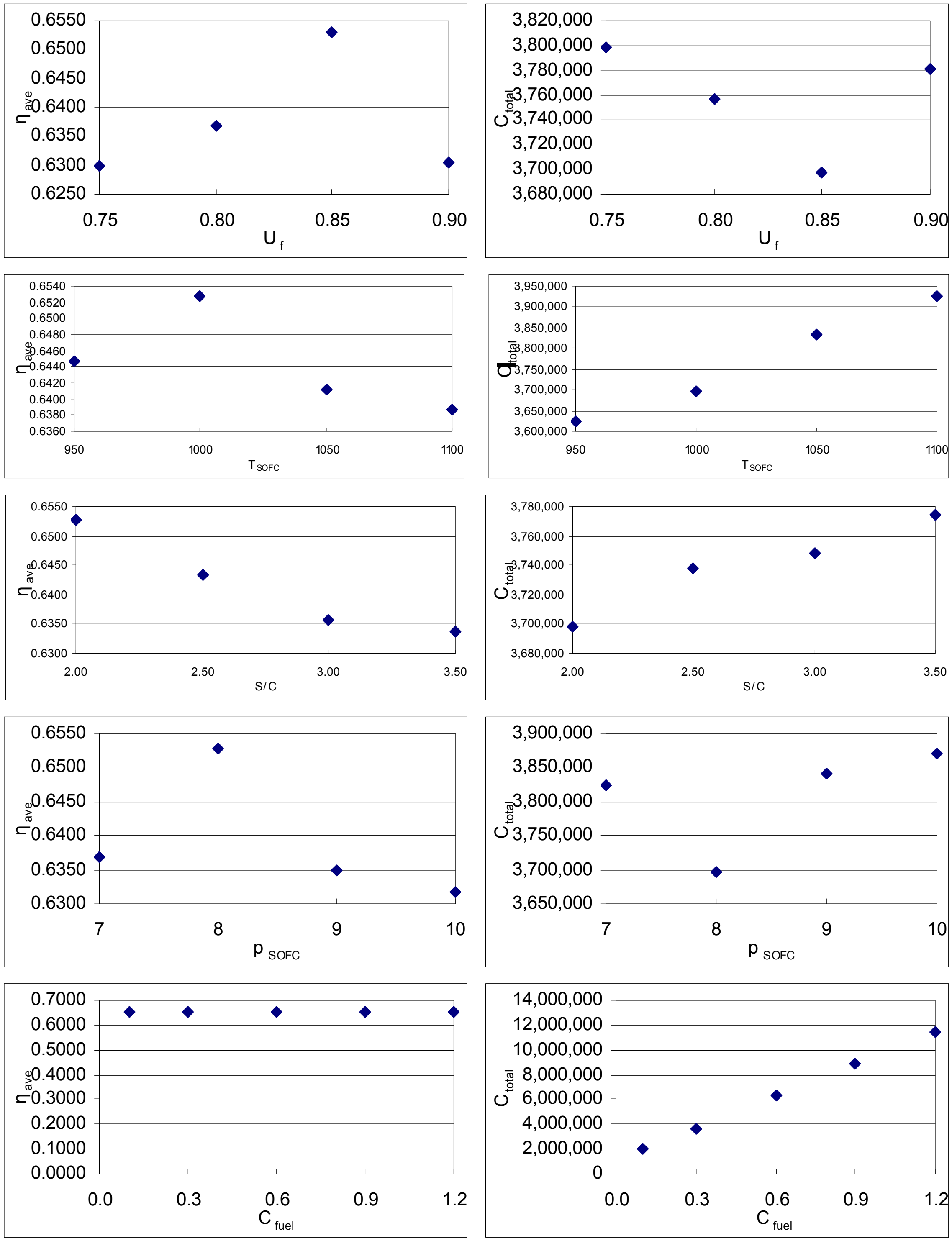

Figure 4.26. Optimizing variables vs. objective functions for the 10 MWe triple-pressure ST large SOFC.

From an observation of the trendlines shown in these figures, some general remarks can be made that apply to all the hybrid plants analyzed here. To begin with, the optimum fuel utilization factor is 0.85. For the small SOFC where the cost is the optimizing function of interest, the minimum total cost is achieved at this value because although the capital cost decreases slightly at lower values of U_f, the more dominating operating cost is decreased at higher values of U_f. Therefore, the higher efficiency is the main reason that the higher fuel utilization is more economical even though only slightly so. For the large SOFC, where the average efficiency is the optimizing function of interest, as expected, the higher the fuel utilization factor is the higher the efficiency. The optimum value is 0.85 and not 0.90 because at the latter value although the SOFC efficiency is slightly higher, the total plant efficiency drops because not much heat is left for recovery by the gas turbine and the steam turbine since almost all the hydrogen produced by the internal reforming reactions is consumed within the fuel cell by the anode electrochemical reaction and more efficient stacks release less heat. Therefore, the electrical power produced by the SOFC increases, causing a raise in its electrochemical rate of reaction. On the other hand, this effect decreases significantly the turbomachine efficiencies.

The optimum SOFC operating temperature for both SOFC sizes and all models is 1000 ^{o}C. For the small SOFC, where the total cost is the optimizing function, the lower the SOFC operating temperature the lower the SOFC capital cost. This trend reaches a minimum at 1000 ^{o}C and not 950 ^{o}C because the operating cost manages to slightly overcome the capital cost. For the large SOFC, where the average efficiency is the optimizing function, the best SOFC operating temperature is still 1000 ^{o}C because although the SOFC stacks operate slightly at increased temperatures the air and fuel compressors require significantly higher power consumption, thereby decreasing slightly the overall efficiency.

The steam-to-carbon ratio reaches its optimum efficiency and lower cost at the lowest possible value of 2. The capital cost remains constant throughout the S/C variation and therefore the only significantly varying cost is the operating cost which will be determined by the overall efficiency. The average efficiency slightly decreases as the S/C increases since higher steam partial pressures cause higher Nernst overvoltages (Calise et al., 2006). Thus, higher efficiencies and lower operating/total costs are achieved at lower S/C values.

Theoretically increasing the SOFC operating pressure will result in an increase of the cell voltage because of the higher reactant partial pressure available, therefore, improving the SOFC efficiency. On the other hand, the expansion of the gas in the turbomachinery is in a temperature region where the turbomachinery produces less power as the pressure increases as indicated in Chen, Wright, and Krist (1997). Also, the additional thermal input to the system for delivering air and fuel at the desired conditions leads to a decreasing trend for the overall efficiency when the pressure is increased beyond a certain level. Therefore, the optimum efficiency for both the total cost and efficiency objectives is at an intermediate point (8 bar) where the capital cost is not as high as compared to a capital cost for an even higher pressure where the capital cost of the turbomachinery would increase to accommodate the higher pressure needed. On the other hand, a lower operating pressure causes lower efficiencies and, therefore, although the capital cost is lower the operating cost is higher resulting in an increased total cost.

Finally, the unit cost of fuel variation helps determine how efficiently the overall hybrid plant should be designed. At lower costs of fuel, e.g., 0.1 $\$/Nm^3$ and 0.3 $\$/Nm^3$, the capital cost competes more evenly with the operating cost to determine the optimum system. On the other hand, at higher values of unit cost of fuel, e.g., 0.9 $\$/Nm^3$ and 1.2 $\$/Nm^3$, the operating cost increases far and away above the capital cost and, therefore, a minimization of fuel consumption is required. In such a case, a more efficient system is required, and, therefore, the large SOFC, although having a higher capital cost than the smaller SOFC would be selected.

4.2.3 Analytical Results

In this section, a particular hybrid plant is selected to be analyzed in depth in terms of thermodynamic and geometric properties, off-design behavior, and cost. The selected plant is the 10 MWe hybrid system integrated with a triple-pressure with reheat steam turbine cycle. This plant is selected because it is the most efficient and also the most complicated of all the hybrid plants under study. For comparison purposes, both SOFC sizes, small and large, are compared in detail. Results for this plant appear in the following sections. Those for all other configurations are given in Appendix B.

Table 4.8. Optimal thermodynamic states for the SOFC-GT-ST 10 MWe plant with triple-pressure reheat ST cycle and the larger SOFC.

Node	T	p	h	ṁ	Node	T	p	h	ṁ
	°C	bar	kJ/kg	kg/s		°C	bar	kJ/kg	kg/s
2	920.2	8.031	1873	1.720	35	485	89.8	3349.4	0.812
3	1000	8.031	1655	2.671	36	482.4	86.2	3347.5	0.812
4	1000	8.031	1655	1.233	37	60	0.3	2234.1	0.048
5	1000	8.031	1655	1.438	38	31	0.045	2008.4	1.043
6	499.7	8.295	3607	6.870	39	31	0.045	130	1.043
7	1000	8.295	1104	5.919	40	31	0.2	130	1.043
8	1227	8.031	1495	7.151	41	60	0.2	251.4	0.214
9	1088	8.031	1308	7.151	42	60	2.74	251.4	0.214
12	25	1	25.2	6.870	43	129.8	2.69	545.7	0.214
13	318.3	8.298	329.5	6.870	44	129.8	2.69	545.7	0.214
14	25	1	52.4	0.281	45	129.8	2.69	545.7	0.214
15	217.6	8.033	535.2	0.281	46	129.8	2.69	2719.9	0.214
20	318.3	8.295	0	0	47	129.8	2.69	2719.9	0.214
21	891.7	8	1053	7.151	48	140	2.5	2743.9	0.214
22	318.3	8.295	329.5	6.870	49	60	0.2	251.4	0.065
23	217.6	8.031	0	0	50	60	13.17	252.7	0.065
24	217.6	8.031	535.2	0.281	51	191.3	12.91	813.4	0.065
25	778.1	8.031	1472	1.720	52	191.3	12.91	813.4	0.065
26	1088	8.031	1308	7.151	53	191.3	12.91	813.4	0.065
27	891.7	8	1053	7.151	54	191.3	12.91	2786.3	0.065
28	891.7	8	1053	7.151	55	191.3	12.91	2786.3	0.065
31	1088	8.031	0	0	56	215	12	2853.6	0.065
33	554.1	1.319	632.8	7.151	57	60	0.2	251.4	0.812
33r	494.7	1.319	561.5	7.151	58	60	98.56	261.4	0.812
33a	453.1	1.319	511.9	7.151	59	308.5	96.62	1393.2	0.812
33b	324.5	1.319	361.5	7.151	60	308.5	96.62	1393.2	0.812
33c	215.7	1.319	237.2	7.151	61	308.5	96.62	1393.2	0.812
33d	215.1	1.319	236.6	7.151	62	308.5	96.62	2731.5	0.812
33e	199.3	1.319	218.7	7.151	63	308.5	96.62	2731.5	0.812
33f	194.8	1.319	213.7	7.151	64	215	12	2853.6	0.812
33g	194.2	1.319	213	7.151	65	212.9	11.64	2850.3	0.812
33h	135.8	1.319	147.9	7.151	66	410	11.29	3283.7	0.812
34	128	1.319	139.1	7.151	67	407.8	10.73	3279.9	0.812

4.2.3.1 Thermodynamic Results

For the configuration shown in Figure 3.5, the corresponding pressures, temperatures, mass flow rates, and enthalpies are shown in Tables 4.1 and 4.2 for the large and small SOFC, respectively. Figure 4.27 illustrates the work rate breakdown between the SOFC and the turbomachinery. When utilizing the larger SOFC, the SOFC, GT, and ST contribute 71.6%, 19.2%, and 9.2%, respectively, to the total power output, while with the small SOFC, the SOFC, GT, and ST contribute 67.7%, 20.3%, and 12.3% respectively, to the total power output.

Table 4.9. Optimal thermodynamic states for the SOFC-GT-ST 10 MWe plant with triple-pressure reheat ST cycle and the smaller SOFC.

Node	T	p	h	$\dot{m}$	Node	T	p	h	$\dot{m}$
	^{o}C	bar	kJ/kg	kg/s		^{o}C	bar	kJ/kg	kg/s
2	922	8.014	1877	1.817	35	485	89.8	3349.4	1.187
3	1002	8.014	1659	2.822	36	482.4	86.2	3347.5	1.187
4	1002	8.014	1659	1.302	37	60	0.3	2234.1	0.070
5	1002	8.014	1659	1.52	38	31	0.045	2008.4	1.283
6	412.7	7.966	430.6	7.56	39	31	0.045	130	1.283
7	1002	7.966	1105	6.555	40	31	0.2	130	1.283
8	1222	7.966	1483	7.857	41	60	0.2	251.4	0.093
9	1137	7.966	1370	7.857	42	60	2.74	251.7	0.093
12	25	1	25.2	7.56	43	129.8	2.69	545.7	0.093
13	302.5	7.969	312.7	7.56	44	129.8	2.69	545.7	0.093
14	25	1	52.4	0.297	45	129.8	2.69	545.7	0.093
15	217.5	8.016	534.9	0.297	46	129.8	2.69	2719.9	0.093
20	302.5	7.966	0	0	47	129.8	2.69	2719.9	0.093
21	949.4	7.929	1124	7.857	48	140	2.5	2743.9	0.093
22	302.5	7.966	312.7	7.56	49	60	0.2	251.4	0.073
23	217.5	8.014	0	0	50	60	5.49	251.9	0.073
24	217.5	8.014	534.9	0.297	51	154.6	5.38	652.2	0.073
25	779.4	8.014	1475	1.817	52	154.6	5.38	652.2	0.073
26	1137	7.966	1370	7.857	53	154.6	5.38	652.2	0.073
27	949,4	7.929	1124	7.857	54	154.6	5.38	2751.4	0.073
28	949,4	7.929	1124	7.857	55	154.6	5.38	2751.4	0.073
31	1137	7.966	0	0	56	160	5	2767.4	0.073
33	628.9	1.451	721.6	7.857	57	60	0.2	251.4	0.832
33r	550.2	1.451	626.2	7.857	58	60	98.56	261.4	1.187
33a	495	1.451	560.1	7.857	59	308.5	96.62	1393.2	1.187
33b	324.5	1.451	360.5	7.857	60	308.5	96.62	1393.2	1.187
33c	180.2	1.451	196.8	7.857	61	308.5	96.62	1393.2	1.187
33d	180.1	1.451	196.6	7.857	62	308.5	96.62	2731.5	1.187
33e	162.6	1.451	177.2	7.857	63	308.5	96.62	2731.5	1.187
33f	159.3	1.451	173.5	7.857	64	215	12	2853.6	1.187
33g	159	1.451	173.2	7.857	65	212.9	11.64	2850.3	1.187
33h	135.8	1.451	147.5	7.857	66	410	11.29	3283.7	1.187
34	132.7	1.451	144	7.857	67	407.8	10.73	3279.9	1.187

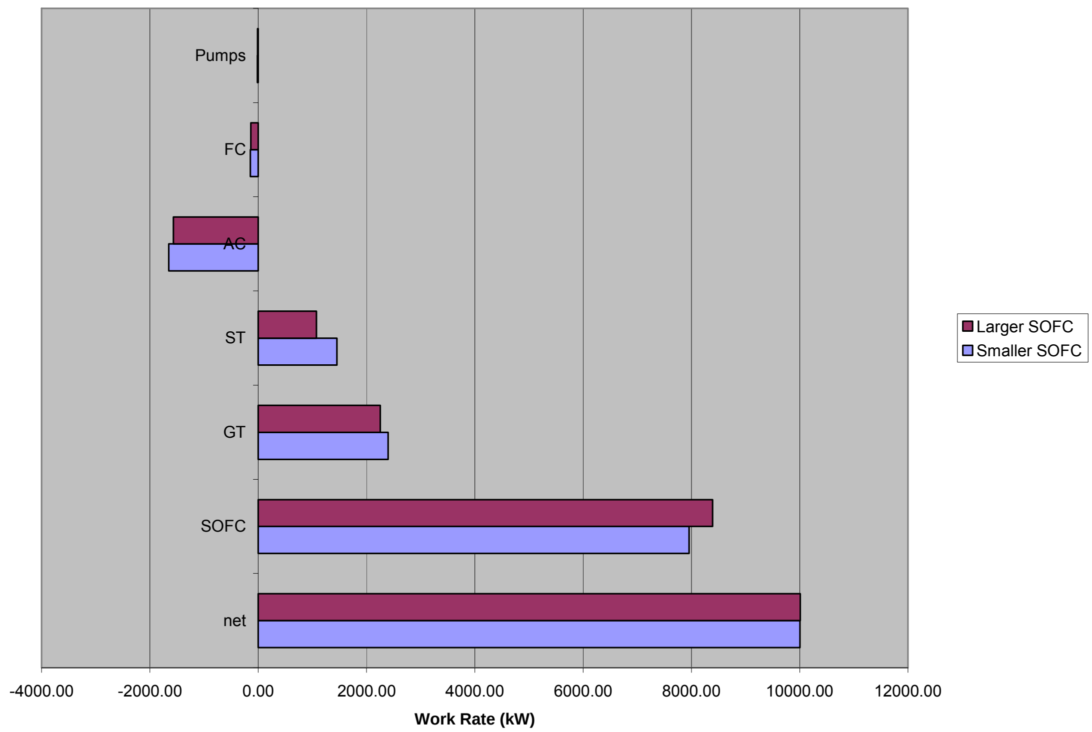

Figure 4.27. Optimal work rate distribution for the 10 MWe SOFC-GT-ST with triple pressure reheat ST cycle.

4.2.3.2 Component Geometry

The component geometries for the 10 MWe SOFC-GT-ST with a triple pressure with reheat hybrid system are necessary to determine off-design behavior as mentioned in Chapter 3. Tables 4.10 and 4.11 indicate the SOFC and the heat exchanger geometries, respectively.

Table 4.10. Optimal SOFC and pre-reformer geometries for the 10 MWe SOFC-GT-ST with triple pressure reheat ST cycle.

Geometric Variable Description		Value	
		Large SOFC	**Small SOFC**
n_{SOFC}	SOFC number of tubes	65000	30000
n_{PR}	Pre-reformer number of tubes	3120	3247
L_{SOFC}	SOFC tube length (m)	1.5	1.5
L_{PR}	Pre-reformer tube length (m)	0.22	0.22
D_{SOFC}	SOFC tube length (m)	0.0156	0.0156
D_{PR}	Pre-reformer tube length (m)	0.0156	0.0156

Table 4.11. Optimal heat exchanger geometries for the 10 MWe SOFC-GT-ST with triple pressure reheat ST cycle.

Geometric Variable Description		Value	
		Small SOFC	Large SOFC
d_i^{LPECO}	LP Economizer inlet diameter (m)	0.02	0.02
L^{LPECO}	LP Economizer tube length (m)	15.2	12.4
n^{LPECO}	LP Economizer number of tubes	14	10
d_i^{IPECO}	IP Economizer inlet diameter (m)	0.02	0.02
L^{IPECO}	IP Economizer tube length (m)	2.1	1.9
n^{IPECO}	IP Economizer number of tubes	12	10
d_i^{HPECO}	HP Economizer inlet diameter (m)	0.02	0.02
L^{HPECO}	HP Economizer tube length (m)	19.7	17.9
n^{HPECO}	HP Economizer number of tubes	58	50
d_i^{LPEVA}	LP Evaporator inlet diameter (m)	0.02	0.02
L^{LPEVA}	LP Evaporator tube length (m)	6.9	5.7
n^{LPEVA}	LP Evaporator number of tubes	24	20
d_i^{IPEVA}	IP Evaporator inlet diameter (m)	0.02	0.02
L^{IPEVA}	IP Evaporator tube length (m)	5.4	5.1
n^{IPEVA}	IP Evaporator number of tubes	14	10
d_i^{HPEVA}	HP Evaporator inlet diameter (m)	0.02	0.02
L^{HPEVA}	HP Evaporator tube length (m)	2.6	2.2
n^{HPEVA}	HP Evaporator number of tubes	56	50
d_i^{LPSUP}	LP Superheater inlet diameter (m)	0.02	0.02
L^{LPSUP}	LP Superheater tube length (m)	2.1	1.75
n^{LPSUP}	LP Superheater number of tubes	3	2
d_i^{IPSUP}	IP Superheater inlet diameter (m)	0.02	0.02
L^{IPSUP}	IP Superheater tube length (m)	3.5	2.85
n^{IPSUP}	IP Superheater number of tubes	16	10
d_i^{HPSUP}	HP Superheater inlet diameter (m)	0.02	0.02
L^{HPSUP}	HP Superheater tube length (m)	2.5	1.75
n^{HPSUP}	HP Superheater number of tubes	24	20
d_i^{RH}	Reheater inlet diameter (m)	0.02	0.02
L^{RH}	Reheater tube length (m)	1.8	1.5
n^{RH}	Reheater number of tubes	25	20
d_i^{CON}	Condenser inlet diameter (m)	0.02	0.02
L^{CON}	Condenser tube length (m)	7.5	6.7
n^{CON}	Condenser number of tubes	65	50

4.2.3.3 Off-Design Behavior

The off-design behavior of the 10 MWe SOFC-GT-ST hybrid system is very important since the system often operates at part load conditions. The off-design efficiency breakdown is shown graphically in Figure 4.28 for both the large and small SOFCs. The current density also decreases at off-design (i.e. part load) since the current density decreases at these loads because the fuel mass flow rate decreases. The graphical representation in Figures 4.29 shows this trend.

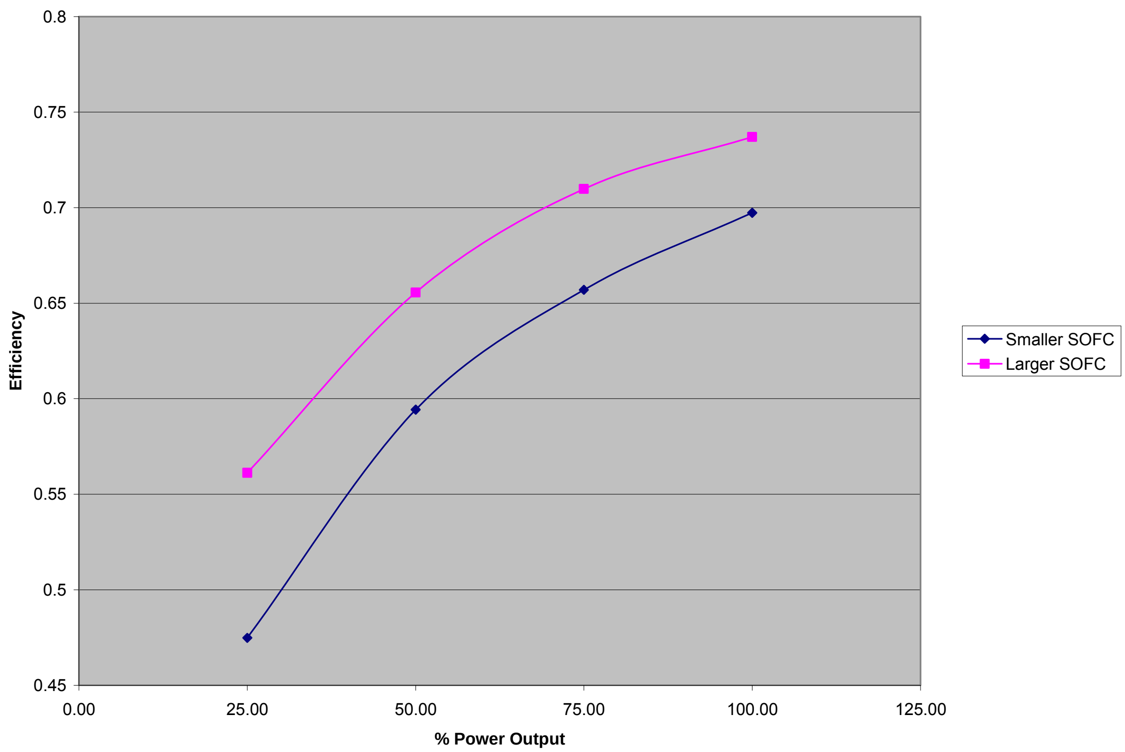

Figure 4.28. Partial-load performance of the optimal 10 MWe SOFC-GT-ST hybrid plant, with a triple reheat ST cycle.

4.2.3.4 Cost Results

The component cost breakdown for the 10 MWe SOFC-GT-ST with triple-pressure reheat ST cycle is shown in Table 4.6 and Figure 4.33 for the large SOFC and in Table 4.7 and Figure 4.34 for the small SOFC. As expected, the most dominant component cost is the SOFC purchase (depreciation) cost (especially when using the large SOFC), while the turbomachinery, combustor, and HRSG costs are also significant.

The capital costs (depreciation, interest on outside capital, maintenance, insurance, taxation), the operating cost and the total cost per annum when using a large SOFC and a small SOFC are shown in Figures 4.35 and 4.36, respectively.

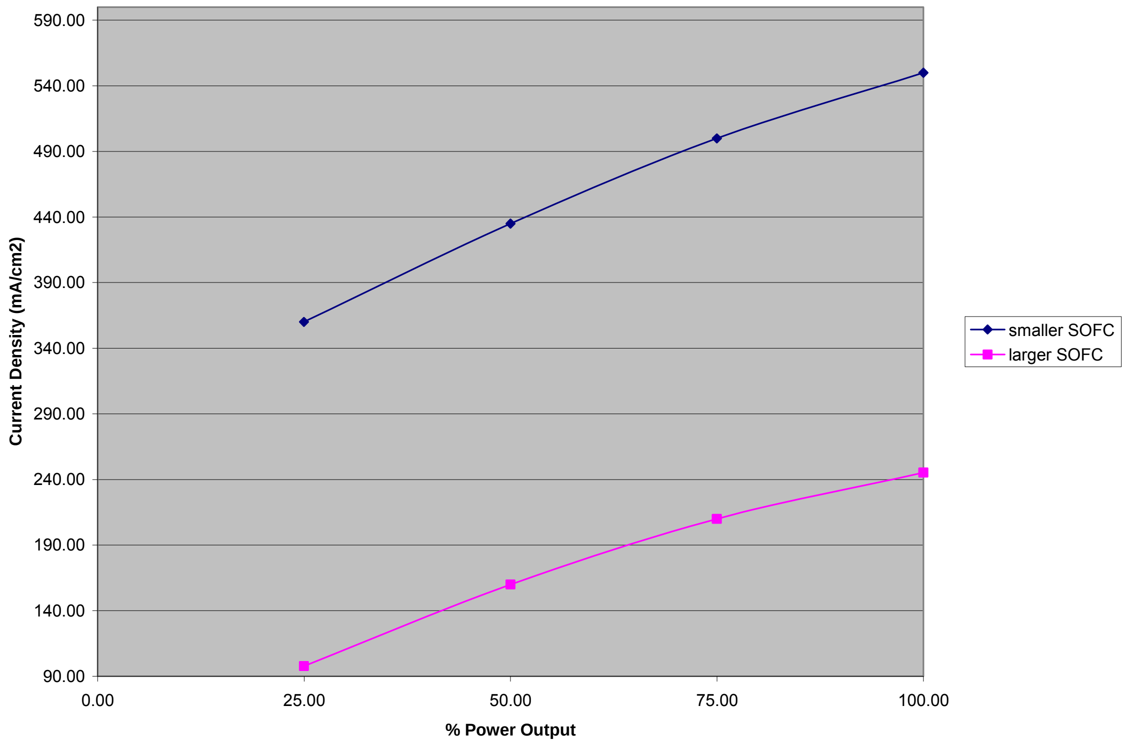

Figure 4.29. Current density variation for the optimal 10 MWe SOFC-GT-ST hybrid plant, with a triple reheat ST cycle.

Table 4.12. Optimal component costs for the optimal 10 MWe SOFC-GT-ST hybrid plant, with a triple reheat ST cycle and large SOFC.

Component	**Cost**	
	Large SOFC	**Small SOFC**
SOFC	5,031,872	2,334,223
GT	1,595,840	1,662,272
Combustor/Mixer	1,236,623	941,679
HRSG	584,085	660,761
ST	438,749	536,340
Inlet Air Tubes	345,616	189,093
AC	258,163	264,960
Deaerator	57,278	67,761
Pre-reformer	45,124	36,994
FC	41,321	42,856
Condenser	8,262	8,262
Pumps	7,958	9,734
Total Investment	**9,650,891**	**6,754,935**

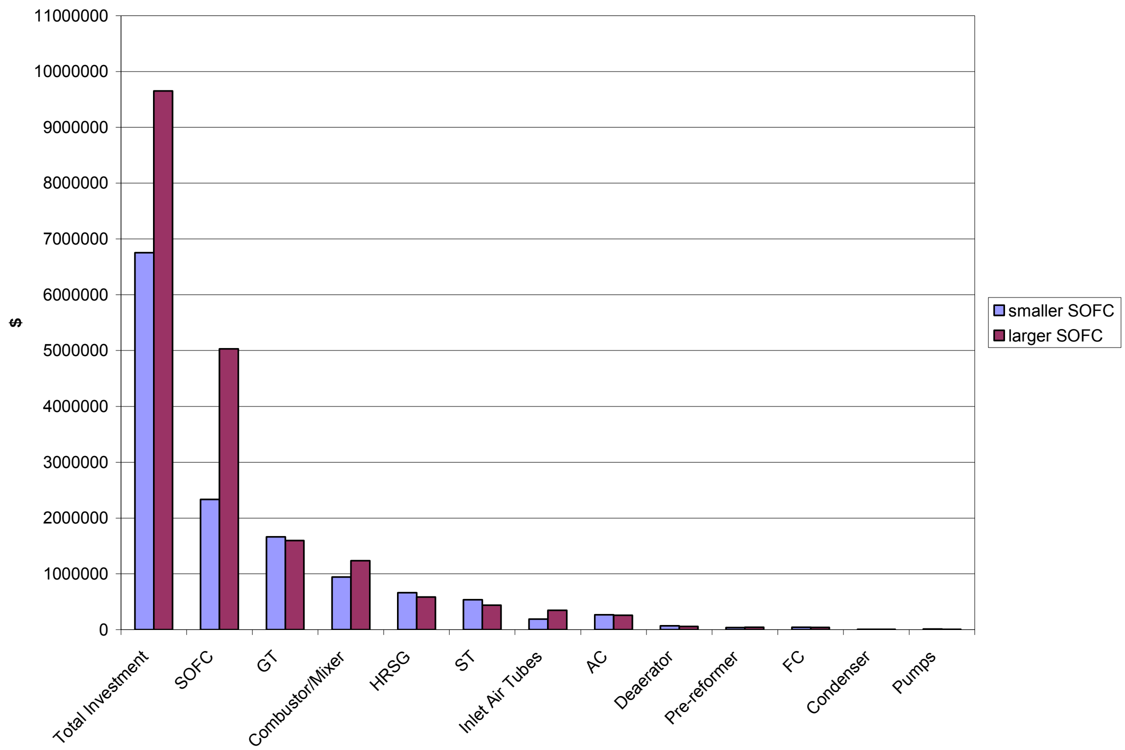

Figure 4.30. Optimal component costs for the optimal 10 MWe SOFC-GT-ST hybrid plant, with a triple reheat ST cycle.

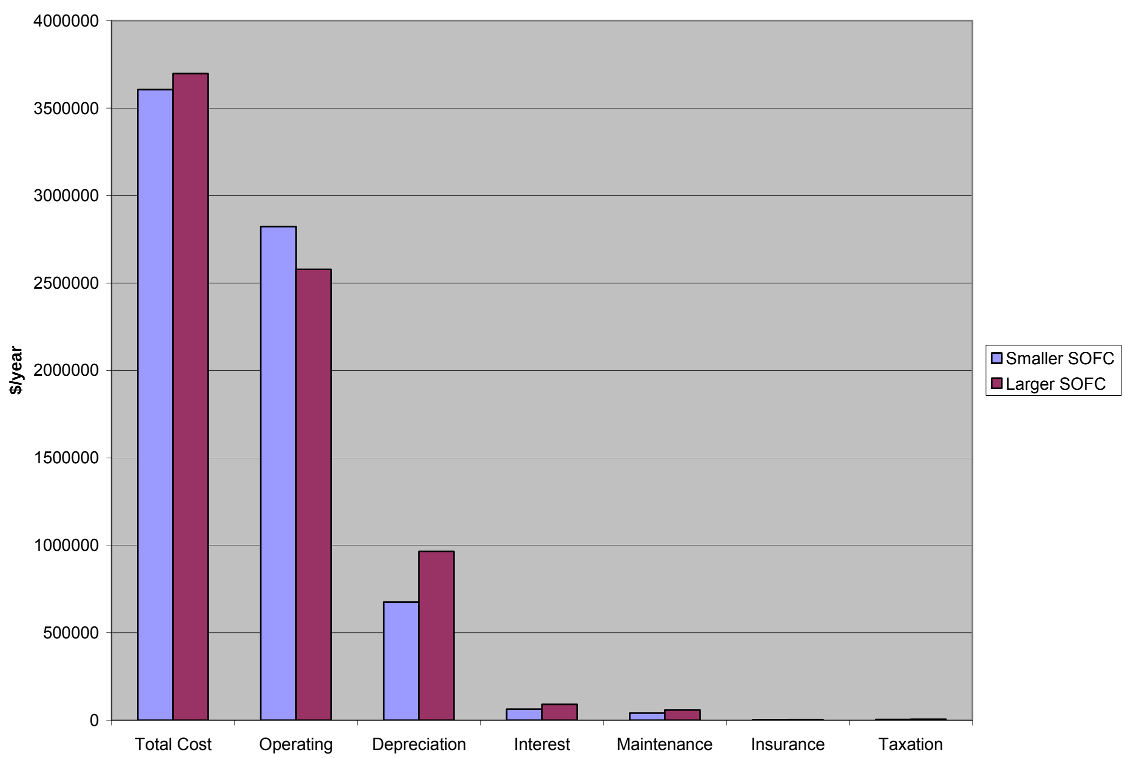

Figure 4.31. Optimal annual costs for the optimal 10 MWe SOFC-GT-ST hybrid plant, with a triple reheat ST cycle.

4.2.3.5 Optimal Model Comparison

All twenty four models are compared in terms of cost (total, operating, and capital) and efficiency (maximum, total, and average) in Table 4.13. These values are also shown graphically in Figures 4.32 and 4.33.

Table 4.13. Cost and efficiency breakdown for all optimal models.

Model	Total Cost	Operating Cost	Capital Cost	η_{ave}	η_{tot}	η_{max}
1.5 MWe single-pressure ST small SOFC	604743	438971	165772	0.5696	0.6022	0.6638
1.5 MWe single-pressure ST large SOFC	613655	405328	208327	0.6235	0.6525	0.6971
1.5 MWe dual-pressure ST small SOFC	602033	435146	166887	0.5705	0.6031	0.6647
1.5 MWe dual-pressure ST large SOFC	611026	401575	209451	0.6243	0.6533	0.6978
1.5 MWe triple-pressure ST small SOFC	599321	431428	167893	0.5712	0.6035	0.6654
1.5 MWe triple-pressure ST large SOFC	608046	397831	210215	0.6251	0.6536	0.6987
1.5 MWe triple RH-pressure ST small SOFC	598691	430598	168093	0.5716	0.6038	0.6657
1.5 MWe triple RH-pressure ST large SOFC	607446	397031	210415	0.6255	0.6539	0.6992
5 MWe single-pressure ST small SOFC	1887264	1437339	449925	0.5791	0.6131	0.6795
5 MWe single-pressure ST large SOFC	1935053	1340421	594632	0.6264	0.6573	0.7115
5 MWe dual-pressure ST small SOFC	1872891	1411966	460925	0.5808	0.6149	0.6815
5 MWe dual-pressure ST large SOFC	1920649	1316017	604632	0.6279	0.6589	0.7132
5 MWe triple-pressure ST small SOFC	1871891	1405966	465925	0.5814	0.6155	0.6825
5 MWe triple-pressure ST large SOFC	1924649	1310017	614632	0.6286	0.6596	0.7142
5 MWe triple RH-pressure ST small SOFC	1869891	1402966	466925	0.5817	0.6159	0.6837
5 MWe triple RH-pressure ST large SOFC	1923649	1307017	616632	0.6289	0.6601	0.7157
10 MWe single-pressure ST small SOFC	3630071	2831362	798710	0.5876	0.6222	0.6922
10 MWe single-pressure ST large SOFC	3717621	2603916	1113705	0.6473	0.6766	0.7272
10 MWe dual-pressure ST small SOFC	3630067	2819358	810710	0.5880	0.6228	0.6943
10 MWe dual-pressure ST large SOFC	3717624	2591919	1125705	0.6478	0.6772	0.7292
10 MWe triple-pressure ST small SOFC	3640067	2805358	834710	0.5884	0.6234	0.6961
10 MWe triple-pressure ST large SOFC	3715624	2577919	1137705	0.6480	0.6774	0.7292
10 MWe triple RH-pressure ST small SOFC	3606144	2822572	783573	0.5891	0.6242	0.6973
10 MWe triple RH-pressure ST large SOFC	3697652	2577948	1119703	0.6529	0.6836	0.7370

From Figure 4.32 it can be concluded that as expected the higher the degree of complexity in the heat recovery steam generator is, the higher the capital cost. On the other hand, the operating cost decreases as this complexity increases because of the increasing efficiency. This decrease in operating cost is significant enough to balance and even slightly decrease the total cost for a more complex system. In terms of SOFC size, the configurations equipped with a smaller SOFC also as expected have a total cost lower than those with the larger SOFC.

Finally, from Figure 4.33 it is evident that the efficiency is higher for a system equipped with a larger SOFC than those with a smaller SOFC for any given configuration pair. In addition, a global comparison of all twenty-four systems shows that the most efficient system is a system at the larger power capacity level i.e. the 10 MWe configuration is more efficient than the 5 MWe configuration or the 5 MWe configuration is more efficient than the 1.5 MWe configuration. This is mainly due to the higher efficiencies achieved by the turbomachinery (gas turbine, steam turbine, air compressor, fuel compressor, pumps) at the larger capacities.

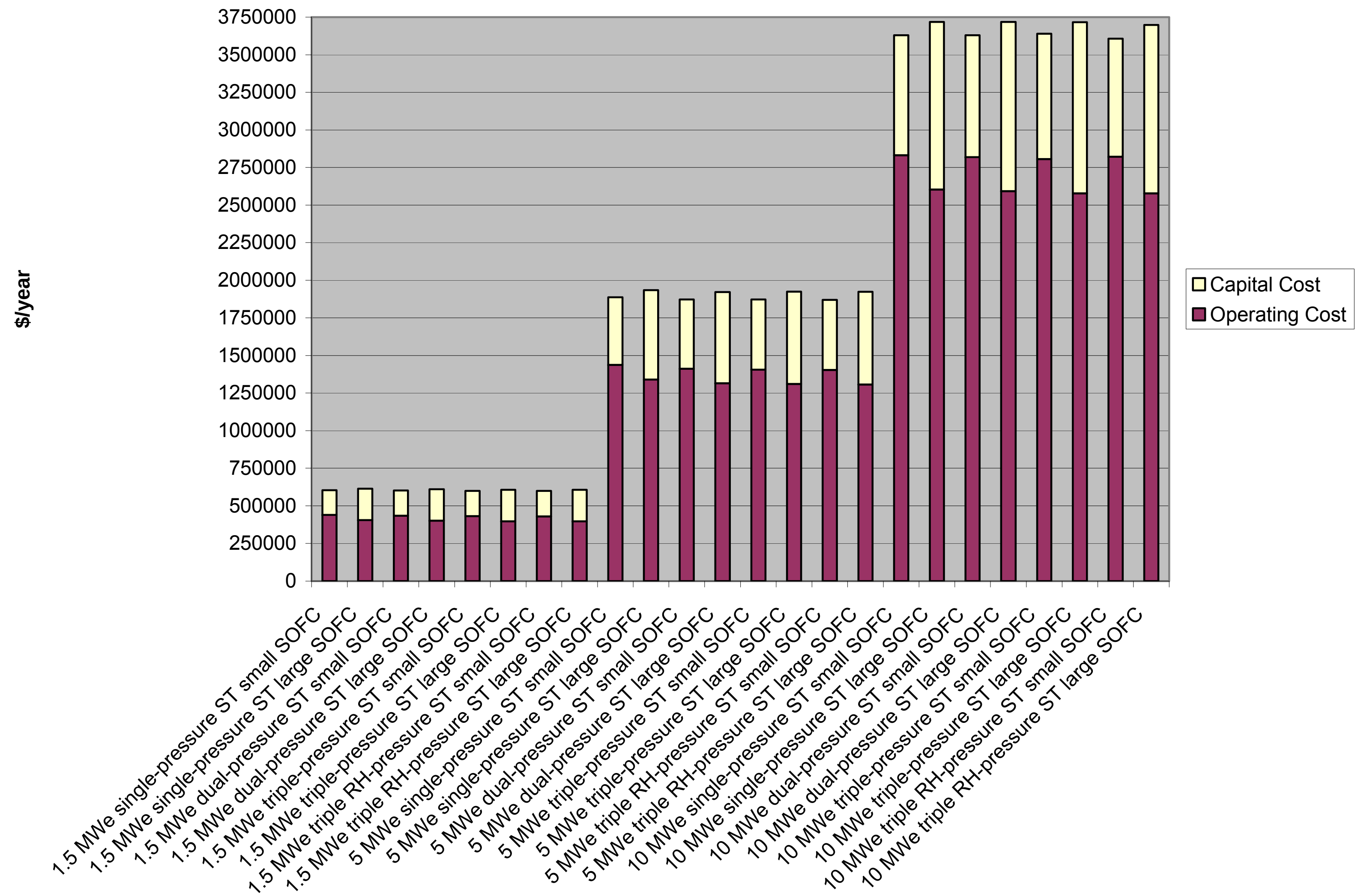

Figure 4.32. Cost breakdown for all optimal configurations.

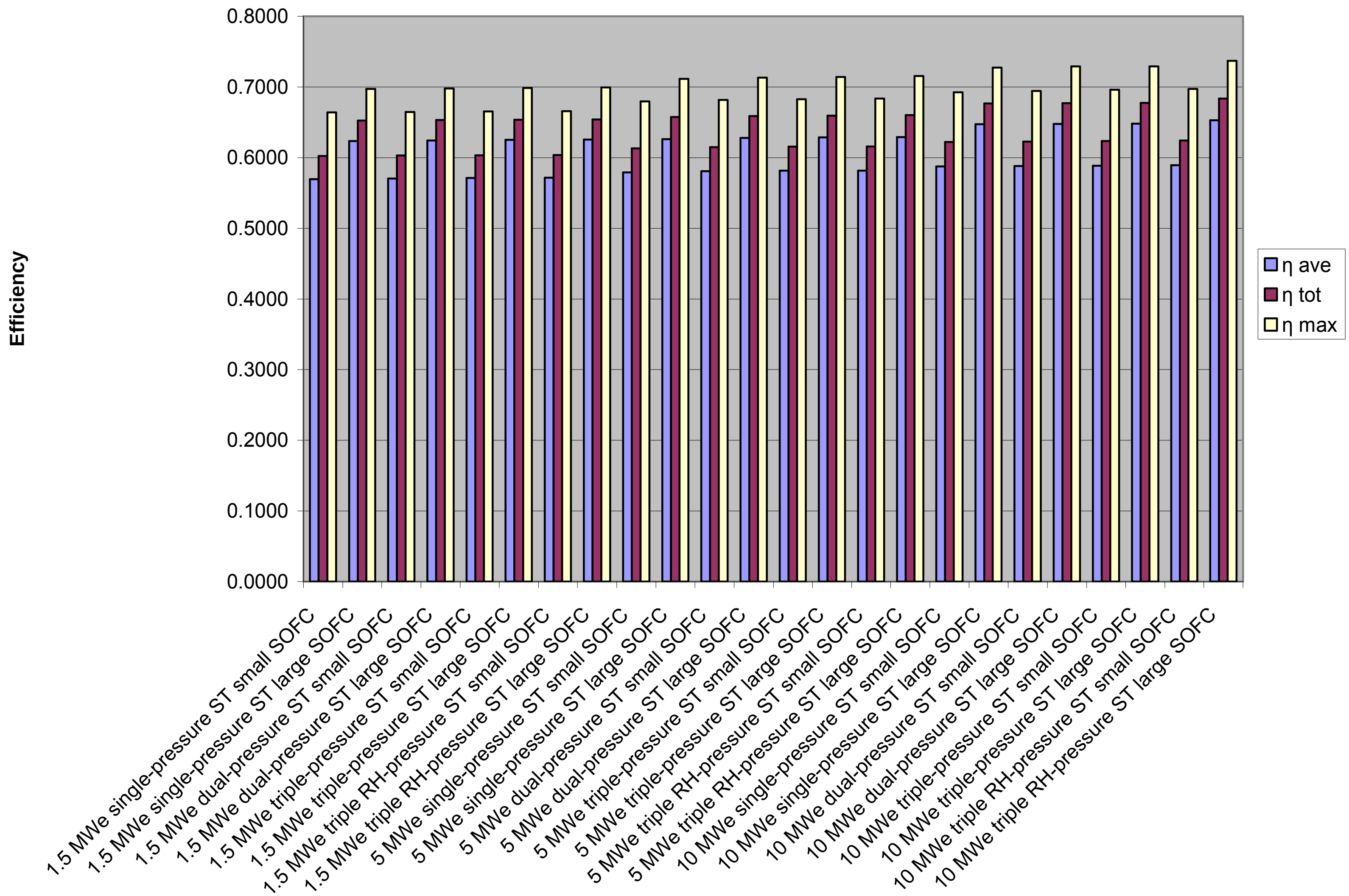

Figure 4.33. Efficiency breakdown for all optimal configurations.

5 Conclusions

The thermoeconomic modeling and the parametric study developed for hybrid SOFC-GT-ST systems leads to a number of useful and unique conclusions regarding this research work:

1. The SOFC-GT-ST system promises high efficiencies with decreased fuel consumption (i.e. lower operating cost and lower emissions to the environment) as already discussed throughout this research work.

2. The SOFC is a novel power producing component which as a standalone system has, as would be expected, any number of operating constraints that must be observed, e.g., that of operating temperature, pressure, steam-to-carbon ratio, and fuel utilization factor. The constraints on operation, however, become even more complex when the SOFC is integrated with conventional heat engines (e.g., gas turbines and steam turbines). In particular, the bottoming cycles (i.e. gas and steam turbine cycles must be properly selected and sized to accommodate not only the inherent limitations and restrictions associated with these cycles but as well those of the SOFC since it operates in a relatively narrow range of synthesis/design parameters as discussed in Chapter 4.

3. The high efficiencies developed by some of the hybrid systems are of great interest since they show the potential for exceeding those of the best commercial heat engine cycles (e.g., the natural gas GT-ST combined cycles) currently available or projected. The latter are combustion limited and are already close to their technological limits. For instance, the 10 MWe SOFC-GT-ST hybrid triple pressure with reheat system exhibits efficiencies (maximum efficiency of 73.8 %, an average efficiency of 65.3 %, and a total efficiency of 68.4 %) that cannot be matched by other conventional and non-conventional cycles (e.g., a standalone SOFC, SOFC-GT hybrid cycles, etc.).

4. Interestingly, the *sui generis* SOFC-GT-ST system develops high efficiencies at off-design conditions as well. However, the off-design strategy followed in this research work was a simplistic one which involved the lowering of the fuel flow rate while keeping constant the air flow rate. This strategy was necessary because a constant air-to-fuel ratio strategy (which maintains high efficiencies) has a very restricted field of operation (above 80% of full load) not applicable for the load profile (down to 25 % of full load) considered in this research study. Therefore, the aforementioned simplistic strategy creates conditions at which, for example, the SOFC operating temperature drops significantly, leading to the difficulty of maintaining higher efficiencies than those actually exhibited. Thus, a more in-depth analysis of the off-design strategy should be done to see if a better strategy can indeed be found (e.g., the removal of part of the SOFC stack at lower loads could conceivably maintain higher efficiencies).

5. The parametric study identified a number of unforeseen complexities which only became evident after the integration and development of the total systems. These difficulties included the proper selection of the SOFC stack size and the difficulty of finding the proper steam turbines to match the system. For a realistic system, a 1.5 MWe SOFC-GT-ST is not as attractive and efficient as a 5 MWe or a 10 MWe system. The reason is that the gas turbine and especially the steam turbine are very inefficient at small sizes resulting in lower overall system efficiencies.

6. A careful selection of component designs (e.g., turbine, pumps, heat exchangers) in the steam turbine cycle was made to achieve efficient conversion of the thermal energy to power output based on the thermodynamic, geometric, and cost models. The uniqueness of the system required in many instances (e.g., pump modeling) the rescaling and remodeling of existing components to fulfill the needs of the system. Thus, if not careful, one risks making unrealistic selections and cost analyses of equipment. Therefore the design of a hybrid SOFC-GT-ST power plant must focus on all the components and not only on the SOFC. Special attention must be given in the coupling of the turbomachinery with the SOFC and

the heat exchanges to achieve the maximum benefits offered by the hybrid system.

7. The air compressors have an unexpectedly high consumption of power (about 3/4 of the gas turbine power output) meaning that a study must be made in order to minimize this trend if possible. Based on current technology, the SOFC operates at pressures of 7-9 bars meaning that a high degree of compression is required to fulfill this need. New developments in lower temperature and pressure SOFCs may benefit the overall system since less compression, will be required. Of course, whether or not this leads to an overall system benefit will depend on the tradeoffs involved.

8. Since the SOFC-GT-ST system involves a large amount of equipment with a much larger number of decision variables than actually considered in this parametric study, a more complete optimization of the systems should be done in order to determine more detailed syntheses/designs than those presented here.

9. Finally, since SOFCs are not fully commercialized, a more accurate economic analysis than that made here cannot be made at this time. The high capital cost suggested in this research work (even adjusted for production volume) could decrease in the near future leading to minimized cost syntheses/designs which exhibit even higher efficiencies than those determined here.

References

Benjamin, T.G., Camera, E.H. and Marianowski, L.G., 1995. *Handbook of Fuel Cell Performance*. Institute of Gas Technology.

Boehm, R.F., 1987, *Design analysis of thermal systems*, John Wiley and Sons, Inc., New York.

Calise, F., 2005. Modellazione, Analisi Exergetica ed Ottimizzazione Termoeconomica di Cicli Ibridi SOFC-GT, Universita Degli Studi di Napoli Federico II, Napoli, Italy.

Calise, F., d'Accadia, M.D., Palombo, A., Vanoli, L. and Vanoli, R., 2004. Modelling, simulation and exergy analysis of a hybrid SOFC-gas turbine system, *Third International Symposium on Energy and Environment*, Sorrento, Italy.

Calise, F., d'Accadia, M.D., Vanoli, L. and von Spakovsky, M.R., 2006. Single-level optimization of a hybrid SOFC-GT power plant. *Journal of Power Sources*, 159(2): 1169-1185

Campanari, S., 1998. "Power plants based on solid oxide fuel cells combined with gas turbine cycles", PhD Dissertation, Politecnico di Milano, Milano, Italy.

Campanari, S., 2000. Full load and part load performance prediction for integrated SOFC and microturbine systems. *Journal of Engineering for Gas Turbines and Power*, 122(2): 239-246.

Campanari, S., 2002. Carbon dioxide separation from high temperature power plants. *Journal of Power Sources*, 112(1): 273-289.

Chan, S.H., Low, C.F. and Ding, O.L., 2002. Energy and exergy analysis of a simple SOFC power system. *Journal of Power Sources*, 103(2): 188-200.

Chemical Engineering Plant Cost Index, 2006, *Chemical Engineering*, McGraw-Hill, New York.

Chen, T.P., Wright, J.D. and Krist, K., 1997. SOFC system analysis, NETL *Proceedings of the Fuel Cells '97 Review Meeting*, GRI study.

Chiesa, P. and Consonni, S., 2003. Co-production of hydrogen, electricity and CO2 from coal using commercially-ready technology, *Second Annual Conference on Carbon Sequestration*, Washington, DC, USA.

Costamagna, P., Magistri, L. and Massardo, A., 2001. Design and part load performance of a hybrid system based on a SOFC reactor and a micro GT. *Journal of Power Sources*, 96(2): 352-368.

Dicks, A.L., Fellows, R.G., Martin Mescal, C. and Seymour, C., 2000. A study of SOFC-PEM hybrid systems. *Journal of Power Sources*, 86(1-2): 501-506.

Dunbar, W.R., Lior, N. and Gaggioli, R., 1991. Combining fuel cells with fuel-fired power plants for improved exergy efficiency. *Energy: The International Journal*, 16(10): 1259-1274.

Energy Information Administration, 2006, “U.S. Natural Gas Prices”, http://www.eia.doe.gov.

Frangopoulos, C.A., 1991. Optimization of Synthesis-Design-Operation of a Cogeneration System by the Intelligent Functional Approach. *International Journal of Energy Environment Economics*, 1(4): 275-287.

Fuel Cell Handbook, 2004, 7th edition, Office of Fossil Energy, National Energy Technology Laboratory, Morgantown, West Virginia, November.

Georgopoulos, N., 2002. Application of a Decomposition Strategy to the Optimal Synthesis/Design and Operation of a Fuel Cell Based Total Energy System, M.S. thesis, advisor: M.R. von Spakovsky, Virginia Polytechnic Institute & State University, Blacksburg, VA.

Grove, W.R., 1843. On the Gas Voltaic Battery. Experiments Made with a View of Ascertaining the Rationale of Its Action and Its Application to Eudiometry, *Philosophical Transactions of the Royal Society of London*, 133: 91-112.

Gyftopoulos, E.P. and Beretta, G.P., 2005. *Thermodynamics : Foundations and Applications*, 2nd edition. Dover Press, Mineola, New York.

Kakaç, S. and Liu, H., 2002. *Heat exchangers : selection, rating, and thermal design*, 2nd edition. CRC Press, Boca Raton, Florida.

Kehlhofer, R., 1999. *Combined-cycle gas & steam turbine power plants*. PennWell Pub. Co., Tulsa, Oklahoma.

Laosiripojana, N. and Assabumrungrat, S., 2007. Catalytic steam reforming of methane, methanol, and ethanol over Ni/YSZ: The possible use of these fuels in internal reforming SOFC. *Journal of Power Sources*, 163(2): 943-951.

Larminie, J. and Dicks, A., 2003. *Fuel cell systems explained*. John Wiley, Chichester, West Sussex.

Lunghi, P., 2001. Highly efficient electricity generation through a Hybrid molten carbonate fuel cell-closed loop gas turbine plant. *Energy Conversion and Management*, 42(5): 1657-1672.

Marechal, F., Favrat, D., Palazzi, F. and Godat, J., 2004. Thermoeconomic modeling and optimization of fuel cell systems, *Fuel Cell Research Symposium*, ETH Zurich, March.

Oyarzabal, B., 2001, "Application of a Decomposition Strategy to the Optimal Synthesis/Design of a Fuel Cell Sub-system", M.S. Thesis, Department of Mechanical Engineering, advisor: M.R. von Spakovsky, Virginia Polytechnic Institute & State University, Blacksburg, VA.

Pelster, S., 1998. "Environomic Modeling & Optimization of advanced combined cycle cogeneration power plants including CO2 separation options", Doctoral thesis, advisors: M.R. von Spakovsky and D. Favrat, Ecole Polytechnique Federale de Lausanne, Lausanne, Switzerland.

Peters, M.S., Timmerhaus, K.D. and West, R.E., 2003. *Plant design and economics for chemical engineers*. McGraw-Hill, New York.

Potter, P.J., 1959. *Power plant theory and design*. Ronald Press Co., New York.

Rancruel, D., 2005. "Optimization of solid-oxide fuel cell balance-of-plant system", PhD Dissertation, advisor: M.R. von Spakovsky, Virginia Polytechnic Institute & State University, Blacksburg, VA.

Salisbury, J.K., 1974. *Steam turbines and their cycles*. R. E. Krieger Publication Company, Huntington, New York.

Singhal, S.C., 1997. Recent progress in tubular SOFC technology, *Fifth International Symposium on SOFC*, Aachen, Germany, July 2-5.

Singhal, S.C. and Kendall, K., 2003. *High temperature solid oxide fuel cells: fundamentals, design, and applications*. Elsevier, Oxford, New York.

Skrotzki, B.G.A. and Vopat, W.A., 1960. *Power station engineering and economy*. McGraw-Hill, New York.

Traverso, A., 2006. Personal communication on the purchase cost function of condensing, axial type steam turbines, Virginia Tech, Blacksburg, Virginia.

Traverso, A., Massardo, A., Cazzola, W. and Lagorio, G., 2004. WIDGET-TEMP: anovel web-based approach for thermoeconomic analysis and optimization of conventional and innovative cycles, ASME Paper 2004-GT-54115, 14-17 June, 2004, *Proceedings of ASME-IGTI TURBO EXPO 2004*, Vienna, Austria.

Appendix A

In this appendix, all the results of the parametric study are shown. Figures 4.3 through 4.26 in Chapter 4 are based on these results. For example Table A.1 corresponds to Figures 4.3 and 4.4. The top half of every table shows the results for the systems with the small SOFC, while the bottom half shows the results for the systems with the large SOFC. Each of the five yellow highlighted decision variables shown in each table (i.e. the first five columns of each table) are plotted in Figures 4.3 to 4.26 of Chapter 4 against the first two objective functions, i.e. average efficiency and total life cycle cost. The total efficiency is not plotted since its trends are identical to those for the average efficiency. Also contained in the tables below are the SOFC, gas turbine, and steam turbine power outputs.

Table A.1. Parametric Results for the 1.5 MWe single pressure ST hybrid system.

Decision Variables					Objective Functions			Power Output (MW)		
U_f	T_{SOFC}	S/C	p_{SOFC}	c_{fuel}	η_{ave}	C_{total}	η_{tot}	$\dot{W}_{SOFC}$	$\dot{W}_{GT}$	$\dot{W}_{ST}$
0.75	1000	2	8	0.3	0.5644	605,048	0.5965	1.233	0.349	0.217
0.8	1000	2	8	0.3	0.5687	661,644	0.6014	1.251	0.356	0.195
0.85	1000	2	8	0.3	0.5696	604,743	0.6022	1.275	0.377	0.176
0.9	1000	2	8	0.3	0.5483	625,737	0.5807	1.291	0.396	0.155
0.85	950	2	8	0.3	0.5503	615,085	0.5837	1.282	0.392	0.160
0.85	1000	2	8	0.3	0.5696	604,743	0.6022	1.275	0.377	0.176
0.85	1050	2	8	0.3	0.5729	615,091	0.6052	1.270	0.360	0.191
0.85	1100	2	8	0.3	0.5732	607,235	0.6047	1.264	0.346	0.206
0.85	1000	2	8	0.3	0.5696	604,743	0.6022	1.275	0.377	0.176
0.85	1000	2.5	8	0.3	0.5601	614,422	0.5929	1.282	0.382	0.170
0.85	1000	3	8	0.3	0.5548	618,614	0.5875	1.289	0.388	0.163
0.85	1000	3.5	8	0.3	0.5458	627,651	0.5790	1.294	0.395	0.154
0.85	1000	2	7	0.3	0.5624	612,845	0.5947	1.249	0.395	0.151
0.85	1000	2	8	0.3	0.5696	604,743	0.6022	1.275	0.377	0.176
0.85	1000	2	9	0.3	0.5604	615,728	0.5931	1.302	0.359	0.194
0.85	1000	2	10	0.3	0.5478	631,542	0.5802	1.329	0.338	0.215
0.85	1000	2	8	0.1	0.5696	312,042	0.6022	1.275	0.377	0.176
0.85	1000	2	8	0.3	0.5696	604,743	0.6022	1.275	0.377	0.176
0.85	1000	2	8	0.6	0.5696	1,043,389	0.6022	1.275	0.377	0.176
0.85	1000	2	8	0.9	0.5696	1,482,198	0.6022	1.275	0.377	0.176
0.85	1000	2	8	1.2	0.5696	1,921,006	0.6022	1.275	0.377	0.176
Decision Variables					**Objective Functions**			**Power Output (MW)**		
U_f	T_{SOFC}	S/C	p_{SOFC}	c_{fuel}	η_{ave}	C_{total}	η_{tot}	$\dot{W}_{SOFC}$	$\dot{W}_{GT}$	$\dot{W}_{ST}$
0.75	1000	2	8	0.3	0.6114	628,729	0.6408	1.300	0.288	0.184
0.8	1000	2	8	0.3	0.6209	617,809	0.6498	1.317	0.302	0.165
0.85	1000	2	8	0.3	0.6235	613,655	0.6525	1.330	0.316	0.144
0.9	1000	2	8	0.3	0.6131	620,864	0.6429	1.345	0.322	0.123
0.85	950	2	8	0.3	0.6076	607,252	0.6395	1.336	0.331	0.130
0.85	1000	2	8	0.3	0.6235	613,655	0.6525	1.330	0.316	0.144
0.85	1050	2	8	0.3	0.6198	632,468	0.6486	1.325	0.301	0.156
0.85	1100	2	8	0.3	0.6197	646,543	0.6479	1.319	0.277	0.168
0.85	1000	2	8	0.3	0.6235	613,655	0.6525	1.330	0.316	0.144
0.85	1000	2.5	8	0.3	0.6196	615,514	0.6491	1.337	0.323	0.138
0.85	1000	3	8	0.3	0.6118	621,084	0.6416	1.344	0.332	0.126
0.85	1000	3.5	8	0.3	0.6069	623,649	0.6369	1.352	0.340	0.116
0.85	1000	2	7	0.3	0.6141	616,829	0.6441	1.303	0.334	0.121
0.85	1000	2	8	0.3	0.6235	613,655	0.6525	1.330	0.316	0.144
0.85	1000	2	9	0.3	0.6089	623,556	0.6390	1.357	0.298	0.162
0.85	1000	2	10	0.3	0.5956	633,740	0.6253	1.381	0.279	0.179
0.85	1000	2	8	0.1	0.6235	343,312	0.6525	1.330	0.316	0.144
0.85	1000	2	8	0.3	0.6235	613,655	0.6525	1.330	0.316	0.144
0.85	1000	2	8	0.6	0.6235	1,018,236	0.6525	1.330	0.316	0.144
0.85	1000	2	8	0.9	0.6235	1,423,190	0.6525	1.330	0.316	0.144
0.85	1000	2	8	1.2	0.6235	1,828,144	0.6525	1.330	0.316	0.144

Table A.2. Parametric Results for the 1.5 MWe dual pressure ST hybrid system.

Decision Variables					Objective Functions			Power Output (MW)		
U_f	T_{SOFC}	S/C	p_{SOFC}	c_{fuel}	η_{ave}	C_{total}	η_{tot}	$\dot{W}_{SOFC}$	$\dot{W}_{GT}$	$\dot{W}_{ST}$
0.75	1000	2	8	0.3	0.5653	602,988	0.5974	1.237	0.389	0.196
0.8	1000	2	8	0.3	0.5697	659,829	0.6023	1.255	0.412	0.178
0.85	1000	2	8	0.3	0.5705	602,033	0.6031	1.275	0.432	0.159
0.9	1000	2	8	0.3	0.5491	623,244	0.5814	1.298	0.455	0.137
0.85	950	2	8	0.3	0.552	613,127	0.5855	1.281	0.451	0.141
0.85	1000	2	8	0.3	0.5705	602,033	0.6031	1.275	0.432	0.159
0.85	1050	2	8	0.3	0.5738	613,833	0.6062	1.269	0.413	0.170
0.85	1100	2	8	0.3	0.5741	605,499	0.6055	1.262	0.393	0.182
0.85	1000	2	8	0.3	0.5705	602,033	0.6031	1.275	0.432	0.159
0.85	1000	2.5	8	0.3	0.5611	612,696	0.5940	1.282	0.451	0.142
0.85	1000	3	8	0.3	0.5558	617,062	0.5885	1.288	0.470	0.125
0.85	1000	3.5	8	0.3	0.5466	624,285	0.5798	1.293	0.485	0.111
0.85	1000	2	7	0.3	0.5632	611,603	0.5955	1.250	0.455	0.135
0.85	1000	2	8	0.3	0.5705	602,033	0.6031	1.275	0.432	0.159
0.85	1000	2	9	0.3	0.5612	614,401	0.5939	1.299	0.416	0.180
0.85	1000	2	10	0.3	0.5483	631,513	0.5808	1.320	0.391	0.198
0.85	1000	2	8	0.1	0.5705	311,935	0.6031	1.275	0.432	0.159
0.85	1000	2	8	0.3	0.5705	602,033	0.6031	1.275	0.432	0.159
0.85	1000	2	8	0.6	0.5705	1,037,173	0.6031	1.275	0.432	0.159
0.85	1000	2	8	0.9	0.5705	1,472,352	0.6031	1.275	0.432	0.159
0.85	1000	2	8	1.2	0.5705	1,907,471	0.6031	1.275	0.432	0.159
Decision Variables					Objective Functions			Power Output (MW)		
U_f	T_{SOFC}	S/C	p_{SOFC}	c_{fuel}	η_{ave}	C_{total}	η_{tot}	$\dot{W}_{SOFC}$	$\dot{W}_{GT}$	$\dot{W}_{ST}$
0.75	1000	2	8	0.3	0.6127	626,669	0.6417	1.301	0.288	0.182
0.8	1000	2	8	0.3	0.6218	615,571	0.6507	1.316	0.301	0.164
0.85	1000	2	8	0.3	0.6243	611,026	0.6533	1.330	0.316	0.143
0.9	1000	2	8	0.3	0.6142	618,338	0.6439	1.345	0.323	0.124
0.85	950	2	8	0.3	0.6082	604,028	0.6402	1.335	0.330	0.131
0.85	1000	2	8	0.3	0.6243	611,026	0.6533	1.330	0.316	0.143
0.85	1050	2	8	0.3	0.6207	627,515	0.6495	1.324	0.299	0.156
0.85	1100	2	8	0.3	0.6205	644,799	0.6489	1.318	0.284	0.169
0.85	1000	2	8	0.3	0.6243	611,026	0.6533	1.330	0.316	0.143
0.85	1000	2.5	8	0.3	0.6205	613,086	0.6500	1.336	0.325	0.137
0.85	1000	3	8	0.3	0.6126	618,079	0.6424	1.342	0.333	0.127
0.85	1000	3.5	8	0.3	0.6079	621,373	0.6378	1.349	0.341	0.115
0.85	1000	2	7	0.3	0.615	615,166	0.6451	1.302	0.333	0.122
0.85	1000	2	8	0.3	0.6243	611,026	0.6533	1.330	0.316	0.143
0.85	1000	2	9	0.3	0.6099	620,315	0.6400	1.356	0.299	0.161
0.85	1000	2	10	0.3	0.5965	632,383	0.6261	1.380	0.277	0.178
0.85	1000	2	8	0.1	0.6243	343,308	0.6533	1.330	0.316	0.143
0.85	1000	2	8	0.3	0.6243	611,026	0.6533	1.330	0.316	0.143
0.85	1000	2	8	0.6	0.6243	1,012,601	0.6533	1.330	0.316	0.143
0.85	1000	2	8	0.9	0.6243	1,414,176	0.6533	1.330	0.316	0.143
0.85	1000	2	8	1.2	0.6243	1,815,751	0.6533	1.330	0.316	0.143

Table A.3. Parametric Results for the 1.5 MWe triple pressure ST hybrid system.

Decision Variables					Objective Functions			Power Output (MW)		
U_f	T_{SOFC}	S/C	p_{SOFC}	c_{fuel}	η_{ave}	C_{total}	η_{tot}	$\dot{W}_{SOFC}$	$\dot{W}_{GT}$	$\dot{W}_{ST}$
0.75	1000	2	8	0.3	0.5653	602,988	0.5975	1.201	0.384	0.192
0.8	1000	2	8	0.3	0.5697	659,829	0.6026	1.219	0.403	0.171
0.85	1000	2	8	0.3	0.5712	599,321	0.6035	1.238	0.429	0.150
0.9	1000	2	8	0.3	0.5499	622,779	0.5817	1.256	0.448	0.131
0.85	950	2	8	0.3	0.5528	610,041	0.5858	1.244	0.443	0.135
0.85	1000	2	8	0.3	0.5712	599,321	0.6035	1.238	0.429	0.150
0.85	1050	2	8	0.3	0.5748	610,469	0.6066	1.232	0.416	0.164
0.85	1100	2	8	0.3	0.5749	602,600	0.6058	1.227	0.403	0.178
0.85	1000	2	8	0.3	0.5712	599,321	0.6035	1.238	0.429	0.150
0.85	1000	2.5	8	0.3	0.5621	609,303	0.5945	1.244	0.435	0.144
0.85	1000	3	8	0.3	0.5566	613,756	0.5888	1.251	0.442	0.137
0.85	1000	3.5	8	0.3	0.5477	622,065	0.5801	1.257	0.447	0.131
0.85	1000	2	7	0.3	0.5641	608,206	0.5957	1.214	0.450	0.124
0.85	1000	2	8	0.3	0.5712	599,321	0.6035	1.238	0.429	0.150
0.85	1000	2	9	0.3	0.562	612,264	0.5943	1.261	0.410	0.174
0.85	1000	2	10	0.3	0.5492	628,912	0.5811	1.286	0.388	0.198
0.85	1000	2	8	0.1	0.5712	311,701	0.6035	1.238	0.429	0.150
0.85	1000	2	8	0.3	0.5712	599,321	0.6035	1.238	0.429	0.150
0.85	1000	2	8	0.6	0.5712	1,030,749	0.6035	1.238	0.429	0.150
0.85	1000	2	8	0.9	0.5712	1,462,177	0.6035	1.238	0.429	0.150
0.85	1000	2	8	1.2	0.5712	1,893,605	0.6035	1.238	0.429	0.150
Decision Variables					Objective Functions			Power Output (MW)		
U_f	T_{SOFC}	S/C	p_{SOFC}	c_{fuel}	η_{ave}	C_{total}	η_{tot}	$\dot{W}_{SOFC}$	$\dot{W}_{GT}$	$\dot{W}_{ST}$
0.75	1000	2	8	0.3	0.6127	626,669	0.6419	1.287	0.305	0.172
0.8	1000	2	8	0.3	0.6218	615,571	0.6509	1.301	0.321	0.153
0.85	1000	2	8	0.3	0.6251	608,046	0.6536	1.314	0.337	0.135
0.9	1000	2	8	0.3	0.6114	615,291	0.6442	1.328	0.342	0.116
0.85	950	2	8	0.3	0.609	601,064	0.6405	1.319	0.351	0.121
0.85	1000	2	8	0.3	0.6251	608,046	0.6536	1.314	0.337	0.135
0.85	1050	2	8	0.3	0.6216	627,515	0.6498	1.308	0.321	0.146
0.85	1100	2	8	0.3	0.6215	641,301	0.6492	1.303	0.306	0.158
0.85	1000	2	8	0.3	0.6251	608,046	0.6536	1.314	0.337	0.135
0.85	1000	2.5	8	0.3	0.6213	609,466	0.6503	1.319	0.342	0.130
0.85	1000	3	8	0.3	0.6135	615,264	0.6427	1.325	0.357	0.123
0.85	1000	3.5	8	0.3	0.6088	619,433	0.6382	1.331	0.373	0.117
0.85	1000	2	7	0.3	0.616	612,599	0.6454	1.287	0.355	0.117
0.85	1000	2	8	0.3	0.6251	608,046	0.6536	1.314	0.337	0.135
0.85	1000	2	9	0.3	0.6107	617,815	0.6404	1.338	0.319	0.152
0.85	1000	2	10	0.3	0.5974	630,100	0.6264	1.361	0.304	0.170
0.85	1000	2	8	0.1	0.6251	342,825	0.6536	1.314	0.337	0.135
0.85	1000	2	8	0.3	0.6251	608,046	0.6536	1.314	0.337	0.135
0.85	1000	2	8	0.6	0.6251	1,005,877	0.6536	1.314	0.337	0.135
0.85	1000	2	8	0.9	0.6251	1,403,708	0.6536	1.314	0.337	0.135
0.85	1000	2	8	1.2	0.6251	1,801,539	0.6536	1.314	0.337	0.135

Table A.4. Parametric Results for the 1.5 MWe triple pressure w/RH ST hybrid system.

Decision Variables					Objective Functions			Power Output (MW)		
U_f	T_{SOFC}	S/C	p_{SOFC}	c_{fuel}	η_{ave}	C_{total}	η_{tot}	$\dot{W}_{SOFC}$	$\dot{W}_{GT}$	$\dot{W}_{ST}$
0.75	1000	2	8	0.3	0.5670	602188	0.5978	1.193	0.388	0.209
0.8	1000	2	8	0.3	0.5701	659229	0.6029	1.212	0.400	0.188
0.85	1000	2	8	0.3	0.5716	598691	0.6038	1.234	0.420	0.169
0.9	1000	2	8	0.3	0.5503	622679	0.5819	1.249	0.441	0.150
0.85	950	2	8	0.3	0.5532	609841	0.5861	1.240	0.406	0.155
0.85	1000	2	8	0.3	0.5716	598691	0.6038	1.234	0.420	0.169
0.85	1050	2	8	0.3	0.5752	610069	0.6069	1.227	0.435	0.183
0.85	1100	2	8	0.3	0.5753	602200	0.6062	1.221	0.452	0.196
0.85	1000	2	8	0.3	0.5716	598691	0.6038	1.234	0.420	0.169
0.85	1000	2.5	8	0.3	0.5625	609103	0.5947	1.240	0.427	0.163
0.85	1000	3	8	0.3	0.5570	613456	0.5891	1.247	0.433	0.156
0.85	1000	3.5	8	0.3	0.5481	621865	0.5804	1.254	0.441	0.150
0.85	1000	2	7	0.3	0.5646	608006	0.5959	1.210	0.439	0.145
0.85	1000	2	8	0.3	0.5716	598691	0.6038	1.234	0.420	0.169
0.85	1000	2	9	0.3	0.5624	612064	0.5947	1.253	0.401	0.188
0.85	1000	2	10	0.3	0.5495	628712	0.5814	1.275	0.382	0.209
0.85	1000	2	8	0.1	0.5716	311626	0.6038	1.234	0.420	0.169
0.85	1000	2	8	0.3	0.5716	598691	0.6038	1.234	0.420	0.169
0.85	1000	2	8	0.6	0.5716	1029289	0.6038	1.234	0.420	0.169
0.85	1000	2	8	0.9	0.5716	1459887	0.6038	1.234	0.420	0.169
0.85	1000	2	8	1.2	0.5716	1890485	0.6038	1.234	0.420	0.169
Decision Variables					Objective Functions			Power Output (MW)		
U_f	T_{SOFC}	S/C	p_{SOFC}	c_{fuel}	η_{ave}	C_{total}	η_{tot}	$\dot{W}_{SOFC}$	$\dot{W}_{GT}$	$\dot{W}_{ST}$
0.75	1000	2	8	0.3	0.6133	626169	0.6422	1.272	0.303	0.189
0.8	1000	2	8	0.3	0.6221	615171	0.6512	1.286	0.317	0.170
0.85	1000	2	8	0.3	0.6255	607446	0.6539	1.300	0.333	0.150
0.9	1000	2	8	0.3	0.6118	615079	0.6445	1.316	0.341	0.132
0.85	950	2	8	0.3	0.6096	600734	0.6409	1.305	0.347	0.134
0.85	1000	2	8	0.3	0.6255	607446	0.6539	1.300	0.333	0.150
0.85	1050	2	8	0.3	0.6220	627215	0.6502	1.294	0.317	0.164
0.85	1100	2	8	0.3	0.6219	640901	0.6496	1.288	0.302	0.178
0.85	1000	2	8	0.3	0.6255	607446	0.6539	1.300	0.333	0.150
0.85	1000	2.5	8	0.3	0.6217	609266	0.6506	1.308	0.342	0.142
0.85	1000	3	8	0.3	0.6138	615264	0.6429	1.315	0.351	0.134
0.85	1000	3.5	8	0.3	0.6090	619133	0.6385	1.322	0.360	0.127
0.85	1000	2	7	0.3	0.6163	612399	0.6458	1.277	0.352	0.132
0.85	1000	2	8	0.3	0.6255	607446	0.6539	1.300	0.333	0.150
0.85	1000	2	9	0.3	0.6111	617615	0.6407	1.328	0.314	0.167
0.85	1000	2	10	0.3	0.5978	629910	0.6268	1.351	0.288	0.182
0.85	1000	2	8	0.1	0.6255	342759	0.6539	1.300	0.333	0.150
0.85	1000	2	8	0.3	0.6255	607446	0.6539	1.300	0.333	0.150
0.85	1000	2	8	0.6	0.6255	1004477	0.6539	1.300	0.333	0.150
0.85	1000	2	8	0.9	0.6255	1401508	0.6539	1.300	0.333	0.150
0.85	1000	2	8	1.2	0.6255	1798539	0.6539	1.300	0.333	0.150

Table A.5. Parametric Results for the 5 MWe single pressure ST hybrid system.

Decision Variables					Objective Functions			Power Output (MW)		
U_f	T_{SOFC}	S/C	p_{SOFC}	c_{fuel}	η_{ave}	C_{total}	η_{tot}	$\dot{W}_{SOFC}$	$\dot{W}_{GT}$	$\dot{W}_{ST}$
0.75	1000	2	8	0.3	0.5740	1,893,880	0.6089	3.912	1.110	0.754
0.8	1000	2	8	0.3	0.5730	1,999,249	0.6082	4.004	1.197	0.698
0.85	1000	2	8	0.3	0.5791	1,887,264	0.6131	4.116	1.268	0.657
0.9	1000	2	8	0.3	0.5630	1,929,901	0.5989	4.223	1.354	0.607
0.85	950	2	8	0.3	0.5606	1,914,234	0.5957	4.197	1.304	0.631
0.85	1000	2	8	0.3	0.5791	1,887,264	0.6131	4.116	1.268	0.657
0.85	1050	2	8	0.3	0.5775	1,927,378	0.6115	4.072	1.210	0.683
0.85	1100	2	8	0.3	0.5795	1,925,591	0.6136	4.014	1.154	0.714
0.85	1000	2	8	0.3	0.5791	1,887,264	0.6131	4.116	1.268	0.657
0.85	1000	2.5	8	0.3	0.5792	1,895,774	0.6133	4.209	1.304	0.621
0.85	1000	3	8	0.3	0.5788	1,905,463	0.6127	4.297	1.357	0.587
0.85	1000	3.5	8	0.3	0.5706	1,911,057	0.6066	4.384	1.389	0.548
0.85	1000	2	7	0.3	0.5783	1,888,776	0.6123	4.024	1.217	0.624
0.85	1000	2	8	0.3	0.5791	1,887,264	0.6131	4.116	1.268	0.657
0.85	1000	2	9	0.3	0.5706	1,913,559	0.6065	4.198	1.324	0.689
0.85	1000	2	10	0.3	0.5688	1,928,034	0.6024	4.247	1.387	0.725
0.85	1000	2	8	0.1	0.5791	928,843	0.6131	4.116	1.268	0.657
0.85	1000	2	8	0.3	0.5791	1,887,264	0.6131	4.116	1.268	0.657
0.85	1000	2	8	0.6	0.5791	3,323,434	0.6131	4.116	1.268	0.657
0.85	1000	2	8	0.9	0.5791	4,760,189	0.6131	4.116	1.268	0.657
0.85	1000	2	8	1.2	0.5791	6,196,943	0.6131	4.116	1.268	0.657
Decision Variables					**Objective Functions**			**Power Output (MW)**		
U_f	T_{SOFC}	S/C	p_{SOFC}	c_{fuel}	η_{ave}	C_{total}	η_{tot}	$\dot{W}_{SOFC}$	$\dot{W}_{GT}$	$\dot{W}_{ST}$
0.75	1000	2	8	0.3	0.6191	1,954,495	0.6502	4.195	1.106	0.598
0.8	1000	2	8	0.3	0.6200	1,950,471	0.6511	4.287	1.142	0.522
0.85	1000	2	8	0.3	0.6264	1,935,053	0.6573	4.333	1.181	0.477
0.9	1000	2	8	0.3	0.6180	1,950,877	0.6493	4.394	1.243	0.419
0.85	950	2	8	0.3	0.6166	1,907,155	0.6484	4.402	1.243	0.404
0.85	1000	2	8	0.3	0.6264	1,935,053	0.6573	4.333	1.181	0.477
0.85	1050	2	8	0.3	0.6236	1,994,555	0.6541	4.257	1.114	0.554
0.85	1100	2	8	0.3	0.6248	2,045,001	0.6554	4.198	1.038	0.609
0.85	1000	2	8	0.3	0.6264	1,935,053	0.6573	4.333	1.181	0.477
0.85	1000	2.5	8	0.3	0.6263	1,958,251	0.6571	4.457	1.228	0.401
0.85	1000	3	8	0.3	0.6248	1,983,657	0.6553	4.526	1.297	0.324
0.85	1000	3.5	8	0.3	0.6237	2,005,625	0.6540	4.613	1.345	0.258
0.85	1000	2	7	0.3	0.6208	1,942,335	0.6520	4.284	1.247	0.429
0.85	1000	2	8	0.3	0.6264	1,935,053	0.6573	4.333	1.181	0.477
0.85	1000	2	9	0.3	0.6168	1,961,780	0.6487	4.396	1.108	0.547
0.85	1000	2	10	0.3	0.6150	1,975,454	0.6471	4.452	1.029	0.586
0.85	1000	2	8	0.1	0.6264	1,041,292	0.6573	4.333	1.181	0.477
0.85	1000	2	8	0.3	0.6264	1,935,053	0.6573	4.333	1.181	0.477
0.85	1000	2	8	0.6	0.6264	3,274,590	0.6573	4.333	1.181	0.477
0.85	1000	2	8	0.9	0.6264	4,614,569	0.6573	4.333	1.181	0.477
0.85	1000	2	8	1.2	0.6264	5,954,549	0.6573	4.333	1.181	0.477

Table A.6. Parametric Results for the 5 MWe dual pressure ST hybrid system.

Decision Variables					Objective Functions			Power Output (MW)		
U_f	T_{SOFC}	S/C	p_{SOFC}	c_{fuel}	η_{ave}	C_{total}	η_{tot}	$\dot{W}_{SOFC}$	$\dot{W}_{GT}$	$\dot{W}_{ST}$
0.75	1000	2	8	0.3	0.5740	1,893,880	0.6113	3.826	1.311	0.648
0.8	1000	2	8	0.3	0.5738	1,994,249	0.6110	3.985	1.367	0.603
0.85	1000	2	8	0.3	0.5808	1,872,891	0.6149	4.069	1.422	0.556
0.9	1000	2	8	0.3	0.5636	1,926,901	0.6006	4.127	1.485	0.504
0.85	950	2	8	0.3	0.5614	1,909,234	0.5987	4.107	1.504	0.504
0.85	1000	2	8	0.3	0.5808	1,872,891	0.6149	4.069	1.422	0.556
0.85	1050	2	8	0.3	0.5782	1,924,378	0.6142	4.017	1.347	0.614
0.85	1100	2	8	0.3	0.5803	1,923,591	0.6145	3.978	1.289	0.658
0.85	1000	2	8	0.3	0.5808	1,872,891	0.6149	4.069	1.422	0.556
0.85	1000	2.5	8	0.3	0.5800	1,899,774	0.6141	4.114	1.489	0.514
0.85	1000	3	8	0.3	0.5795	1,902,463	0.6135	4.207	1.547	0.471
0.85	1000	3.5	8	0.3	0.5712	1,909,057	0.6082	4.286	1.602	0.413
0.85	1000	2	7	0.3	0.5791	1,884,776	0.6129	3.987	1.459	0.527
0.85	1000	2	8	0.3	0.5808	1,872,891	0.6149	4.069	1.422	0.556
0.85	1000	2	9	0.3	0.5715	1,910,559	0.6084	4.109	1.388	0.584
0.85	1000	2	10	0.3	0.5697	1,924,034	0.6068	4.175	1.356	0.610
0.85	1000	2	8	0.1	0.5808	931,580	0.6149	4.069	1.422	0.556
0.85	1000	2	8	0.3	0.5808	1,872,891	0.6149	4.069	1.422	0.556
0.85	1000	2	8	0.6	0.5808	3,284,857	0.6149	4.069	1.422	0.556
0.85	1000	2	8	0.9	0.5808	4,696,823	0.6149	4.069	1.422	0.556
0.85	1000	2	8	1.2	0.5808	6,108,789	0.6149	4.069	1.422	0.556
Decision Variables					**Objective Functions**			**Power Output (MW)**		
U_f	T_{SOFC}	S/C	p_{SOFC}	c_{fuel}	η_{ave}	C_{total}	η_{tot}	$\dot{W}_{SOFC}$	$\dot{W}_{GT}$	$\dot{W}_{ST}$
0.75	1000	2	8	0.3	0.6191	1,954,495	0.6502	4.247	1.102	0.602
0.8	1000	2	8	0.3	0.6200	1,947,471	0.6511	4.286	1.134	0.537
0.85	1000	2	8	0.3	0.6279	1,920,649	0.6589	4.325	1.169	0.490
0.9	1000	2	8	0.3	0.6185	1,947,877	0.6496	4.389	1.197	0.412
0.85	950	2	8	0.3	0.6172	1,903,155	0.6481	4.398	1.214	0.408
0.85	1000	2	8	0.3	0.6279	1,920,649	0.6589	4.325	1.169	0.490
0.85	1050	2	8	0.3	0.6243	1,991,555	0.6552	4.284	1.127	0.574
0.85	1100	2	8	0.3	0.6257	2,042,001	0.6562	4.216	1.068	0.634
0.85	1000	2	8	0.3	0.6279	1,920,649	0.6589	4.325	1.169	0.490
0.85	1000	2.5	8	0.3	0.6269	1,955,251	0.6578	4.457	1.224	0.414
0.85	1000	3	8	0.3	0.6256	1,981,657	0.6559	4.524	1.297	0.357
0.85	1000	3.5	8	0.3	0.6246	2,003,625	0.6551	4.603	1.358	0.306
0.85	1000	2	7	0.3	0.6216	1,940,335	0.6527	4.298	1.227	0.407
0.85	1000	2	8	0.3	0.6279	1,920,649	0.6589	4.325	1.169	0.490
0.85	1000	2	9	0.3	0.6175	1,957,780	0.6483	4.422	1.116	0.556
0.85	1000	2	10	0.3	0.6158	1,971,454	0.6464	4.508	1.062	0.598
0.85	1000	2	8	0.1	0.6279	1,043,304	0.6589	4.325	1.169	0.490
0.85	1000	2	8	0.3	0.6279	1,920,649	0.6589	4.325	1.169	0.490
0.85	1000	2	8	0.6	0.6279	3,236,666	0.6589	4.325	1.169	0.490
0.85	1000	2	8	0.9	0.6279	4,552,683	0.6589	4.325	1.169	0.490
0.85	1000	2	8	1.2	0.6279	5,868,700	0.6589	4.325	1.169	0.490

Table A.7. Parametric Results for the 5 MWe triple pressure ST hybrid system.

Decision Variables					Objective Functions			Power Output (MW)		
U_f	T_{SOFC}	S/C	p_{SOFC}	c_{fuel}	η_{ave}	C_{total}	η_{tot}	$\dot{W}_{SOFC}$	$\dot{W}_{GT}$	$\dot{W}_{ST}$
0.75	1000	2	8	0.3	0.5740	1,893,880	0.6095	3.978	1.385	0.659
0.8	1000	2	8	0.3	0.5744	1,985,249	0.6101	4.014	1.402	0.603
0.85	1000	2	8	0.3	0.5814	1,871,891	0.6155	4.054	1.439	0.556
0.9	1000	2	8	0.3	0.5642	1,923,901	0.5990	4.098	1.458	0.504
0.85	950	2	8	0.3	0.5650	1,907,234	0.5998	4.127	1.498	0.521
0.85	1000	2	8	0.3	0.5814	1,871,891	0.6155	4.054	1.439	0.556
0.85	1050	2	8	0.3	0.5787	1,923,378	0.6132	3.997	1.387	0.587
0.85	1100	2	8	0.3	0.5809	1,921,591	0.6149	3.924	1.324	0.608
0.85	1000	2	8	0.3	0.5814	1,871,891	0.6155	4.054	1.439	0.556
0.85	1000	2.5	8	0.3	0.5806	1,896,774	0.6142	4.107	1.497	0.524
0.85	1000	3	8	0.3	0.5802	1,902,463	0.6137	4.147	1.558	0.487
0.85	1000	3.5	8	0.3	0.5719	1,908,057	0.6055	4.189	1.596	0.432
0.85	1000	2	7	0.3	0.5795	1,884,776	0.6133	4.007	1.496	0.504
0.85	1000	2	8	0.3	0.5814	1,871,891	0.6155	4.054	1.439	0.556
0.85	1000	2	9	0.3	0.5722	1,907,559	0.6076	4.107	1.384	0.601
0.85	1000	2	10	0.3	0.5703	1,922,034	0.6050	4.158	1.335	0.642
0.85	1000	2	8	0.1	0.5814	934,580	0.6155	4.054	1.439	0.556
0.85	1000	2	8	0.3	0.5814	1,871,891	0.6155	4.054	1.439	0.556
0.85	1000	2	8	0.6	0.5814	3,277,857	0.6155	4.054	1.439	0.556
0.85	1000	2	8	0.9	0.5814	4,683,823	0.6155	4.054	1.439	0.556
0.85	1000	2	8	1.2	0.5814	6,089,789	0.6155	4.054	1.439	0.556
Decision Variables					Objective Functions			Power Output (MW)		
U_f	T_{SOFC}	S/C	p_{SOFC}	c_{fuel}	η_{ave}	C_{total}	η_{tot}	$\dot{W}_{SOFC}$	$\dot{W}_{GT}$	$\dot{W}_{ST}$
0.75	1000	2	8	0.3	0.6191	1,954,495	0.6503	1.196	1.083	0.557
0.8	1000	2	8	0.3	0.6207	1,946,471	0.6515	4.247	1.124	0.524
0.85	1000	2	8	0.3	0.6286	1,924,649	0.6596	4.317	1.166	0.499
0.9	1000	2	8	0.3	0.6220	1,944,877	0.6523	4.368	1.209	0.476
0.85	950	2	8	0.3	0.6178	1,903,155	0.6490	4.384	1.198	0.457
0.85	1000	2	8	0.3	0.6286	1,924,649	0.6596	4.317	1.166	0.499
0.85	1050	2	8	0.3	0.6248	1,996,555	0.6497	4.259	1.137	0.526
0.85	1100	2	8	0.3	0.6263	2,039,001	0.6519	4.217	1.105	0.552
0.85	1000	2	8	0.3	0.6286	1,924,649	0.6596	4.317	1.166	0.499
0.85	1000	2.5	8	0.3	0.6275	1,958,251	0.6588	4.368	1.198	0.454
0.85	1000	3	8	0.3	0.6265	1,979,657	0.6575	4.415	1.224	0.429
0.85	1000	3.5	8	0.3	0.6251	2,001,625	0.6562	4.458	1.251	0.383
0.85	1000	2	7	0.3	0.6222	1,945,335	0.6534	4.268	1.189	0.458
0.85	1000	2	8	0.3	0.6286	1,924,649	0.6596	4.317	1.166	0.499
0.85	1000	2	9	0.3	0.6181	1,955,780	0.6490	4.387	1.137	0.534
0.85	1000	2	10	0.3	0.6163	1,977,454	0.6477	4.425	1.103	0.582
0.85	1000	2	8	0.1	0.6286	1,051,304	0.6596	4.317	1.166	0.499
0.85	1000	2	8	0.3	0.6286	1,924,649	0.6596	4.317	1.166	0.499
0.85	1000	2	8	0.6	0.6286	3,234,666	0.6596	4.317	1.166	0.499
0.85	1000	2	8	0.9	0.6286	4,544,683	0.6596	4.317	1.166	0.499
0.85	1000	2	8	1.2	0.6286	5,854,700	0.6596	4.317	1.166	0.499

Table A.8. Parametric Results for the 5 MWe triple pressure w/ RH ST hybrid system.

Decision Variables					Objective Functions			Power Output (MW)		
U_f	T_{SOFC}	S/C	p_{SOFC}	c_{fuel}	η_{ave}	C_{total}	η_{tot}	$\dot{W}_{SOFC}$	$\dot{W}_{GT}$	$\dot{W}_{ST}$
0.75	1000	2	8	0.3	0.5743	1,891,880	0.6091	3.986	1.258	0.574
0.8	1000	2	8	0.3	0.5748	1,983,249	0.6099	3.994	1.307	0.612
0.85	1000	2	8	0.3	0.5817	1,869,891	0.6159	4.037	1.346	0.653
0.9	1000	2	8	0.3	0.5642	1,921,896	0.5992	4.095	1.393	0.691
0.85	950	2	8	0.3	0.5653	1,905,231	0.6006	4.086	1.385	0.614
0.85	1000	2	8	0.3	0.5817	1,869,891	0.6159	4.037	1.346	0.653
0.85	1050	2	8	0.3	0.5791	1,921,375	0.6140	3.987	1.303	0.688
0.85	1100	2	8	0.3	0.5812	1,920,590	0.6152	3.925	1.264	0.715
0.85	1000	2	8	0.3	0.5817	1,869,891	0.6159	4.037	1.346	0.653
0.85	1000	2.5	8	0.3	0.5810	1,894,770	0.6148	4.096	1.387	0.614
0.85	1000	3	8	0.3	0.5807	1,900,463	0.6145	4.128	1.426	0.587
0.85	1000	3.5	8	0.3	0.5723	1,903,059	0.6074	4.156	1.453	0.526
0.85	1000	2	7	0.3	0.5802	1,883,776	0.6147	3.985	1.399	0.615
0.85	1000	2	8	0.3	0.5817	1,869,891	0.6159	4.037	1.346	0.653
0.85	1000	2	9	0.3	0.5727	1,906,561	0.6168	4.096	1.302	0.674
0.85	1000	2	10	0.3	0.5707	1,922,031	0.6149	4.145	1.268	0.692
0.85	1000	2	8	0.1	0.5814	933,580	0.6159	4.037	1.346	0.653
0.85	1000	2	8	0.3	0.5817	1,869,891	0.6159	4.037	1.346	0.653
0.85	1000	2	8	0.6	0.5814	3,271,857	0.6159	4.037	1.346	0.653
0.85	1000	2	8	0.9	0.5814	4,674,823	0.6159	4.037	1.346	0.653
0.85	1000	2	8	1.2	0.5814	6,077,789	0.6159	4.037	1.346	0.653
Decision Variables					Objective Functions			Power Output (MW)		
U_f	T_{SOFC}	S/C	p_{SOFC}	c_{fuel}	η_{ave}	C_{total}	η_{tot}	$\dot{W}_{SOFC}$	$\dot{W}_{GT}$	$\dot{W}_{ST}$
0.75	1000	2	8	0.3	0.6195	1,952,495	0.6498	4.186	4.058	0.614
0.8	1000	2	8	0.3	0.6210	1,944,471	0.6511	4.214	1.104	0.586
0.85	1000	2	8	0.3	0.6289	1,923,649	0.6601	4.281	1.141	0.555
0.9	1000	2	8	0.3	0.6220	1,942,874	0.6522	4.324	4.198	0.517
0.85	950	2	8	0.3	0.6181	1,901,152	0.6492	4.299	1.168	0.521
0.85	1000	2	8	0.3	0.6289	1,923,649	0.6601	4.281	1.141	0.555
0.85	1050	2	8	0.3	0.6253	1,994,552	0.6577	4.268	1.107	0.589
0.85	1100	2	8	0.3	0.6267	2,037,999	0.6589	4.204	1.057	0.618
0.85	1000	2	8	0.3	0.6289	1,923,649	0.6601	4.281	1.141	0.555
0.85	1000	2.5	8	0.3	0.6279	1,956,250	0.6590	4.357	1.189	0.507
0.85	1000	3	8	0.3	0.6272	1,978,653	0.6583	4.399	1.227	0.476
0.85	1000	3.5	8	0.3	0.6254	2,001,623	0.6560	4.446	1.278	0.431
0.85	1000	2	7	0.3	0.6229	1,943,335	0.6533	4.204	1.197	0.527
0.85	1000	2	8	0.3	0.6289	1,923,649	0.6601	4.281	1.141	0.555
0.85	1000	2	9	0.3	0.6187	1,955,785	0.6508	4.359	1.102	0.580
0.85	1000	2	10	0.3	0.6167	1,976,457	0.6485	4.385	1.067	0.607
0.85	1000	2	8	0.1	0.6289	1,050,304	0.6601	4.281	1.141	0.555
0.85	1000	2	8	0.3	0.6289	1,923,649	0.6601	4.281	1.141	0.555
0.85	1000	2	8	0.6	0.6289	3,228,666	0.6601	4.281	1.141	0.555
0.85	1000	2	8	0.9	0.6289	4,535,683	0.6601	4.281	1.141	0.555
0.85	1000	2	8	1.2	0.6289	5,842,700	0.6601	4.281	1.141	0.555

Table A.9. Parametric Results for the 10 MWe single pressure ST hybrid system.

Decision Variables					Objective Functions			Power Output (MW)		
U_f	T_{SOFC}	S/C	p_{SOFC}	c_{fuel}	η_{ave}	C_{total}	η_{tot}	$\dot{W}_{SOFC}$	$\dot{W}_{GT}$	$\dot{W}_{ST}$
0.75	1000	2	8	0.3	0.5853	3,714,737	0.6201	7.885	2.387	1.427
0.8	1000	2	8	0.3	0.5842	3,855,263	0.6196	7.927	2.434	1.386
0.85	1000	2	8	0.3	0.5876	3,630,071	0.6222	7.999	2.499	1.345
0.9	1000	2	8	0.3	0.5677	3,732,025	0.6034	8.084	2.557	1.302
0.85	950	2	8	0.3	0.5655	3,694,959	0.6013	8.044	2.547	1.307
0.85	1000	2	8	0.3	0.5876	3,630,071	0.6222	7.999	2.499	1.345
0.85	1050	2	8	0.3	0.5951	3,662,019	0.6345	7.935	2.441	1.386
0.85	1100	2	8	0.3	0.6021	3,724,544	0.6389	7.887	2.402	1.422
0.85	1000	2	8	0.3	0.5876	3,630,071	0.6222	7.999	2.499	1.345
0.85	1000	2.5	8	0.3	0.5810	3,656,267	0.6164	8.057	2.558	1.302
0.85	1000	3	8	0.3	0.5796	3,664,915	0.6151	8.096	2.603	1.267
0.85	1000	3.5	8	0.3	0.5708	3,716,876	0.6059	8.136	2.644	1.229
0.85	1000	2	7	0.3	0.5837	3,651,623	0.6190	7.951	2.451	1.305
0.85	1000	2	8	0.3	0.5876	3,630,071	0.6222	7.999	2.499	1.345
0.85	1000	2	9	0.3	0.5863	3,646,582	0.6213	8.076	2.548	1.379
0.85	1000	2	10	0.3	0.5843	3,663,124	0.6194	8.128	2.586	1.401
0.85	1000	2	8	0.1	0.5876	1,742,412	0.6222	7.999	2.499	1.345
0.85	1000	2	8	0.3	0.5876	3,630,071	0.6222	7.999	2.499	1.345
0.85	1000	2	8	0.6	0.5876	6,460,926	0.6222	7.999	2.499	1.345
0.85	1000	2	8	0.9	0.5876	9,292,034	0.6222	7.999	2.499	1.345
0.85	1000	2	8	1.2	0.5876	12,123,143	0.6222	7.999	2.499	1.345
Decision Variables					**Objective Functions**			**Power Output (MW)**		
U_f	T_{SOFC}	S/C	p_{SOFC}	c_{fuel}	η_{ave}	C_{total}	η_{tot}	$\dot{W}_{SOFC}$	$\dot{W}_{GT}$	$\dot{W}_{ST}$
0.75	1000	2	8	0.3	0.6287	3,805,294	0.6589	8.344	2.304	0.925
0.8	1000	2	8	0.3	0.6355	3,760,705	0.6647	8.409	2.348	0.898
0.85	1000	2	8	0.3	0.6473	3,717,621	0.6766	8.495	2.376	0.876
0.9	1000	2	8	0.3	0.6297	3,780,486	0.6598	8.554	2.408	0.855
0.85	950	2	8	0.3	0.6437	3,629,057	0.6708	8.544	2.410	0.845
0.85	1000	2	8	0.3	0.6473	3,717,621	0.6766	8.495	2.376	0.876
0.85	1050	2	8	0.3	0.6401	3,833,153	0.6666	8.462	2.327	0.896
0.85	1100	2	8	0.3	0.6376	3,951,396	0.6574	8.425	2.279	0.922
0.85	1000	2	8	0.3	0.6473	3,717,621	0.6766	8.495	2.376	0.876
0.85	1000	2.5	8	0.3	0.6421	3,742,498	0.6692	8.541	2.418	0.854
0.85	1000	3	8	0.3	0.6347	3,767,409	0.6634	8.586	2.445	0.832
0.85	1000	3.5	8	0.3	0.6330	3,780,776	0.6621	8.623	2.480	0.811
0.85	1000	2	7	0.3	0.6354	3,847,806	0.6644	8.441	2.417	0.849
0.85	1000	2	8	0.3	0.6473	3,717,621	0.6766	8.495	2.376	0.876
0.85	1000	2	9	0.3	0.6336	3,865,958	0.6628	8.543	2.341	0.850
0.85	1000	2	10	0.3	0.6309	3,887,602	0.6594	8.589	2.308	0.833
0.85	1000	2	8	0.1	0.6473	1,981,637	0.6766	8.495	2.376	0.876
0.85	1000	2	8	0.3	0.6473	3,717,621	0.6766	8.495	2.376	0.876
0.85	1000	2	8	0.6	0.6473	6,321,298	0.6766	8.495	2.376	0.876
0.85	1000	2	8	0.9	0.6473	8,925,095	0.6766	8.495	2.376	0.876
0.85	1000	2	8	1.2	0.6473	11,528,891	0.6766	8.495	2.376	0.876

Table A.10. Parametric Results for the 10 MWe dual pressure ST hybrid system.

Decision Variables					Objective Functions			Power Output (MW)		
U_f	T_{SOFC}	S/C	p_{SOFC}	c_{fuel}	η_{ave}	C_{total}	η_{tot}	$\dot{W}_{SOFC}$	$\dot{W}_{GT}$	$\dot{W}_{ST}$
0.75	1000	2	8	0.3	0.5857	3,712,736	0.6188	7.845	2.657	1.287
0.8	1000	2	8	0.3	0.5847	3,855,263	0.6179	7.887	2.721	1.223
0.85	1000	2	8	0.3	0.5880	3,630,067	0.6228	7.929	2.772	1.154
0.9	1000	2	8	0.3	0.5681	3,740,025	0.6022	7.958	2.839	1.089
0.85	950	2	8	0.3	0.5658	3,692,959	0.5994	7.960	2.821	1.101
0.85	1000	2	8	0.3	0.5880	3,630,067	0.6228	7.929	2.772	1.154
0.85	1050	2	8	0.3	0.5954	3,660,019	0.6287	7.884	2.722	1.202
0.85	1100	2	8	0.3	0.6025	3,698,544	0.6344	7.825	2.693	1.247
0.85	1000	2	8	0.3	0.5880	3,630,067	0.6228	7.929	2.772	1.154
0.85	1000	2.5	8	0.3	0.5818	3,654,267	0.6143	7.958	2.814	1.099
0.85	1000	3	8	0.3	0.5803	3,637,915	0.6129	7.998	2.855	1.048
0.85	1000	3.5	8	0.3	0.5713	3,688,876	0.6045	8.041	2.896	1.008
0.85	1000	2	7	0.3	0.5845	3,635,623	0.6179	7.886	2.714	1.100
0.85	1000	2	8	0.3	0.5880	3,630,067	0.6228	7.929	2.772	1.154
0.85	1000	2	9	0.3	0.5866	3,634,582	0.6212	7.988	2.824	1.207
0.85	1000	2	10	0.3	0.5846	3,652,121	0.6193	8.046	2.880	1.244
0.85	1000	2	8	0.1	0.5880	1,750,496	0.6228	7.929	2.772	1.154
0.85	1000	2	8	0.3	0.5880	3,630,067	0.6228	7.929	2.772	1.154
0.85	1000	2	8	0.6	0.5880	6,449,426	0.6228	7.929	2.772	1.154
0.85	1000	2	8	0.9	0.5880	9,268,784	0.6228	7.929	2.772	1.154
0.85	1000	2	8	1.2	0.5880	12,088,142	0.6228	7.929	2.772	1.154
Decision Variables					Objective Functions			Power Output (MW)		
U_f	T_{SOFC}	S/C	p_{SOFC}	c_{fuel}	η_{ave}	C_{total}	η_{tot}	$\dot{W}_{SOFC}$	$\dot{W}_{GT}$	$\dot{W}_{ST}$
0.75	1000	2	8	0.3	0.6291	3,803,304	0.6601	8.354	2.189	1.096
0.8	1000	2	8	0.3	0.6360	3,757,705	0.6670	8.409	2.243	1.031
0.85	1000	2	8	0.3	0.6478	3,717,624	0.6772	8.485	2.290	0.965
0.9	1000	2	8	0.3	0.6301	3,777,486	0.6612	8.536	2.341	0.908
0.85	950	2	8	0.3	0.6440	3,626,057	0.6744	8.521	2.354	0.921
0.85	1000	2	8	0.3	0.6478	3,717,624	0.6772	8.485	2.290	0.965
0.85	1050	2	8	0.3	0.6406	3,831,153	0.6702	8.432	2.233	0.996
0.85	1100	2	8	0.3	0.6380	3,925,396	0.6677	8.391	2.188	1.045
0.85	1000	2	8	0.3	0.6478	3,717,624	0.6772	8.485	2.290	0.965
0.85	1000	2.5	8	0.3	0.6427	3,739,498	0.6714	8.541	2.354	0.911
0.85	1000	3	8	0.3	0.6351	3,741,409	0.6658	8.589	2.402	0.857
0.85	1000	3.5	8	0.3	0.6334	3,774,776	0.6645	8.645	2.441	0.813
0.85	1000	2	7	0.3	0.6362	3,823,806	0.6664	8.422	2.233	0.922
0.85	1000	2	8	0.3	0.6478	3,717,624	0.6772	8.485	2.290	0.965
0.85	1000	2	9	0.3	0.6339	3,841,958	0.6647	8.536	2.344	0.998
0.85	1000	2	10	0.3	0.6311	3,873,599	0.6624	8.590	2.396	1.032
0.85	1000	2	8	0.1	0.6478	1,989,678	0.6772	8.485	2.290	0.965
0.85	1000	2	8	0.3	0.6478	3,717,624	0.6772	8.485	2.290	0.965
0.85	1000	2	8	0.6	0.6478	6,309,543	0.6772	8.485	2.290	0.965
0.85	1000	2	8	0.9	0.6478	8,901,462	0.6772	8.485	2.290	0.965
0.85	1000	2	8	1.2	0.6478	11,493,381	0.6772	8.485	2.290	0.965

Table A.11. Parametric Results for the 10 MWe triple pressure ST hybrid system.

Decision Variables					Objective Functions			Power Output (MW)		
U_f	T_{SOFC}	S/C	p_{SOFC}	c_{fuel}	η_{ave}	C_{total}	η_{tot}	$\dot{W}_{SOFC}$	$\dot{W}_{GT}$	$\dot{W}_{ST}$
0.75	1000	2	8	0.3	0.5863	3847803	0.6212	7.786	2.685	1.059
0.8	1000	2	8	0.3	0.5851	3853263	0.6199	7.841	2.728	1.106
0.85	1000	2	8	0.3	0.5884	3640067	0.6234	7.905	2.781	1.162
0.9	1000	2	8	0.3	0.5685	3739024	0.6039	7.955	2.847	1.202
0.85	950	2	8	0.3	0.5664	3690959	0.6017	7.960	2.844	1.100
0.85	1000	2	8	0.3	0.5884	3640067	0.6234	7.905	2.781	1.162
0.85	1050	2	8	0.3	0.5956	3660019	0.6297	7.856	2.726	1.203
0.85	1100	2	8	0.3	0.6032	3694544	0.6344	7.814	2.669	1.246
0.85	1000	2	8	0.3	0.5884	3640067	0.6234	7.905	2.781	1.162
0.85	1000	2.5	8	0.3	0.5821	3654267	0.6170	7.952	2.832	1.108
0.85	1000	3	8	0.3	0.5809	3644915	0.6154	7.999	2.879	1.057
0.85	1000	3.5	8	0.3	0.5715	3688876	0.6073	8.041	2.932	1.003
0.85	1000	3	7	0.3	0.5847	3645623	0.6197	7.856	2.714	1.110
0.85	1000	3	8	0.3	0.5884	3640067	0.6234	7.905	2.781	1.162
0.85	1000	3	9	0.3	0.5869	3642583	0.6215	7.954	2.832	1.206
0.85	1000	3	10	0.3	0.5851	3649121	0.6203	8.003	2.888	1.245
0.85	1000	3	8	0.1	0.5884	1745829	0.6234	7.905	2.781	1.162
0.85	1000	3	8	0.3	0.5884	3640067	0.6234	7.905	2.781	1.162
0.85	1000	3	8	0.6	0.5884	6421424	0.6234	7.905	2.781	1.162
0.85	1000	3	8	0.9	0.5884	9226781	0.6234	7.905	2.781	1.162
0.85	1000	3	8	1.2	0.5884	12044138	0.6234	7.905	2.781	1.162
Decision Variables					Objective Functions			Power Output (MW)		
U_f	T_{SOFC}	S/C	p_{SOFC}	c_{fuel}	η_{ave}	C_{total}	η_{tot}	$\dot{W}_{SOFC}$	$\dot{W}_{GT}$	$\dot{W}_{ST}$
0.75	1000	2	8	0.3	0.6297	3801306	0.6588	8.388	2.178	1.058
0.8	1000	2	8	0.3	0.6366	3755705	0.6659	8.417	2.224	1.011
0.85	1000	2	8	0.3	0.6480	3715624	0.6774	8.474	2.272	0.979
0.9	1000	2	8	0.3	0.6303	3780486	0.6601	8.523	2.317	0.922
0.85	950	2	8	0.3	0.6446	3625057	0.6741	8.516	2.316	0.923
0.85	1000	2	8	0.3	0.6480	3715624	0.6774	8.474	2.272	0.979
0.85	1050	2	8	0.3	0.6408	3834151	0.6703	8.426	2.225	1.020
0.85	1100	2	8	0.3	0.6386	3926396	0.6678	8.387	2.179	1.068
0.85	1000	2	8	0.3	0.6480	3715624	0.6774	8.474	2.272	0.979
0.85	1000	2.5	8	0.3	0.6432	3737498	0.6731	8.526	2.319	1.032
0.85	1000	3	8	0.3	0.6355	3747409	0.6642	8.580	2.348	1.088
0.85	1000	3.5	8	0.3	0.6336	3774776	0.6621	8.624	2.392	1.134
0.85	1000	2	7	0.3	0.6366	3823806	0.6657	8.419	2.226	0.928
0.85	1000	2	8	0.3	0.6480	3715624	0.6774	8.474	2.272	0.979
0.85	1000	2	9	0.3	0.6346	3840958	0.6636	8.516	2.313	1.021
0.85	1000	2	10	0.3	0.6316	3871599	0.6603	8.553	2.360	1.068
0.85	1000	2	8	0.1	0.6480	1985012	0.6774	8.474	2.272	0.979
0.85	1000	2	8	0.3	0.6480	3715624	0.6774	8.474	2.272	0.979
0.85	1000	2	8	0.6	0.6480	6281543	0.6774	8.474	2.272	0.979
0.85	1000	2	8	0.9	0.6480	8859462	0.6774	8.474	2.272	0.979
0.85	1000	2	8	1.2	0.6480	11449381	0.6774	8.474	2.272	0.979

Table A.12. Parametric Results for the 10 MWe triple pressure w/ RH ST hybrid system.

Decision Variables					Objective Functions			Power Output (MW)		
U_f	T_{SOFC}	S/C	p_{SOFC}	c_{fuel}	η_{ave}	C_{total}	η_{tot}	$\dot{W}_{SOFC}$	$\dot{W}_{GT}$	$\dot{W}_{ST}$
0.75	1000	2	8	0.3	0.5864	3,846,790	0.6240	7.863	2.308	1.337
0.8	1000	2	8	0.3	0.5852	3,852,258	0.6213	7.902	2.356	1.398
0.85	1000	2	8	0.3	0.5889	3,637,267	0.6242	7.958	2.400	1.454
0.9	1000	2	8	0.3	0.5685	3,741,024	0.6039	8.001	2.447	1.510
0.85	950	2	8	0.3	0.5665	3,690,959	0.6030	7.999	2.439	1.407
0.85	1000	2	8	0.3	0.5889	3,637,267	0.6242	7.958	2.400	1.454
0.85	1050	2	8	0.3	0.5960	3,660,018	0.6300	7.902	2.358	1.506
0.85	1100	2	8	0.3	0.6032	3,692,544	0.6368	7.856	2.310	1.548
0.85	1000	2	8	0.3	0.5889	3,637,267	0.6242	7.958	2.400	1.454
0.85	1000	2.5	8	0.3	0.5822	3,653,267	0.6178	8.006	2.447	1.405
0.85	1000	3	8	0.3	0.5810	3,644,914	0.6166	8.059	2.489	1.360
0.85	1000	3.5	8	0.3	0.5716	3,689,910	0.6079	8.102	2.537	1.307
0.85	1000	2	7	0.3	0.5848	3,645,623	0.6192	7.906	2.354	1.403
0.85	1000	2	8	0.3	0.5889	3,637,267	0.6242	7.958	2.400	1.454
0.85	1000	2	9	0.3	0.5869	3,641,883	0.6214	8.001	2.441	1.498
0.85	1000	2	10	0.3	0.5852	3,648,621	0.6197	8.054	2.496	1.543
0.85	1000	2	8	0.1	0.5889	1,744,829	0.6242	7.958	2.400	1.454
0.85	1000	2	8	0.3	0.5889	3,637,267	0.6242	7.958	2.400	1.454
0.85	1000	2	8	0.6	0.5889	6,415,426	0.6242	7.958	2.400	1.454
0.85	1000	2	8	0.9	0.5889	9,217,784	0.6242	7.958	2.400	1.454
0.85	1000	2	8	1.2	0.5889	12,032,142	0.6242	7.958	2.400	1.454
Decision Variables					**Objective Functions**			**Power Output (MW)**		
U_f	T_{SOFC}	S/C	p_{SOFC}	c_{fuel}	η_{ave}	C_{total}	η_{tot}	$\dot{W}_{SOFC}$	$\dot{W}_{GT}$	$\dot{W}_{ST}$
0.75	1000	2	8	0.3	0.6298	3,798,306	0.6616	8.303	2.154	1.187
0.8	1000	2	8	0.3	0.6367	3,756,709	0.6659	8.347	2.203	1.126
0.85	1000	2	8	0.3	0.6529	3,697,652	0.6836	8.391	2.254	1.079
0.9	1000	2	8	0.3	0.6304	3,781,486	0.6605	8.442	2.304	1.005
0.85	950	2	8	0.3	0.6447	3,625,057	0.6741	8.440	2.997	1.007
0.85	1000	2	8	0.3	0.6529	3,697,652	0.6836	8.391	2.254	1.079
0.85	1050	2	8	0.3	0.6412	3,834,151	0.6707	8.344	2.201	1.130
0.85	1100	2	8	0.3	0.6386	3,926,399	0.6677	8.301	2.149	1.189
0.85	1000	2	8	0.3	0.6529	3,697,652	0.6836	8.391	2.254	1.079
0.85	1000	2.5	8	0.3	0.6433	3,737,498	0.6722	8.442	2.305	1.011
0.85	1000	3	8	0.3	0.6357	3,748,615	0.6657	8.496	2.347	0.952
0.85	1000	3.5	8	0.3	0.6337	3,774,777	0.6641	8.534	2.396	0.894
0.85	1000	2	7	0.3	0.6368	3,823,306	0.6658	8.346	2.203	1.008
0.85	1000	2	8	0.3	0.6529	3,697,652	0.6836	8.391	2.254	1.079
0.85	1000	2	9	0.3	0.6348	3,840,558	0.6644	8.435	2.301	1.136
0.85	1000	2	10	0.3	0.6316	3,871,101	0.6610	8.493	2.348	1.189
0.85	1000	2	8	0.1	0.6529	1,985,021	0.6836	8.391	2.254	1.079
0.85	1000	2	8	0.3	0.6529	3,697,652	0.6836	8.391	2.254	1.079
0.85	1000	2	8	0.6	0.6529	6,281,601	0.6836	8.391	2.254	1.079
0.85	1000	2	8	0.9	0.6529	8,859,549	0.6836	8.391	2.254	1.079
0.85	1000	2	8	1.2	0.6529	11,449,497	0.6836	8.391	2.254	1.079

Appendix B

In this appendix, the results showing the work outputs/inputs, part and full load performance, and costs for all twelve configurations are given. These same results for the 10 MWe hybrid system with a triple-pressure reheat steam turbine cycle appear and are discussed in Section 4.2.3 of Chapter 4. The figures below include the optimal work rate distributions (Figures B.1 to B.12), the optimal partial-load performances (Figures B.13 to B.24), the optimal component costs (Figures B.25 to B.36), and the optimal annual costs (Figures B.37 to B.48).

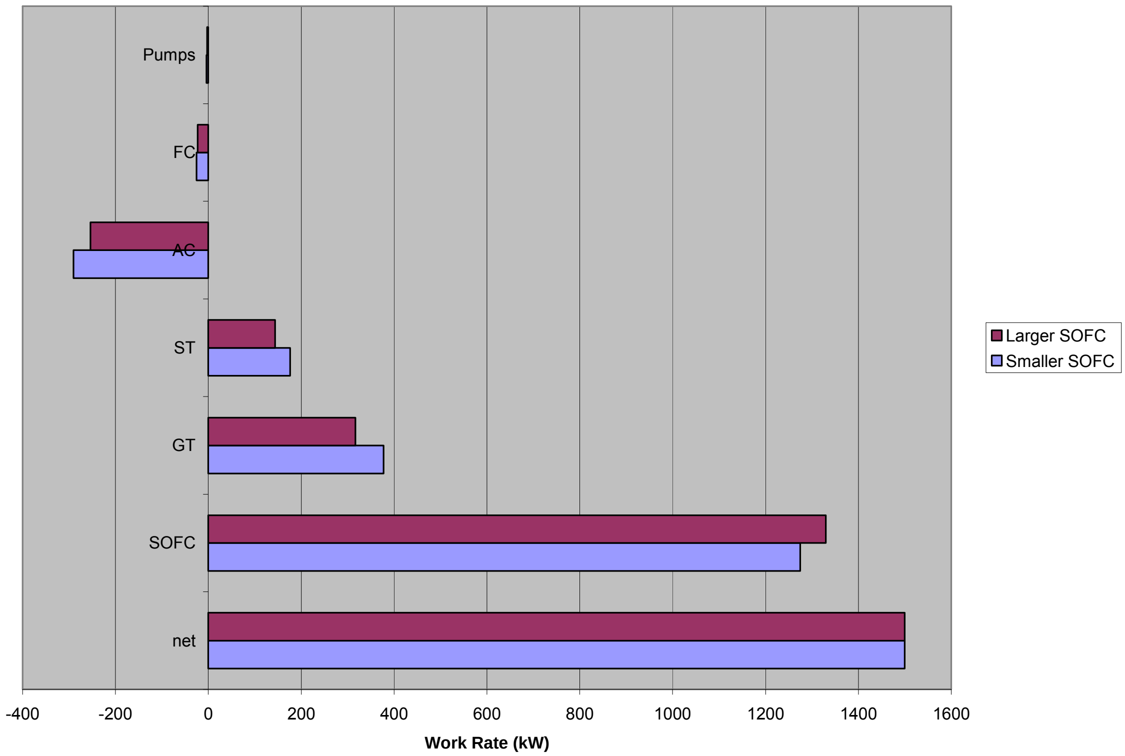

Figure B.1. Optimal work rate distribution for the 1.5 MWe SOFC-GT-ST with single pressure ST cycle.

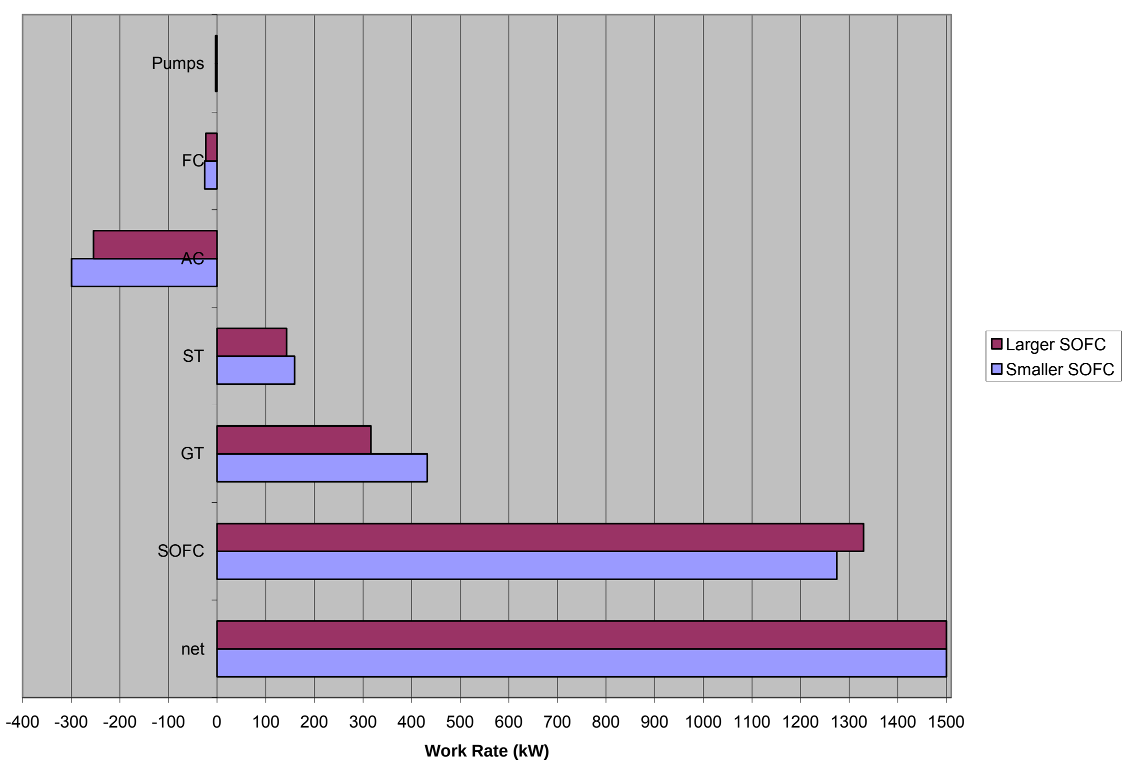

Figure B.2. Optimal work rate distribution for the 1.5 MWe SOFC-GT-ST with dual pressure ST cycle.

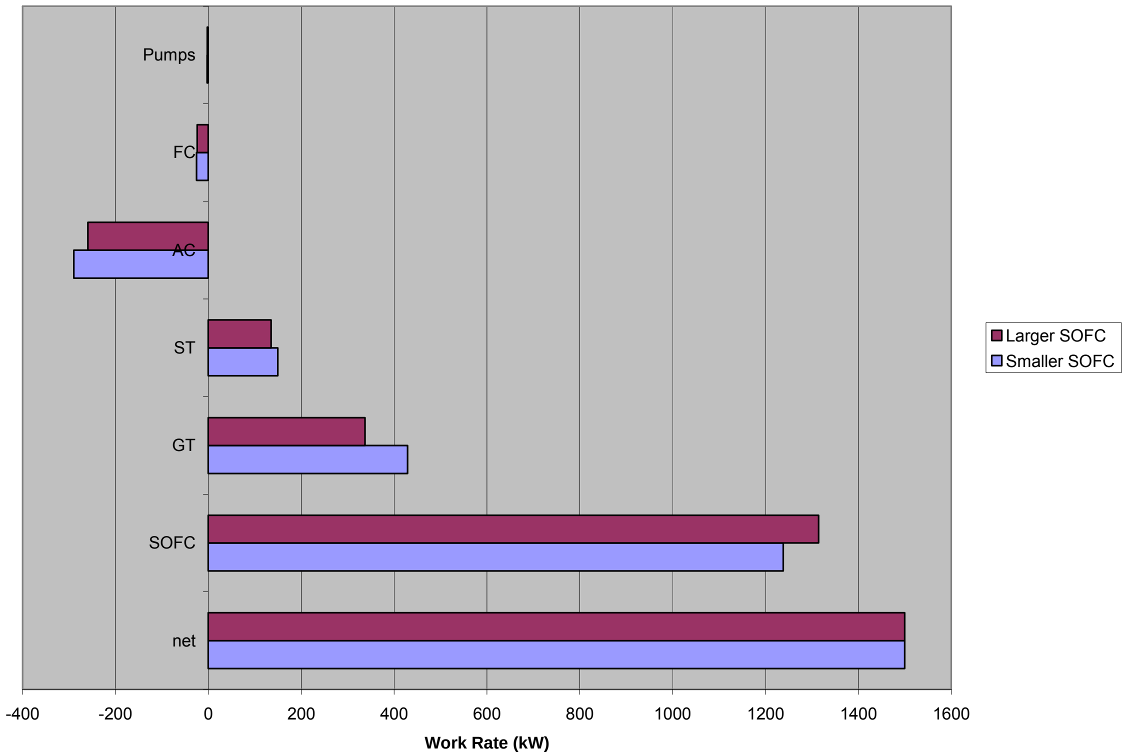

Figure B.3. Optimal work rate distribution for the 1.5 MWe SOFC-GT-ST with triple pressure ST cycle.

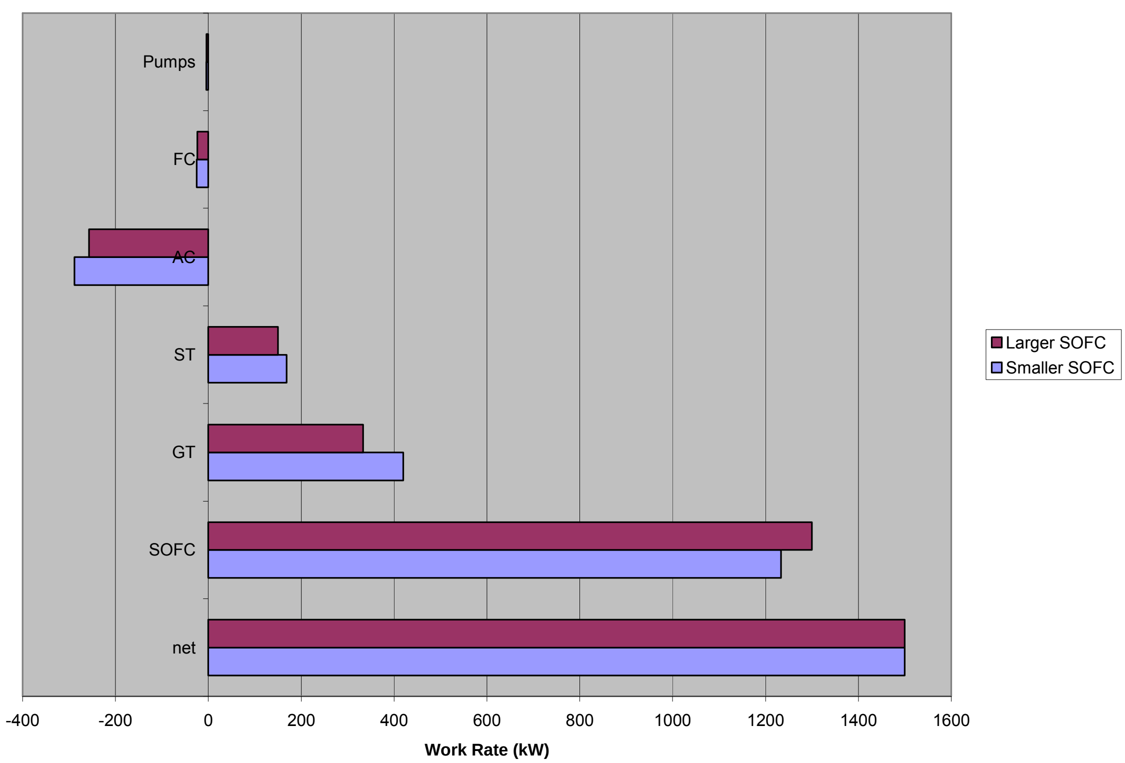

Figure B.4. Optimal work rate distribution for the 1.5 MWe SOFC-GT-ST with triple pressure with reheat ST cycle.

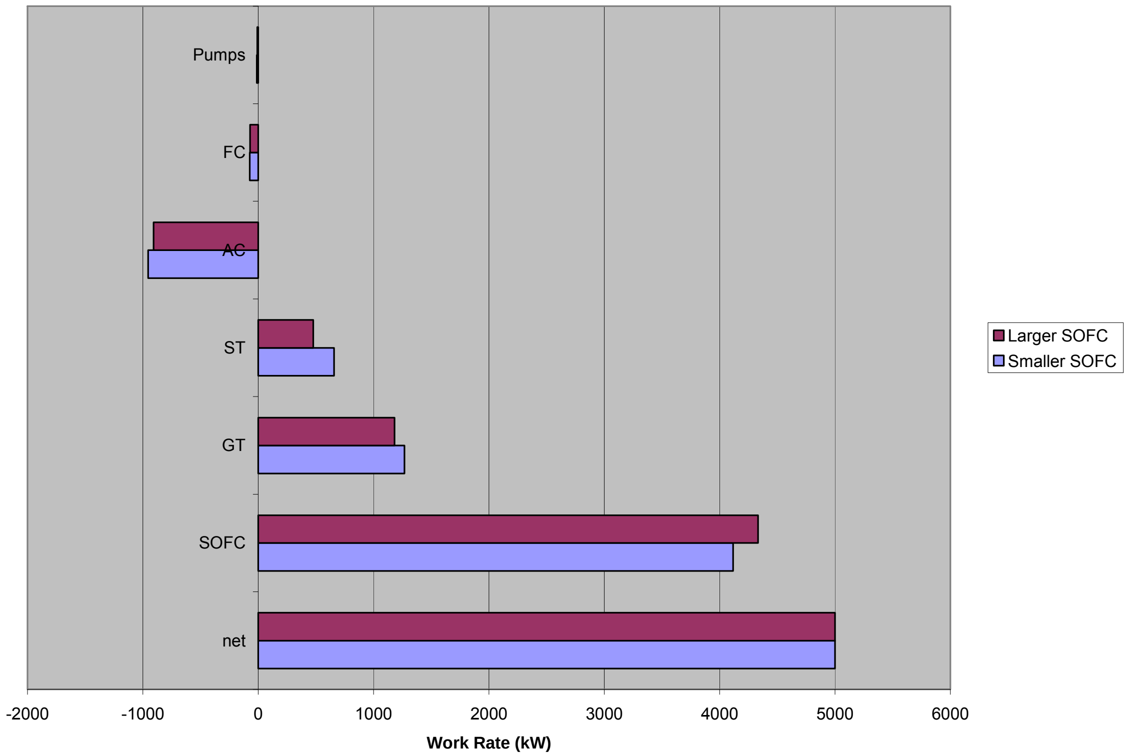

Figure B.5. Optimal work rate distribution for the 5 MWe SOFC-GT-ST with single pressure ST cycle.

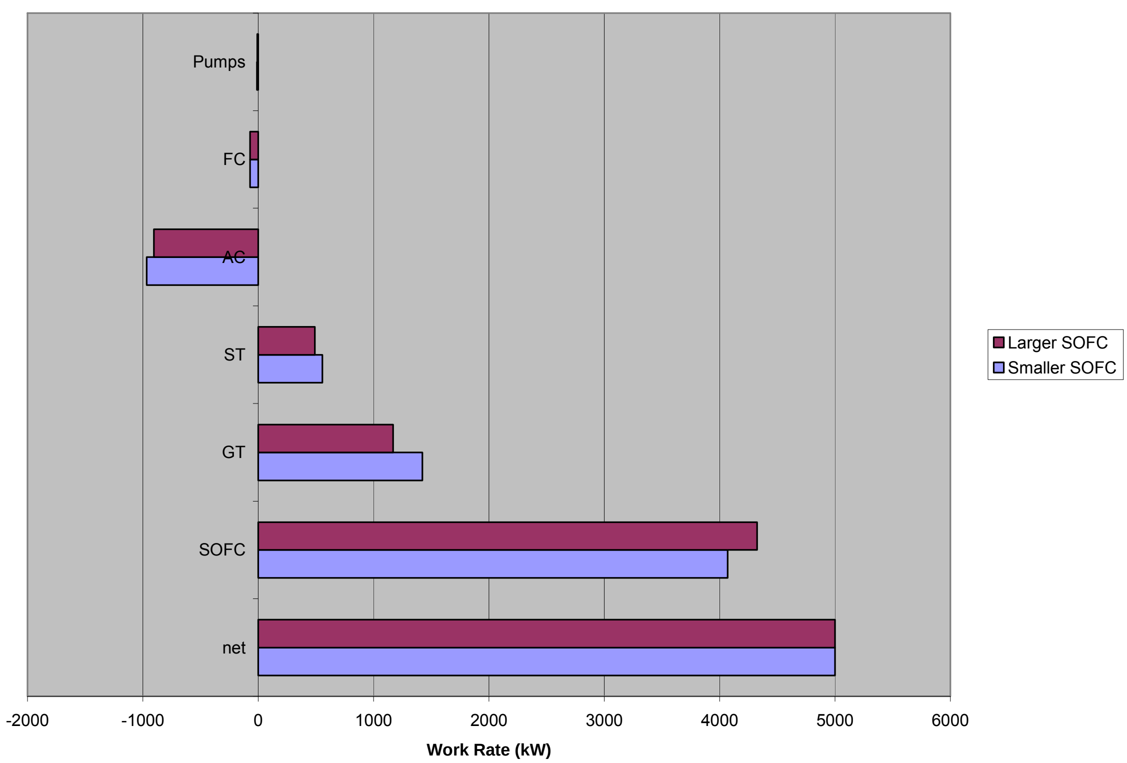

Figure B.6. Optimal work rate distribution for the 5 MWe SOFC-GT-ST with dual pressure ST cycle.

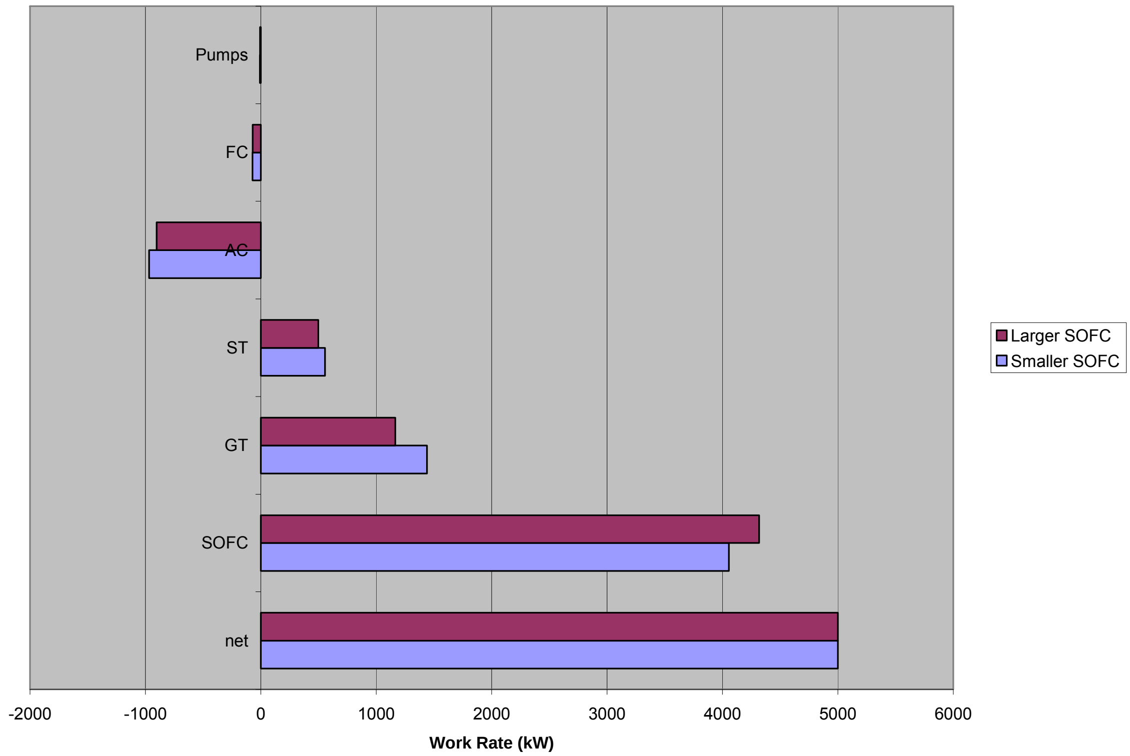

Figure B.7. Optimal work rate distribution for the 5 MWe SOFC-GT-ST with triple pressure ST cycle.

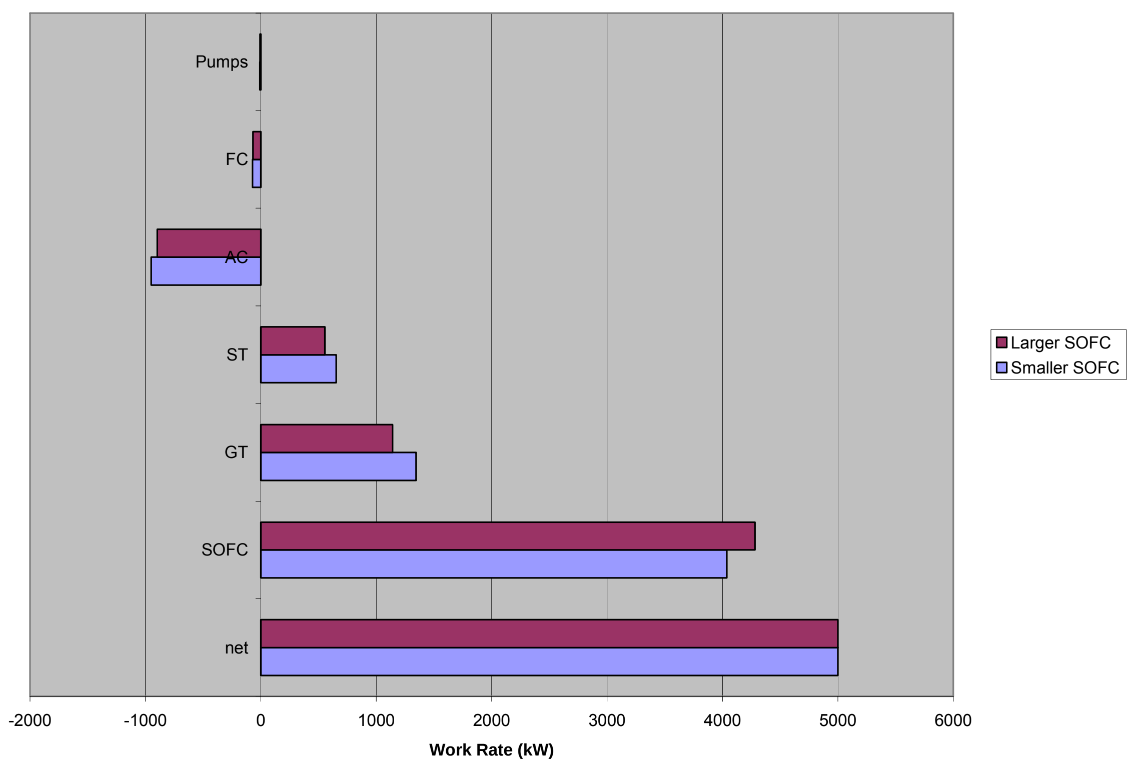

Figure B.8. Optimal work rate distribution for the 5 MWe SOFC-GT-ST with triple pressure with reheat ST cycle.

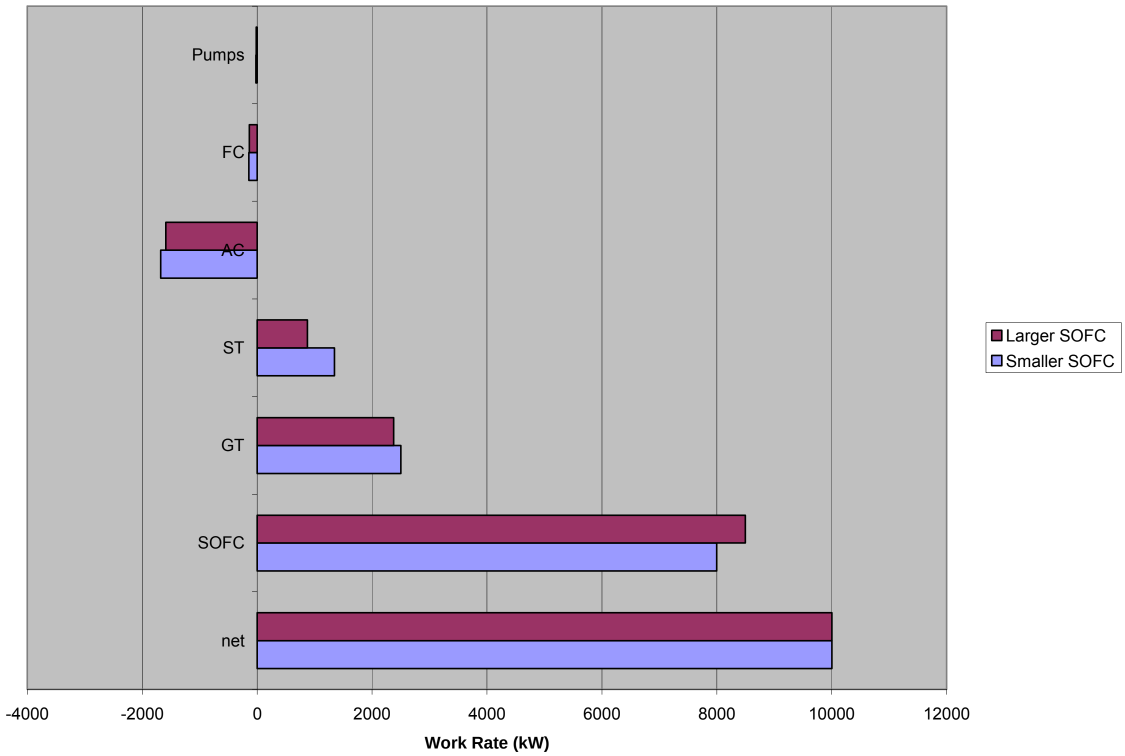

Figure B.9. Optimal work rate distribution for the 10 MWe SOFC-GT-ST with single pressure ST cycle.

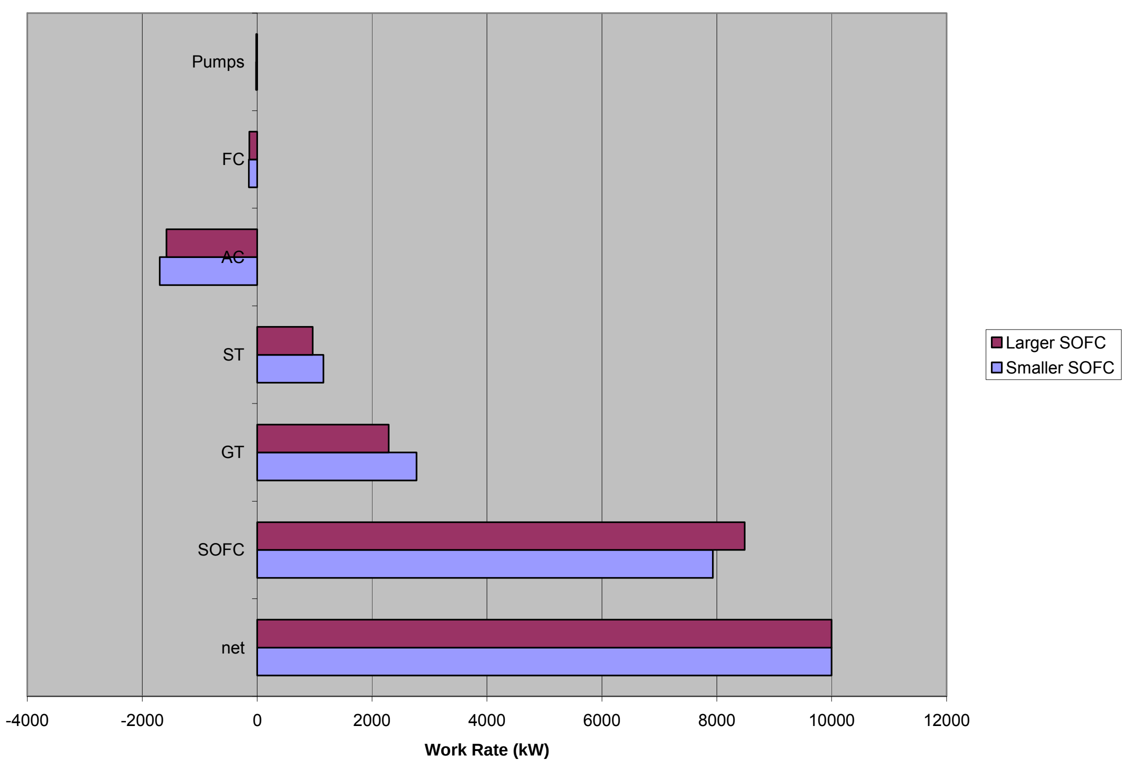

Figure B.10. Optimal work rate distribution for the 10 MWe SOFC-GT-ST with dual pressure ST cycle.

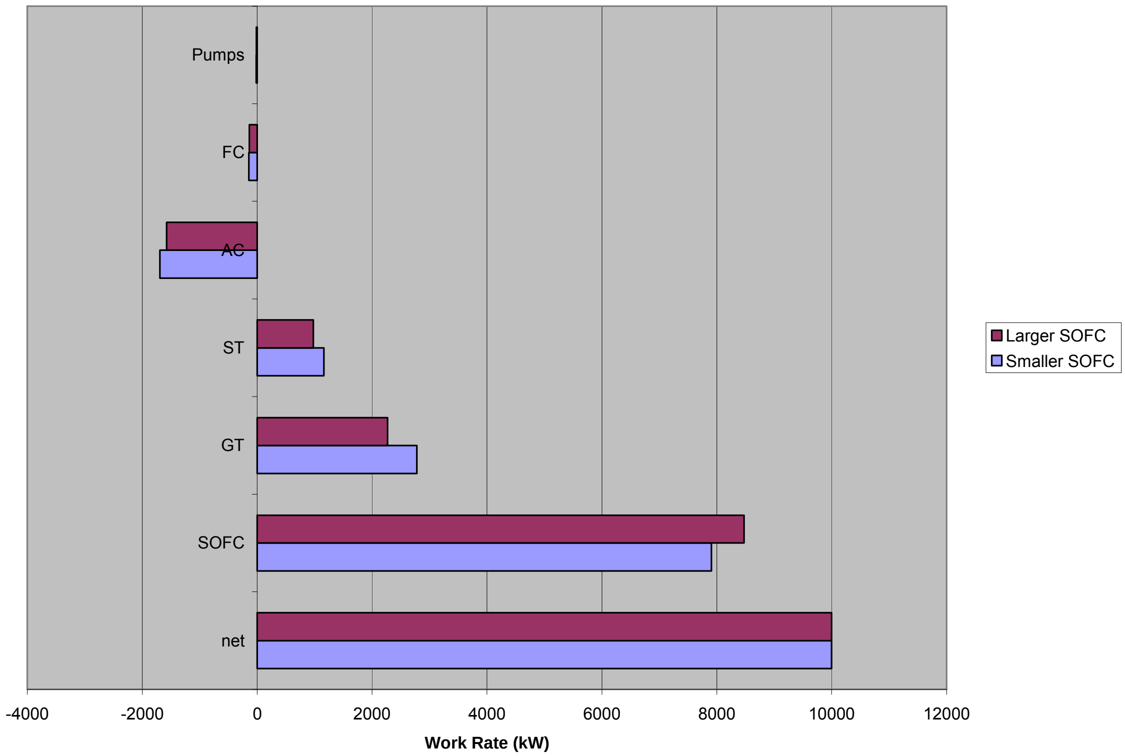

Figure B.11. Optimal work rate distribution for the 10 MWe SOFC-GT-ST with triple pressure ST cycle.

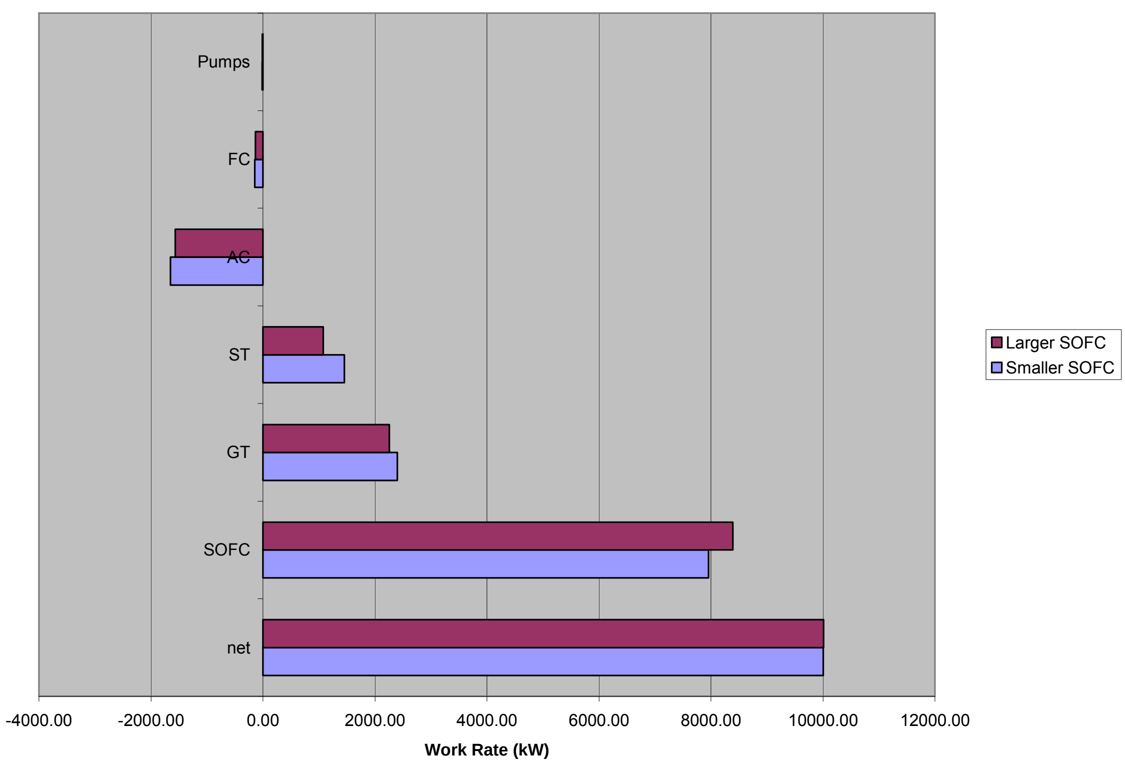

Figure B.12. Optimal work rate distribution for the 10 MWe SOFC-GT-ST with triple pressure with reheat ST cycle.

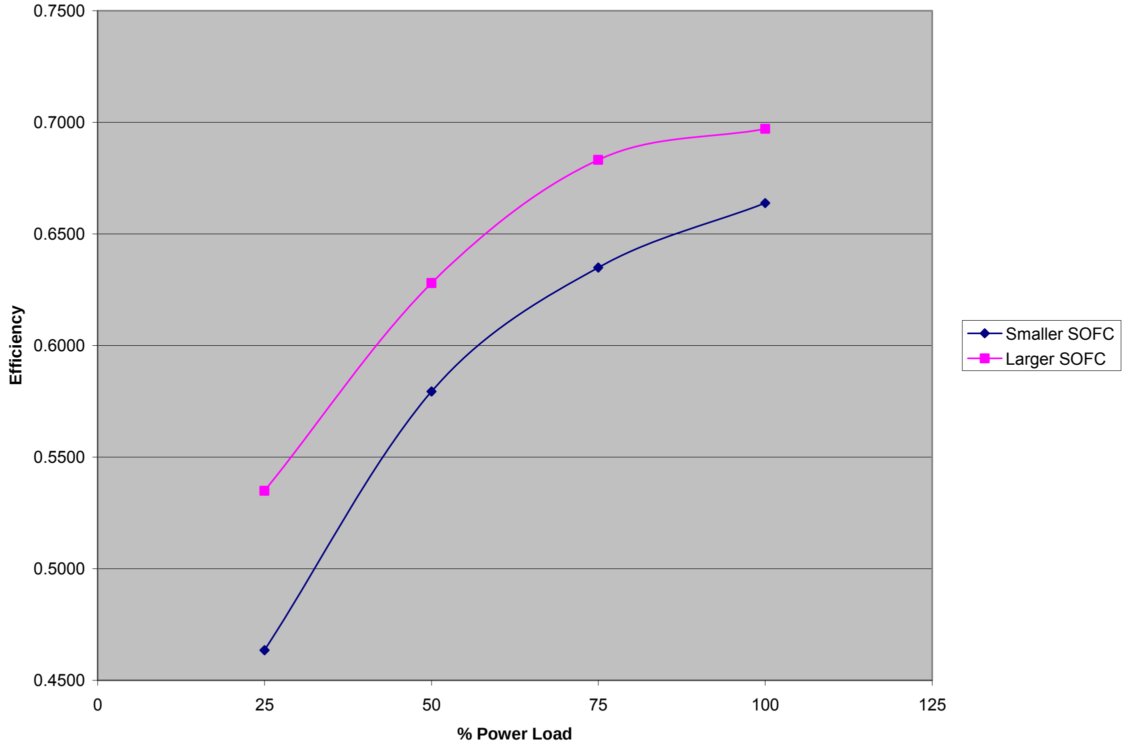

Figure B.13. Partial-load performance of the optimal 1.5 MWe SOFC-GT-ST hybrid plant, with a single ST cycle.

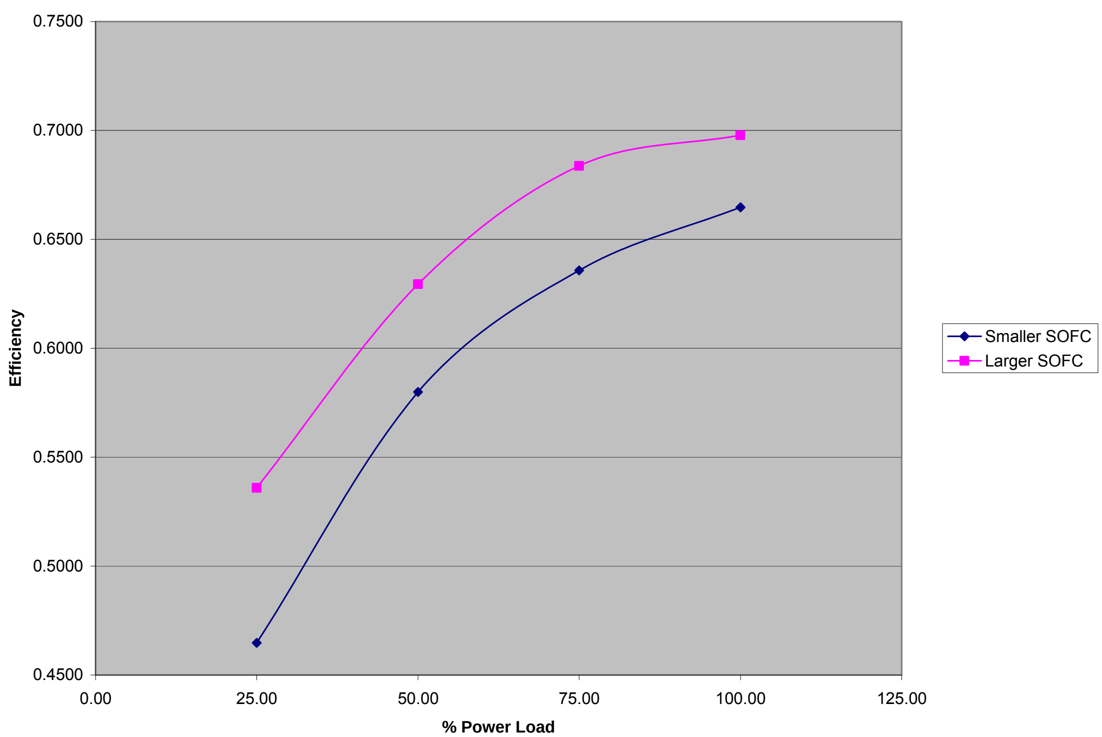

Figure B.14. Partial-load performance of the optimal 1.5 MWe SOFC-GT-ST hybrid plant, with a dual ST cycle.

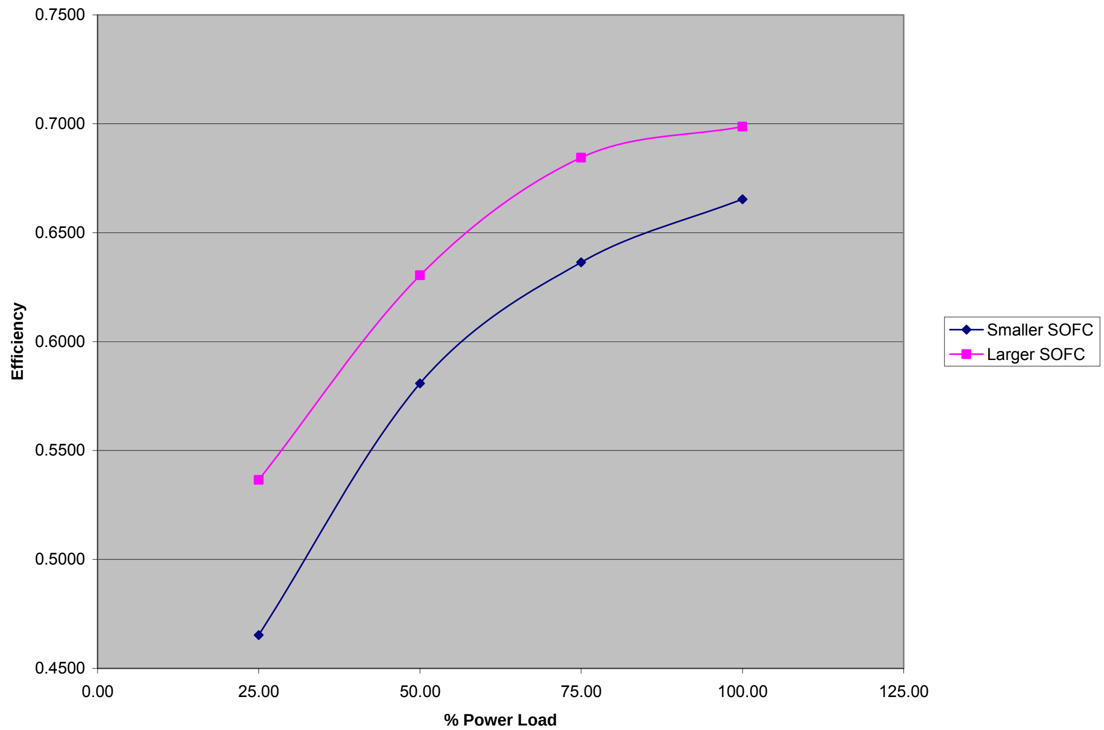

Figure B.15. Partial-load performance of the optimal 1.5 MWe SOFC-GT-ST hybrid plant, with a triple pressure ST cycle.

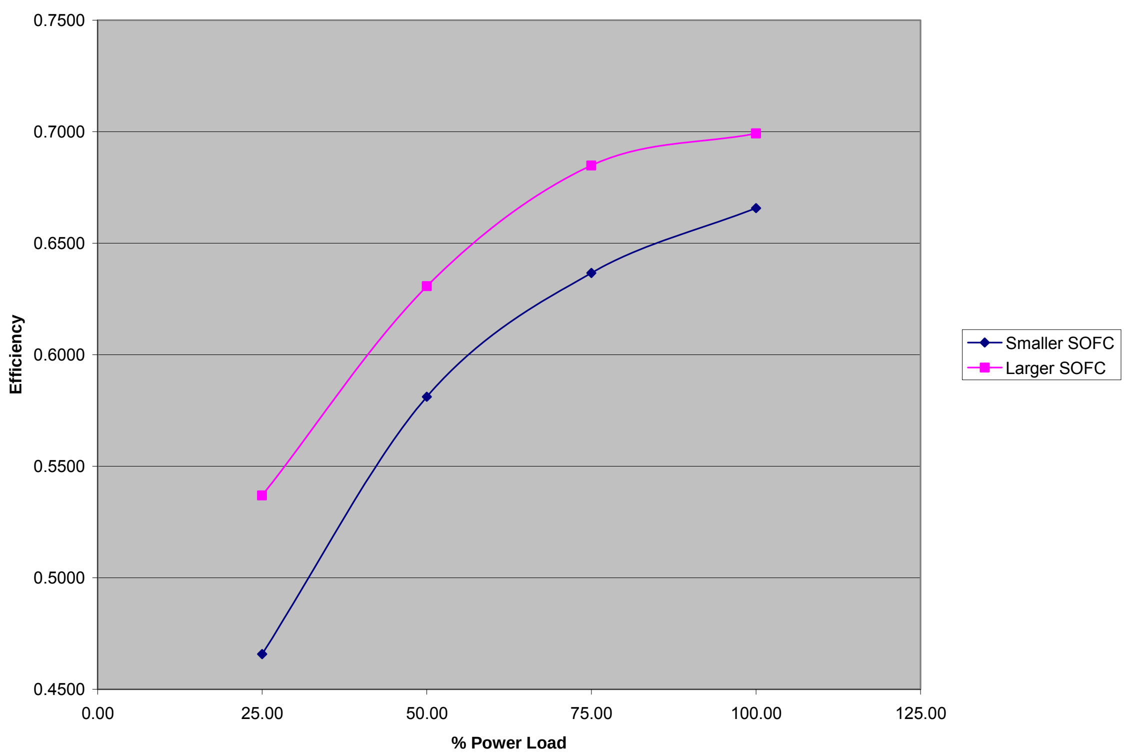

Figure B.16. Partial-load performance of the optimal 1.5 MWe SOFC-GT-ST hybrid plant, with a triple pressure with reheat ST cycle.

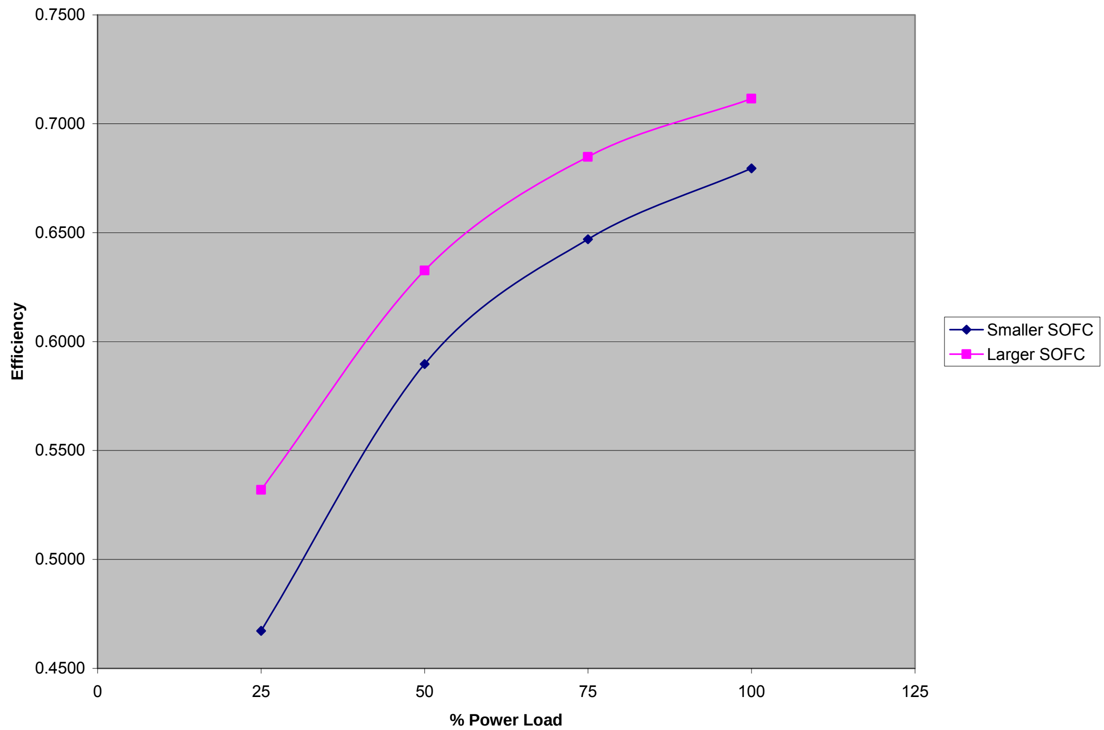

Figure B.17. Partial-load performance of the optimal 5 MWe SOFC-GT-ST hybrid plant, with a single ST cycle.

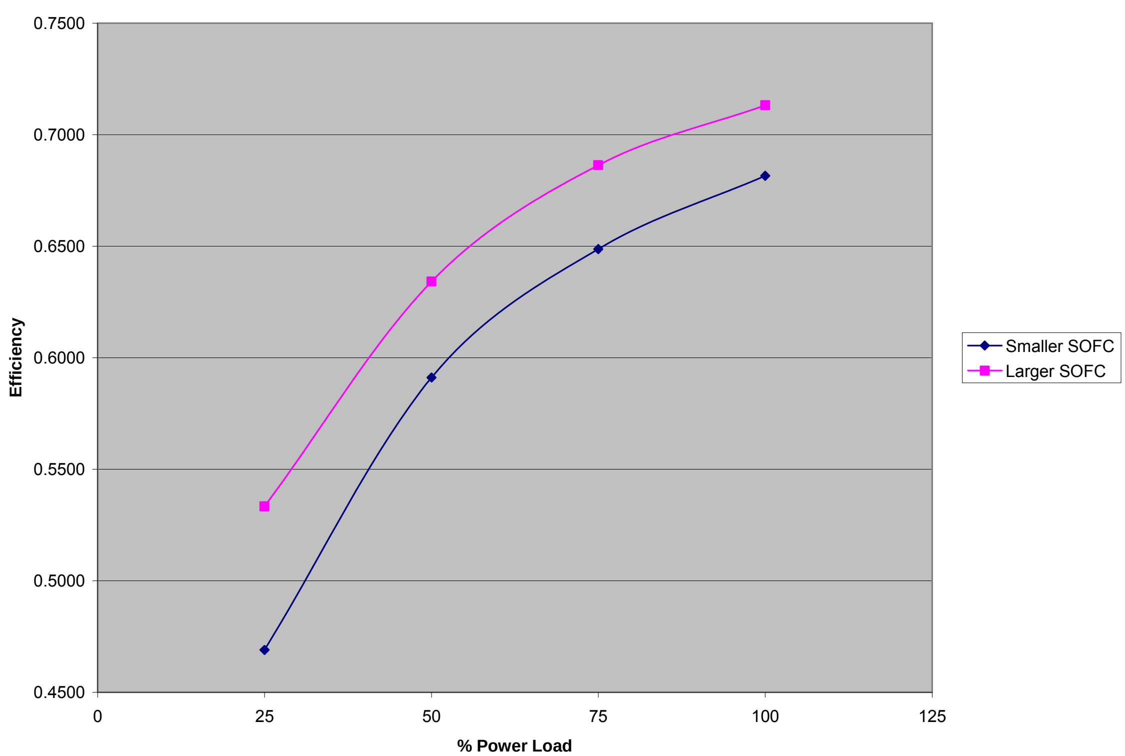

Figure B.18. Partial-load performance of the optimal 5 MWe SOFC-GT-ST hybrid plant, with a dual ST cycle.

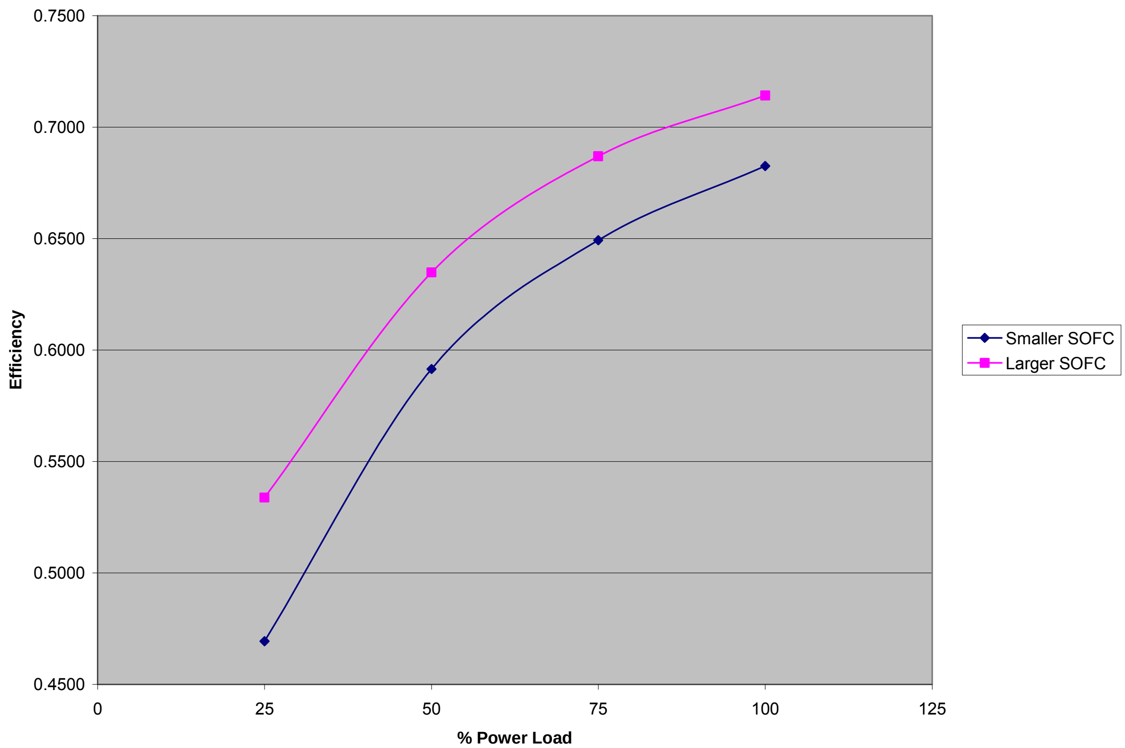

Figure B.19. Partial-load performance of the optimal 5 MWe SOFC-GT-ST hybrid plant, with a triple pressure ST cycle.

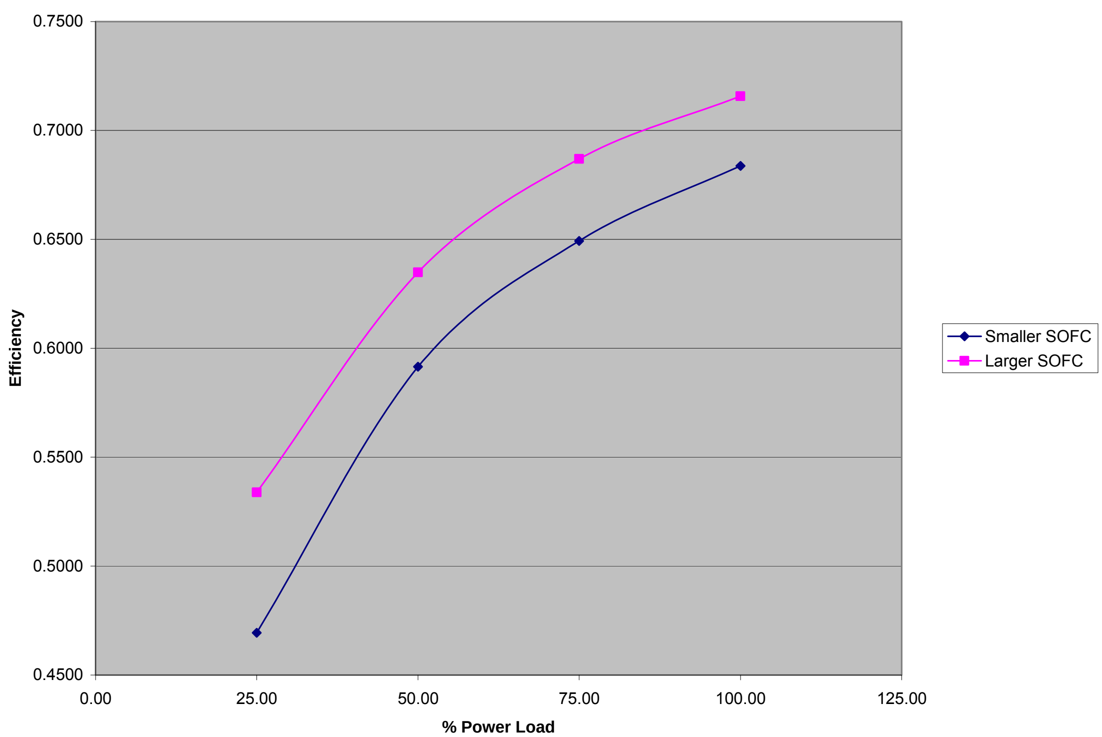

Figure B.20. Partial-load performance of the optimal 5 MWe SOFC-GT-ST hybrid plant, with a triple pressure with reheat ST cycle.

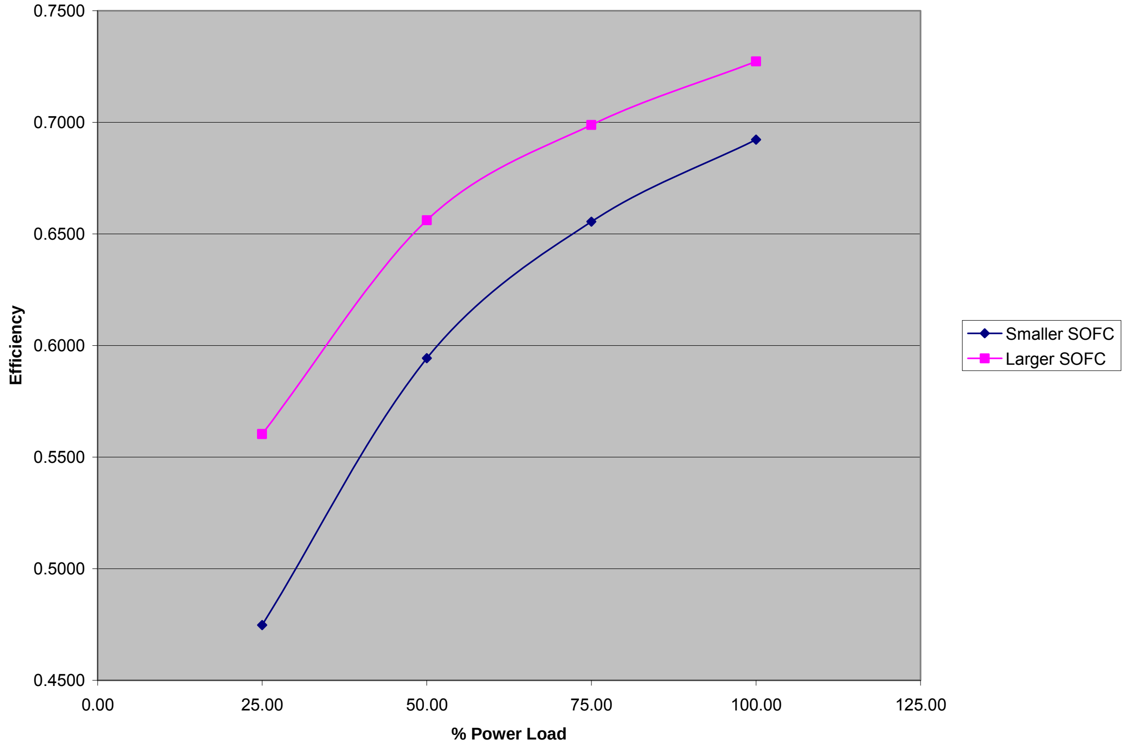

Figure B.21. Partial-load performance of the optimal 10 MWe SOFC-GT-ST hybrid plant, with a single ST cycle.

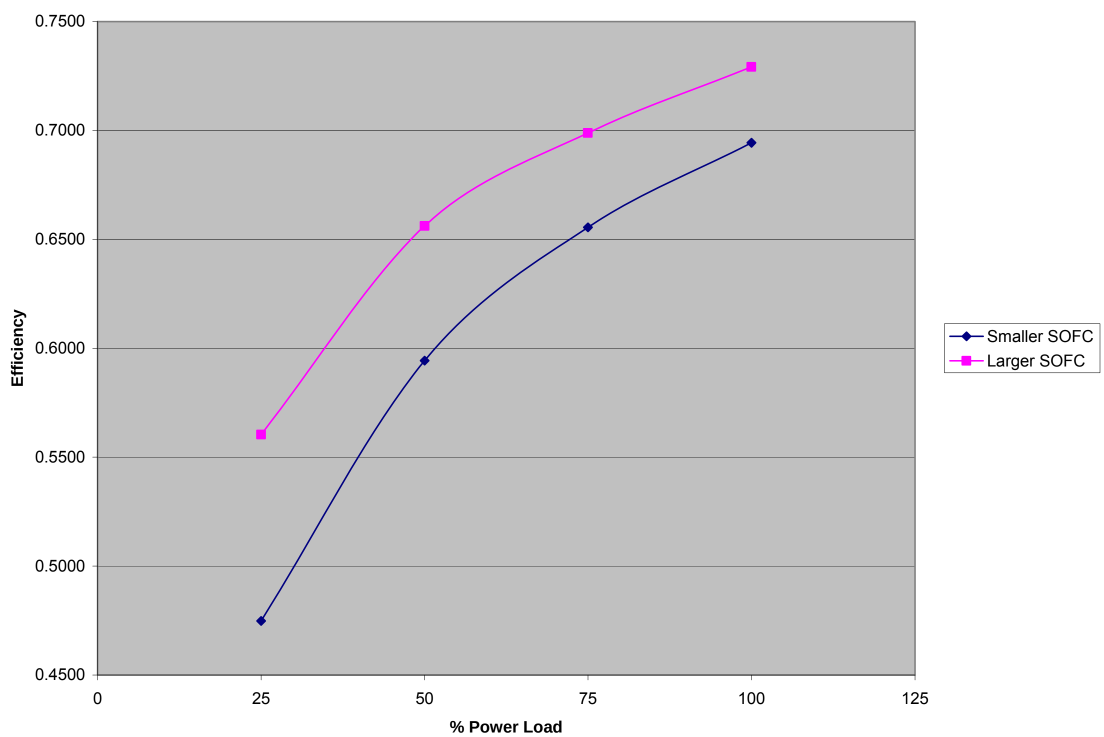

Figure B.22. Partial-load performance of the optimal 10 MWe SOFC-GT-ST hybrid plant, with a dual ST cycle.

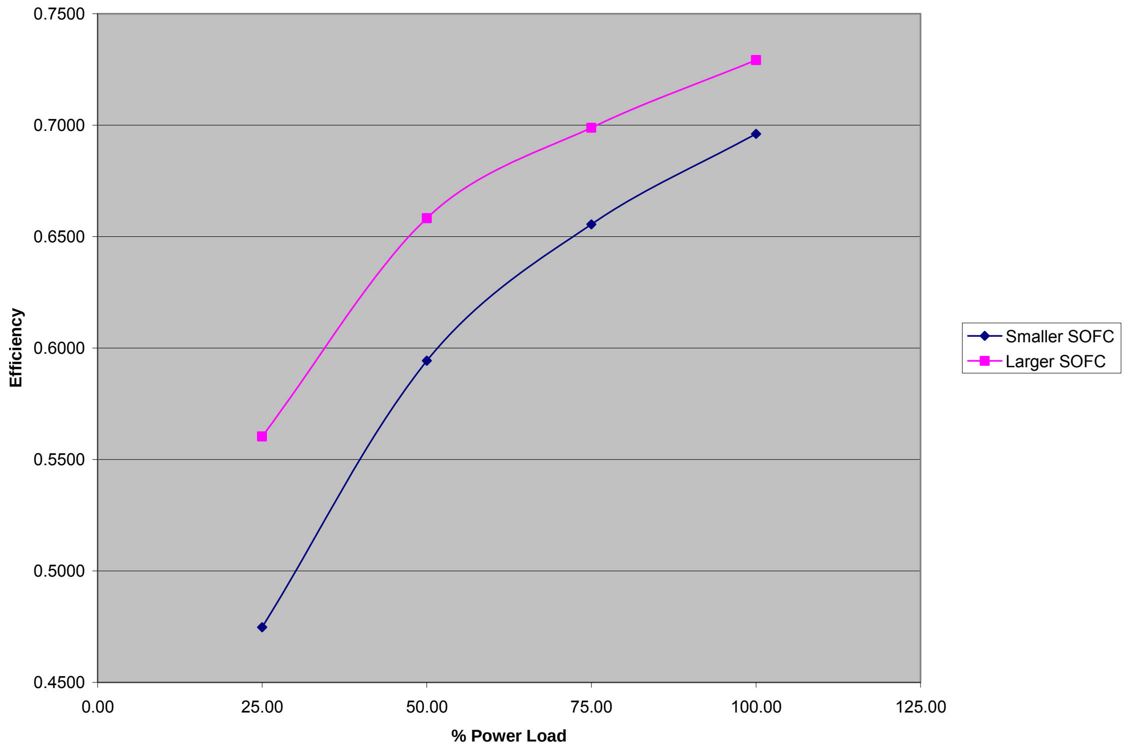

Figure B.23. Partial-load performance of the optimal 10 MWe SOFC-GT-ST hybrid plant, with a triple pressure ST cycle.

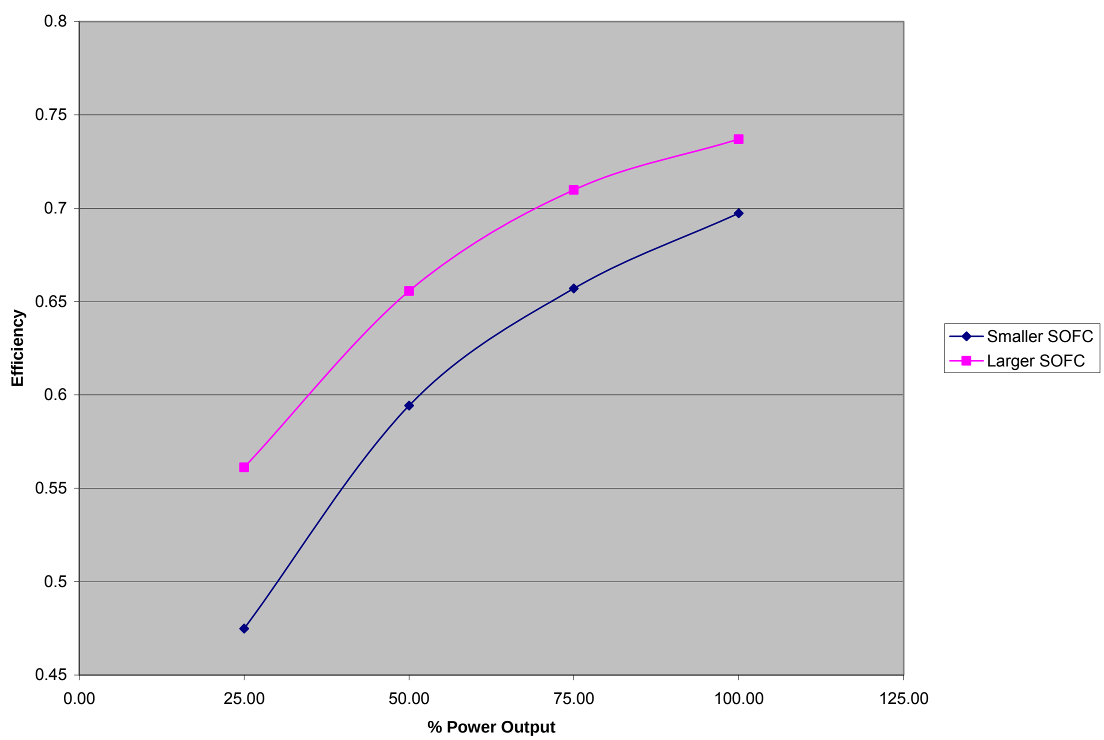

Figure B.24. Partial-load performance of the optimal 10 MWe SOFC-GT-ST hybrid plant, with a triple pressure with reheat ST cycle.

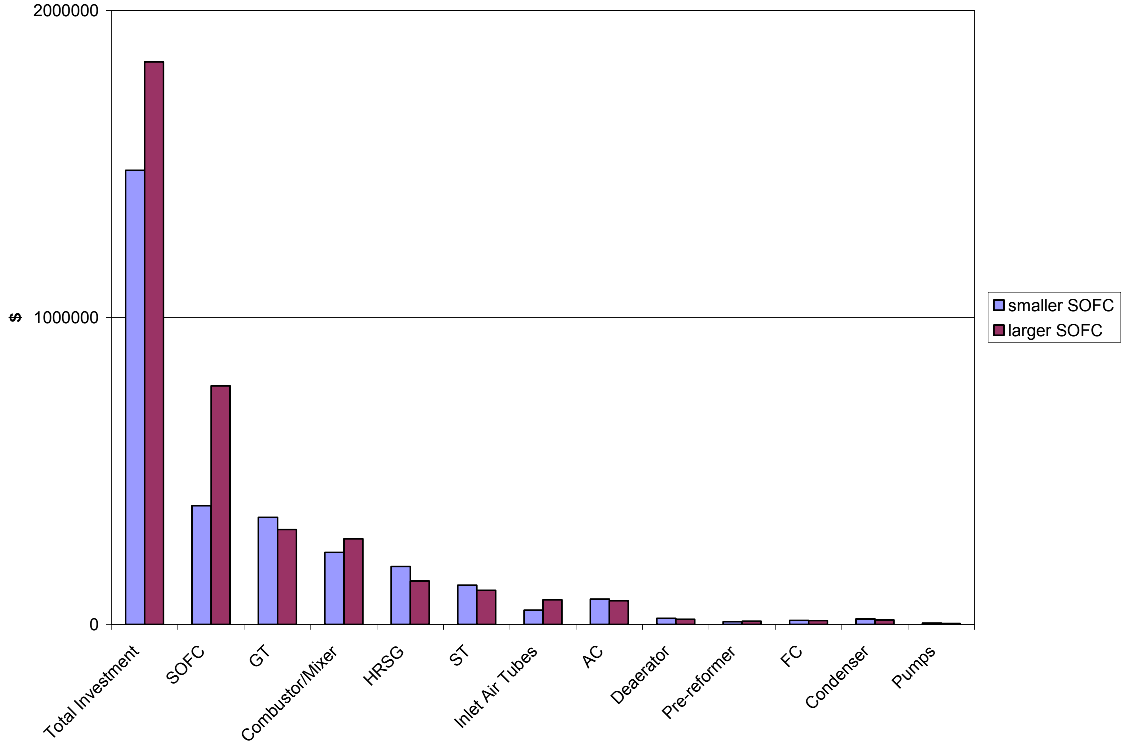

Figure B.25. Optimal component costs for the optimal 1.5 MWe SOFC-GT-ST hybrid plant, with a single pressure ST cycle.

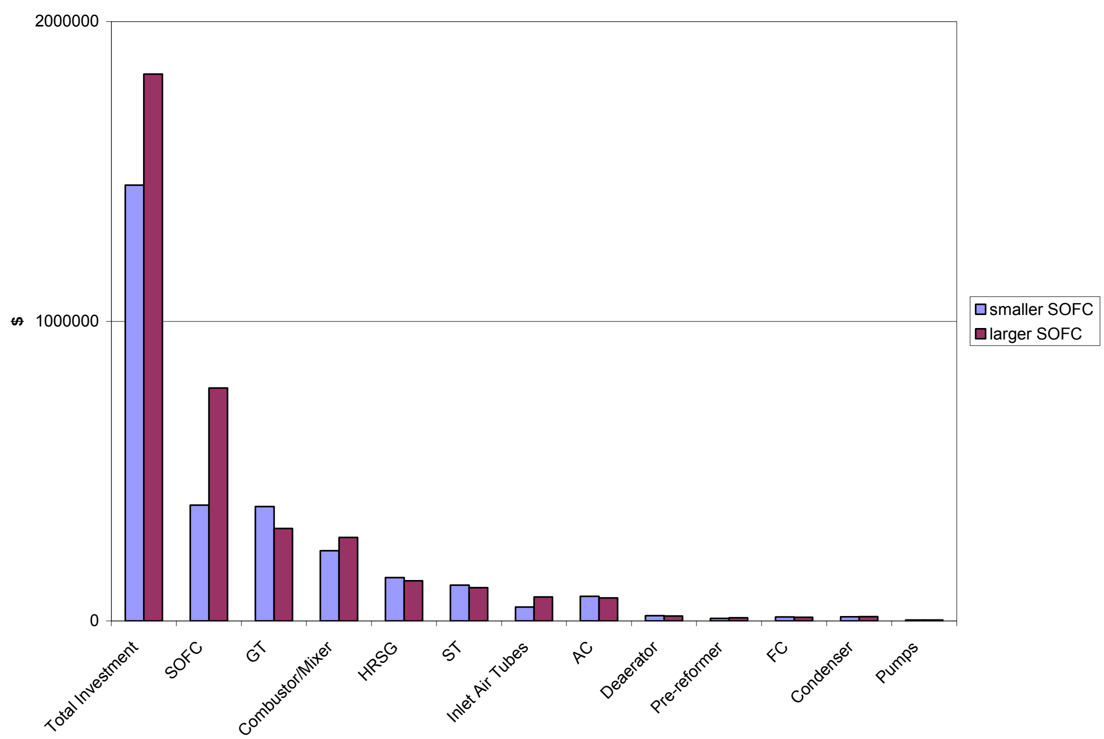

Figure B.26. Optimal component costs for the optimal 1.5 MWe SOFC-GT-ST hybrid plant, with a dual pressure ST cycle.

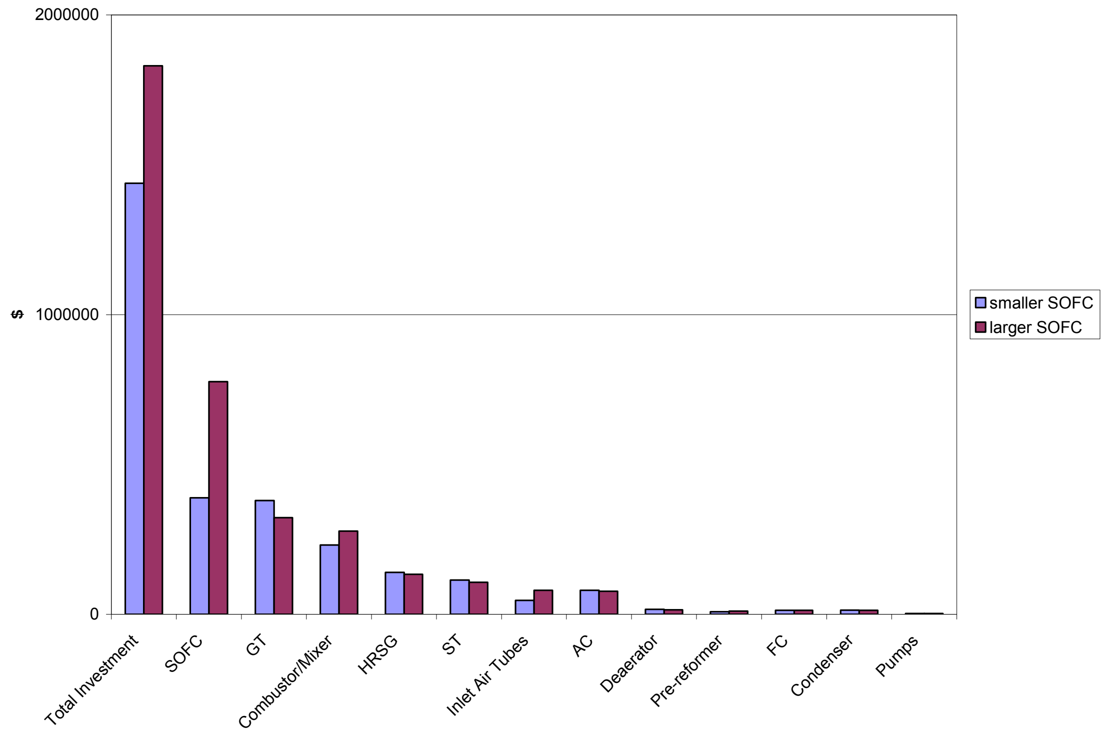

Figure B.27. Optimal component costs for the optimal 1.5 MWe SOFC-GT-ST hybrid plant, with a triple pressure ST cycle.

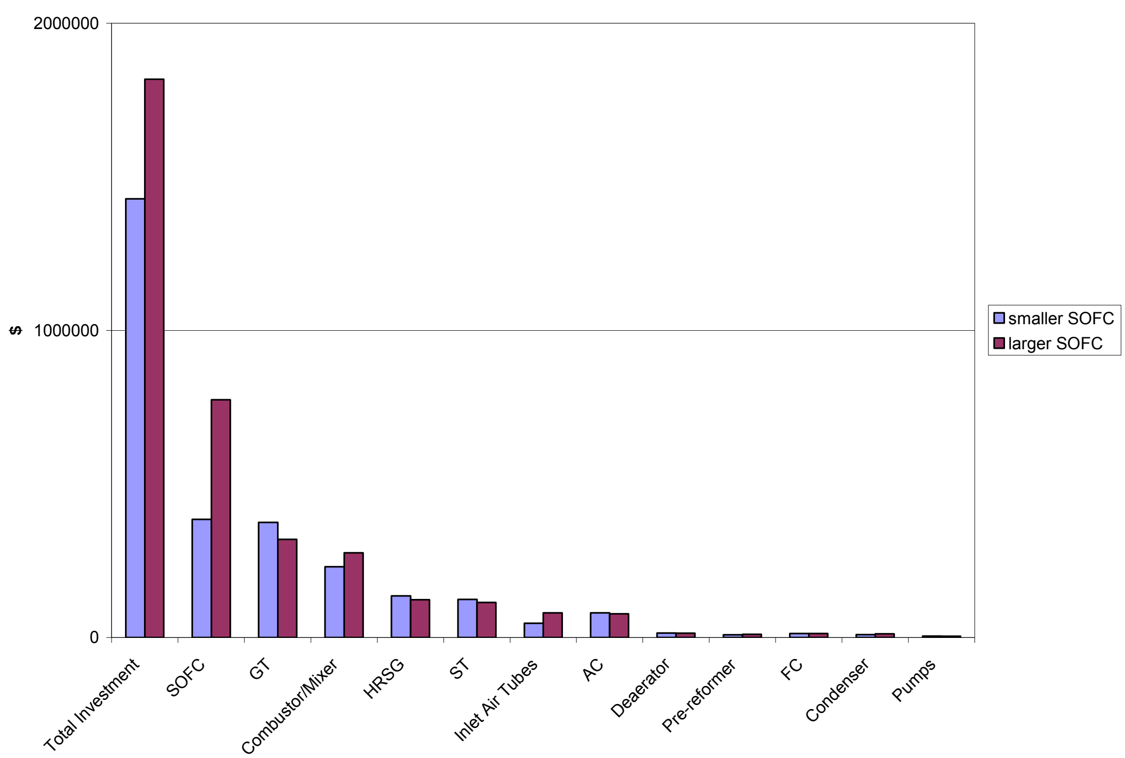

Figure B.28. Optimal component costs for the optimal 1.5 MWe SOFC-GT-ST hybrid plant, with a triple pressure with reheat ST cycle.

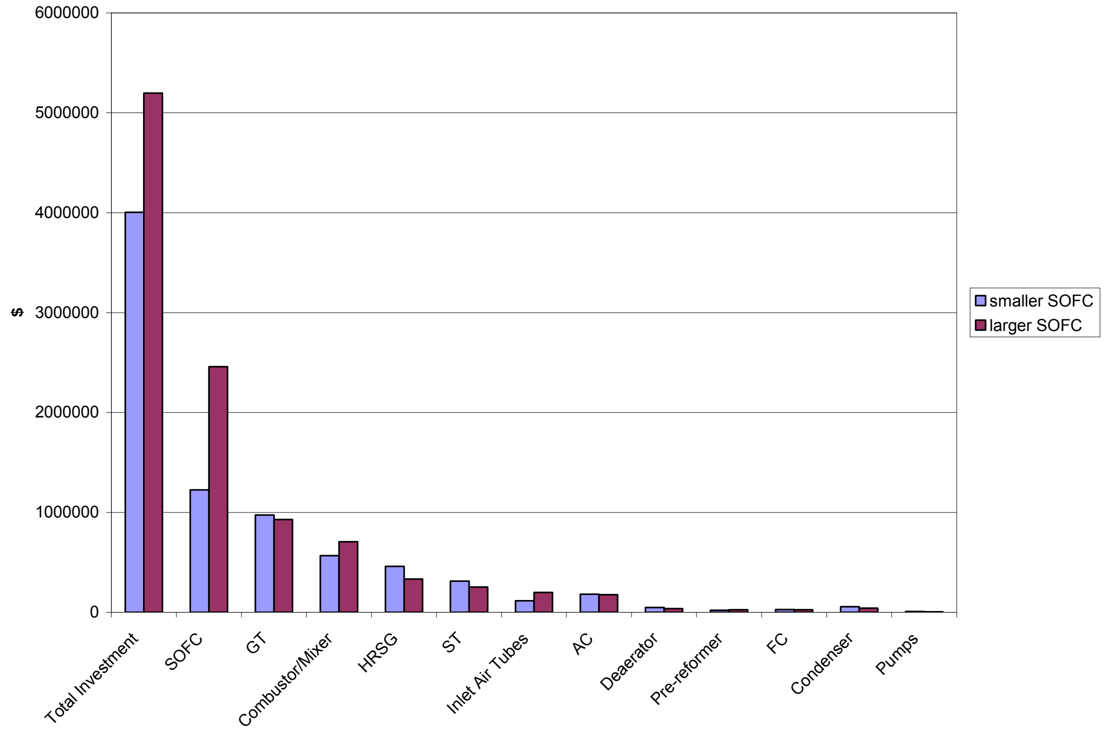

Figure B.29. Optimal component costs for the optimal 5 MWe SOFC-GT-ST hybrid plant, with a single pressure ST cycle.

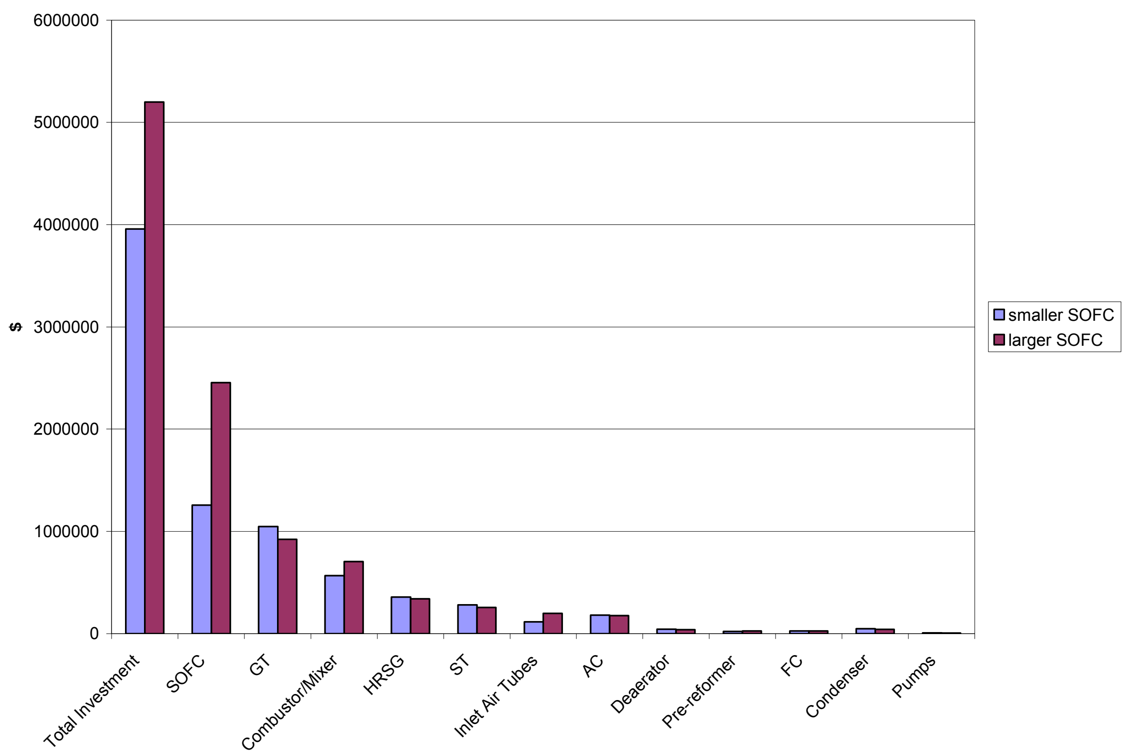

Figure B.30. Optimal component costs for the optimal 5 MWe SOFC-GT-ST hybrid plant, with a dual pressure ST cycle.

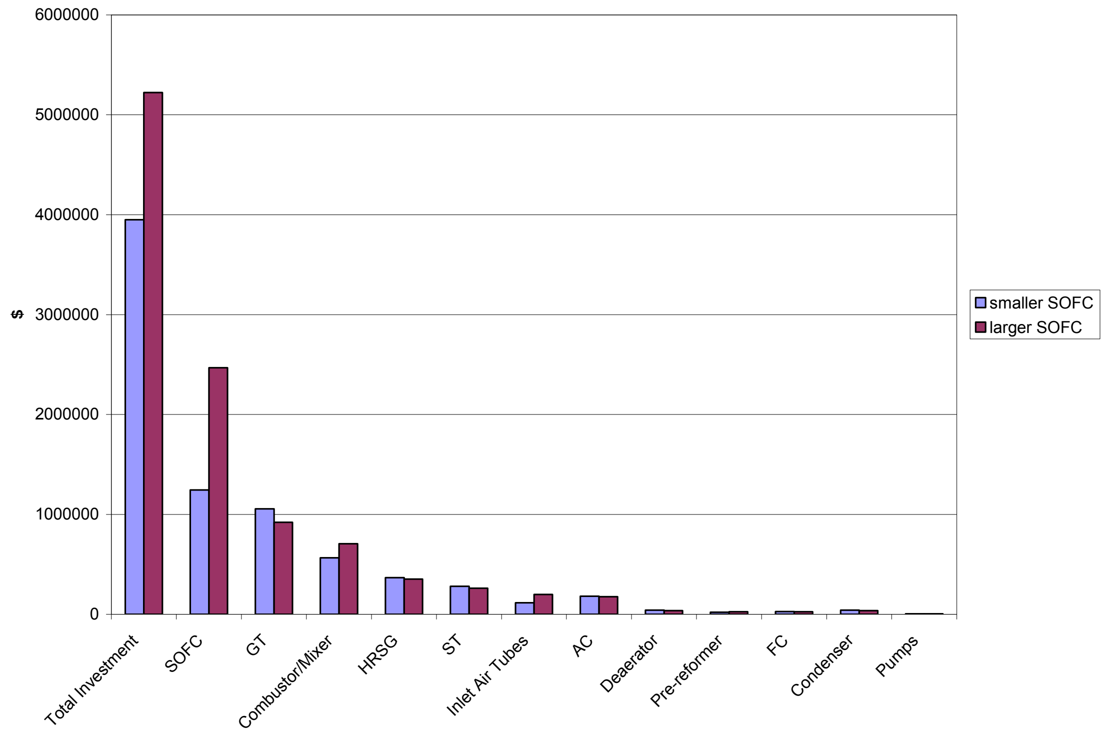

Figure B.31. Optimal component costs for the optimal 5 MWe SOFC-GT-ST hybrid plant, with a triple pressure ST cycle.

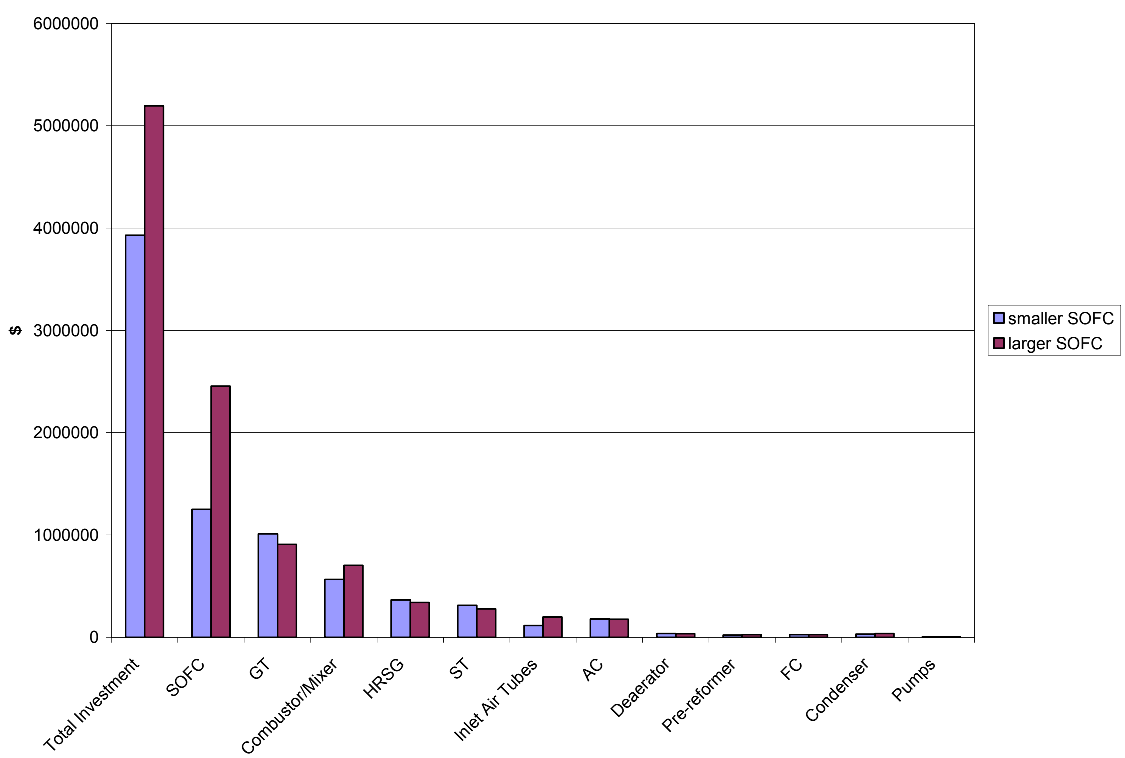

Figure B.32. Optimal component costs for the optimal 5 MWe SOFC-GT-ST hybrid plant, with a triple pressure with reheat ST cycle.

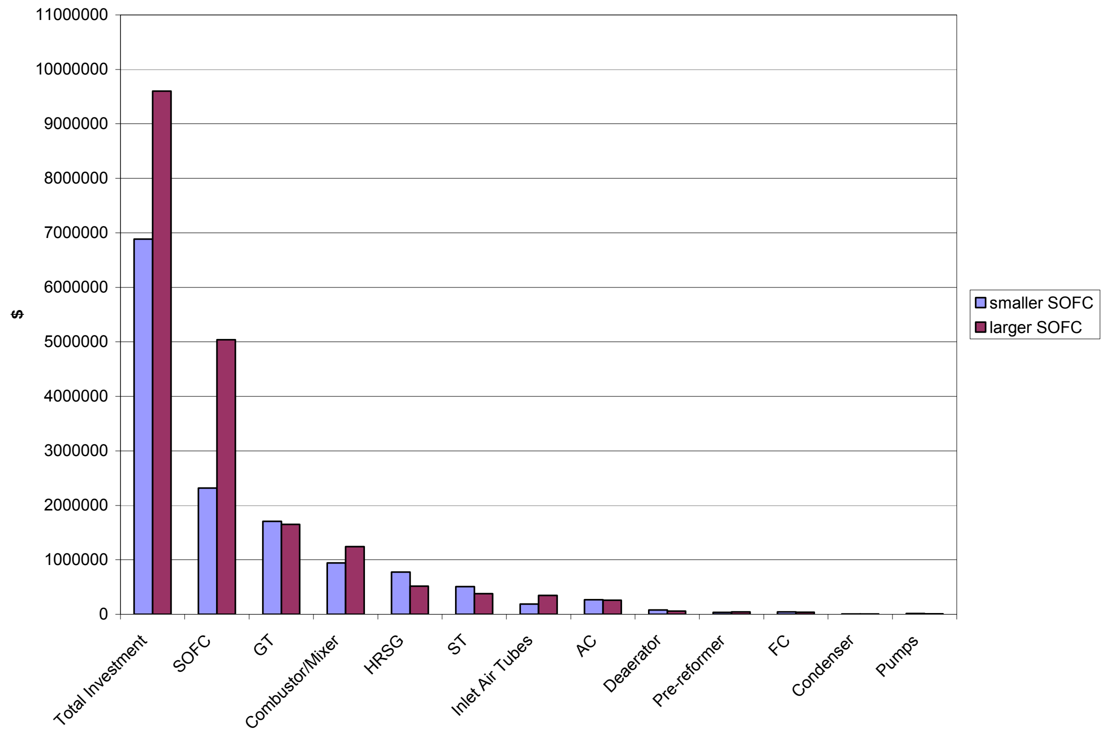

Figure B.33. Optimal component costs for the optimal 10 MWe SOFC-GT-ST hybrid plant, with a single pressure ST cycle.

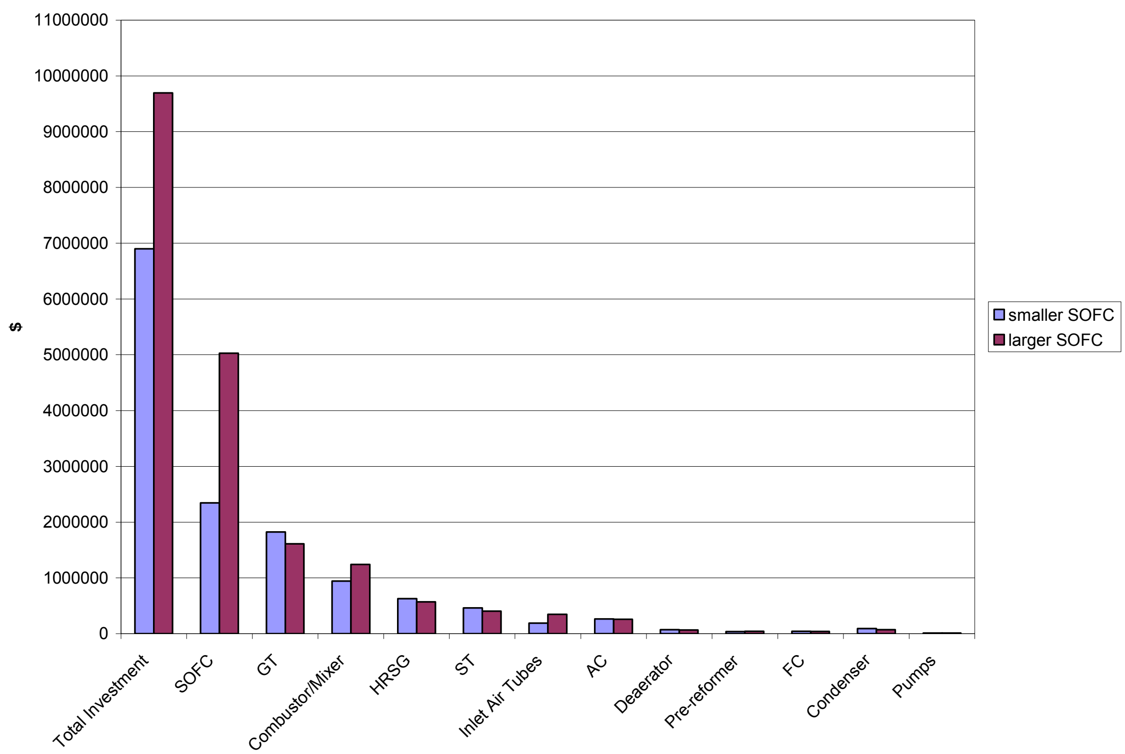

Figure B.34. Optimal component costs for the optimal 10 MWe SOFC-GT-ST hybrid plant, with a dual pressure ST cycle.

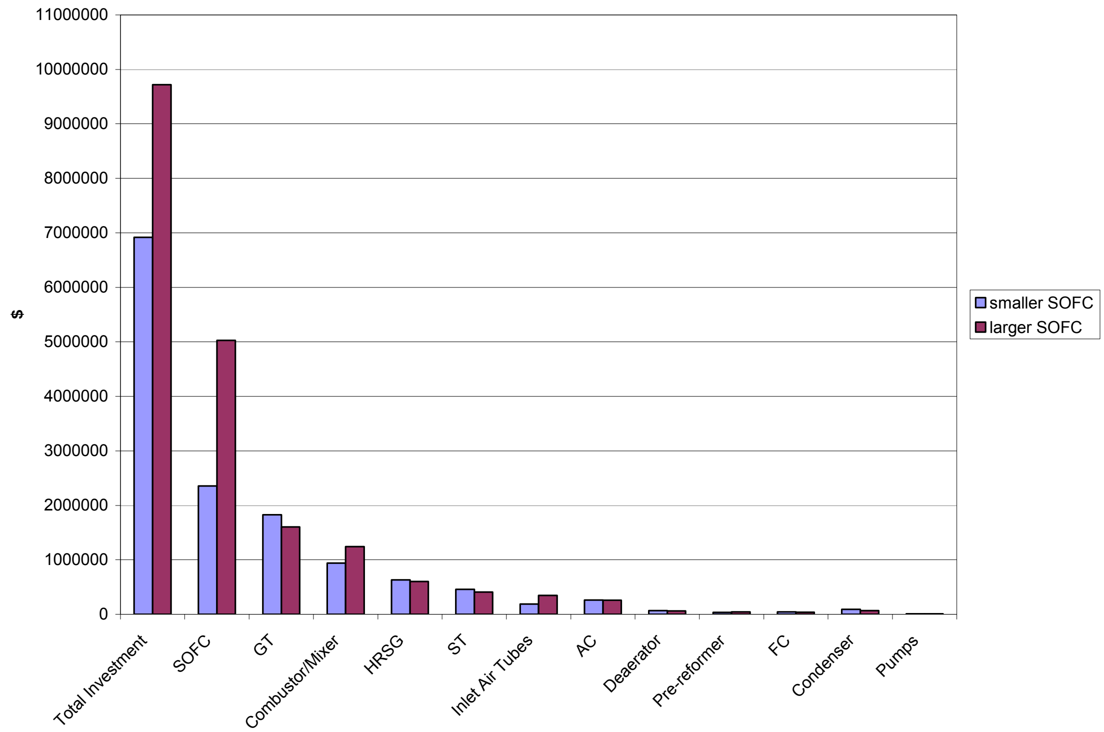

Figure B.35. Optimal component costs for the optimal 10 MWe SOFC-GT-ST hybrid plant, with a triple pressure ST cycle.

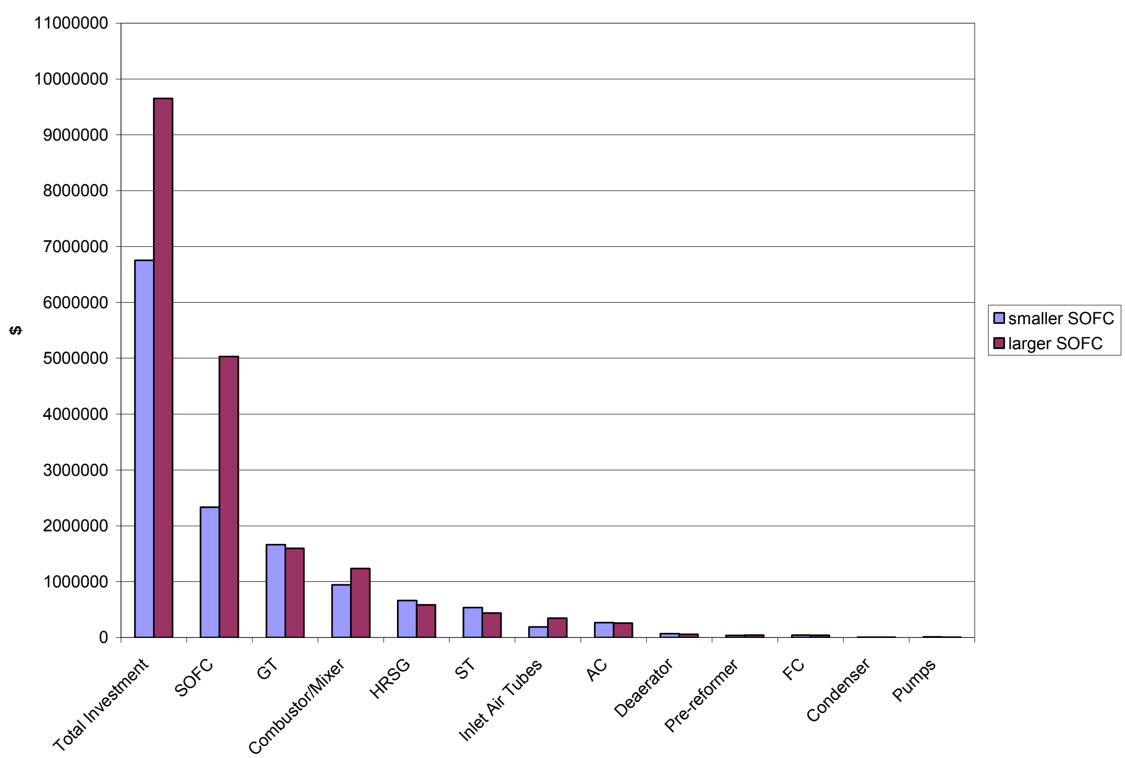

Figure B.36. Optimal component costs for the optimal 10 MWe SOFC-GT-ST hybrid plant, with a triple pressure with reheat ST cycle.

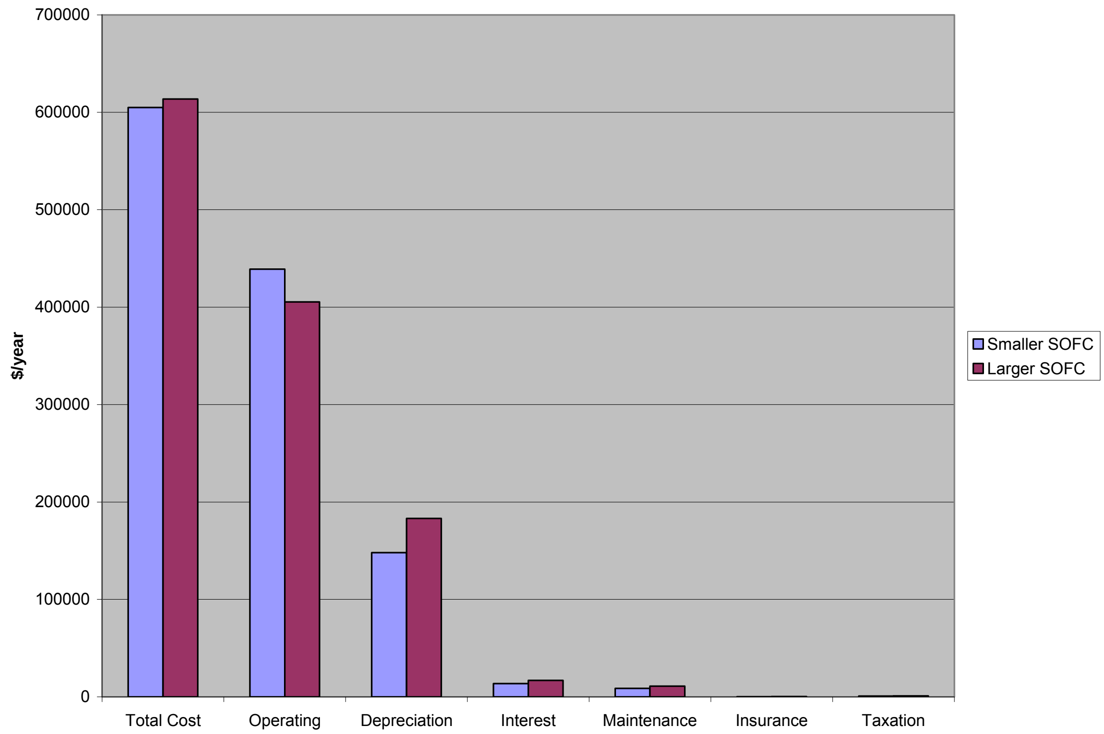

Figure B.37. Optimal annual costs for the optimal 1.5 MWe SOFC-GT-ST hybrid plant, with a single pressure ST cycle.

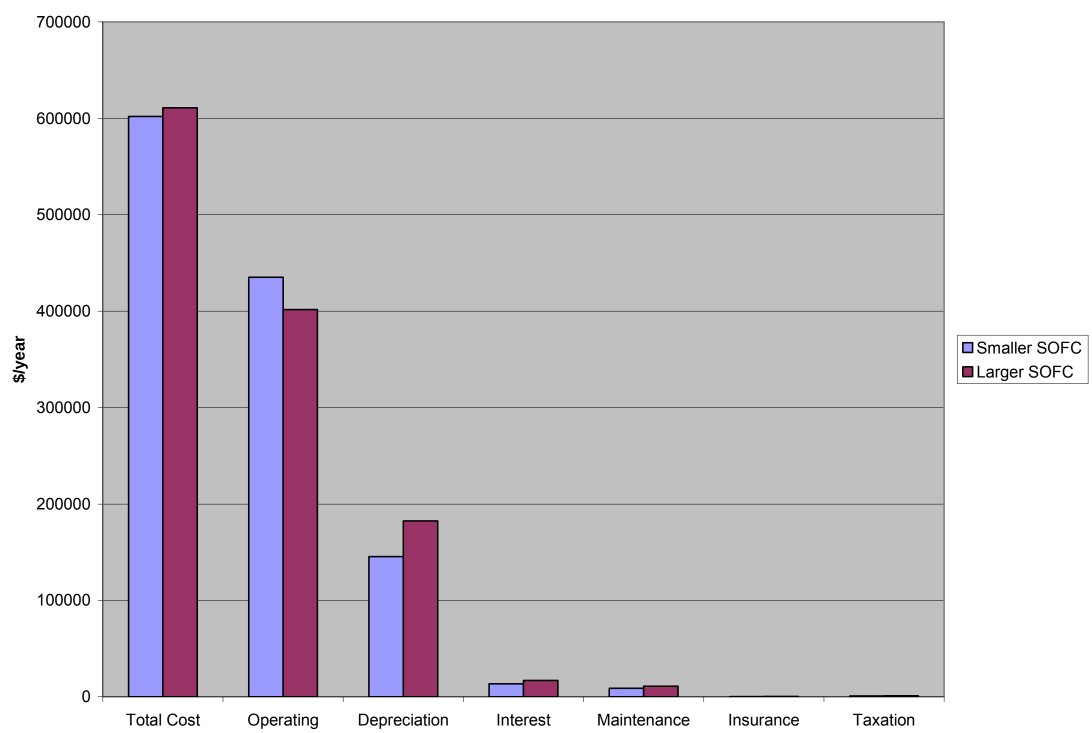

Figure B.38. Optimal annual costs for the optimal 1.5 MWe SOFC-GT-ST hybrid plant, with a dual pressure ST cycle.

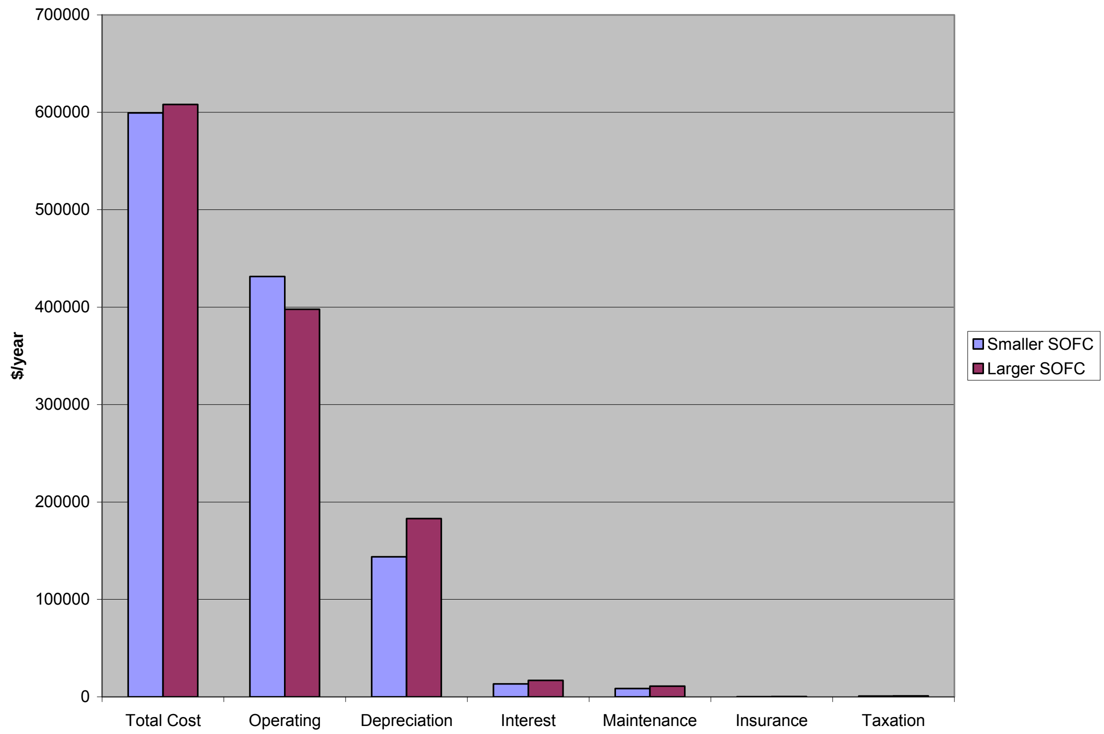

Figure B.39. Optimal annual costs for the optimal 1.5 MWe SOFC-GT-ST hybrid plant, with a triple pressure ST cycle.

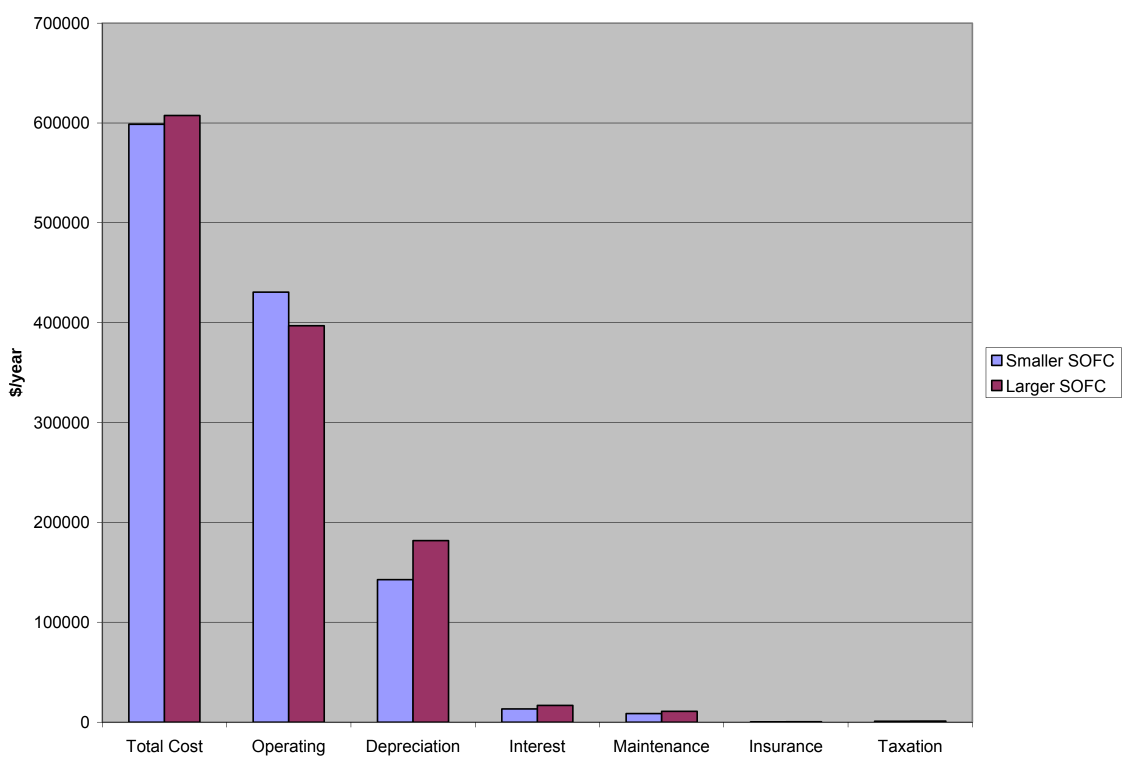

Figure B.40. Optimal annual costs for the optimal 1.5 MWe SOFC-GT-ST hybrid plant, with a triple pressure with reheat ST cycle.

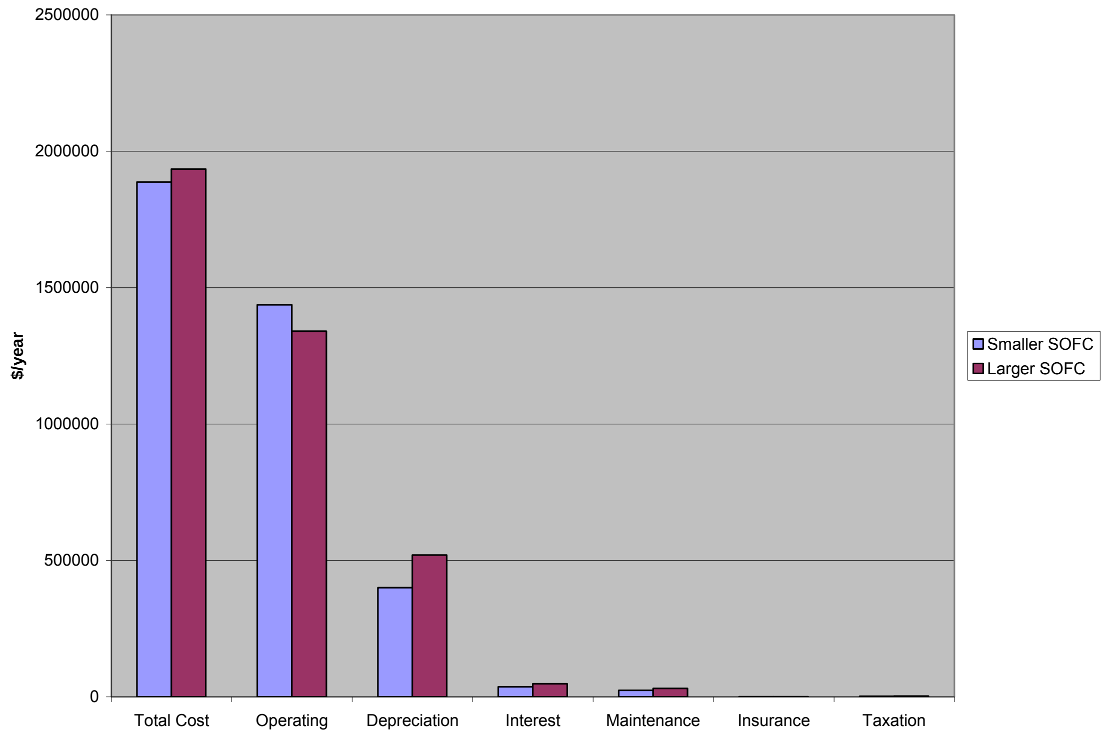

Figure B.41. Optimal annual costs for the optimal 5 MWe SOFC-GT-ST hybrid plant, with a single pressure ST cycle.

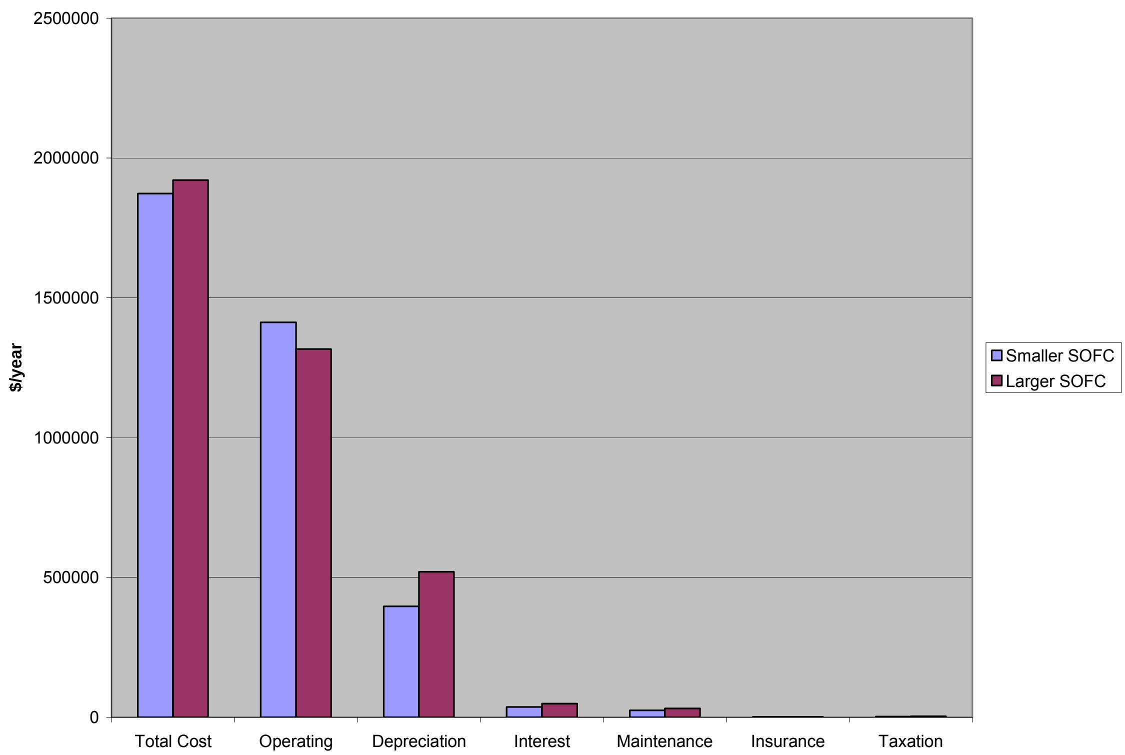

Figure B.42. Optimal annual costs for the optimal 5 MWe SOFC-GT-ST hybrid plant, with a dual pressure ST cycle.

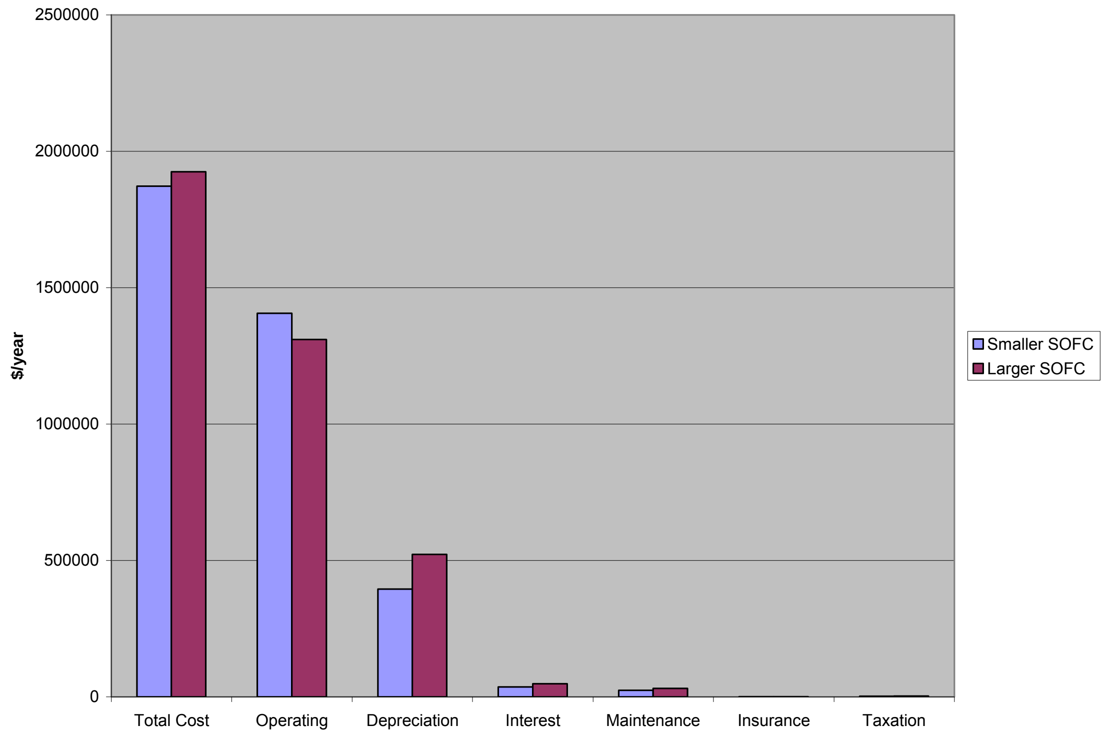

Figure B.43. Optimal annual costs for the optimal 5 MWe SOFC-GT-ST hybrid plant, with a triple pressure ST cycle.

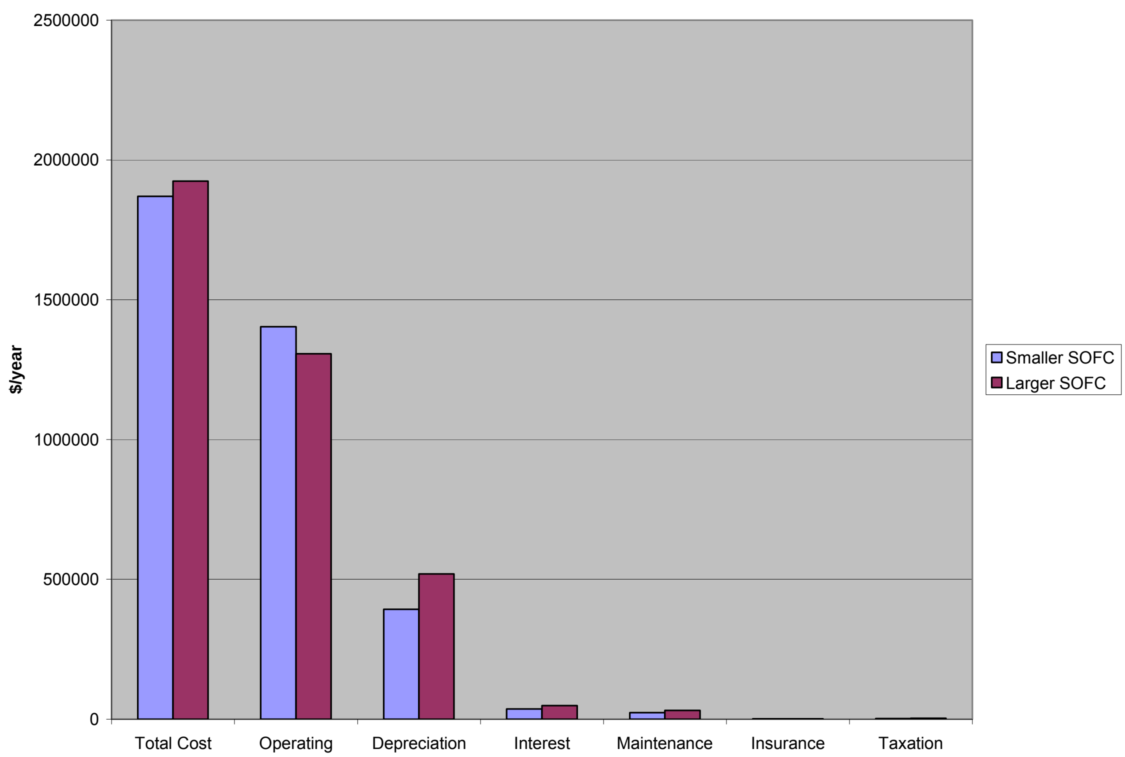

Figure B.44. Optimal annual costs for the optimal 5 MWe SOFC-GT-ST hybrid plant, with a triple pressure with reheat ST cycle.

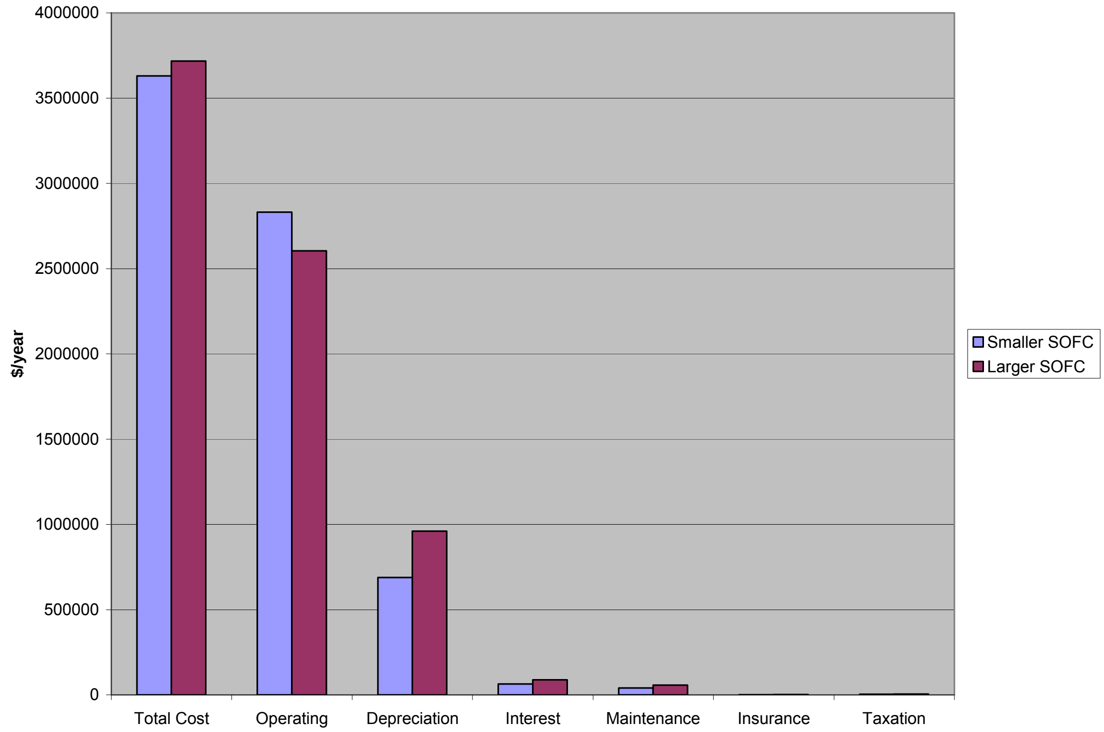

Figure B.45. Optimal annual costs for the optimal 10 MWe SOFC-GT-ST hybrid plant, with a single pressure ST cycle.

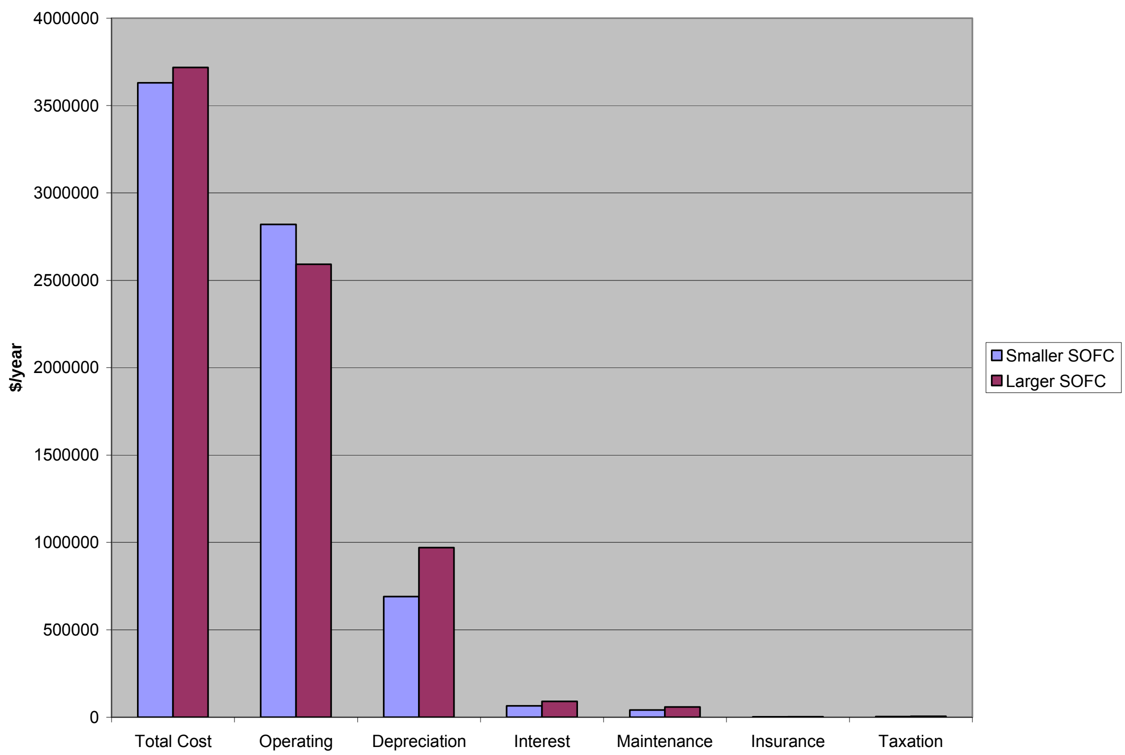

Figure B.46. Optimal annual costs for the optimal 10 MWe SOFC-GT-ST hybrid plant, with a dual pressure ST cycle.

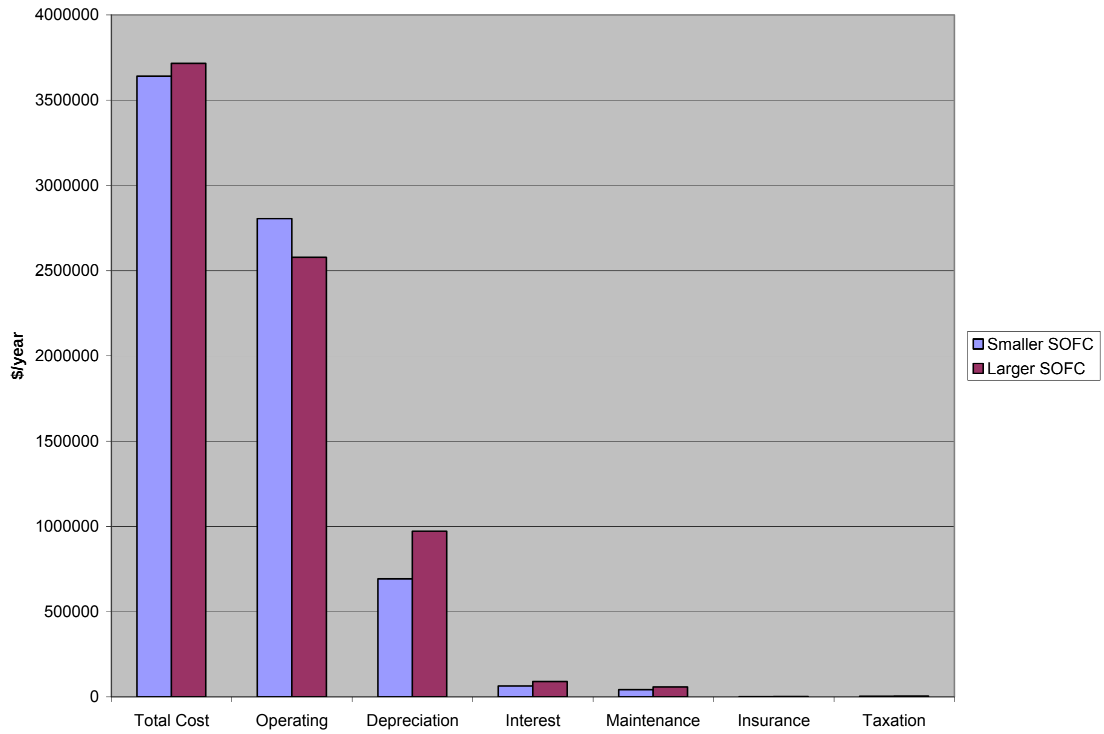

Figure B.47. Optimal annual costs for the optimal 10 MWe SOFC-GT-ST hybrid plant, with a triple pressure ST cycle.

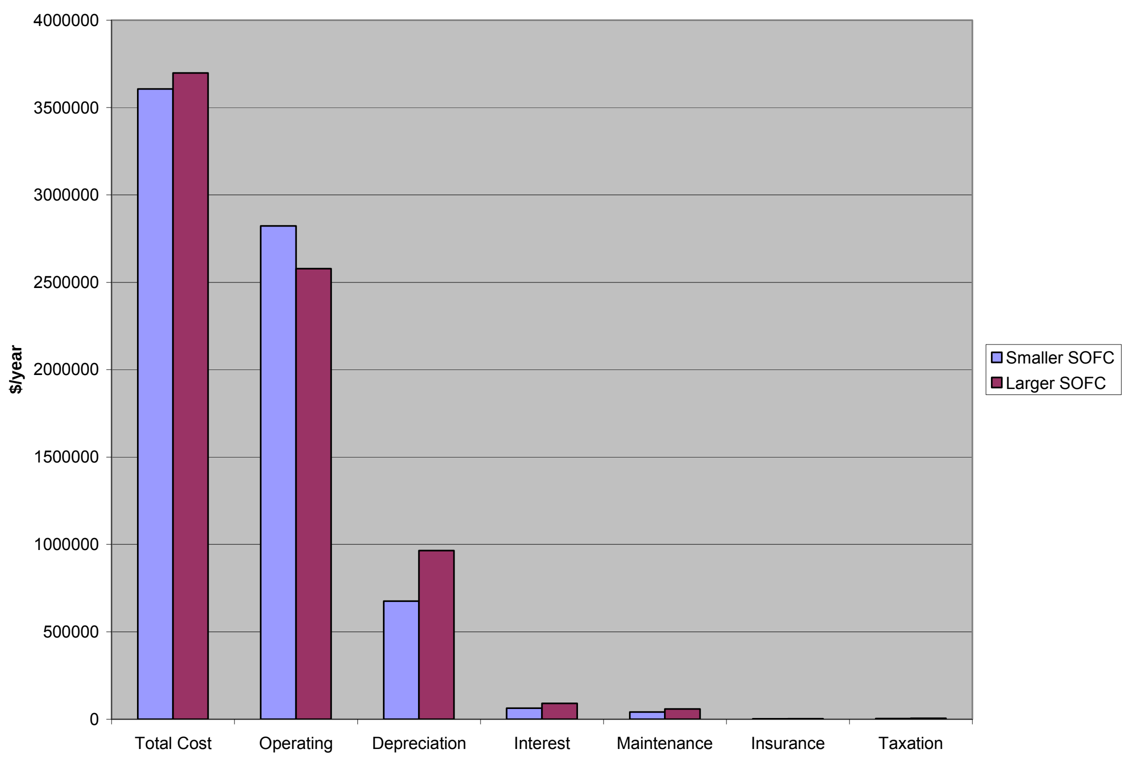

Figure B.48. Optimal annual costs for the optimal 10 MWe SOFC-GT-ST hybrid plant, with a triple pressure with reheat ST cycle.

Vita

Alexandros Arsalis

Alexandros Arsalis was born in Nicosia, Cyprus on July 4, 1977. In 1999 he graduated with a Higher National Diploma in Marine Engineering, Higher Technical Institute, Nicosia, Cyprus. During these studies he also gained some practical experience as a cadet engineer in commercial shipping (M/V Salamis Glory, 1998). After completing a two-year military service from 1999 to 2001 he joined the mechanical engineering undergraduate program at Old Dominion University, Norfolk, Virginia, USA. In 2004 he graduated with a B.S. degree in mechanical engineering with a minor in mathematics, cum laude. In 2005 he joined the mechanical engineering graduate program at the Virginia Polytechnic Institute and State University, Blacksburg, Virginia, USA where he conducted research in the area of hybrid fuel cell systems.